UNIVERSIDAD COMPLUTENSE DE MADRID
FACULTAD DE CIENCIAS FÍSICAS

TESIS DOCTORAL

From 2D to 3D chiral systems made of plasmonic and magnetoplasmonic building blocks: fabrication, characterization and analysis

De Sistemas quirales 2D a 3D fabricados a partir de bloques plasmónicos y magnetoplasmónicos: fabricación, caracterización y análisis

MEMORIA PARA OPTAR AL GRADO DE DOCTORA

PRESENTADA POR

Carolina de Dios Fernández

DIRECTOR

José Luis Costa Krämer

Madrid

UNIVERSIDAD COMPLUTENSE DE MADRID
FACULTAD DE CIENCIAS FÍSICAS

FROM 2D TO 3D CHIRAL SYSTEMS MADE OF PLASMONIC AND MAGNETOPLASMONIC BUILDING BLOCKS: FABRICATION, CHARACTERIZATION AND ANALYSIS

De Sistemas quirales 2D a 3D fabricados a partir de bloques plasmónicos y magnetoplasmónicos:
Fabricación, caracterización y análisis

Carolina de Dios Fernández

Memoria presentada para optar al título de doctor

Director
Dr. José Luis Costa Krämer

Tutora
Dra. Rocío Ranchal Sánchez
2020

TABLE OF CONTENT

ACKNOWLEDGEMENTS

Esta tesis para mí ha sido una compleja etapa en la vida, como esos puzles de miles de piezas donde hay mucho cielo y nunca parece que van a terminar...Ha sido difícil, a veces demasiado larga, pero ha sido maravillosa y la repetiría sin dudarlo. A lo largo de estos 4 años, he madurado y he aprendido sobre Ciencia, pero también sobre la vida y las personas, y a veces he pensado que la ciencia es más sencilla.

En primer lugar, quiero agradecer a Alfonso Cebollada y Gaspar Armelles, la confianza depositada en mí en este proyecto. Me abristeis las puertas de vuestro grupo, me enseñasteis todo sobre Plasmónica y me ayudasteis en lo que he reflejado en este trabajo. Gracias Alfonso por tu dedicación, por tus enseñanzas en el laboratorio sobre la fabricación de nanoestructuras y el cuidado de los sistemas experimentales, he aprendido mucho de tu organización en el laboratorio. Gracias Gaspar, por enseñarme parte de tu conocimiento infinito sobre la óptica y por discutir los datos y desentrañar los secretos tras las medidas del elipsómetro, que generalmente con un simple vistazo intuías. Entre los dos me distéis la oportunidad de comenzar una carrera científica y estoy muy agradecida por ello, gracias.

Quiero hacer una mención especial a José Luis Costa porque me ayudó en una compleja situación y en muy poco tiempo, me apoyó y me dirigió hasta lo que hoy presento, gracias por salirte de lo normal y mojarte, gracias.

Quiero dar las gracias a Carmen Simón, Federico Mompeán y Rocío Ranchal que me han apoyado y ayudado muchísimo, gracias por permitirme llegar hasta aquí. Carmen y Federico, gracias porque en poco tiempo habéis hecho posible lo imposible. Rocío, tengo que serte sincera, tú eres vital en mi vida científica. Eres la persona con la que descubrí mi amor por la ciencia, haciendo el TFM contigo en el ISOM y siempre me has ayudado en el proceso. Gracias por todo.

En el IMN, muchas gracias al grupo de MetalNano por toda la ayuda durante la realización de la tesis. A Huayu que con paciencia me enseñó la litografía coloidal. Gracias Chemi por enseñarme tanto ciencia con clases sobre AFM o Sputtering, como deportes, cine, arte…gracias por tus charlas en el comedor.

Acknowledgements

Gracias Fernando por ayudarme a optimizar las nanoestructuras mediante tus programas de Labview. A MaríaU por estar siempre sonriente y dispuesta a resolver cualquier duda que surgiese. Y, por último, gracias Antonio sobre todo por ser tú. Me has enseñado la pasión por la ciencia, eres mi modelo de científico, gracias por esas tardes de cafecito y esa pasión por comprender la ciencia y divertirse. Por ser mi compañero de congresos y mostrarme lo importante que es la colaboración en ciencia. Te recuerdo un día explicando redes con botellines a estudiantes. Eres un gran científico y una gran persona, gracias.

Tengo que decir, que estos años he compartido despacho con gente maravillosa a la que agradezco su ayuda. A Martín, que me enseñó el mate y a soñar con la Comarca. A Sahba que me ha enseñado a luchar por un sueño sin importar cuál, cuida mucho de Chopin. Por último, Alba gracias por tu apoyo y tu amistad, te debo ir a Ávila, aunque Madrid mole más (la le lo).

Tienen un lugar especial en todo este viaje las personas con las que he convivido día a día en el laboratorio, especialmente Raquel y Lorena, que me guiaron por el laboratorio y tuvieron la paciencia de enseñarme todo sobre medidas de equipos. Gracias por las medidas de SEM presentadas en esta tesis. Me quedo con las charlas gatunas y fotos de Azpi. Gracias a David, Patricia y Carmen por toda la ayuda en el laboratorio estos años atrás. Gracias a Manuel, que para mí siempre será el corazón del IMN. Gracias por tu pasión y por creer en mí siempre. Eres una buenísima persona y te agradezco tus caras sonrientes.

Aunque a veces tuve situaciones difíciles en el laboratorio, siempre encontré una sonrisa amiga en el grupo de becarios y postdocs del IMM-IMN por el ambiente en el trabajo durante estos años. Especialmente a Marina, Álvaro, Vero, compañeros de comida y café. Gracias a Alberto por ser mi compañero de Findes Científicos y por tu conocimiento infinito desde los Simpson hasta legislación. A Andrés por esas charlas sobre la vida en la biblioteca. Muchas gracias al personal Administrativo y al resto del personal titular del instituto.

Ahora, fuera del IMN, quiero agradecer a mi segunda familia científica, al grupo GFMC de la UCM, por hacerme sentir un miembro más. Gracias a Gloria, David, Andrea, Fabián, Víctor, Javi, Alberto, Mariona y Ana por ser mi familia científica. Gloria gracias por tu amistad y tus viajes por las islas. A David, gracias por estar siempre dispuesto a ayudarme y por no decir nunca que no

Acknowledgements

a una quedada de juegos de mesa con veinte desconocidos, estoy segura de que serás un gran investigador. Por último, gracias a Alberto y a Jacobo, por su ayuda científica y personal. Especialmente al capitán de este grupo, que como buen Profesor ha sido el motor para que esto saliera, gracias por todo.

Gracias a la Gallega, Asunción y Carmen por su pasión por la enseñanza de la ciencia. Vosotras despertasteis mi espíritu crítico y el interés por la ciencia y la docencia.

Gracias a mis compañeros de Físicas y osciloscopiojos, a Rober, Alicia, Víctor, Icíar, Guille, Carlos, Manu, Ana, Adri y Sara. Gracias a Rober por su revisión del inglés en la tesis, por su paciencia y sus consejos. Os quiero a todos muchísimo y os agradezco vuestros consejos científicos y personales. Cada uno sabéis lo que significáis para mi…gracias por creer en mí, por apoyarme en todo, por todos los momentos buenos y malos juntos. Mando mi cariño especialmente a Sara y a Víctor, que este año han demostrado que son muy fuertes y luchadores.

Gracias a los chumachos, a Chema, Jordi y Laura, por nuestros viajes a Salamanca y nuestras charlas científicas. Gracias a Jorge, Gonzalo Tito, Bea, Tania, Sousa, Álvaro, Julia, Adri y Cris por vuestro apoyo incondicional. Muchas gracias a Jose, Luz y Eva por vuestra amistad desde que tengo memoria.

Quiero agradecer a mi familia todo el amor en estos años. A mi tía Nati por amar y cuidar a Candela. A mis primos Suso, Ana y a mi tía Encarna, por sus mensajes positivos. A María Luisa por ser mi segunda madre y a Juan por sus consejos y sus intensos debates de sobremesa. Gracias a mis hermanas de vida, Raquel y Nadia, que me han enseñado el verdadero significado de la familia. A mi madre, que inventó la palabra madre coraje y siempre ha demostrado la fuerza y valentía. A mi hermana que es el pilar de mi vida.

Por último, quiero dar las gracias a Fer, mi mitad, mi amigo y compañero de aventuras. Juntos somos fuertes, invencibles…nada es imposible a tu lado… Y por ti saltaré todas las vallas, vayas donde vayas. Besaré tus huellas en el suelo, porque te quiero.

Acknowledgements

RESUMEN

Se presenta un estudio experimental exhaustivo y detallado para entender la respuesta quiral de nanoestructuras plasmónicas quirales complejas a partir de las respuestas aquirales de sus bloques constituyentes. Esto conlleva diferentes estructuras fabricadas, desde simples nano-objetos como barras o dímeros de discos compuestos por metal o dieléctrico, hasta nanoestructuras más complejas ensambladas en el plano (estructuras bidimensionales) o apiladas perpendicularmente al plano (estructuras tridimensionales). En el proceso de fabricación se utiliza la litografía coloidal de máscara de agujeros y la evaporación multieje, una técnica de fabricación potente y económicamente asequible, capaz de obtener una gran variedad de estructuras en grandes áreas. Además de los cambios morfológicos, se han variado parámetros tales como la composición y la disposición espacial de las piezas constituyentes, a fin de estudiar su influencia en la respuesta óptica. Estos parámetros se optimizan para obtener metaestructuras quirales activas con las mejores propiedades. Posteriormente, las estructuras fabricadas se caracterizan morfológica, óptica y magneto ópticamente. Para identificar plenamente las propiedades físicas ocultas en las medidas de estas estructuras, se desarrolla un análisis alternativo de los elementos de la matriz de Mueller. Con este método, se validan las propiedades ópticas, quiroópticas y magnetoópticas de estos complejos nanosistemas.

Se han fabricado estructuras bidimensionales compuestas por simples nano bloques de construcción dispuestos en el plano. Se estudian los papeles de la composición y el ordenamiento planar en la respuesta óptica de las estructuras. La respuesta quiroóptica de las estructuras es sensible al entorno eléctrico. Esto se evidencia analizando las contribuciones de las estructuras con diferente naturaleza dieléctrica sobre el dicroísmo circular (CD). La incorporación de material magnético introduce una contribución magnética en el CD (MCD).

Las estructuras tridimensionales, dímeros de Au apilados helicoidalmente con diferentes orientaciones relativas y separación entre ellos, se han fabricado utilizando una técnica de deposición única. Se ha comprendido plenamente la dependencia de su dicroísmo lineal y circular, realizando un cuidadoso análisis de los elementos de la matriz de Mueller obtenidos, tanto de medidas

Resumen

experimentales como de enfoques teóricos basados tanto en un modelo sencillo de osciladores de Lorentz y como en una simulación numérica avanzada usando FDTD (*Finite-Difference Time Domain*). Estos análisis teóricos permiten determinar la dependencia de la señal dicroica con parámetros como el ángulo relativo de las barras, la separación o la variación espectral de sus modos correspondientes. Estos resultados se contrastan con las estructuras fabricadas, confirmando el comportamiento teórico.

El formalismo de la matriz de Mueller se utiliza para analizar las contribuciones a las propiedades quiroópticas, así como para distinguir los efectos magnéticos y los no magnéticos en la respuesta quiral, crucial para un correcto análisis de los datos. Hay un aumento casi proporcional de la quiralidad intrínseca, y un marcado cambio de la anisotropía óptica en las estructuras tanto en el caso planar como en el caso en que se separan eléctricamente en tres dimensiones. Estas evidencias ponen de relieve que las diferentes contribuciones al dicroísmo circular pueden controlarse modificando cuidadosamente la morfología de la nanoestructura.

El presente trabajo establece el escenario para el diseño, fabricación, y caracterización de nanoestructuras plasmónicas quirales optimizadas. Estas estrategias novedosas pueden utilizarse en el futuro para el diseño de nuevas funcionalidades en aplicaciones de dispositivos, como sensores y para la detección de compuestos químicos y moléculas biológicas.

ABSTRACT

A comprehensive work in plasmonic chiral and achiral nanostructures is presented. The bottom-up fabricated structures range from simple building blocks such as metallic and dielectric disk dimers or rods, to more complex nanostructures built from these individual blocks, arranged in the plane (two dimensional structures) or out of plane (three dimensional structures). The fabrication process uses hole-mask colloidal lithography and multiaxial evaporation, a powerful and cost-effective fabrication technique able to obtain a variety of structures in large areas. Besides morphology changes, parameters such as the composition and the spatial arrangement of the building blocks which compose them have been varied to comprehend their role in the optical response of the structures. These parameters are tailored to obtain active chiral meta-structures with optimum properties. The fabricated structures are morphologically, optically and magneto-optically characterized in depth.

A thorough and step-by-step experimental study to explain the chiro-optical response of complex chiral plasmonic nanostructures from the achiral responses of its constituents is shown. To fully characterize the physical properties hidden in the measurements of these structures, an alternative analysis of the Mueller matrix elements is developed. Using this method, the optical, chiro-optical and magnetooptical properties of these complex nano-systems are validated.

Two dimensional structures composed of simple building blocks arranged in the plane have been fabricated. The roles of the composition and the in-plane arrangement in the optical response of the structures are studied. The chiro-optical response of the structures is sensitive to the electrical environment. This is evidenced by analyzing the contributions of structures with different dielectric nature on the circular dichroism (CD). The incorporation of magnetic material introduces a magnetic contribution to the CD.

Abstract

Three dimensional structures, Au nanorod dimers helically stacked with different relative orientations and separation between them, have been fabricated using a single deposition run technique. The dependence of their linear and circular dichroism, performing a careful analysis of the Mueller Matrix Elements obtained from both experimental measurements and theoretical approaches based on a simple Lorentz oscillators model and a dedicated FDTD numerical simulations, has been fully comprehended. These theoretical analyses allow determining the dependence of the dichroic signal with parameters such as rod relative angle, separation, or spectral detuning of their corresponding modes. These results are contrasted with fabricated structures, confirming the theoretically predicted behavior.

The Mueller matrix formalism is used to distinguish the contributions to the chirooptical properties, as well as to separate the magnetic and non-magnetic effects to this chirooptical response, crucial for a correct data analysis. There is a nearly proportional increase of the intrinsic chirality, and a marked change of the optical anisotropy in structures from the planar to the physically separated case. These evidences highlight that the different contributions to circular dichroism can be controlled by carefully modifying the morphology of the sample.

The present work sets the scenario for fabrication, characterization and design of chiral plasmonic nanostructures, understanding their global behavior in terms of constituent blocks. These novel strategies may be used in the future for the design of novel functionalities in device applications such as chemical and biological molecule detection and sensing.

Abstract

1. INTRODUCTION

Fabrication and experiments on chiral and achiral plasmonic nanoobjects are presented. Plasmonic building blocks have optical properties which are sensitive to dimensions, shape and neighbors. These structures may be coupled to induce chirality; in two and three-dimensional assemblies. The magnetic modulation of this dichroism is also analyzed introducing magneto-optical building blocks.

1.1. General Overview

Nanotechnology concerns the understanding and use of matter at the nanometer scale to develop devices that improve our quality of live. As such it involves all aspects of condensed matter physics, electronic, magnetic, interaction with light… The associated research and applications explore from the fabrication of devices to the development of new materials with tunable properties. In the field of optics, Plasmonics study how electromagnetic fields can be confined over dimensions of the range or smaller than the light wavelength and their interactions with electrons in small metallic nanostructures or at metallic interfaces[1]. Surface Plasmons (SP) are coherent oscillations of electrons on a metal surface that are excited by an incident electromagnetic radiation at a metal dielectric interface, when excited in confined structures they are called Localized Plasmons (LP). Their applications span many areas of science and technology, including ultra-sensitive biological and chemical sensing and labeling and spectroscopy or quantum communications[2]. Furthermore, the properties of these nano structures depend on the shape, size, composition and their surrounding environment[3]. These objects constitute the emerging field of Plasmonics, where one can in principle perform “pseudooptics” going beyond the diffraction limit. The trick being the conversion of the radiation electric field in an electronic wave. Due to the small size of the nanostructures, one expects large electrical field enhancement close to the surface of the nano objects, that with the appropriate size and orientation with respect to the incident wave, can serve as an “amplifier” of the radiation field at certain locations, enhancing, for example, the interaction with molecules at a very small scale. Mainly due to these last two considerations plasmonics is naturally suited in the field of

biosensing. Among the fields expected to have a large increase in the near future are chiral and magneto Plasmonics. As cited in reference [2],three major areas have been identified as the most promising: chiral Plasmonics, magnetoplasmonics, and quantum Plasmonics.

This thesis deepens in the development of such fields, performing an in-depth study of chiral and magneto Plasmonics. I briefly introduce the main ingredients that put in context the work in the rest of this introduction, and outline the experimental approach taken before going in detail to the experiments, results, and discussion.

1.2. Motivation

The nature of light propagation has been a topic of interest for humankind during centuries and it has been studied since ancient times by Greek philosophers. They developed several theories such as the rectilinear propagation and the interaction of light with objects such as lenses[4]. Until the XIX century, the physical fundaments of the theory of light were based on structures whose dimensions were many wavelengths larger. After that, in the nineteenth century, the advances in science and technology were focused in the interaction of light with structures with size and spacing much smaller than the wavelength of interest. The inconveniences, most of them based on the diffraction limit, limited the possibilities of applications and manipulation of light at nanoscale. The search of strategies conveys the design and fabrication of nanostructures with unconventional properties which are not present in nature or the improvement of existent properties, and has stimulated great interest[5]. These nanostructures are called metamaterials. They are composed of periodically or randomly distributed artificial structures with exotic properties[6–9]. From the design of metamaterials, plenty of promising properties have been developed, namely negative refractive indices[8–10], artificial magnetism[11], subdiffractional imaging[12] and cloaking[13]. Humankind, then, has taken advantages of these metamaterials in generation, control and detection of light for different fields such as medicine, computing, chemistry or biology, making photonics one of the most interesting topics in science.

Introduction

Plasmonics

Plasmonic metamaterials are artificially designed structures utilizing plasmons, which are collective oscillations of free electrons, whose optical properties are unusual in nature[6]. The key properties of plasmonic structures are the capability of manipulating and controlling light, enhancing electromagnetic fields and confining energy, even at nanometric scales[1]. Furthermore, the properties of these structures depend on shape, size, composition, and the surrounding environment of the nanostructure[3].These parameters can be controlled through the fabrication process. In the last decades, a variety of plasmonic structures with different morphologies have been fabricated from nanodisks[14,15], nanorods[16–18] or nanorings[19,20] to more complex designs[21]. These structures have been extensively used as plasmonic devices, being high sensitive biological sensors[22–24] or enhancing photovoltaic devices[25]. However, the control and manipulation of light by optical components has had difficulties in the integration of components with macroscopic dimensions into the nanoscale.

Magnetoplasmonics

The search for a correct implementation of these optical devices have boost the use of metamaterials whose properties can be manipulated via external means such as electrical, thermal and optical agents. The aim of finding materials with plasmonic properties in a specific spectral range (visible and near infrared) and the ability to control and modify the polarization of light by external magnetic fields due to intrinsic magneto-optical Kerr and Faraday effects[26], has led to the emergence of hybrid structures which combine both plasmonic and magnetoplasmonic properties.

Chirality

Chirality in nanomaterials is introduced as the lack of mirror symmetry of an object, being impossible to superimpose it with their mirror image through any rotation or translation. This property has acquired attention in both Science and Technology since its first studies in the nineteenth century[27] and has become one of the most important research topics in the study at molecular levels in the fields of Biology or Chemistry[28]. The extension of chirality from the molecular case to nanomaterials has led to new opportunities in the study of chiral materials and applications. On one hand,

the dimensions of the nanostructures in the ranges from 0.5 to several hundreds of nanometers allow to connect molecules with bulk materials. On the other hand, the mechanisms to obtain chirality in nanomaterials such as dipole-dipole interactions introduce different phenomena that would be imperceptible in conventional chirality[29] The scientific interest in plasmonic chiral systems obeys principally to two reasons. One: chirality is a fundamental constituent in biology and chemistry[29]. Two: there are strong interactions with circularly polarized light in planar two-dimensional plasmonic structures[30–33] and 2D structures interact with chiral molecules[34–36]. The combination between chiral plasmonic metastructures and stereochemistry provides the new field of plasmonically enhanced chiral optical response in hybrid systems for the design of novel optical devices to the detection and modulation of chiral molecules. This has interesting applications in medicine and drug development[37]. However, the fabrication and design of artificial chiral structures at nanoscale, although complex, makes the search for different strategies to obtain chirality a topic of great interest.

Fabrication of nanostructures

Technologically, recently advances in the bottom-up and top-down fabrication techniques have led to more complex design and fabrication of nanostructures with plasmonic and chirooptical properties[5,38]. Most of the structures presented require accurate control in the design and then, lithographic techniques such as *electron beam lithography* (EBL) or *Focused ion beam* (FIB) or the combination of chemical methods to obtain plasmonic structures with the use of DNA- origami templates, are the choice. However, there is a needed to search for alternative fabrication methods which solve some problems in the mentioned fabrication techniques. These involve fabrication in large areas, and also the incorporation of active agents such as ferromagnetic materials allowing to manipulate the intrinsic properties by external magnetic fields[39–41].Then, it seems necessary to explore other techniques such as *Hole-Mask Colloidal Lithography* (HCML). This could be a big technological step towards the combination of chemistry and chiral plasmonic metastructures.

1.3. Plasmonics

1.3.1. History and fundamentals of Plasmonics

The interest in plasmonic properties started in Roman Empire times, when artists employed their unique properties to generate vibrant colors in glass objects and in the staining of church windows[22,42]. The most famous example of this is the Lycurgus cup, dated on the 4th century AD. The first scientific studies that observed surface plasmons are from 1902, when Prof. Robert W. Wood observed unexplained features in optical reflection measurements on metallic gratings[43]. Almost at the same time, M. Garnett tried to find the origin of bright colors observed in metal doped glasses[44] using the Drude theory of metals and the electromagnetic properties of spheres developed by Lord Rayleigh. In 1908, G. Mie proposed the theory of light scattering by spherical particles[45]. It wasn't until the 1950s that the phenomenon was completely understood[46]. During this decade, D. Pines studied theoretically the energy losses experienced by electrons travelling through metals[47] and associated them to collective oscillations of free electrons within the metal. One year later, R. Ritchie showed that plasmon modes exist close to the metal surface[46]. Finally, in 1968, A. Otto et al. presented methods for the optical excitation of surface plasmons in metal systems[48,49].

Plasmonics is a field that takes advantage of the coupling of light to charges like electrons in metals and allows breaking the diffraction limit for the localization of light into subwavelength dimensions, enabling strong field enhancements as well. Plasmonics deals with collective modes of electrons associated with an electromagnetic wave generated at the interface between a metal and an insulator. Surface plasmons consist on light waves that interact with the free electrons of a conductor. In this interaction, the free electrons of the material respond collectively by oscillating in resonance with the wavelength of the light wave. The surface plasmon is defined by the resonant interaction between the surface charge oscillation and the electromagnetic field that generates it. Typically, surface plasmons can be classified into two categories, depending on their possibility to propagate along the surface of the sample: The first category are the Localized Surface Plasmons (LSP), which are the localized modes of metallic nanoparticles that have similar dimensions to the incoming light wavelength. The second type are the Surface Plasmon Polaritons (SPP), which can propagate along the planar metal surface.

Plasmons can also originate from a metallic nanoparticle (size between 5 and 100 nm approximately) and are called Localized Surface Plasmon Resonances (LSPR).

1.3.2. Localized Surface Plasmons

Localized Surface Plasmons (LSP) are collective oscillations of the conduction electrons in a metallic nanoparticle, triggered by the oscillating electric field of the incident light (Figure 1)[3,50].

During these oscillations, electrons are confined in the nuclear framework due to both the restoring force due to the Coulomb attraction between the electrons and the nucleus, and the collisions with the boundaries, especially when the structures are smaller than the electrons mean free path. This confinement determines the coherent oscillation frequency. The coherent oscillation of the electrons with the light field in a nanoparticle is called Localized Plasmon Resonance (LPR).

One of the most important features of LSP resonance is that the close electromagnetic field is strongly enhanced near the resonance excitation. The resonance wavelength of a structure depends on different factors, such as size, shape as well as on the optical properties of the surrounding dielectric[3,51,52].

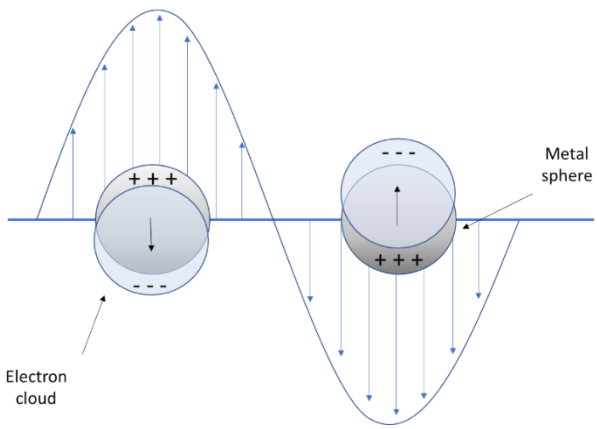

Figure 1.1.1: Scheme of the plasmon oscillation of a metallic sphere inside an electric field. Metallic grey circle represents the metallic sphere and light blue circle represents the conduction electron cloud. The electron cloud is displaced following the electric field of the incident light.

Introduction

The analytical expressions of LSP are shown for a small ellipsoid considering the dielectric tensor and shape effects[3,50]. The dielectric tensor contains all the optical information of the material. It is a diagonal tensor $\widetilde{\varepsilon_m}$ if the constituent material of the nanoparticle is a non-magnetic and optically isotropic metal. Then the dielectric tensor is expressed as:

$$\widetilde{\varepsilon_m} = \begin{pmatrix} \varepsilon_m & 0 & 0 \\ 0 & \varepsilon_m & 0 \\ 0 & 0 & \varepsilon_m \end{pmatrix} \quad (1)$$

When the material is a metal, all the $\widetilde{\varepsilon_m}$ elements are complex numbers. The surrounding dielectric medium is considered non-magnetic and isotropic for this study.

When light illuminates the particle, the applied electromagnetic field induces a dipole that is proportional to the field:

$$\vec{p} = \varepsilon_d \tilde{\alpha} \vec{E}_0 \quad (2)$$

Being $\tilde{\alpha}$ the polarizability of the nanoparticle and $\vec{E}_0$ the electric field of the incident light.

Now consider the particular example of a nanoellipsoid, with dimensions of width, length and height defined by (*a,b,c*). Assuming that the three dimensions are lower than λ, the incident light field can be considered as a uniform static electric field within the nanoparticle volume. Thus, the polarizability tensor, $\tilde{\alpha}$, of the nanoellipsoid will be diagonal, each of its diagonal elements can be expressed as:

$$\alpha_{ii} = 4\pi abc \frac{\varepsilon_m - \varepsilon_d}{3\varepsilon_d + 3L_i(\varepsilon_m - \varepsilon_d)'} \quad (3)$$

According to Maxwell's equations[50] $i = x, y, z$, and L_i corresponds to the depolarization factor for the respective axis, which, for a prolate particle along the x-direction, is given by:

$$L_x = \frac{1 - e^2}{e^2}\left(-1 + \frac{1}{2e}\ln\frac{1+e}{1-e}\right) \quad (4)$$

$$L_{y,z} = \frac{(1 - L_x)}{2} \tag{5}$$

For *b*=*c*. *e* is the rod ellipticity defined by $e^2 = 1 - (b/a)^2$. The values of *L* depend on the shape of the structure, ranging from 0 to 1.

The polarizability tensor will be maximum for the condition:

$$Re[3\varepsilon_d + 3L_i(\varepsilon_m - \varepsilon_d)] = 0 \tag{6}$$

With the polarizability tensor expression the absorption and scattering cross-sections of the nanoparticles can be obtained from[53,54]

$$\sigma_{sca} = \frac{k^4}{6\pi}\frac{|\alpha_{xx}|^2|E_x|^2 + \left|\alpha_{yy}\right|^2\left|E_y\right|^2 + |\alpha_{zz}|^2|E_z|^2}{|E_x|^2 + \left|E_y\right|^2 + |E_z|^2} \tag{7}$$

$$\sigma_{abs} = kIm\left(\frac{(\alpha_{xx} - \frac{k^3}{6\pi}|\alpha_{xx}|^2)|E_x|^2 + (\alpha_{yy} - \frac{k^3}{6\pi}\left|\alpha_{yy}\right|^2)\left|E_y\right|^2 + (\alpha_{zz} - \frac{k^3}{6\pi}|\alpha_{zz}|^2)|E_z|^2}{|E_x|^2 + \left|E_y\right|^2 + |E_z|^2}\right) \tag{8}$$

where *k* is the magnitude of the wavevector for the incident light. With this, the extinction cross-section can be defined as

$$\sigma_{ext} = \sigma_{abs} + \sigma_{sca} \tag{9}$$

In experimental systems the extinction is normally related to the transmission as Extinction = $1 - T$ where *T* is the ratio between the transmitted and the incident radiation.

From the previous equations the spectral position of the plasmonic resonance can be extracted. It can be tuned with the characteristics of the nanoparticle and of the surrounding dielectric medium. For nanoparticles, the constituent material determines ε, and the dimensions (L_i) play their roles in the determination of the optical responses: For a general ellipsoid ($a \neq b \neq c$), three different L_i will be present, and thus, dipole plasmon resonances could be excited in three different spectral positions. For a spheroid, there will be two different resonances since there are two different L_i. Accordingly, for a sphere, there will be only one resonance. By tuning the L_i value, plasmon resonances can be achieved for a wide range of wavelengths for different metallic nanoparticles.

Apart from the morphological properties of the nanoparticles, the resonance wavelength depends also on the value of ε_d, which is proportional to the refractive index of the medium. The sensitivity of the plasmon resonances to changes in the surrounding medium is what makes plasmonics a powerful tool in applications such as biosensing or molecular detection.

From the previous equations it can be also concluded that the extinction (transmission) cross-section will be maximum (minimum) at the plasmon excitation. The extinction peaks will be sharp and intense for noble metals due to their low optical losses, and broader and lower for ferromagnetic metals that have higher losses.

It is important to notice that the spectral position of LSP resonance is accurately predicted with equation 6 for small nanoparticles, but for larger particles, additional corrections to the polarizability tensor should be made[3,55]. Furthermore, dispersions in size and shape, as well as edge roughness in experimental nanoparticles, that are not considered in the analytical model, can also contribute to a broader peak. However, this electrostatic approximation can be useful in order to estimate the optical properties of ellipsoidal-like structures.

Experimentally, the most studied structures are derived from nanoellipsoids with different dimensions and aspect ratios, like nanospheres, nanodisks or nanorods. When light is incident normally to the structure plane, the extinction peak is shifted to red as the aspect ratio (diameter/height) of the structures increase[55].

1.4. Chirality

Chirality is defined as an asymmetry in a wide range of systems, from molecules to materials. It refers to the geometrical property of a structure without mirror symmetry, i.e., an object or a system is chiral if it is distinguishable from its mirror image, it cannot be superimposed onto it.

An object is achiral if it can be superimposed onto their mirror image through any 3D rotation or translation. The lack of mirror symmetry of the structures leads to chirality. In general, there are two main kinds of chirality: induced[56] and structural[57]. In this thesis the focus is on structural chirality by means of the fabrication of complex chiral structures by the spatial arrangement of

achiral building blocks[29]. The recent advances in the bottom-up and top-down approaches for the fabrication of nanostructures have opened up new opportunities in the growth of complex chiral structures for large-scale with improvements in their reproducibility, precision and high tunability[58,59].

1.4.1. History and fundamentals of chirality

The term chirality is derived from the Greek word *χειρ* (cheir, hand) and it was introduced in 1884 by Lord Kelvin[27]: "*I call any geometrical figure, or group of points, chiral, and say that it has chirality, if its image in a plane mirror, ideally realized, cannot be brought to coincide with itself*". Moreover, he also mentioned the terms of enantiomorphs to describe similar left and right hands (heterochiral) and two right hands (homochiral). According to the concept of Lord Kelvin, Chirality is a purely mathematic property based on its geometry. Three dimensional geometrically chiral objects may not exhibit rotation-reflection axes of symmetry $\boldsymbol{S_n}$ whereas the rotational symmetry ***Cn*** is not forbidden. In these chiral objects, the response is dependent on the handedness of their structures[27]. Louis Pasteur in 1848 was the first to observe chirality in molecules while he was investigating the structure of sodium ammonium (±) -tartrate. Subsequently, Mislow in 1962 introduced this terminology in chemistry.

In the last decades, the aim to get plasmonic chiral systems has obtained notable recognition due to their great potential in optical, electronic, and biomedical fields in applications such as chiral sensing, catalysis, or ultrasensitive detection and therapy of diseases[5].

Chirality also plays an important role in the origin of life, being in a wide variety of biological structures such as amino acids, proteins or sugars. Chiral objects are in our daily life in shells, screws and even our hands. The last one is the most famous example of chirality where both hands are mirror images of each other, but they cannot be superimposed. Another relevant example of chirality is in the double-helix structure of DNA. Nowadays, chirality has presence in the properties of some biological species such as the vivid color of the wings in butterflies[60] or the colors in jeweled beetles due to gyroid nanostructures[61,62] and the microstructure patterns respectively.

1.4.2. Chirality in sensing and detection

The handedness is a characteristic property of chirality important in many areas of knowledge such as Biology, where some molecules have a representative handedness as amino-acids or sugars, being left-handed and right-handed respectively. In Chemistry this feature plays an important role. Some drugs formed by the same molecule may change their properties and even may rise their toxicity depending on the chiral configuration. Similarly, the biological stereoselectivity improves the effectivity of some molecules which is noteworthy in pharmaceutical industry. Unfortunately, chirality may also do less active a treatment, or even it may produce adverse side effects like in the case of the drug thalidomide[63].

Consequently, the ability to distinguish between the enantiomers is essential as well as the improvement of sensitivity in the detection of molecules whose signal due to their interactions is weak. To solve this, the use of plasmonic nanosystems with geometrically chiral configuration provides some of the larger signals to detect them. It is a fact that the chiral responses of the nanostructures can be used to analyze the handedness of a chiral substance. This physical response gives us information about the interaction between objects and it is a quantifiable magnitude. Then, the chiral response is defined as a response that depends on the handedness of the objects and can be used to discern the handedness of the interacting object or substance.

To illustrate this concept, Figure 1.2 shows a simple example based on geometrical considerations where there are three keys with different shapes ("***1-3***") and three keyholes ("***A-C***").Whereas the geometrically chiral keyholes

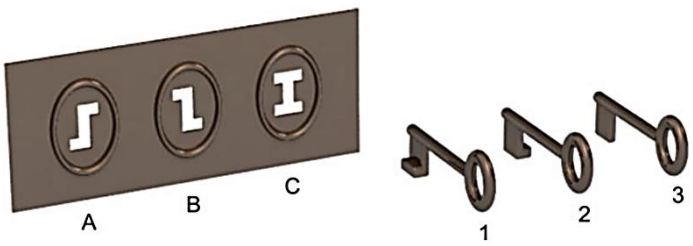

Figure 1.2 Illustrative example of the chiral interaction. Only if both objects are geometrically chiral, there is a response which depends on the handedness of the objects. Figure extracted from reference28.

("***A-B***") are enantiomorphs, the geometrically chiral keys ("***1-2***") of one handedness will fit in each of one enantiomers but not in the other[28].

Furthermore, it should be mentioned that the geometrically achiral key ("***3***") will fit both keyholes ("***A-B***") because its response does not depend on the handedness. Similarly, it happens if the keyhole itself is geometrically achiral ("***C***"). Therefore, what is at stake is that only the combination of both geometrically chiral keyholes and keys can give responses which depend on the relative handedness of the objects.[28]. This shows the fact that it is necessary to use chiral probes to analyze chiral structures, and hence, their properties.

1.4.3. Circular Dichroism in nanostructures

Apart from the structural property, the chiral response can manifest itself optically. One of the clearest features in optically active media is the difference in absorption of left- and right-handed circularly polarized light. This phenomenon is known as Circular Dichroism (CD). There can be other effects in nanostructures, like the optical rotation of the plane of linearly polarized light with respect to the initial polarization Optical Rotary Dispersion (ORD) [64]. Both properties are closely connected by the Kramers-Kronig relations[65]. Although both properties are intrinsic and they allow to analyze the spectral dependence in nanostructures, the simplicity and the direct relation to the structure have made the study of the circular dichroic response a widely used field [64].

The CD measurement is a useful method in fields such as Biology, Chemistry or Medicine which allows to observe conformational changes of complexes such as peptides, DNA or proteins. However, one of the inconveniences of this technique is the intensity of the CD signals in biological molecules. These signals are weak in the visible range whereas are strongest in the UV range (200-300nm) and they are necessary large concentrations of the analyte to detect them. A possible solution to these problems is the fabrication of artificial plasmonic nanostructures with chiral properties [66].

Artificial plasmonic chiral nanomaterials have larger chiral responses, orders of magnitude stronger than those found in chiral molecules. Moreover, controlling the tuning of the plasmon resonances, the chiral response of

molecules can be established in the visible spectral range (naturally most of them are found in the UV range). The ability to tune these responses open the possibility to obtain emerging new properties in the structures such as negative refractive index materials[9].

Considerable efforts have focused on the enhancement of the CD signals of chiral molecules using nanostructures placed closely. In this case, the local near-fields generated by the nanostructure produce plasmon-induced chirality close to the plasmon resonance position of the nanostructure[67].

$$CD_{total} = CD_{Molecule} + CD_{plasmon-induced} \quad (10)$$

To explain the origin of these plasmonic CD phenomena, a look into the electromagnetic interactions inside the assemblies of nanoparticles is required[22,68]. In this assembly, both geometry and the spatial arrangement are relevant parameters. Nanostructures composed of individual metallic nanoparticles arranged in chiral geometries can present strong plasmonic-enhanced chirality in the visible and near-infrared spectral regions. This is because the plasmonic modes of the individual particles interact through their respective electromagnetic fields to generate collective modes on the overall structure. When the distance between particles, *R*, is larger than the metallic nanoparticle size, *a*, the dipolar limit is applied, and the plasmonic CD follows the equation:

$$CD_{plasmon-plasmon} \propto \frac{a^{12}}{R^8} \quad (11)$$

where even the addition of a single particle that modify the interparticle distance can change dramatically the CD signal behavior. Thus, the chiroptical response of nanostructures is very sensitive to the particle number, size, and shape, being even able to flip the spectrum sign with the addition of just one nanoparticle to the structure [69]. Some strategies for the accurate control of the interactions between the nanoparticles are the use of DNA origami templates [70–72] or the fabrication of complex chiral structures from building blocks or basic elements. These are combined with each other, allowing the generation of structures with hybrid or new properties. Composition and configuration of these basic elements are responsible for their intrinsic electronic properties, also influenced by the spatial arrangement[73,74]. These properties determine how the electrons wave functions mix and hybridize, giving rise to new shared orbitals, which leads to charge redistributions. This

causes strong interaction and binding between the atoms in molecules[75]. In these systems dimensionality is an extremely important factor. Changing the size, or the composition of the building blocks of the "plasmonic molecules", their optical response can be tuned to the desired wavelength regimes[73]. The origin of the chiral response in metallic nanostructures has some similarities with the chirality due to the Coulomb dipole interactions in chiral molecules. However, there are some relevant differences to consider.

The mechanism of the optical response is plasmonic, while in biomolecules is due to excitons. Another difference is the spectral range, most of the molecules lay in the ultraviolet range instead of on the visible range as in the metal nanostructures. Moreover, biomolecules have chromophores as interacting elements which can be described as a simple dipole while these elements are described by three dipoles in nanoparticles[76].

There are different methodologies to induce chirality into nanostructures including the fabrication of structures with chiral shape[77,78], the interaction of achiral nanostructures with chiral molecules[56,67,79] or the chiral arrangement of achiral nanostructures[70,80,81]. The complex understanding of the resulting chiro-optical response when chiral and achiral structures are placed together has not been completely understood to date[21]. The CD modification has been found at the resonance peak of achiral structures that are near others that are chiral. Recent works have also shown that chiral plasmonic molecules can be created by the arrangement of a group of achiral structures[73], and that symmetry is an important factor in the system chirality[82]. These wide variety of metamaterials exhibit a unique CD, and the possibility of modifying it with the shape and composition of the structure[83,84]. These results not only provide a new approach to generate and regulate the CD effect, but also broaden the potential applications in polarization sensitive devices, quantum measurements, telecommunications, etc[85].

1.4.4. Fabrication of Chiral plasmonic nanostructures

One of the most interesting approaches to obtain chiral nanostructures is to mimic nature itself. Some magnificent examples are all the essential amino acids, that are chiral and have the same handedness, sugars, enzymes, or the olfactory receptors of humans, which make that enantiomers of the same molecule smell different[86] There are different strategies to fabricate artificial

chiral structures. Most of them are related to concepts presented in chiral molecules. Figure 1.3 shows the general concepts of chirality (artificial or natural) in six different classes, namely as[87]: helical chirality, chiral coupling, supramolecular chirality, pseudo or extrinsic chirality and assembly upon chiral scaffolds.

Helical chirality is a property of chiral system that do not contain stereogenic centers (any point in a molecule bearing different substituents, such that interchanging any two substituents leads to a stereoisomer[88]). It is presented in spiral and propeller types of structures. From molecules such as tetrachloroethylene with a similar shape to three-arm helix (Figure 1.3(a)), artificial nanostructures with the shape of propellers with curved arms are fabricated[89] (Figure1.3 (b)) In the case of structures with spiral chirality, the molecule is expanded over its spiral length as in the helicinebisquinone molecule (fig1.3 (c)), where electrons move along the structure, generating large non/linear chiroptical effects. Examples of 2D spiral nanostructures[90] and 3D spirals[91] are shown in Fig 1.3(e) and Fig 1.3 (f) respectively.

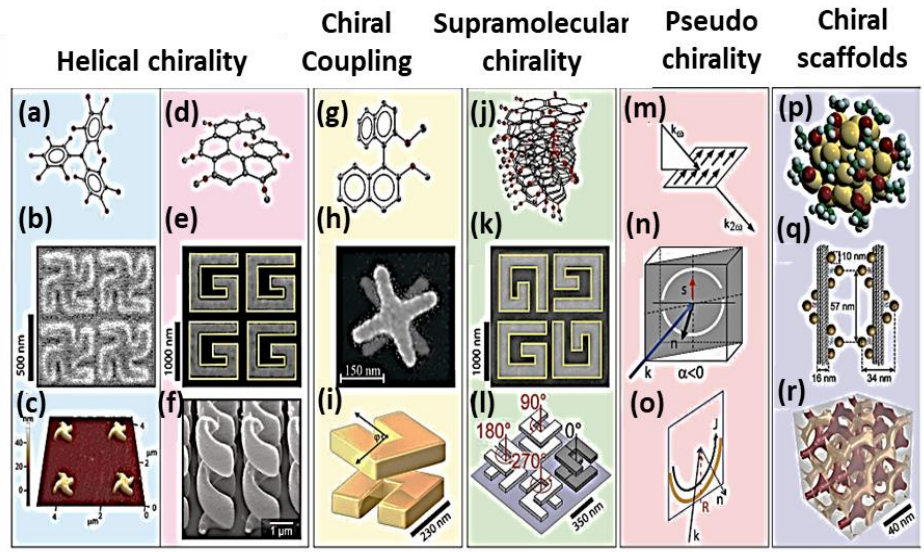

Figure 1.3 Scheme of the different strategies to obtain chirality in artificial nanostructures. Figure adapted from reference 87.

The source of chirality of some structures can originate from the coupling of achiral structures used as building blocks, as explained in more detail in chapter 3. Some examples of this coupling chirality are two building elements of the 2,2'-dimethoxy-binaphthyl molecule (Fig 1.3 (g)) or artificial structures

composed of crosses[92] (Fig 1.3 (h)) or split-ring resonators[93] (fig 1.3 (i)). Each of these building blocks alone are achiral, but their combination forms a structure with chirality.

Supramolecular chirality is commonly applied in chemistry. In this type of chirality, the building blocks are chiral, and their coupling produces a boost in the optical activity. For instance, biological molecules such as DNA double helix present supramolecular chirality (Fig 1.3 (j)). Following this type of chirality in artificial nanostructures, some important examples are structures with spiral chirality which have been fabricated in a chiral arrangement[90] (Fig 1.3 (k)), giving rise to nonlinear circular dichroism attributed to chiral coupling of the nanostructures, or even 3D structures composed of layers with structures in chiral configuration[94] (Fig 1.3 (l)).

A special case is pseudochirality. Under a chiral environment, it is possible that achiral molecules exhibit chirooptical effects due to changes in the angle between the incident beam and the nanostructures. This extrinsic or pseudo chirality is observed in 2-docosylamino- 5-nitropyridine molecules in nonlinear regime[95] (fig 1.3 (m)). It is also present in nanostructures in the linear and nonlinear optical regimes[31,96] (fig 1.3 (n) and fig 1.3 (o)).

Finally, the chiral scaffolds or chiral gold clusters are defined as groups of achiral and chiral structures or molecules which can enhance the chiral response of that cluster[97] (fig 1.3 (p)) or the nanoparticles that bind into a chiral platform such as helical DNA to obtain a chiral arrangement[72,98] (Fig 1.3 (q)).The fabrication of structures by self-assembling of chiral block copolymers has given the possibility of building 3D chiral structures[98] (Fig 1.3(r)).

1.5. Magnetoplasmonics

Magneto-optics is the influence of magnetic fields in light propagation. This usually involves changing the physical properties of the medium through which light travels. An example is the Faraday effect in which the polarization of light is rotated by an angle proportional to the magnetic field applied and the thickness of the material. The combination of noble metals, like gold, with magnetic metals, cobalt or nickel, for instance, in nanofabricated structures, results in coupled phenomena, called magnetoplasmonics[99]. The principal advantage of the magnetoplasmonic effect consists on a large increase of the

MO activity of these systems due to the electromagnetic field associated with the plasmon resonance. Simultaneously, the magnetic functionality permits the control of the plasmonic properties by an external magnetic field, which allows the development of active plasmonic devices. These materials find applications in gas and biosensing areas, and in integrated photonic devices for telecommunications.

As shown in Eq. 1, the dielectric tensor is diagonal unless there exists a magnetic field interaction with the particles. If a magnetic field is present, when light reaches the surface of the particles, the polarizability tensor becomes:

$$\tilde{\alpha} = 4\pi abc(\widetilde{\varepsilon_m} - \varepsilon_d \tilde{I})(3\varepsilon_d \tilde{I} + 3\tilde{L}(\widetilde{\varepsilon_m} - \varepsilon_d \tilde{I}))^{-1} \quad (12)$$

where $\tilde{L}$ is the diagonal tensor that contains the geometric factors L_i, being *i=x,y,z*. For simplicity, a polar Kerr configuration with an elliptical nanorod with the magnetic field normal to the rod plane and parallel to the incidence plane of light is considered. In this case, the dielectric tensor $\widetilde{\varepsilon_m}$ presents off-diagonal elements, and thus, due to this conversion between the *p* and *s* components of the light field after the reflection, this will result in elliptically polarized light. With this assumption, the polarizability tensor can be written as[16]:

$$\tilde{\alpha} = \frac{4\pi abc}{3} \frac{1}{\overline{L_x} \cdot \overline{L_y} \cdot \overline{L_z}} \begin{pmatrix} (\varepsilon_m - \varepsilon_d)\overline{L_y} \cdot \overline{L_z} & \varepsilon_{xy}\varepsilon_d \overline{L_z} & 0 \\ -\varepsilon_{xy}\varepsilon_d \overline{L_z} & (\varepsilon_m - \varepsilon_d)\overline{L_x} \cdot \overline{L_z} & 0 \\ 0 & 0 & (\varepsilon_m - \varepsilon_d)\overline{L_x} \cdot \overline{L_y} \end{pmatrix} \quad (13)$$

being $\overline{L_i} = L_i(\varepsilon_m - \varepsilon_d) + \varepsilon_d$.

derived from the polarizability tensor, the rotation (θ_k) and the ellipticity (φ_k) can be obtained. For a x-polarized light at normal incidence to the nanodisk, the polar Kerr effect can be expressed as function of the rotation and ellipticity:

$$\theta_k + i\varphi_k \approx \frac{\alpha_{yx} E_x}{\alpha_{xx} E_x} = \frac{\varepsilon_{xy}\varepsilon_d}{(\varepsilon_m - \varepsilon_d)\overline{L_y}} = \frac{3}{4\pi abc} \frac{\varepsilon_{xy}\varepsilon_d}{(\varepsilon_m - \varepsilon_d)^2} \alpha_{yy} \quad (14)$$

From the last two equations some conclusions about the intertwined MO and LSP effects can be extracted:

- At the LSP resonance excitation, the polar Kerr effect will be maximized.

- For a nanorod at the dipolar resonance, the effect of the magnetic field in the polar Kerr configuration is to generate a rotation in the plasmonic dipole along the direction parallel to the incident light ($\alpha_{ii}E_i$), obtaining a perpendicular MO dipole component along the perpendicular direction.
- From equation 14, the Polar Kerr effect is proportional to both the MO constant (ε_{xy}) of the nanoparticle and also to the polarizability component α_{yy}, which is orthogonal to the incident x-polarization of the light.
- MO effect depends on the surrounding dielectric medium of the structure (ε_d). This is the most exploited property in sensing applications with LSP enhancing the MO effect[100].

For larger nanoparticles, and similarly to the LSP resonance, where the electrostatic approximation is not valid, additional corrections such as the radiative correction[54] and the dynamic depolarization correction[101] are necessary for the polarizability tensor.

1.5.1. Au/Co Nanostructures.

Although almost all materials have MO activity, the intensity of this signal can vary up orders of magnitude between materials due to the physical origin of this phenomena. For instance, Au is a diamagnetic material, whose MO activity is 3 orders of magnitude lower than the magnetic Co. In the case of diamagnetic materials such as Au or Ag, the MO activity comes from the conduction electrons whereas in ferromagnetic materials such as Fe, Co or Ni; this effect is mainly due to the spin-orbit interactions of d- electrons.

Another important aspect to consider in the choice of the materials are the plasmonic properties. Whereas the LSPRs are well defined in noble metals, the effect of high optical losses produces the broadening of the LSPRs in ferromagnetic materials.

Combining both materials, magnetoplasmonic nanostructures improve their plasmonic and magnetooptical properties. These properties depend on size, the amount of material and the arrangement within the structure.

One example of how the MO activity is sensible to the changes in the dimensions of Au/Co/Au structures in polar Kerr configuration is presented in Figure 1.4.

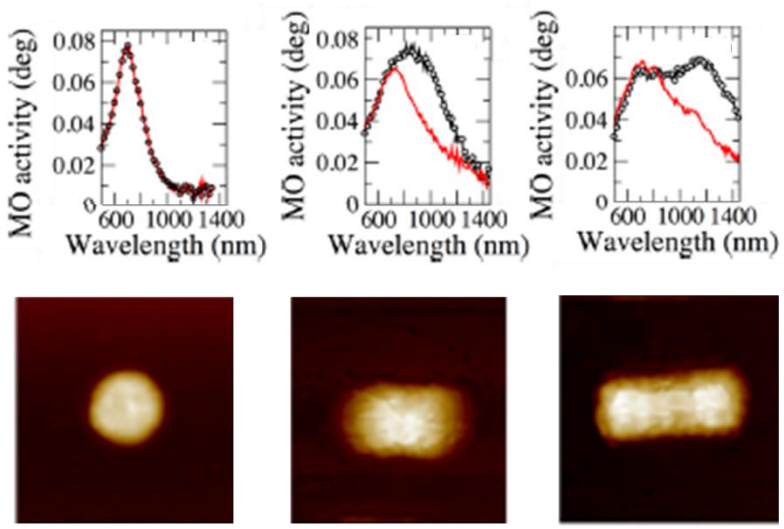

Figure 1.4: Spectral dependence of the Kerr rotation for light impinging at normal incidence with respect to the sample plane for polarized light along the short (black lines) and long (red lines) axis for the Au/Co/Au structures shown in the right panel. Figure adapted from reference 16.

A blue shift can be appreciated in the MO activity as the diameter increases. This behavior demonstrates the enhancement in MO effect by the LSP resonance excitation[16]. In these structures, the evolution of the MO spectra according the aspect ratio is studied. Whereas the MO spectra show a single maximum peak in the disk-like shape ($AR \approx 1$ and $\alpha_{xx} = \alpha_{yy}$)[102], the break of the symmetry in the structures produces a MO spectra with two peaks along the short and long axis, which depend on the in plane optical anisotropy s ($AR \neq 1$ and $\alpha_{xx} \neq \alpha_{yy}$)[16,101]. In this thesis, focus is paid on the analysis of the spectra along the long axis of the nanorod although an additional component along the short axis of the structures is presented. The MO activity can be tuned by modifying parameters during the fabrication of the structures such as dimensions, spatial arrangement, composition or the distribution of the materials within the nanostructure.

In other structures composed of Au/Co/Au such as nanodisk sandwiches (Figure 1.5), there is a spectral dependence of the MO activity relative to changes in the size and diameter (from 60 to 110 nm)[102] . The MO spectra exhibits the enhancement of the effect by the excitation of the LSP resonances. The spectra show a similar shape to the Kerr ellipticity spectra for the disks, although there is a redshift as the diameter increases.

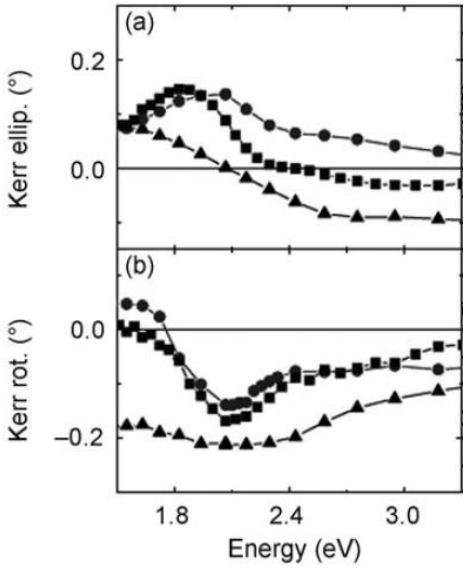

Figure 1.5: Polar Kerr ellipticity (a) and rotation (b) spectra for Au/Co/Au nanosandwich pillars with different diameters. 60nm diameter pillars sample is represented by circles, 110 nm diameter is represented by squares. The triangles represent a continuous Au/Co/Au trilayer. Figure adapted from reference 103.

Other relevant aspects in the MO activity are the ratio between the ferromagnetic material and noble-metal and the material distribution within the nanostructures[103]. The presence of the Co in the MO spectra produces slightly blueshifts as well as the broadening of the peaks[104]. Moreover, the intensity of the MO activity increases with the Co amount, being much larger than that in those composed of just noble metals[15,104].

Concerning the distribution of Cobalt within the structure, the electromagnetic field distribution in the structures is not homogeneous and it is modified according to the position of the MO active component, obtaining maximum values when Co is located near the interfaces within the disk[103].

In the structures mentioned, the constituents are in direct contact. One step further is to separate the ferromagnetic and noble metals by a dielectric layer[105,106].

The proximity of these elements can induce a MO activity via near field dipole-dipole interactions[105–108] or the far-field coupled periodical disk arrays[109,110]. Furthermore, both the in-plane ordered and a randomly arrangement of magnetoplasmonic structures have been studied in arrays of nanodisks where a sharp feature is found in the MO spectra of ordered arrays[110] (Figure 1.6).

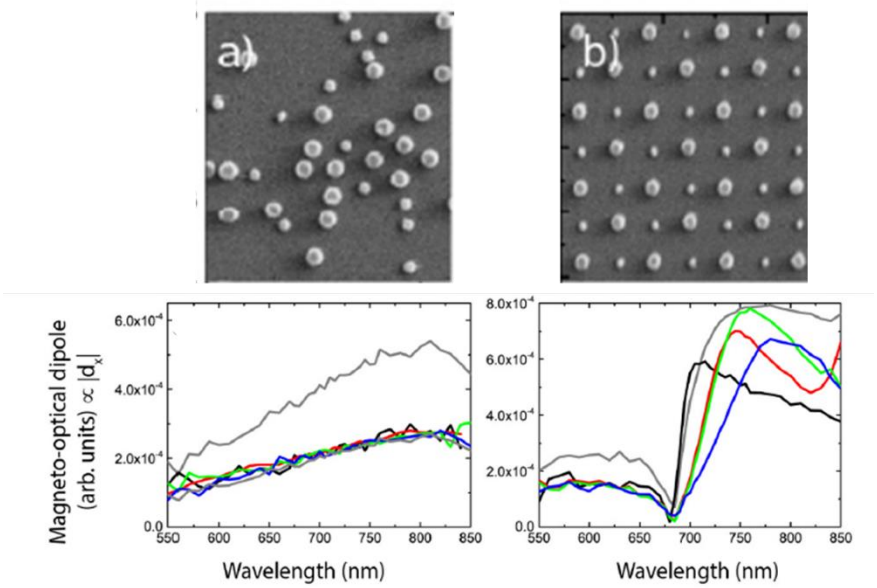

Figure 1.6: a) MO activity of randomly distributed nanoparticles made of different materials: Nickel (diameter 120nm) (grey line) and a mixture of gold and nickel (d_{Au}=80nm (black), d_{Au}=100nm (red), d=110nm (green) and d_{Au}=120nm (blue). d_{Ni}= 120nm). b) MO activity of nanoparticle arrays of different materials. Nickel (diameter 120nm) (grey line) and a mixture of gold and nickel (d_{Au}=80nm (black), d_{Au}=100nm (red), d=110nm (green) and d_{Au}=120nm (blue). d_{Ni}= 120nm). Figure adapted from reference 110.

1.6. Active chiral plasmonic nanostructures

In the last decades, the possibility to control the tuning of the LSPRs in the nanostructures has been a useful tool in applications such as photovoltaics[25], catalysis[111], chiral plasmonics[38], biological sensing[6,112] or detection[113]. However, control is not direct and cannot be reconfigured postfabrication. This reason has led to a search for alternative approaches using active external agents such as thermal[114], magnetic[99] or electrical[115] stimulus, which can be used as controls. Chiral plasmonic nanostructures have also attracted attention due to their promising potential applications as molecular sensors[116] and detection of analytes[5]. Both reasons have promoted the interest to obtain active chiral plasmonic materials.

In Figure 1.7, some examples of these active chiral nanostructures are shown. Here, the accuracy control in the fabrication techniques allows to switch the chiral response via external stimulus[26].

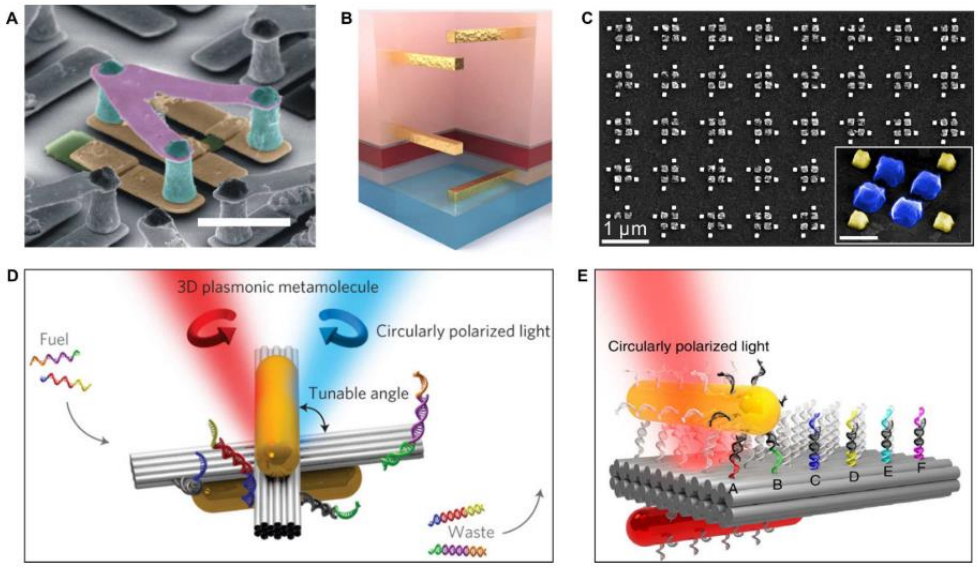

Figure 1.7. ***Switchable chiral plasmonic structures****. (a) Three-dimensional molecule with green pads which allow to control the chirooptical response. (b) Two chiral unit whose response can be manipulated the chiral response by changing the GST-326 layer. (c) Hybrid chiral plasmonic system where the magnesium switches the plasmon off via hydration. (d) DNA strands functionalized with gold nanorods where the response is manipulated by changes in the UV light. (e) DNA nanowalker where the upper yellow rod can walk over the origami sheet, switching the chirality of the system. Figure extracted from reference.26.*

An example of these nanostructures is presented in Figure 1.5 (b) where the use of a switchable media as an active agent such as $Ge_3Sb_2Te_6$ (GST-326). This material modifies its phase under thermal changes, being a good candidate to modify the interactions between gold dimers as a separator[117]. Another example of active chiral plasmonic structures is shown in Figure 1.7(c), where the changes in the structural properties after the fabrication modify the chiral response. In these structures, the concentration or composition of the entities can tune the optical response of the total system. For instance, nanostructures composed of gold and magnesium nanoparticles in a gammadion (figure composed of various Greek gamma letters, like the Nazi swastika) arrangement turn off the chiral response in presence of hydrogen due to changes in the magnesium component[118].

Despite the advances in top-down fabrication methods, these techniques have limitations such as the difficulties to control and manipulate the orientation between the structures in three-dimensional chiral plasmonic nanostructures. A possible route to solve this problem is by using the intrinsic chirality in biological molecules (e.g., DNA), to fabricate some reconfigurable structures.

Some examples of assemblies of nanoparticles with the DNA Origami templates are shown in fig 1.8. In this figure, different nanostructures such as gold nanoparticles or gold nanorods decorate the DNA strands. The chirality in these structures switches due to changes in the polymerization state of the DNA under the external UV(VIS) illumination [72,85,119].

Another route to control and modulate externally the plasmonic and chiral responses of the structures is by the incorporation of magnetooptical active materials. In these systems the responses can be manipulated applying a magnetic field, being useful in applications such as chiral sensing[120]. Some examples of these active metastructures are arrays of $(Au/Co)_{ML}$ gammadions in which the presence of the MO active element produces an additional contribution to the chiral response. This contribution is known as magnetic chiral contribution (MCD) which does not depend on the handedness of the structures but rather on the electromagnetic field intensity inside the Co. Another complex plasmonic split-ring structures with dots composed of

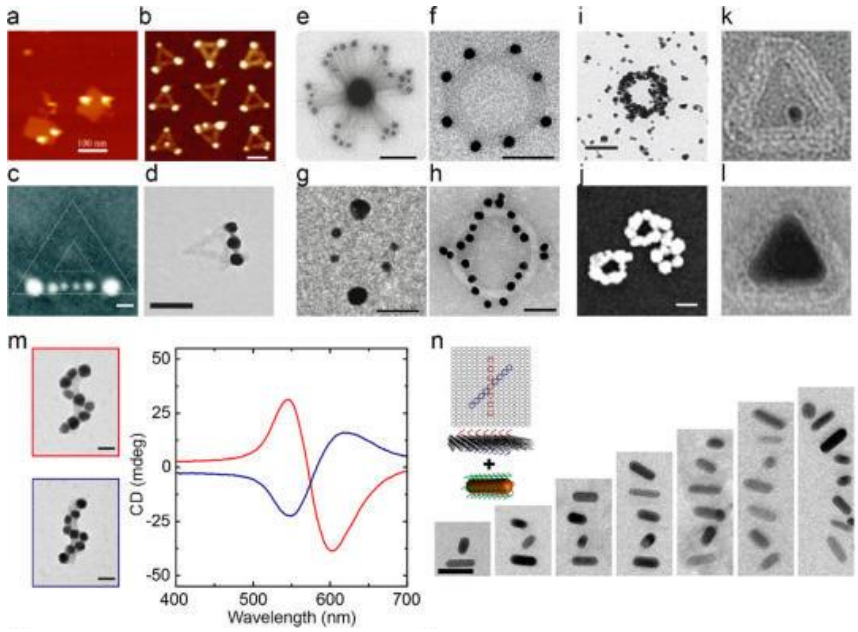

Figure 1.8. ***DNA origami for plasmonics****. (a–d) metal nanoparticles assemblies templated by DNA origami. (e–h) Metal nanoparticles assemblies on three-dimensional origami templates. (i) Metallization of DNA origami ring structures (j) Metal NPs fused together on DNA origami through electroless metal deposition (k,l) DNA origami structures as moulds for growth of metal colloids (m) DNA origami-templated assembly of helical NP assemblies together with their CD response (n) Chiral plasmonic assemblies with gold nanorods. Figure extracted from reference 59.*

multilayers of (Au/Co) show a magnetic modulation of the chiral response of about 25%[40]. In a suspension of randomly oriented helices of nanoparticles coiled around an Au nanorod, it is demonstrated that the plasmon induced strong localization of the electromagnetic fields within the nanoparticles enhances the Magnetic contribution to the CD[121].

Another approach to obtain these active structures is by combining achiral and chiral nanoparticles as building blocks in a chiral arrangement. Moreover, the addition of magnetic components, like of Co or magnetite, produce chirooptical response. The MO activity has led to fabricate 3D chiral structures with MO active multilayers[122] or 2D composite trimer antennas of Ni and Au structures[100].

1.7. Fabrication of the nanostructures

In last years, Optics and Material science have experienced an enormous development, gaining large relevance, principally due to progress in nanofabrication technology[7]. The possibility of fabricating nanodevices of a great variety of materials opens a new world of properties and applications in material science[99]. The significant progress in top-down and bottom-up methods to fabricate structures is due to the improvement of novel techniques like *optical lithography* (OL), *Electron Beam lithography* (EBL), *Focused ion Beam lithography* (FIB) or *nanosphere lithography*. Although some techniques such as EBL or FIB have a great resolution (~50nm) and are frequently used in the plasmonic area[123],there are some disadvantages to its use, such as the economic cost of the systems and the excessive structure fabrication time. To solve these problems, there are some *soft lithography* methods based on the use of nanospheres such as *Hole-Mask Colloidal Lithography*[58] (HMCL), whose principal characteristics are the low cost and the possibility of massive production of structures in large areas. In this fabrication method, the shape of the nanosphere arrays is transferred to nanoholes in the metal films by depositing the material by evaporation techniques such as *thermal* or *e-beam evaporation* (more details in Chapter 2).

1.7.1. Fabrication processes

This thesis focuses on the manufacture, design and characterization of structures obtained by combining HMCL and multiaxial evaporation. This fabrication method has been widely used to achieve structures with different shapes such as discs[103], rings[19], rods[16] or chiral structures[40]However, other routes from top-down approaches have been reported.

In the case of the building blocks or simplest structures used as building blocks such as Au nanodisk dimers can be fabricated by combining HMCL and tilted-angle deposition technique[108,124], electron beam lithography[125] as well as chemical methods[126]. Similarly, single Au rods have been fabricated by different techniques such as chemical techniques[18],HMCL[58] and electron beam lithography[127].

The fabrication of more complex structures composed of the building blocks, have been produced mainly with EBL, due to the precision and resolution of the structures, e.g. structures formed by one L-shaped gold particle and one gold disk [81]or particles arranged in asymmetric configurations[57].

Finally, 3D rod dimers can be attempted in different ways. Some of these techniques include multistep lithographic techniques[73,128] (focused ion beam or electron beam deposition[129], physical vapour deposition at non-normal incidence[130–132]) or chemical routes[26,133–136]. For instance, nanorod [103]dimers

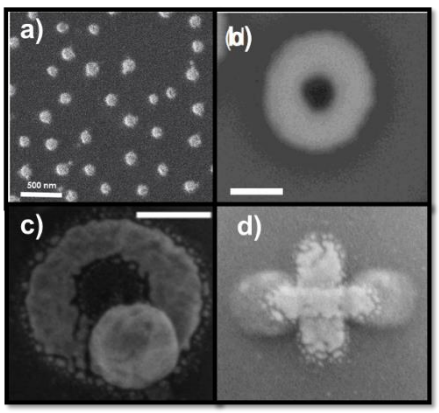

Figure 1.5. SEM images of structures with different shapes fabricated in our group with Hole-mask colloidal lithography and multiaxial evaporation: (a) disks[103] (b) rings (c) chiral structures[40] and (d) crossed rod dimers. Figure adapted from references: (a) 103(scale bar 500nm),(b)40 (scale bar 100nm) and (c)137 (scale bar 100nm).

with inter rods distance of more than 40 nm and with variable relative orientation between the rods have been fabricated by multistep lithographic techniques[137,138]. Similarly, nanorods dimers with inter rods distance of few nanometers have been obtained by chemical routes. Nevertheless, there is less accurate control of the relative orientation between the rods[71,135,139–142].

1.8. Chapter Structure

The description of the active structures with plasmonic and chiral properties proceeds in two sections: a first section focused on the study of simple plasmonic structures without chirality, where the evolution of optical and magneto-optical properties according to different morphologies is analyzed. The second section studies more complex structures formed by these simple structures used as building blocks, where chiral properties appear due to the spatial configuration. In this last section, the role of morphology and composition of these advanced structures over optical and magneto-optical properties is studied.

With all this in mind, the work description is organized as follows:

- **Chapter 1** describes the context and motivation. It also introduces basic theoretical fundaments in order to understand Plasmonic chiral nanostructures obtained by Hole-mask colloidal lithography.
- **Chapter 2** contains the common methodology and the experimental techniques used during the fabrication and characterization of the nanostructures.
- **Chapter 3** shows experimental results of the basic plasmonic structures (building blocks) without chirality in different morphologies. The multiresonant plasmonic responses of dielectric and gold dimers and single gold and dielectric nanorods as well as rods combining noble metals and ferromagnetic materials are presented.
- **Chapter 4** describes the evolution of the optical and MO properties in two-dimensional structures according to fabrication parameters such as composition, in plane spatial arrangement and morphology. The effect in these structures of the composition and their arrangement with respect to the single rod is analyzed. Ferromagnetic materials are also incorporated introducing magnetooptical activity in the structures.

- **Chapter 5** shows the design of three-dimensional systems of stacked Au rods with the analysis using a simple Lorentz oscillator model to simulate the optical response. Within this simple model, the variations in the relative angle between the rods, the spacer thickness and the energetic position of the top rod response are studied. The simulated response is compared with fabricated structures.
- **Chapter 6** presents the experimental optical response of chiral stacked Au rods structures. The optical responses to linearly and circularly polarized incident light as a function of the relative angle of the rods and the vertical spacer are studied. Moreover, a rigorous theoretical model is presented to analyze the vertical dependence of the optical properties.

Introduction

2. METHODOLOGY AND EXPERIMENTAL TECHNIQUES

The fundamental physics and experimental techniques used to fabricate the structures and analyze their properties in the visible and near-infrared range are described. For the sake of clarity, the methodology is presented in Figure 2.1, showing sequentially the process from fabrication to characterization and the analysis of their properties. This chapter is divided in two subsections accordingly.

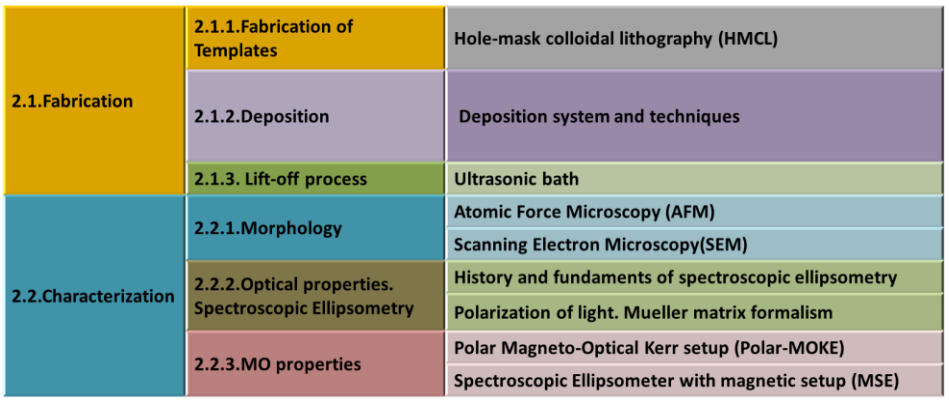

Figure 2.1: Scheme of the various experimental techniques implied in the different processes. The techniques are divided into two principal groups: Fabrication and characterization.

The first one is devoted to the fabrication techniques: i) fabrication of the templates (intermediate steps) by *Hole-Mask Colloidal Lithography* (HMCL), ii) structure growth through the templates by e-beam and Kcell evaporation, and finally iii) lift-off. In the second subchapter, the characterization techniques are described. These include i) analysis of the morphological properties by SEM and AFM techniques, ii) characterization of the optical properties by spectroscopic ellipsometry, and iii) magneto-optical measurements by both spectroscopic ellipsometry with magnetic setup and Polar Kerr measurements.

In the upper part of Figure 2.1 is displayed the fabrication method protocol divided in three subsections: the fabrication of the templates, the growth of the structures through these templates and the final removal of the PMMA by the lift-off process. All these steps are common procedures that are used multiple times in order to fabricate the final structures.

2.1. Fabrication

The fabrication of the structures is realized via the combination HMCL and multiaxial evaporation in ultrahigh vacuum. In what follows the HMCL technique is described and the main parameters that affect the shape and distribution of the fabricated structures are discussed.

2.1.1. Templates

Hole-Mask Colloidal Lithography (HMCL) is a versatile method to fabricate nanostructure arrays over a large surface (up to dm^2) with a reduced cost and high speed. The concept was created in 2007 by Fredriksson et al.[124]. Large area self-assembled colloidal polymer nanospheres are used as a mask. The shape of the colloidal nanosphere array is then transferred to nanostructures by depositing the desired materials inside the holes leaved when the spheres are retired. In HMCL, the holes are created inside an Au thin film that is supported by a sacrificial layer and acts as a mask. After the patterning process, both the sacrificial mask and the Au mask are removed, leaving the evaporated material pattern. There are a variety of examples of nanostructures fabricated with this method, that include arrays of nanodisks[143], nanorings[144], rods[16], pillars[145], bowls[146], crescents[147], dimers[148], trimers[39], etc. The possible applications for this kind of nanostructures include *Surface Enhanced Raman Scattering* (SERS)[124], magnetics[149], sensing[150], enhanced solar cells[151,152] and photonics[153,154]. The main advantages of the technique are:

- The method is material independent, meaning that a wide range of materials can be used to form the nanostructures: Ag, Au, Pd, Co, SiO_2, CaF_2, etc.
- The process is independent of the substrate. All the nanostructure can be performed using the same initial mask.

- The process is easy to do it in sequence, offering the possibility to fabricate complex multilayers.

A typical HMCL procedure consists on the following steps[58]:

1- **A sacrificial PMMA (Polymethyl methacrylate) layer is spin-coated on the substrate**. The first step of the process is to select the substrate, to clean it and spin-coat it with PMMA resist. The borosilicate glass substrate (BK7) is the selected substrate for this thesis. The reason is that the studied structures exhibit plasmonic resonance in the range from visible to near infrared, where the BK7 is transparent. The typical shape of the glass substrate is a square of 1x1cm^2. After cutting the substrate a standard cleaning process is done. This cleaning process consists on immersing the substrate into ethanol and bathed into a sonicator for 5 minutes at 60ºC, followed by a similar bath into acetone and another into isopropanol. Last step is to rinse the substrate with distilled water and dry it with dry N_2 gas blow. The cleaned substrate is then spin-coated with PMMA resist (around 200nm). The parameters for the coating are: 40 µL PMMA solution over the surface at 6000 rpm for 60s, followed by a soft bake of 5 minutes at 180ºC on a hot plate.

2- **The surface electrostatic charging properties of the PMMA are modified by a treatment into an oxygen plasma and sequent wetting by electrolyte solutions.**

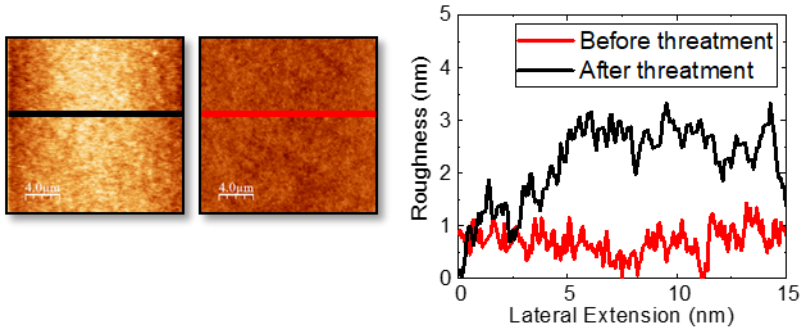

Figure 2.2.(a) AFM images of the two PMMA surfaces before (red line) and after (black line) the O_2 plasma treatment. (b) AFM profiles of each surface where the roughness is presented.

In order to try to avoid spontaneous dewetting of the PMMA surface, the resist is subjected to an O_2 plasma treatment with typical working parameters are: 50W power, 15s and 450 mTorr pressure. This reduces the surface hydrophobicity and favors the roughness of the surfaces (Figure 2.2).

Moreover, this improves the adhesion of the Poly (DiallylDimethylAmmonium chloride) (PDDA) on top. This polyelectrolyte solution functionalizes with positive net charge the surface of PMMA. The spinning parameters of PDDA are: 70µL of PDDA solution into distilled water with a concentration of 0.02 wt.%, and 60s at 100 rpm. The PDDA layer has a thickness of tens of angstroms and a homogeneous distribution across the surface[155].

3- **Negatively charged colloidal polystyrene nanospheres are drop-casted onto the sacrificial polymer film, forming a self-assembled random array**. The way to do that is by introducing the sample into a water suspension from Sigma-Aldrich containing the negatively charged nanospheres with a known diameter (a homogeneous averaged diameter of 124nm). The parameters of the process are as follows: 70µL PS sphere suspension diluted into distilled water with 0.02 w/v% concentration and spun at 100 rpm for 60s. Electrostatic forces between negatively charged spheres and positively charged PDDA causes spheres to be attracted to the surface. Electrostatic repulsion between spheres makes them to distribute uniformly in a short-range-ordered array. Parameters such as solution concentration and deposition time determine sphere distribution and density on the sample surface, allowing us to tune it.

4- **A metal film layer is evaporated on top of the structure creating a mask. Tape stripping is used to remove the spheres and then etching to remove the exposed resist.** Here the template is covered with a homogeneous layer of gold with a thickness of 30nm. Then the PS spheres are removed by tape-stripping, leaving holes with the diameter of the spheres in the Au thin film. This gold mask has two purposes: to protect the resist form the subsequent O_2 reactive ion etching process and to work as mask during the material deposition process. The *reactive ion etching* (RIE) with O_2 is used to transfer the Au Hole-mask into the sacrificial PMMA layer. The Reactive Ion

Etching (RIE) is performed with 50W power, and an O_2 flux of 50sscm/min. After 150s, the PMMA sections exposed to the plasma form cavities, leaving the template covered with a thin film mask supported by a perforated polymer film. The size of the cavity below the mask can be tuned modifying the etching time.

5- **Desired materials are deposited by electron-beam or thermal evaporation through the holes generated in the mask.** This will be explained in detail in section 2.2.

6- **The sacrificial PMMA resist and the metal mask are removed by lift-off.** After deposition process, the template (mask+resist) is removed by a lift-off process in acetone and a supersonic bath for 2 hours, leaving only the nanostructures on the substrate.

A scheme of the process is presented in (Figure 2.3). The control of the azimuthal and polar (φ,θ) orientations during the growth process allows the fabrication of various complex structures.

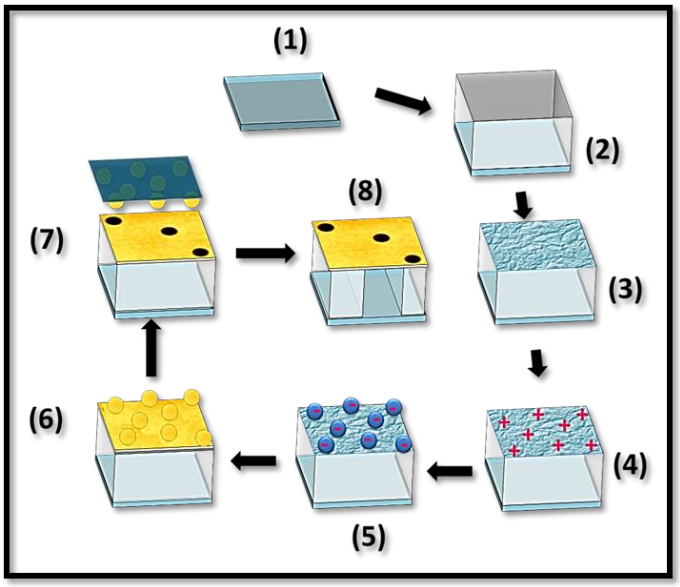

Figure 2.3: Scheme of the fabrication process of templates. (1) Bk7 glass is the selected substrate. (2) Substrate is spin-coated with PMMA. (3) An O_2 plasma texturizes the PMMA surface. (4) Positively charged poly-diallydimethyl-ammonium (PDDA) is deposited onto the resist. (5) Polystyrene spheres distribution. (6) Gold coating. (7) Spheres are removed by tape stripping. (8) RIE etching to form cavities below the Au coating. Center: Final step: Nanostructure deposition. The template is removed by lift-off in acetone after the process.

PS sphere density issues

The same hole is used to fabricate structures such as nanorods and adjacent disks, which means that they have to be at a certain distance to avoid overlapping. The nanospheres cover the surface in a self-assembly process, where competing electrostatic interactions between the dipoles of colloidal nanospheres at the interface (repulsive), and the nanospheres with the film (attractive) lead to their arrangement on the surface. In order to control these interactions, the concentration of PDDA solution, the density of the nanospheres, and the incubation time have been modified. The best conditions to obtain templates are at 0.02% w/v for the nanospheres density, 0.02% v/v of PDDA solution, and a deposition time of 60s.These parameters allow obtaining templates with homogeneous coverage, although the spheres are randomly distributed in the surface[124].

Au/PMMA film thickness issues

The Au layer thickness has a direct influence on the morphology of the holes that develop. The shape and diameter of the hole are critical for controlling the morphology of the deposited nanostructure because its shape is a "shadow" projection of the hole.

First, the mechanical rigidity of the Au film strongly depends on its thickness, *t*. Thick gold films tend to be rigid, while thinner Au films bend at their ends, increasing the hole diameter and compromising the experiment reproducibility. Therefore, it is important to find the optimal gold thickness that have large stiffness and simultaneously allow large deposition angles, θ. A thorough AFM study revealed that the optimum thickness for the gold layer is 30nm.

Shrinking hole issues

The deposition of all the structures using a HMCL template is carried out by controlling two main angles during the evaporation through the templates: the polar angle, θ, and the azimuthal angle, φ of the flux respect to the mask. Controlling these angles, the hole diameter (which is determined by the size of the PS spheres), and the thickness of the PMMA and the Au mask, the resulted morphological parameters of the nanostructure can be derived by simple trigonometry. From[156,157] it is deduced that each parameter has its own effect on the morphology of the structure and allows controlling it. Different

materials can be deposited inside the holes forming multilayered structures by changing evaporation sources. Each layer growth parameters can be controlled independently. For instance, a growth process with a fixed θ will lead to a disk, sequential deposition at two θ of opposite signs will produce a disk dimer, whereas continuous deposition while oscillating θ a certain amplitude angle will lead to a rod.

However, it is important to remark that both the mask thickness *t* and the hole diameter *D* are not strictly constant during the deposition process, due both to the material accumulation on the mask (increasing *t*) and onto the rims of the nanoholes (decreasing *D*). This is known as the shrinking effect and can be used to control the hole diameter and generate ultra-tiny nanoparticles with large accuracy. The mask hole shrink promotes a moderate conic-like shape growth of the structures and a significant reduction of the deposition rate and eventually a blockage of the hole[124,157]. The hole-shrinking rate strongly depends on the evaporation technique and the deposited material types.

2.1.2. Thin film Deposition

Thin film deposition has been used for almost a century, and a large variety of methods has been developed, many are widely used in Industry. In general, film growth methods can be classified into two groups: chemical and physical depositions[158,159]. Examples of deposition techniques are thermal evaporation, molecular beam epitaxy (MBE), sputtering, chemical vapor deposition (CVD) and atomic layer deposition (ALD). In this chapter, some fundaments about the experimental techniques used specifically in this thesis are presented.

The deposition system and deposition techniques. The deposition system is composed by different Ultra-High-Vacuum (UHV) enclosures connected to a main chamber. The system has e-Beam and thermal evaporation facilities (Figure 2.4(a)).

It also has several magnetrons for sputter deposition (Figure 2.4(b)), although these are not used in this work. The systems have an ion pump for the standby vacuum and a turbo pump for the working vacuum. There is a schematic representation of the distribution of the deposition system in Figure 2.4(c).

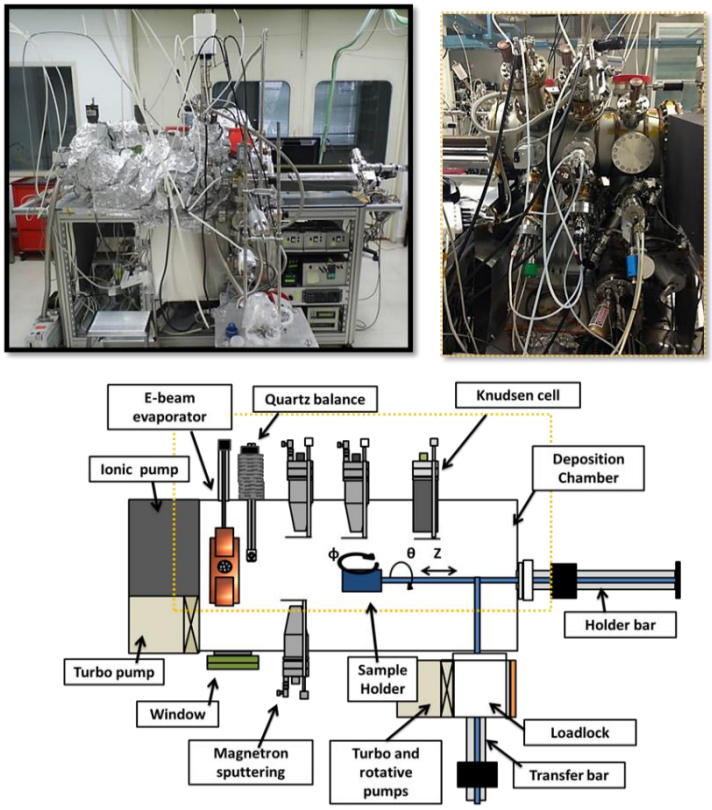

Figure 2.4: a),b) Pictures of the deposition system. c) Scheme of the general system with the Sputtering, the PVD and the e-Beam evaporator inserted into the same deposition chamber

Electron-beam evaporation

Electron Beam Evaporation (EBE) is a physical vapor deposition technique in which a source of material or target is heated up to its evaporation point by focusing an electron beam on a source material under high vacuum atmosphere. EBE allows the precise control of the structural and morphological properties due to the wide range of deposition rates from 1 to 10^3 nanometers per minute at relatively low substrate temperatures[158].

In Figure 2.5(a) a sketch of the fundamentals of the EBE technique is presented. In the deposition chamber, the electron gun generates an electron beam from a tungsten filament by thermionic effect. The e-beam is steered via magnetic fields towards the crucible[160]. The material with different forms, such as pellets or tablets, is contained in these crucibles, that can be made of graphite, tungsten, ceramic, molybdenum, etc. depending on their chemical stability with the hot source material. By interactions between the electrons

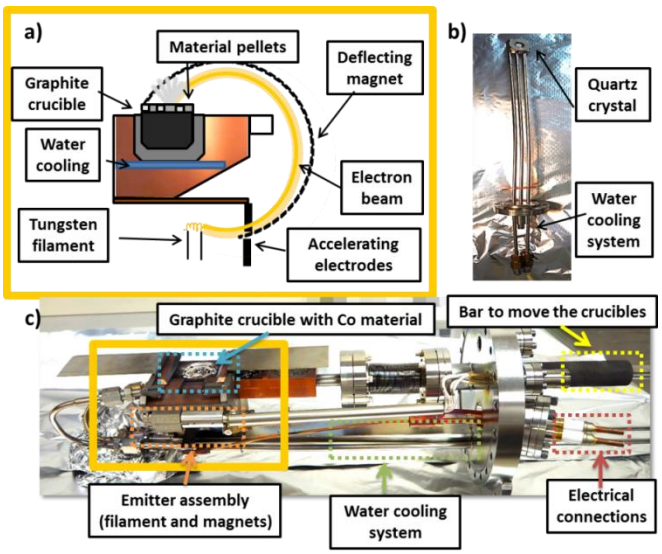

Figure 2.5: (a) Sketch for the principle of the e-beam evaporation. (b-c) e-beam evaporation components used during the fabrication process.

with high kinetic energy and the surface atoms of the material, the atoms of the ingot acquire enough energy to leave the material, which is melted, evaporated or sublimated and then deposited on the substrate.

The control of losses due to thermal dissipation during the fabrication process is carried out by a water-cooling system. An electromagnetic coil ("sweep coil") allows adjusting the shape, position and steering of the electron beam onto the source material to be evaporated.

Some significant factors such the pressure of the chamber and the working distance δ (between the source and the substrate) must be taken into consideration in EBE technique. Typical deposition pressures are in the 10^{-9} Torr range and the substrate-to-crucible distance between 0.3 to 1m, minimizing substrate heating effects by radiation.

In Figure 2.5(c) the Telemark Model 568 UHV multipocket electron beam source used in the thesis is shown. It has three pockets for the materials, in our case Co, Ti and CaF_2. In the picture, the crucible contains cobalt pellets into a graphite crucible. Additionally, the bar to move the crucibles, the electrical connections and water-cooling system are shown. There is an emitter assembly where the main components are the electron gun with the filament and the permanent magnet. The working accelerating voltage of -7kV is

supplied with the Telemark TT-6 Cheetah E-beam source power supply, which provides an emission current (up to 750mA) and output voltage (from -8 to 6KV). In order to control and to fit the deposition rate of the materials in 0.2Å/s, parameters such as the electron beam current and the shape of the sweep of the beam have been adjusted. The e-beam currents used were Co: 45mA, Ti: 42mA and CaF_2: 7mA with a common accelerating voltage of -7kV. The shape of the sweep is controlled by a Telemark electron beam source XY Sweeper, which distribute the e-beam energy within the material and has four operation modes (triangular, circular, spiraling and point in a fixed position). The sweep of the e-beam is important in materials with poor heat conductivity such as the dielectric CaF_2.

The deposition rate is controlled by a quartz balance (Figure 2.5(b)) whose mechanism consists in a piezoelectric quartz crystal, vibrating at its resonant frequency. This oscillation frequency is sensitive to deposited mass onto its surface. For this purpose, the quartz balance is adjusted to parameters such as the density (ρ) and Z factor (Z) of the deposited materials, which are tabulated [Co(Z:0.343, ρ:8.9g/cm^3), Ti(Z:0.628, ρ:4.5g/cm^3), CaF_2(Z:0.775, ρ:3.18g/cm^3)] and also, in order to avoid thermal drifts, it is refrigerated by a water cooling system.

Resistive thermal evaporation

Thermal Evaporation (TE) is one of the most used physical vapor deposition techniques because of its capability to control the temperature of the source material, and to enable the precise fabrication of the nanostructures. The technique consists in transferring heat to a crucible with the material by resistance heating in a vacuum atmosphere until the material evaporates and it is deposited on a substrate.

There are three types of crucible heating systems: resistive, electron beam and inductive systems. One of the most used is a resistive heated system, which is an effusion evaporator source or Knudsen cell (K-cell). A typical K-cell consists of a heating element, the heat shield, crucible thermocouple assembly and a water-cooling system. Most of the materials used are refractory materials such as tantalum or Mo and insulators as alumina and pyrolytic boron nitride (PBN)[161]. The sketch in Figure 2.6(a) presents the mechanism of these sources

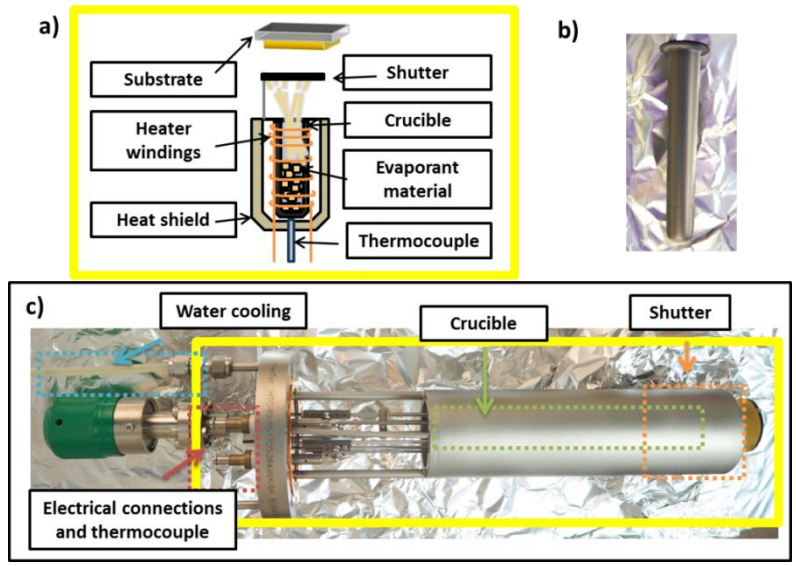

Figure 2.6: (a) Sketch for the principle of the thermal evaporation. (b-c) The commercial Knudsen cell used in the experiments. Right image: the graphite crucible where the gold material is evaporated.

where the material in a crucible is heated by a resistance wire of tungsten and/or tantalum. Under high vacuum atmosphere, the atoms of the evaporated material have a mean free path (λ_{mfp}) longer than the working distance (δ) and the deposition is more precise because of the reduction of collisions between the atoms (Knudsen model). To control the temperature, a thermocouple and a controller are used.

The experimental setup of this system is seen in Figure 2.6(c). A commercial K-cell model (HTC-63-10-1700-284-WK-SHM, CreaTec Fischer & Co. GmbH) made entirely from tantalum and tungsten is designed to evaporate the material at high temperatures (up to 1700°C) by radiative heating. The Tungsten/rhenium alloy thermocouple (type C) is suitable to measure high temperatures, typically from 0 to 2315°C and the PID controller (CU-3504-S1-DC, Eurotherm) allows the control of the temperature. The K-cell is cooled by an external chiller at a constant temperature of 9°C. The crucible is made of pyrolytic graphite (CreaTec Fischer & Co. GmbH), (Figure 2.6(b)). In our experiments, the Knudsen-cell is used to evaporate Au at 1400°C with a deposition rate around 0.25 Å/s.

2.2. Characterization

2.2.1. Morphology

Atomic Force Microscopy

The *Atomic Force Microscopy* (AFM) was developed in 1986 by *Binning et al,* as a successor of the *Scanning Tunneling Microscope* (STM)[162]. AFM is a non-destructive surface analysis (mainly morphology) technique. It has a high lateral resolution (1-10 nm), and a very high vertical resolution (0.2 nm). This is useful to determine the three-dimensional topological characteristics of the materials (for example, roughness, defects, etc.), but it also allows us to study the properties of nanometric structures fabricated using lithographic techniques.

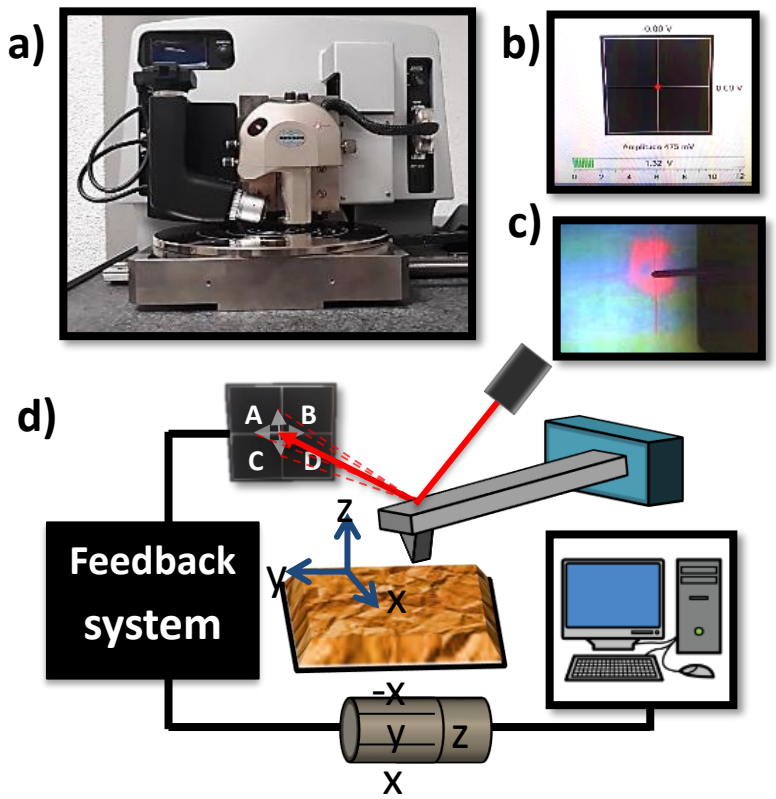

Figure 2.7: a) Image of the AFM system installed in the IMN (CSIC). b) Image of the photodiode responsible for collecting the data. c) Image of the tip moving over the surface of the sample. d) Scheme of the AFM operation.

The AFM structure is relatively simple (Figure 2.7(d)). It consists on a *Si* micrometric tip, sited at the end of a cantilever which can deflect a few nanometers. The tip is scanned over the sample surface (Figure 2.7(c)). The cantilever will deflect proportionally to the interaction forces (typically a few nN) between the tip and the sample surface. When the topography changes, the force varies, modifying the cantilever deflection.

In order to detect and quantify the deflection a laser system is installed. The laser is reflected of the back of the cantilever and collected by a 4-quadrant photodiode (Figure 2.7(b)), which registers the (*x,y*) position of the laser. The corresponding light intensities in the different quadrants will give the information of the cantilever deflection in form of a voltage which is stored by an electronic system and transformed into a 3D image. The cantilever is sustained by a holder that is connected to a piezoelectric tube. This tube is responsible for the movement of the tip.

Depending on the nature of the samples, there are different operating methods for the AFM:

- *Contact mode*
- *Non-contact mode*
- *Tapping mode*

Contact mode: the force produced between the surface and the tip is constant during the scan. This mode is appropriate to measure rough samples with a high scan rate and atomic resolution. However, this method is not recommended for soft samples because the tip can apply very large pressures in a micrometric area (~ 0.1GPa) that could damage the surface.

Non-contact mode: The cantilever oscillates at a frequency near the resonant frequency., During the tip scan the oscillation is modulated by the tip-surface interaction forces. The difference between the oscillation of the cantilever and an external referential oscillation serves as a feedback and provides information about the surface. This mode works well in UHV, because in ambient conditions tip and the sample are covered with a water layer that modifies the cantilever oscillation.

Tapping mode: This mode was developed in order to avoid the problem mentioned above. Here an additional piezoelectric makes the cantilever vertically oscillate at a particular frequency with amplitude between 20-100

nm, so that the tip contacts the sample one time per oscillation. Since the cantilever is vibrating, the signal recorded at the photodiode is sinusoidal, and the voltage will be AC. This Voltage is converted to DC with the lock-in amplifier and is proportional to the cantilever oscillation amplitude. When the tip encounters a high region of the surface the oscillation amplitude decreases. Conversely, if it finds a lower region of the surface then the amplitude increases. As in the Non-contact mode, the signal is compared with a reference DC signal in order to fabricate the image with the difference between the vertical position and the setpoint position. The tapping mode has a high lateral resolution (1-5 nm), and at the typical oscillation frequencies, the tip does not get stuck in the surface fluid. The tip only contacts the surface very briefly so the damage for both is reduced. The phase of the oscillation is also interesting as can give additional information about material properties. The oscillation phase and amplitude can be recorded at the same time.

The *atomic force microscopy* has two principal characteristics complementary of *Scanning Electron Microscopy* (SEM); the first one is that, unlike SEM, AFM can obtain reliable 3D information about dimensions of features in the sample, while the depth determination in SEM images is not as precise as in AFM. In addition, sample preparation in AFM is minimal.

The AFM measurements of this work have been performed with the Veeco™ DIMENSION icon system. The cantilevers, made of Silicon with a tip radius of 10 nm and a force constant of 0.3 N/m, are from Nanosensors™.

Scanning Electron Microscopy

Scanning Electron Microscopy is a well-established and widely used technique to visualize morphological characteristics in the nanometric scale.

The development started in 1930, when *Louis de Broglie* predicted that electrons could behave as electromagnetic waves under certain conditions, and they would have a wavelength determined by:

$$\lambda = \frac{h}{p_e} \tag{15}$$

where h is the *Planck* constant and p_e is the linear moment of the electrons. Based on this study, in 1937, *M. Von Ardenne* fabricated the first *Scanning*

Electron Microscope[163]. In this microscope, the metallic cathode emits electrons with a λ depending on the applied voltage; as voltage increases, the λ will be decreased.

The principal function of the SEM technique is to obtain a topographic image of the sample surface. The technique consists on generating an electron beam and accelerating it towards the sample. The interaction between the primary electrons and the sample generates different types of electrons, each one at different depth, as seen in Figure 2.8. Mainly two types of electrons are generated: *Secondary Electrons* (SE) and *Backscattered Electrons* (BSE):

- *Secondary Electrons*: Coming from an inelastic diffusion produced at the sample surface (few tens of nanometers). Their energy is less than 50 eV.
- *Backscattered electrons*: These electrons come from multiple diffusions produced inside the sample, up to some micrometer depth. They come out with energies larger than 50 eV. The number of backscattered electrons generated increases with the atomic number, Z. These electrons give information about the topography and the composition of the samples.

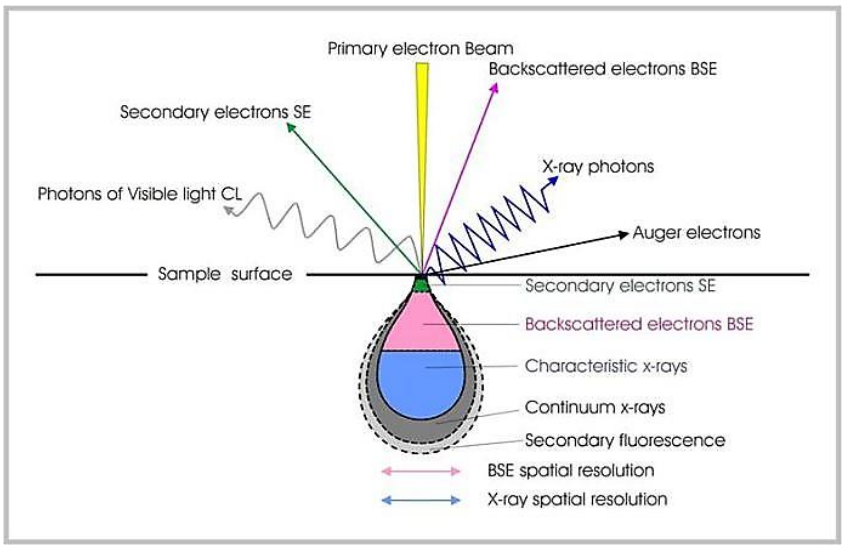

Figure 2.8: Sketch adapted from reference 141 where the result of the interaction between the electrons and the surface of a material is shown. The emission consists on electromagnetic radiation (X-Rays and light) and electrons (Secondary, backscattered and Auger). It is also represented the interaction volume of each phenomena into the sample.

The electron gun can use the *Thermionic* or the *Field Effect*, the system used in this work is a Field Effect SEM (FE-SEM).

Field Effect emission SEM

In this system the electrons are generated by the application of an electric field. The electrons are accelerated with enough energy to avoid the potential barrier, which is called work function, and leave the cathode. The necessary electric field to extract the electrons is 10V/nm. In order to obtain these electric fields, is necessary to apply voltages of the order of 1 kV to a filament typically with a diameter of 100 nm.

The SEM source is a *Schottky* model, consisting on a single crystal of Tungsten, covered by zirconium oxide (ZrO), which reduces the work function at the tip. In this model, the electrons removal is thermally assisted, so this SEM is a *warm cathode* type. The FE SEMs have considerably bigger resolutions than the thermionic ones since the e^- beam can be focused much more. Typically, the resolution increases with the electron acceleration voltage. In fact, a SEM with a LaB_6 filament can reach a resolution of 3.0 nm when a voltage of 30 kV is applied. Meanwhile, a FE-SEM can offer a resolution of 1.0 nm with only 20 kV applied. This makes the FE-SEM an ideal system for the acquisition of high-resolution images, even at low acceleration voltages.

Electron gun

Once the electron beam is emitted by the filament, it is necessary to make it go through an electrostatic accelerating lens. Inside the electron gun, the electrons generated at the cathode are accelerated by the electric field produced by the anode (at a positive potential), sited next to it. Between the cathode and the anode there is a third electrode with a negative potential with respect to the cathode. The accelerating potential modifies the electrons path, making it vertical. If the system had no aberrations, all the trajectories would merge in the same point. However, when the electrons are produced in the cathode, they have a radial component in the velocity, so the diameter will be finite and dependent on the velocity radial components (*chromatic aberration*). The FE-SEM requires an UHV in the emission zone (10^{-10}mbar). The vacuum is essential to avoid filament contaminations, which would reduce dramatically the current density.

Scanning electron microscope architecture

The principal parts of a SEM are:

- *Electro-Optic column*
- *Sample chamber*
- *Detection system*
- *Electronic system* to elaborate the images

Once the electrons have been generated, they go through the electro-optic column, which is composed by a group of apertures and magnetic lenses (*Figure 2.9*). These have the role of adjusting the geometric (diameter, astigmatism, focal distance) and electronic (current density) parameters. Later, the signal produced in the interaction between the beam and the sample is detected and processed in a computer. Finally, the software reconstructs the image of the surface.

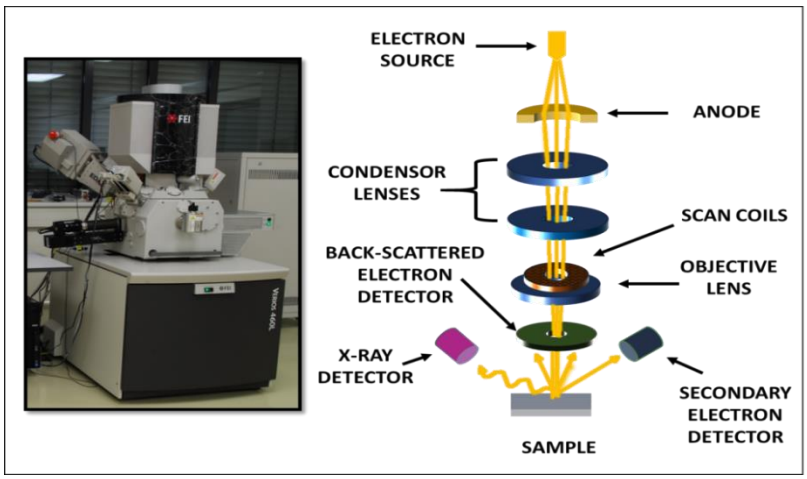

Figure 2.9: a) Image of the Scanning Electron Microscope from the Instituto de Micro y Nanotecnología (CSIC). b) Scheme of a conventional scanning electron microscope.

The sample chamber is situated in the low part of the column. Its principal component is a stage which is under the sample holder. This part is at High vacuum (10^{-6}-10^{-7} mbar). The secondary and backscattered electrons detectors are also inside the sample chamber in order to receive the interaction signals from the sample. The chamber also has an infrared camera that gives a panoramic image of the chamber inside.

The microscope used during the thesis work is a FEI VERIOS 460 SEM of Field Effect emission, with monochromatic source, magnetic immersion mode, and a beam decelerating system[164]. Its four principal characteristics are:

1) Maximum resolution in the sub-nanometric range: 0.6nm at 15 kV.
2) Maximum versatility regardless of the nature of the samples, allowing maximum resolution for insulating and magnetic samples.
3) Availability for simultaneous image modes (topography, composition and crystalline structure) based on the possibility of using 6 detectors simultaneously: secondary electrons in column, and chamber; backscattered electrons in column, upper column and chamber and finally, electrons transmitted.
4) Capacity of composition analytical characterization using X-ray spectroscopy and EDX.

This microscope was obtained through the project CSIC 13-4E-1794 funded by the European Regional Development Fund and is one of the best in Spain with the best lateral resolution of 0.6nm.

2.2.2. Optical properties. Spectroscopic Ellipsometry

Spectroscopic Ellipsometry (SE) is a fast, non-destructive and versatile optical characterization technique that permits to determine the optical properties of different materials. A spectroscopic ellipsometer can be found in most of the thin film analytical labs, but also in biology and medicine labs, due to the possibility to use it for in-situ and ex-situ measurements in a wide variety of situations[165]. It can measure optical and structural properties of different compounds such as the complex refractive index ($N=n-ik$), dielectric constants ($\varepsilon=N^2$), absorption coefficient ($\alpha=4\pi k/\lambda$), film thickness (of single and multiple layers) with high precision (≈ 0.1Å), carrier concentration, roughness or optical anisotropies. Moreover, the ellipsometer can obtain the *p*- and *s*- intensity values from the AC signal. These values represent the *Rp* and *Rs* for reflection and *Tp* and *Ts* for transmission. The Mueller matrix spectroscopic ellipsometry is a widely used optical and nondestructive technique suitable for the analysis of the optical response of structures. It allows to study several optical anisotropies from the analysis of the change in polarization state between the incident and the transmitted light when the beam pass through the sample. Although it is a powerful tool to describe from isotropic thin films[166,167], anisotropic structures[168], biological species such as butterflies, beetles[61,62] to even human tissues[169]; the interpretation of the physical meaning of the experimental measurements is still complicated because the optical anisotropies are mixed[170]. One of the objectives fulfilled in this thesis is to

provide a complete description of anisotropic samples with structures with different morphologies by using the Mueller matrix formalism.

One advantage compared with other optical techniques is that ellipsometry does not require any sample preparation like contacts, liquid immersion, etc[165].

Spectroscopic ellipsometry measures the variation of the polarization state of the reflected light in comparison with the incident light. As this measurement is related to the phase change of the polarized light, it is more sensitive than a conventional intensity variation measurement. Thus, no special reference samples are needed since the absolute intensity of the reflected light does not need to be measured.

However, SE does not measure the sample parameters of interest directly, but it obtains a quantity that is a function of the parameters of interest. Therefore, the realization of the extraordinary sensitivity of the SE requires that the experimental data must be fit to a model with fitting parameters. In this thesis, the *CompleteEASE* and *WVASE* software[171] packages are used to fit the experimental data.

A light field incident to a sample can be separated into two orthogonal components, as illustrated in Figure 2.10. The p-polarized light and s-polarized light, which are parallel and perpendicular to the incident plane, respectively. The ratio between the two reflected lights can be expressed as:

$$\rho = \frac{r_p}{r_s} \tag{16}$$

The ellipsometer measures this ratio as a function of two angles, Δ and Ψ:

$$\rho = tan(\Psi)e^{i\Delta} \tag{17}$$

The Δ and Ψ angles determine the amplitude ratio and phase difference between the s- and p- components of the reflected light. The system measures pairs of angles (Δ,Ψ) for each wavelength.

For an ideal bulk sample without oxide, roughness or any overlayer, the optical constants can be extracted using the following equation[172]:

$$\varepsilon = \varepsilon' + i\varepsilon'' = (n + ik)^2 = \sin(\varphi)^2[1 + \tan(\varphi)^2(\frac{1-\rho}{1+\rho})^2] \quad (18)$$

where φ is the angle of the incident light. But for real samples, it is necessary

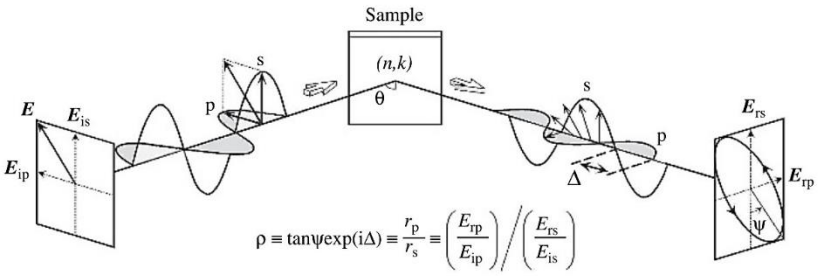

Figure 2.10: Measurement principle of ellipsometry

to use optical models that describe more precisely the properties in order to extract the optical constants ε', ε'', *n* and *k.* For that, first, a theoretical model is proposed for the structure studied. Each layer of the system is parametrized by its thickness and optical constants. Then the reflection coefficients r_s and r_p are calculated using classical optics laws[4]. The most effective process is to construct the system by using easy models. The simplest case is a thin film on top of a plane substrate, where the incident light will experience multiple reflections and refractions at the two interfaces (film-air and film-substrate). By summing the total reflected beams for *p*- and *s*- polarized light using the Snell's law, the total Fresnel reflection coefficients (r_p and r_s) are obtained. The (Δ, Ψ) angles can then be obtained from eq. 17.

The previous method is useful for single layers, but the difficulty of the calculations increases when applied in multilayers. Hence, Transfer matrix method should be used for this kind of samples[173], being a method that admits *Effective Medium Approximations* (EMA)[44,174]

Once the measured SE data is fitted to the model, the quality of the agreement between the (Δ, Ψ) pairs from the fitting and the experimental data is analyzed by the *mean squared error* (MSE), which is a method implemented into the

CompleteEASE software, the software responsible of controlling the ellipsometer and acquires the data. The MSE can be expressed as:

$$MSE = \sqrt{\frac{1}{3a-b}\sum_{i=1}^{a}[(N_{Ei}-N_{Fi})^2+(C_{Ei}-C_{Fi})^2+(S_{Ei}-S_{Fi})^2]} \times 1000 \quad (19)$$

Where *a* is the number of wavelengths, *b* is the number of fit parameters, *N=cos(2Ψ)*, *C=sin(2Ψ)cosΔ* and *S=sin(2Ψ)sinΔ*. The parameters subscribed with Ei and Fi are the experimental and fitted data, respectively. Therefore, the lower the MSE value, the better the accuracy of the fitting.

2.2.2.1. Polarization of light. Mueller matrix formalism

In 1941, the Physicist R. Clark Jones introduced a mathematical formalism to describe completely polarized light[175]. The Jones formalism describes ellipsometry measurements or variations in polarized light when pass through optical elements. The polarization state of the light is presented by superimposing two waves oscillating parallel to the x and y axes (eq. (20)). The Jones vector is defined by the electric field vectors in the x and y directions. From eq. (20) the Jones vector is expressed by omitting the term *exp[i(ωt-kz)]* and simplifying to

$$\mathbf{E}(z,t) = \begin{pmatrix}\mathbf{E_x}\\ \mathbf{E_y}\end{pmatrix} = \begin{pmatrix}[\mathbf{E_{xo}}e^{[i\delta_x]}]\\ [\mathbf{E_{yo}}e^{[i\delta_y]}]\end{pmatrix} \quad (20)$$

where the electric field amplitudes E_x and E_y are complex vectors. Assuming the amplitudes as positive values and using the phase difference (δ_x-δ_y) the previous equation can be rewritten as

$$\mathbf{E}(z,t) = \begin{pmatrix}\mathbf{E_x}\\ \mathbf{E_y}\end{pmatrix} = \begin{pmatrix}|\mathbf{E_x}|e^{i[\delta_x-\delta_x]}]\\ |\mathbf{E_y}|\end{pmatrix} \quad (21)$$

From this equation (20), light intensity can be obtained by multiplying the Jones vector ***E*** by its Hermitian adjoint $\boldsymbol{E}^{\dagger}$:

$$I = \boldsymbol{E}\boldsymbol{E}^{\dagger} = E_x^* E_x + E_y^* E_y \quad (22)$$

The Jones Matrix is a 2x2 complex matrix ***J*** which describes light interaction with a medium or an optical system. In this matrix the incident electric field $E_{x,y}$ and the outgoing electric field of the light $E'_{x,y}$ are related as

$$\begin{pmatrix} \mathrm{E'_x} \\ \mathrm{E'_y} \end{pmatrix} = \mathbf{J} \begin{pmatrix} \mathrm{E_x} \\ \mathrm{E_y} \end{pmatrix} \tag{23}$$

Using this mathematical formalism, it is possible to study the evolution of an incident plane wave $\boldsymbol{E}_i$ when it crosses a system of *N* optical elements from the optical element 1 first and then successively the rest of the elements by analyzing the Jones matrix product of each of these optical elements.

$$\boldsymbol{E}_o = \boldsymbol{J}_N \boldsymbol{J}_{N-1} \dots \boldsymbol{J}_2 \boldsymbol{J}_1 \boldsymbol{E}_i \tag{24}$$

In ellipsometry measurements, there are compensators and polarizers with a rotation angle relative to the x or y axes. The analysis of the Jones formalism under the transformation of the x-y coordinates into the x'-y' coordinates by coordinate rotation. In matrix form is represented by

$$\begin{pmatrix} \mathrm{E'_x} \\ \mathrm{E'_y} \end{pmatrix} = \begin{bmatrix} cos \propto & sin \propto \\ -sin \propto & cos \propto \end{bmatrix} \begin{pmatrix} \mathrm{E_x} \\ \mathrm{E_y} \end{pmatrix} = \boldsymbol{R}(\propto) \begin{pmatrix} \mathrm{E_x} \\ \mathrm{E_y} \end{pmatrix} \tag{25}$$

where α is the rotation angle and $R(\alpha)$ represents the matrix of the coordinate system.

The Jones matrix formalism only can be used in completely polarized light. To describe the case of partially polarized or unpolarized light the Stokes formalism is used.

The Stokes parameters were described in 1852 as an alternative to describe all kinds of polarization. The Stokes parameters are directly connected to the measurable intensities and are real numbers instead of complex numbers.

If the light intensity of the polarized light is used, the four parameters are expressed as

$$\boldsymbol{S} = \begin{pmatrix} S_0 \\ S_1 \\ S_2 \\ S_3 \end{pmatrix} = \begin{pmatrix} I_x + I_y \\ I_x - I_y \\ I_{45} + I_{-45} \\ I_{LCP} + I_{RCP} \end{pmatrix} \tag{26}$$

Here, S_0 represents the total light intensity, and S_1 shows the difference of polarized light between the y direction (I_y) and the x direction (I_x). On the other hand, S_2 represents the polarized light obtained by subtracting the light intensity of linear polarization at-45° from that at 45°.Finally the parameter S_3 is related to the relative difference of circular polarized light between the Left-Circular Polarized (LCP) and the Right Circular Polarized light (RCP). All parameters represent the relative difference in light between each state of polarization.

Although the Stokes vector was introduced in the XIX century, the matrix method for manipulating the Stokes vectors was developed by Hans Mueller in 1943.The transformation matrix of the optical system between the input and output Stokes vectors is called Mueller matrix and is defined as follow:

$$\boldsymbol{S'}_{out} = \boldsymbol{M}\boldsymbol{S}_{\boldsymbol{in}}$$

$$\begin{pmatrix} S'_0 \\ S'_1 \\ S'_2 \\ S'_3 \end{pmatrix} = \begin{pmatrix} m_{11} & m_{12} & m_{13} & m_{14} \\ m_{21} & m_{22} & m_{23} & m_{24} \\ m_{31} & m_{32} & m_{33} & m_{34} \\ m_{41} & m_{42} & m_{43} & m_{44} \end{pmatrix} \begin{pmatrix} S'_0 \\ S'_1 \\ S'_2 \\ S'_3 \end{pmatrix} \qquad (27)$$

To introduce the Mueller matrix formalism, the procedure to obtain it from the Jones matrix by calculating the light intensities (the Stokes vector) from the electric fields (the Jones vector) is described next.

From eq.(22), the direct product of the Jones vectors of the input and output light waves is calculated as

$$\boldsymbol{E}_{out} \otimes \boldsymbol{E}^*_{out} = \boldsymbol{J}\boldsymbol{E}_{in} \otimes \boldsymbol{J}^*\boldsymbol{E}^*_{in} = (\boldsymbol{J} \otimes \boldsymbol{J}^*)(\boldsymbol{E}_{in} \otimes \boldsymbol{E}^*_{in}) \qquad (28)$$

and the coherence vector $C = \left(\langle E_x E_x^* \rangle, \langle E_x E_y^* \rangle, \langle E_y E_x^* \rangle, \langle E_y E_y^* \rangle\right)^T$ is obtained.

This coherence vector is related to the transformation matrix of the optical system between the input Stoke vector ***S*** and the output Stokes vector ***S'*** by the electric field matrix ***A:***

$$\boldsymbol{S} = \boldsymbol{AC} = \begin{pmatrix} 1 & 0 & 0 & 1 \\ 1 & 0 & 0 & -1 \\ 0 & 1 & 1 & 0 \\ 0 & i & -i & 0 \end{pmatrix} \begin{pmatrix} \langle E_x E_x^* \rangle \\ \langle E_x E_y^* \rangle \\ \langle E_y E_x^* \rangle \\ \langle E_y E_y^* \rangle \end{pmatrix} \tag{29}$$

From this equation, it follows that $C_{in} = A^{-1} S_{in}$ and $C_{out} = A^{-1} S_{out}$ .Finally, substituting these expressions into eq.(27) obtains the Mueller matrix

$$\boldsymbol{S_{out}} = \boldsymbol{A}(\boldsymbol{J} \otimes \boldsymbol{J}^*)\boldsymbol{A^{-1}}\boldsymbol{S_{in}} = \boldsymbol{M}\boldsymbol{S_{in}} \tag{30}$$

In ellipsometry measurements, the Mueller matrix is normalized by scaling the matrix to the m_{11} element. The elements of the normalized Mueller matrix have values between -1 and 1.

As mentioned above, the Stokes vector give us information about partially polarized and unpolarized light. However, this mathematical method does not provide directly the information obtained during the ellipsometry measurements. Thus, the use of Mueller matrix formalism to obtain the physical meaning of the optical properties is appropriate.

Understanding the optical properties of the nanostructure, Jones matrix formalism gives the evolution of the intensity and/or polarizations states of the beam of light when it passes through a chiral medium. Periodic metamaterials can be classified according to their symmetric considerations by means of Jones Matrix[33,176,177]. In absence of depolarization, the components of the Jones vector of the outgoing wave (*E'*) are given as a linear transformation of the components of the Jones vector of the incident wave (***E***). The transmission matrix connects the transmitted and incident fields by this equation:

$$\begin{pmatrix} \mathrm{E'}_s \\ \mathrm{E'}_p \end{pmatrix} = \begin{pmatrix} t_{ss} & t_{\mathrm{sp}} \\ t_{ps} & t_{pp} \end{pmatrix} \begin{pmatrix} \mathrm{E}_s \\ \mathrm{E}_p \end{pmatrix} \tag{31}$$

where the Jones matrix contains information about the transmission intensities along the directions perpendicular (s-polarization) and parallel (p-polarization) to the plane of incidence. This equation is also valid for reflection. For instance, t_{sp} shows how much intensity of the s-polarized wave is transmitted into p-polarized wave.

Moreover, anisotropic structures have in-plane anisotropy ($t_{xy} \neq t_{yx}$) and assuming that the non-diagonal elements are smaller than the diagonal elements $|t_{xy}|^2 << |t_{xx}|^2$. In a chiral structure with in-plane anisotropy, its non-diagonal elements t_{xy} (t_{yx}) can be divided into symmetric ($tsy = (t_{xy}+t_{yx})/2$) and antisymmetric ($ta = (t_{xy}-t_{yx})/2$) components[122]. The symmetric component (t_{sy}) is related to the optical anisotropy in the plane. On the other hand, the antisymmetric component is a combination of the magneto optical[16] (t_{MO}) and the chiral effects (t_{CH}): $ta = t_{CH} \pm M t_{MO}$, where M is the normalized magnetization of the nanostructure along the surface normal. Therefore, the transmission matrix of the structure can be described as:

$$\begin{pmatrix} t_{xx}\, t_{xy} \\ t_{yx}\, t_{yy} \end{pmatrix} = \begin{pmatrix} t_{xx} & t_{sy} + t_a \\ t_{sy} - t_a & t_{yy} \end{pmatrix} \tag{32}$$

To be able to discern each component, the experimental measurements are performed in forward (*F*) and backward (*B*) configurations. In back illumination, the element related to the in-plane optical anisotropy (t_{sy}) undergoes a change of sign, while the asymmetric component (ta) remains unchanged because it does not depend on the in-plane orientation of the samples.

$$F: \begin{pmatrix} t_{xx} & t_{sy} + t_a \\ t_{sy} - t_a & t_{yy} \end{pmatrix} \; B: \begin{pmatrix} t_{xx} & -t_{sy} + t_a \\ -t_{sy} - t_a & t_{yy} \end{pmatrix} \tag{33}$$

Using the procedure to obtain the specific Mueller matrix for the nondepolarizing and anisotropic sample, the Jones-Mueller matrix is obtained[178]. This Mueller matrix is a 4x4 matrix that provides information about the polarization properties (diattenuation, retardance, depolarizations and polarization states[165]). In anisotropic materials the off diagonal elements of the Mueller matrix (m_{12}, m_{13}, m_{14}, m_{23}, m_{24}, and m_{34}) are related to optical and morphological changes in the properties[179]. In the present thesis, some of these off-diagonal elements are selected in order to understand the optical properties of plasmonic structures. Combining equations (29-33), the elements in the Mueller matrix in forward and backward configurations are extracted:

$$
\begin{aligned}
m_{12}^{F} &= \frac{1}{2}\left(t_{xx}t_{xx}^{*} - t_{yy}t_{yy}^{*} - 4Re\left(t_{a}t_{sy}^{*}\right)\right) \\
m_{12}^{B} &= \frac{1}{2}\left(t_{xx}t_{xx}^{*} - t_{yy}t_{yy}^{*} + 4Re(t_{a}t_{sy}^{*})\right) \\
m_{13}^{F} &= Re\left(\left(t_{xx} + t_{yy}\right)t_{sy}^{*}\right) + Re\left(\left(t_{xx} - t_{yy}\right)t_{a}^{*}\right) \\
m_{13}^{B} &= -Re((t_{xx} + t_{yy})t_{sy}^{*}) + Re((t_{xx} - t_{yy})t_{a}^{*}) \\
m_{14}^{F} &= Im((t_{xx} - t_{yy})t_{sy}^{*}) + Im((t_{xx} + t_{yy})t_{a}^{*}) \\
m_{14}^{B} &= -Im((t_{xx} - t_{yy})t_{sy}^{*}) + Im((t_{xx} + t_{yy})t_{a}^{*})
\end{aligned}
\tag{34}
$$

All the elements are conventionally normalized to the m_{11} element which is the total transmitted intensity. The off-block diagonal elements of the matrix give us information about polarization conversion effects. Our analysis is focused in the information extracted from the m_{12}, m_{13} and m_{14} elements which are related to the optical anisotropies in the samples. On the basis of these results, the Mueller matrix spectroscopic ellipsometry (MMSE)[180–182] experimental technique has been developed to extract information about the depolarization or polarization[183,184] of nanostructures with magnetism[185], plasmonic[40,186,187] or even biological properties[62,169,188,189].

Interpretation and physical meaning of the Mueller matrix elements. Optical anisotropies

To improve the interpretation of the Mueller matrix elements in the nanostructures, a decomposition method based on a continuous medium is used to determine the physical meaning of these elements[190]. Considering the particular case of homogeneous samples without depolarization, it is possible to simplify the decomposition of Mueller matrices. This way, the experimental measurements obtained by ellipsometry give us direct information about optical anisotropies in the structures.

$$M = \begin{pmatrix} 1+\frac{1}{2}(LD'^2+LD^2) & -LD & -LD' & CD+\frac{1}{2}(LBLD'-LB'LD) \\ -LD & 1+\frac{1}{2}(LD^2-LB'^2) & CB+\frac{1}{2}(LBLB'+LDLD') & LB' \\ -LD' & -CB+\frac{1}{2}(LBLB'+LDLD') & 1+\frac{1}{2}(LD'^2+LB^2) & -LB \\ CD-\frac{1}{2}(LBLD'-LB'LD) & -LB' & LB & 1+\frac{1}{2}(LB^2+LB'^2) \end{pmatrix} \quad (35)$$

From this differential decomposition, there are eight effects that can be measured: mean absorption *k*, mean refraction *η*, linear birefringence *LB* and *LB'* (along x-y and 45 axes respectively), the linear dichroism *LD* and *LD'*, circular birefringence *CB* and circular dichroism *CD*. The definition of these effects is shown in the table 2.1, where *κ* is extinction coefficient; *n* is the refractive index; *d* is the optical path through the medium; λ_o is the vacuum wavelength of light and the polarization of the light is expressed as *x*, *y*, 45° and 135 ° for linear polarized light and +,- for right and left circularly polarized light[191].

Table 2.1: Definition of the optical anisotropies measured in the Mueller matrix. Table extracted from reference [149].

Effect	Symbol	Definition
Isotropic phase retardation	*η*	$2\pi nd/\lambda_o$
Isotropic amplitude absorption	*k*	$2\pi\kappa d/\lambda_o$
(x-y) linear dichroism	*LD*	$2\pi(\kappa_x-\kappa_y)d/\lambda_o$
45° linear dichroism	*LD'*	$2\pi(\kappa_{45}-\kappa_{135})d/\lambda_o$
(x-y) linear birefringence	*LB*	$2\pi(n_x-n_y)d/\lambda_o$
45 ° linear birefringence	*LB'*	$2\pi(n_{45}-n_{135})d/\lambda_o$
Circular dichroism	*CD*	$2\pi(\kappa_+-\kappa_-)d/\lambda_o$
Circular birefringence	*CB*	$2\pi(n_+-n_-)d/\lambda_o$

Figure 2.11 gives an overview of the structures that are be studied in this thesis and of the evolution of the elements of the Mueller matrix directly related to linear and circular dichroism.

As observed, the m_{12} elements in these structures have similar shape independently of the morphologies, and this element does not give us information about the handedness of the structures. On the other hand, the m_{13} element allows us to know the handedness of the structure and it is related to the arrangement of the building structures. Finally, the m_{14} element provides us information about the circular dichroism of the structures.

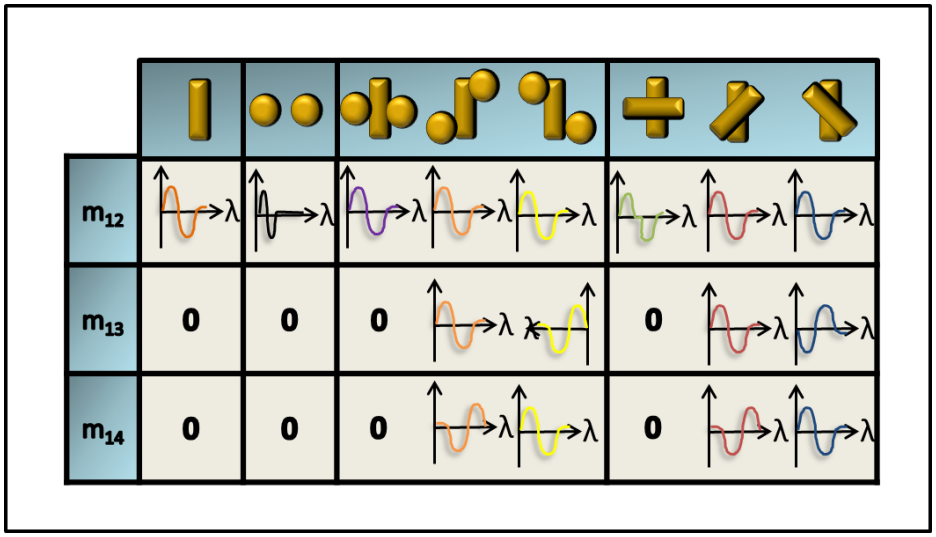

Figure 2.11: General sketch of the Mueller matrix elements studied in this thesis. The optical response of the structures is simplified to the shapes of the optical responses.

Linear Dichroism (LD)

The linear dichroism (LD) is defined as the difference between the absorption of light polarized along the parallel and perpendicular directions to an orientation axis of the nanostructure ($LD=A_{//}-A_{\perp}$)[192,193].

In spectroscopic ellipsometry, the analysis of the Mueller matrix element m_{12} gives information about the linear dichroic response[194,195]. Furthermore, the optical behavior of the samples is complemented with the transmission spectra of the structures for different orientations of the incident radiation polarization (*s*- and *p*- polarizations), in order to extract the response (there is an absence of linear dichroism when they intersect).

The LD signal increases with the degree of orientation and it is proportional to the absorbance of the sample (Figure 2.12). The linear dichroic response provides information about the orientation of the nanostructures or molecules. This is due to the dependence on the square of the scalar product between the transition moment vector of the nanostructure and the electric field vector of the incident light. When the structures are aligned with the electric field, the electrons move from ground states to excited states. The direction of the displacement of electrons during the electric transition is known as the electric dipole transition moment. Therefore, the intensity of the

linear dichroism is maximized when the electric dipole transition moments of the structures are polarized parallel to the sample orientation direction and minimum when they are polarized perpendicular to the sample orientation direction. In structures whose symmetry axis is along its orientation axis (uniaxial case), a negative signal is obtained if the dielectric dipole transition moments are polarized perpendicular to the axis. To have a non-zero signal at any wavelength, the structure needs to have the absorption at that wavelength and to be oriented[192]. In the case of isotropic samples, where the structures are randomly oriented, the total response of the structures is zero.

This optical property is commonly used in the study of the functionality and structure of molecules[193] such as tracers during the assembly of the supramolecular assemblies by analyzing the LD response in each stages of the process[196]. Apart from that, anisotropic photonic materials with linear dichroism play an important role as polarizers, filters or wave-plates, phase-matching elements in photonic devices and circuits in applications in sensing, imaging and emerging light based on quantum communication applications.

Despite the heightened interest in the study of optical properties in nanostructures, most of surveys are focused on the circular dichroic response. The optical characterization of the anisotropic medium is not simple and there are artifacts from both linear and circular contributions that can affect the measurement. Accordingly, the analysis of this linear dichroism is an useful way which allows to discern the origin of these optical effects[39,140,197–199].

The linear anisotropies such as Linear Birefringence (LB) and Linear Dichroism (LD) responses are usually 10-10^4 times larger than the circular responses (CB and CD) in typical single crystals. For example, in our hybrid structures with disks and rods the responses have the values of LD=10^{-2} and the CD=10^{-3}. To estimate the contribution from the linear dichroism to the circular dichroism, an experiment is performed where the sample is illuminated at normal incidence and the CD was measured as a function of the in-plane rotation angle. The insensitivity of the CD spectra to the in-plane rotation of the structures confirms the non-contribution from LD to the CD [39,200,201]. In homogeneous and nondepolarizing media, the differential decomposition method allows directly to connect the experimental Mueller matrix element m_{12} to the LD. Moreover, the LD at 45° is also related to the m_{13} element and contains the same information but rotating the plane of incidence +45°.

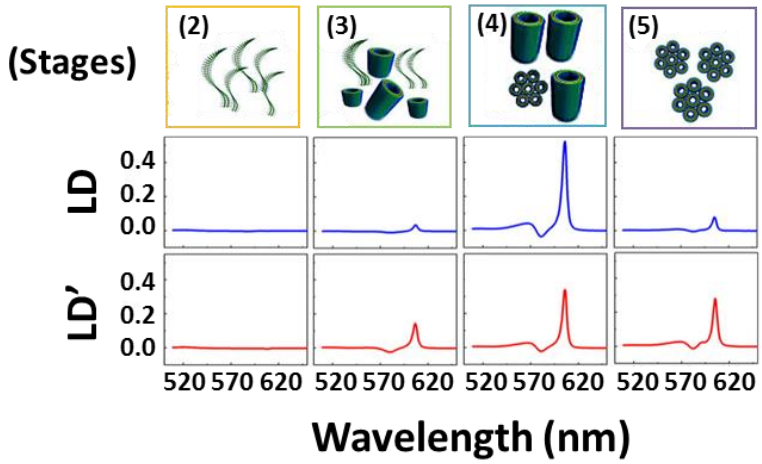

Figure 2.12: Schematic representation of the molecular ordering at various stages of assembly, (2) isolated C8O3 monomers, (2) symmetry-broken C8O3 assembly indicating the primary nucleation process, (3) formation of chiral C8O3 J-aggregate, (4) growth of tubular assemblies, and (5) bundling of cylindrical C8O3 aggregates resulting in exciton coupling. Figure adapted from reference201.

Circular dichroism (CD)

The circular dichroism is defined as different absorption for the left and right circularly polarized light ($CD=(2\pi(k_- - k_+)d)/\lambda_o$) where κ is extinction coefficient; n is the refractive index; d is the optical path through the medium; λ_o is the vacuum wavelength of the +,- for right and left circularly polarized light[191]. In spectroscopic ellipsometry, the analysis of the Mueller matrix element m_{14} gives information about the circular dichroic response[187,202]. CD can be used to analyze chiral structures such as protein secondary structure in molecules and to probe the interactions between chiral molecules. Despite this differential absorption being very small in biological systems like enantiomers (values around 10^{-4}-10^{-5}), the use of spectroscopy based on the CD has become a common technique for chemistry in stereochemical analysis and biotechnology. Some of the reasons are the sensibility to the configuration and to conformational features[203]. The CD effect can be observed in liquids and solutions where the chromophores are randomly oriented. According to the analysis from the Jones to Mueller matrix formalism, the element m_{14} is described as the combination of different optical properties where

$$m_{14} = CD_{Ch} + \frac{1}{2}(LBLD' - LB'LD) \quad (36)$$

The last equation shows the two contributions to the total m_{14} element in absence of magnetic fields. The first part is related to the pure chiral response. However, this contribution is smaller than the anisotropic contribution due to the combination of linear effects (linear birefringence and linear dichroism)[170].

Contributions to the CD signal

The active metastructures are measured in Forward (F) and Backward (B) configurations. To obtain information from the missing column of the Mueller matrix, the experimental measurements were carried out in forward (F) and backward (B) configurations (Figure 2.13).

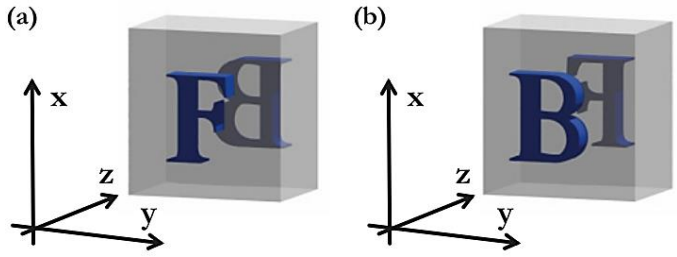

Figure 2.13: Sketch of the geometry of the sample from opposite sides to show the forward and backward configurations. Figure extracted from reference 33.

To get a general vision of the different contributions to the circular dichroism, a sketch of them and the experimental method to determine them are shown in Fig 2.14.

According to the definition of the Mueller matrix elements, the measurement of m_{12} in forward m_{12}^F vs backward m_{12}^B illumination does not alter the result. However, reversing illumination direction for the m_{13} implies that the top rod element will move from the y' to the x' direction resulting in a sign change. Finally, if there are only chiral contributions in the structure, the m_{14} element measured in forward vs backward should be the same value, because of the helicity of the structure does not depend on the illumination direction. However, the presence of in-plane anisotropies (t_{sy}) generates another contribution to the m_{14} element which varies with the illumination direction by changing sign[33,176].

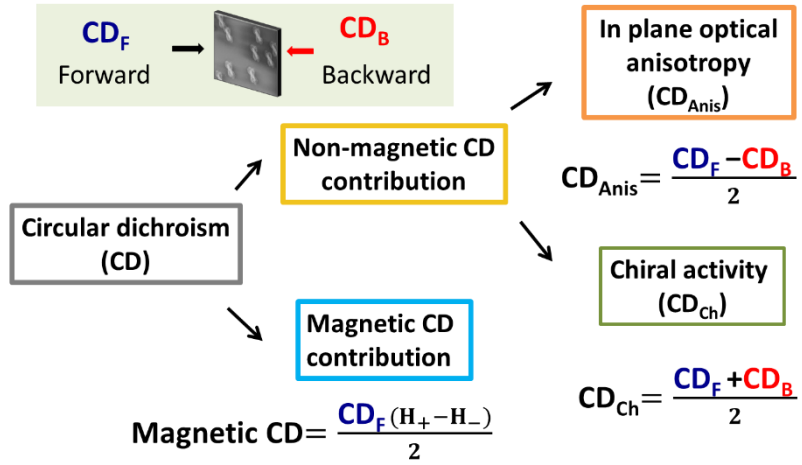

Figure 2.14: Sketch of the contributions to the circular dichroic response obtained from the ellipsometry measurements. The CD response is measured in forward and backward configurations. The response is divided according to the response to the magnetic field. In the absence of magnetic fields, the non-magnetic CD is the combination of the optical anisotropies (CD_{anis}) and the intrinsic chirality (CD_{ch}). In the presence of magnetic fields, the magnetic contribution appears.

From their sum and difference the in plane optical anisotropy (CD_{Anis}) and chirooptical activity (CD_{Ch}) are obtained. Furthermore, the magnetic response of the CD is obtained by applying an external magnetic field ($\pm H$).

Magnetic circular dichroism (MCD)

The search for strategies to improve the sensitivity of detection of chiral substances has attracted consideration attention in recent years. One of the routes consists on the incorporation of an active component that externally modulates matter-light interaction[34,204]. For this ferromagnetic materials are incorporated as active components whose magneto-optical activity allows modulation by external magnetic fields[120,122].

In these active metamaterials or meta-structures, the total CD response will not only be due to a configurational or intrinsic chiral contribution(CD_{anis}) and the presence of optical anisotropies that influence in the response (CD_{anis}), but also it will have a contribution dependent on the magnetic field. This due to the MO activity of the ferromagnetic material. In order to discern between the different sources of circular dichroism, this subsection incorporates a measurement protocol based on Mueller matrix formalism to identify the

origin of contributions to the circular dichroism. A permanent magnet setup, described later, is incorporated to provide out-of-plane fields to the spectroscopic ellipsometer. In the Mueller matrix formalism, the m_{14} element is related to the CD response of the structures. Unfortunately, the mixture of the contributions to the total response, complicates the task of distinguish them. In order to separate the different contributions, the measurement is performed in forward and backward configurations, and a mathematical calculation is developed to account for the addition and subtraction of these elements.

To describe the effect of applying a magnetic field into nanostructures, the circular dichroism can be expressed by[205,206].

$$CD(B) = CD(B = 0) + MCD \tag{37}$$

Where *CD(B=0)* represents the natural or intrinsic circular dichroism in absence of magnetic field. The other term is the purely magnetic contribution. The nanostructures in this thesis interact strongly with light and their optical response can be modulated with an external magnetic field. If the nanomaterial is chiral, it exhibits a natural circular dichroic response (*CD*(*B*=0)) and also, a contribution dependent on the field strength called magnetic circular dichroism (MCD). This contribution can be experimentally obtained from the subtraction of the m_{14} elements in forward configuration by applying the magnetic field as

$$MCD = \frac{(m_{14}(H) - m_{14}(-H))}{2} \tag{38}$$

The presented analysis of the magnetic circular dichroic response is in accordance with the theoretical analysis and the dependence with the magnetic field applied presented in the Chapter 1.

Anisotropy Factor g

In chiral structures, the absorption is not equal for left (A^+) and right CPL (A^-):. A useful derived parameter to characterize the chiro-optical activity of systems is the anisotropy or dissymmetry g factor (g-factor), defined as[203,205]:

$$g = 2\frac{A^+ - A^-}{A^+ + A^-}; A^{+,-} = \log\left(T^{+,-}\right) \quad (39)$$

where $A^{+,-}$ is the absorption for right- and left-handed circularly polarized light, respectively. It is worth noting that the sign of this factor is determined by the absorption bands, being always opposite in two enantiomers[40].

This *g*-factor is commonly used, and it can be related to the measured element m_{14} of the Mueller matrix as follows:

$$g = \frac{\log\left(\frac{1+m_{14}}{1-m_{14}}\right)}{\log\left(T(1-m_{14}^2)\right)}; T = \frac{T^+ + T^-}{2} \quad (40)$$

From equation 40, the relation between both magnitudes can be obtained. Some aspects such as the fabrication methods, composition and even the concentration of the structures modify the g-factor from values from 10^{-1} to 10^{-4}. Naturally occurring chiral optical materials show low CD signals and g values about 10^{-5} to 10^{-7} [207]. On the other hand, the anisotropic factor of chiral metal clusters increases up to a magnitude of 10^{-4}. It is even larger in discrete nanoparticles[139], with values of 10^{-3} to 10^{-2} in assembled structures[40,119] such as the structures fabricated in this thesis. Some examples of the *g*-factor values in chiral structures are nanodisk arrangements which gives maximum values of 0.14 [73]. In metal nanoparticles with dumbbell-like geometry the maximum value is 0.25[208] which is similar to the g_{max} value of 0.4 observed in in-plane gold rod dimers with extrinsic chirality[209]. Thus, similar values are obtained in planar chiral metamaterials such as gammadions fabricated by EBL, whose range are between 10^{-2} to 10^{-1} [34]. For instance, nanostructures composed by silver tetramers the anisotropy factor have values around 10^{-2} [210]. In gold crosses fabricated by EBL it is of the order of 10^{-3} [56]. Silver plasmonic array of nanoparticles have values of 10^{-3} [211]. In chiral plasmonic gold rod chains, the experimental values are about 10^{-3} with a maximum value of 0.005[212].In gold dimers fabricated by chemical methods, the values are around 10^{-3}. [135,213].In helical structures, the g-factor has larger values, around 0.15, than in single molecules[130,131,200].

2.2.2.2. Spectroscopic Ellipsometry system

Spectroscopic ellipsometer systems have shown a strong interest over the past few years. According the configuration of the optics elements in the ellipsometer they can be classified into two groups: ellipsometers with rotating components (*Rotating Analyzer Ellipsometer* (RAE) and *Rotating Compensator Ellipsometer* (RCE)) and ellipsometers with *PhotoElastic Modulators* (PEM)[214]. In this thesis, nanostructures with optical anisotropies are characterized by Mueller matrix ellipsometry and using a commercial spectroscopic ellipsometer (model M2000Fi J. A. Woollam Co.TM) in RCE configuration. The description of the configuration according the order of the components is shown in Fig 2.15. The components are a light source (Xe lamp of 75W), a fixed polarizer (calcite Glan-Taylor polarizer) at zero degrees (**P (0°)**), a continuously rotating compensator (**C_R**) with a rotation rate of 20Hz, a fixed analyzer (**A**) and finally the spectrometer and the detector (silicon arrays in the range of UV and VIS (up to 1100nm) and InGaAs photo diode array to cover the NIR (to 1700nm))[215].

There are many advantages in this configuration such as the capability to measure depolarization effects, the wide spectral range from 193nm to 1690nm and the accuracy of the measurement of the ellipsometric parameters (Ψ=0-90°, Δ=0-360°).

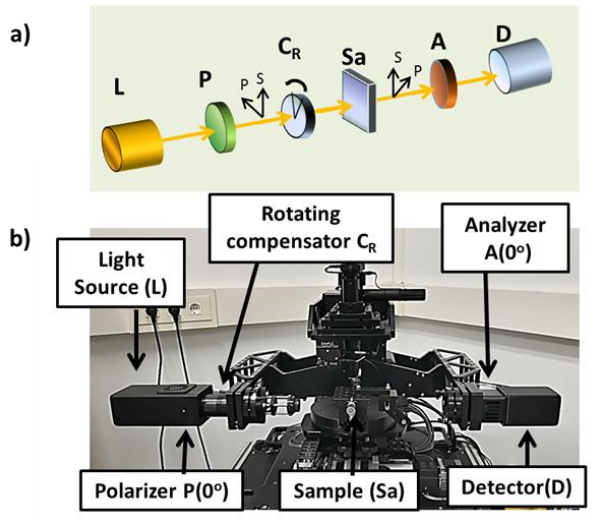

Figure 2.15: Schematic sketch for the optical components of an ellipsometer. (b) Spectroscopic system used during the experiments.

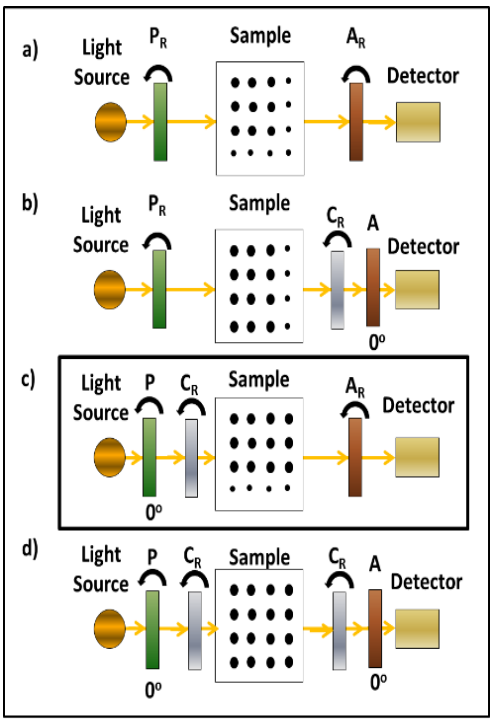

Figure 2.16: Optical configurations for rotating elements ellipsometry. Mueller matrix elements of the sample are denoted by dots. Large dots represent measurable elements.

In order to characterize the optical properties of anisotropic samples, the design of the ellipsometer has been also revised. In Figure 2.16. the information about the Mueller matrix obtained from the measurements is shown according the position of the optical elements in the systems.

Large dots represent the elements of the Mueller matrix that can be obtained by measurements. All the instruments have a light source and polarizer (P) before the sample and an *Analyzer* (A) (rotating or at fixed angle) and a detector after the sample. When a *Rotating Compensator* (C_R) is placed after the sample, it is possible to obtain three columns whereas if it is placed before the sample is possible to measure three rows. The addition of dual rotating compensators provides all the Mueller matrix elements. In this thesis, the structures are analyzed with a commercial ellipsometer with the configuration described in c) and by symmetric considerations, the rest the MM elements of the remaining column can be deduced[202].

To illustrate the dependence of the Mueller matrix elements m_{12}, m_{13} and m_{14} with respect to the rotation angle, Figure 2.17 displays the optical response of a single gold rod for different angles.

$$F:\begin{pmatrix} t_{xx} & t_{sy}+t_a \\ t_{sy}-t_a & t_{yy} \end{pmatrix} B:\begin{pmatrix} t_{xx} & -t_{sy}+t_a \\ -t_{sy}-t_a & t_{yy} \end{pmatrix} \quad (41)$$

The optical anisotropies such as the linear dichroisms (along x-y direction and at 45º) are related to the m_{12} and m_{13} elements. These elements response depends on the orientation of the sample, obtaining maxima values when the rod is parallel to the direction of the linear polarized light at 0º and 45º, respectively (Figure 2.17 (a) and (c)). The optical anisotropy related to circularly polarized light is analyzed in Figure 2.17(b), showing an independent behavior with respect to the sample orientation angle. Furthermore, the evolution of the intensity of the m_{12} and m_{13} peaks with respect to the orientation angle of the sample at a fixed wavelength of 1300nm is shown in Figure 2.17(d). An angular shift of 45º between the m_{12} and m_{13} elements is observed.

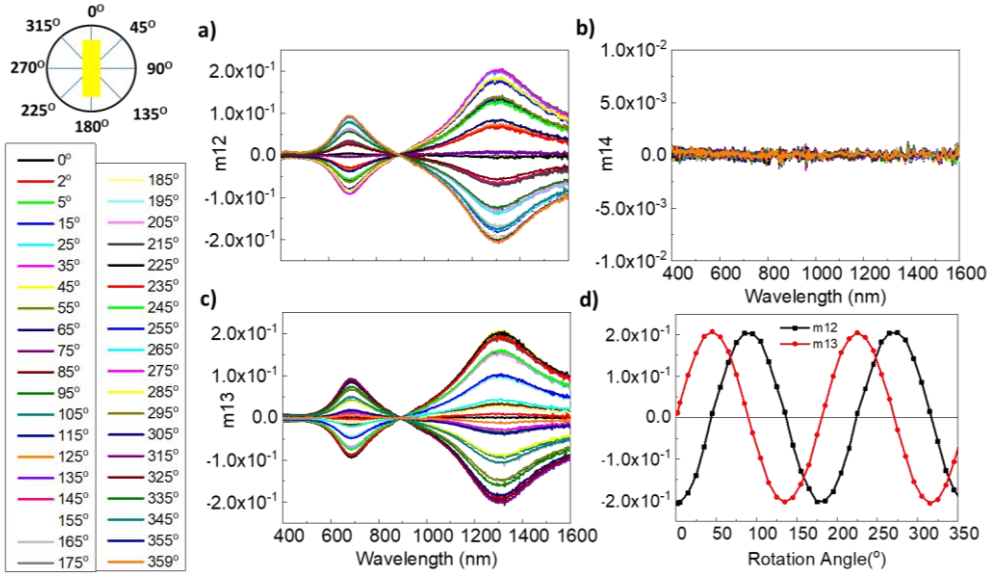

Figure 2.17: Analysis of the evolution of the Mueller Matrix elements with the rotation angle for a single gold nanorod structure. a), b) and c) show the behaviour of the m_{12}, m_{13} and m_{14} MME, respectively; for rotation angles from 0º to 360º. d) the evolution of m_{12} and m_{13} intensity with the rotation angle.

2.2.3. Magneto optical properties

In 1846, Michael Faraday discovered that the polarization plane of light rotates when it passes through a glass inside a magnetic field[216]. The interaction between light and magnetism is known as a magneto-optic (MO) effect. This effect was originally observed in transparent and semitransparent mediums, but not in opaque mediums, due to the impossibility of light to cross them. In 1876, John Kerr found out a rotation of the plane of polarization of the light when it is reflected from the iron poles of a magnet[217] . Contrary to the Faraday effect, the Kerr effect is observable in any magnetic material that reflects light.

Macroscopically, the magneto-optical and optical activity for the different optical configurations can be described by means the dielectric tensor. In absence of magnetic fields, materials have a symmetric dielectric tensor $\tilde{\varepsilon}$ ($\varepsilon_{ij} = \varepsilon_{ji}$). This dielectric tensor is affected when a magnetic field is applied, introducing elements off the diagonal, called MO constants, and the tensor becomes antisymmetric ($\varepsilon_{ij}(H) = \varepsilon_{ji}(-H)$). It is expressed as:

$$\tilde{\varepsilon} = \begin{pmatrix} \varepsilon & \varepsilon_{xy} & \varepsilon_{xz} \\ -\varepsilon_{xy} & \varepsilon & -\varepsilon_{yz} \\ -\varepsilon_{xz} & \varepsilon_{yz} & \varepsilon \end{pmatrix} \tag{42}$$

Where ε_{ii} represent the optical properties of the material and ε_{ij} the MO properties. The off-diagonal elements are proportional to the magnetic field for paramagnetic and diamagnetic materials, and to the magnetization for the ferromagnetic materials. In the dielectric tensor, the dependence of each element with the magnetization depends on the symmetry of the material and can be expressed as[218]

$$\varepsilon_{ij} = \varepsilon_{ij}^{0} + \sum_{k} a_{ijk} M_k + \sum_{k} \sum_{l} b_{ijkl} M_k M_l + \cdots \tag{43}$$

where the dielectric tensor elements for zero magnetization are ε^{0}_{ij}, and M_k and M_l are the magnetization components and the linear and quadratic dependence of these elements respect to the magnetization are the a_{ijk} and b_{ijk} elements. Thus, the general dielectric tensor in isotropic materials with only linear terms from the equation 42 in an arbitrary direction of the magnetization is described as

$$\tilde{\varepsilon} = \begin{pmatrix} \varepsilon_{xx} & aM_z & aM_y \\ -aM_z & \varepsilon_{yy} & -aM_x \\ -aM_y & aM_x & \varepsilon_{zz} \end{pmatrix} \quad (44)$$

where the diagonal components (ε_{xx}, ε_{yy}, ε_{zz}) are the elements in absence of magnetization and the term *a* is known as the linear MO component.

According the Voight classification[219,220], there exist three possible configurations for the Kerr effect, depending on the relative orientation of the magnetization plane and the incident plane of light: Polar, transversal and longitudinal configurations[219,221]. The three cases are presented in Figure 2.18.

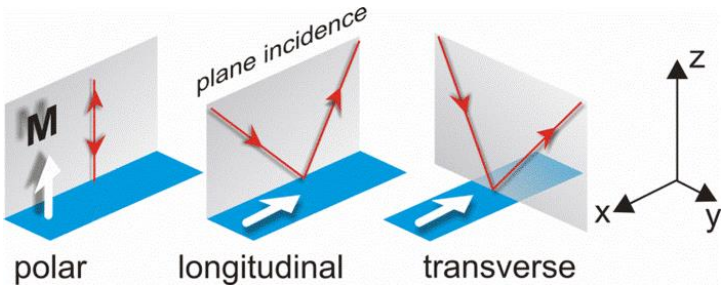

Figure 2.18: Representation of the three possible configurations: Polar, longitudinal and transverse. White arrows indicate the magnetization direction and red arrows indicate the incidence direction of the light. Adapted from reference[147].

The magneto-optical Kerr and Faraday geometries can be classified accordingly as:

- **Polar configuration**. In this configuration, the magnetization **M** is perpendicular to the sample plane and parallel to the light incident plane. In the Faraday effect, the light experiences a rotation with an angle θ_K and an ellipticity of ε_K. These parameters are proportional to the thickness of the layer as well as the perpendicular component of **M**. Figure 2.19 shows a representation of these two parameters into the polarization ellipse. For both p- and s- polarized light, the reflected light will be elliptically polarized with the polarization plane rotated an angle θ and with an ellipticity ε. In this ellipse of polarization, the ellipticity is defined according the mayor (*b*) and minor (*a*) axes as *ε=arctan(a/b)*. In the case of Kerr effect (p-MOKE), the magnetization **M** is perpendicular to the sample plane and parallel to the plane of incidence of the light. In Kerr effect, the reflected light experiences

also a rotation and ellipticity which is proportional only to the perpendicular component of the magnetization[222].
In the case of the magnetization parallel to the z-axis, the macroscopic description of the dielectric tensor in polar configuration can be written as:

$$\tilde{\varepsilon} = \begin{pmatrix} \varepsilon_{xx} & \varepsilon_{xy} & 0 \\ -\varepsilon_{xy} & \varepsilon_{xx} & 0 \\ 0 & 0 & \varepsilon_{zz} \end{pmatrix} \quad (45)$$

Being $\varepsilon_{ij} = \varepsilon'_{ij} + \varepsilon''_{ij}$.
The linearly polarized light at normal incidence that reach the sample surface can be decomposed into two components, right (+) and left (-) circularly polarized light waves. According to Maxwell equations, the two waves will experience different complex refractive indices[223]:

$$N^{\pm} = n^{\pm} \pm ik^{\pm} = \left(\varepsilon_{xx} \pm i\varepsilon_{xy}\right)^{1/2} \quad (46)$$

Therefore, there will be two circularly polarized waves which will propagate in the sample. This propagation will produce an elliptically polarized light with differences of phase (magnetic circular birefringence) and amplitude (magnetic circular dichroism) between the circular polarized waves. In the Faraday effect, the differences of phase and amplitude between the right and left circularly polarized

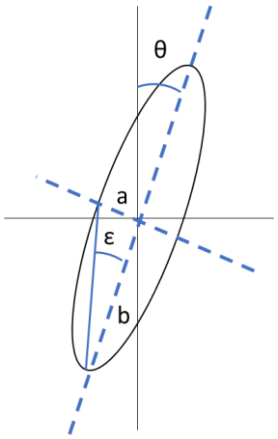

Figure 2.19: Polarization ellipse. a and b are the minor and major axis of the ellipse, and ε and θ are the ellipticity and rotation angles respectively.

light generate the Faraday rotation angle per unit length (θ_k) and ellipticity (ε_k) respectively.

$$\theta_f(\omega) = \frac{\omega}{2c} Re(N_+ - N_-)$$
$$\varepsilon_f(\omega) = -\frac{\omega}{2c} Im(N_+ - N_-) \quad (47)$$

In ferromagnetic materials (ε''=0), the last equations can be expressed as

$$\theta_f(\omega) = -\frac{\omega}{c} \frac{\varepsilon''_{xy}}{Re(N_+ - N_-)}$$
$$\varepsilon_f(\omega) = -\frac{\omega}{c} \frac{\varepsilon'_{xy}}{Re(N_+ - N_-)} \quad (48)$$

where these differences in phase and amplitude are proportional to the off-diagonal elements of the dielectric tensor[223].

In the case of two media, one of them as a semi-infinite non-magnetic medium with isotropic and symmetric dielectric tensor ε_d and the other medium as semi-infinite magnetic medium with the dielectric tensor showed in Equation 42. The general complex Kerr effect can be expressed as

$$\phi_k = \theta_k + i\varepsilon_k$$
$$\phi_k = -\frac{\frac{\varepsilon}{\varepsilon_d}\left(\sqrt{\left(\frac{\varepsilon}{\varepsilon_d}\right) - \sin^2\theta} \pm sin\theta tan\theta\right)}{\left(\frac{\varepsilon}{\varepsilon_d} - 1\right)\left(\frac{\varepsilon}{\varepsilon_d} - \tan^2\theta\right)} \varepsilon_{xy} \quad (49)$$

where the incidence angle of the light is θ.
In the special case of only a magnetic medium, under light incidence normal to the sample ($\theta=0$) from the vacuum media ($\varepsilon_d = 1$), the expression 49 is reduced to

$$\phi_k = \theta_k + i\varepsilon_k \phi_k = -\frac{\varepsilon_{xy}}{(\varepsilon_{xx} - 1)\sqrt{\varepsilon_{xx}}} \quad (50)$$

- **Longitudinal configuration (L-MOKE).** In this configuration, the magnetization **M** is in the same plane of the sample and it is parallel to the incidence plane of the light. There are two configurations according to the polarization states of the incident of the light with respect to the incidence plane of the light: p- polarized light (in parallel configuration) and s-polarized light (perpendicular configuration). For both configurations, there is an elliptical polarized light with both rotation and ellipticity angles. This effect can be used to study the domain structure of a material whose magnetization lies in the sample plane.

The dielectric tensor takes the form

$$\varepsilon = \begin{pmatrix} \varepsilon_{xx} & 0 & 0 \\ 0 & \varepsilon_{yy} & -\varepsilon_{yz} \\ 0 & \varepsilon_{yz} & \varepsilon_{zz} \end{pmatrix} \tag{51}$$

In the particular case of semi-infinite ferromagnetic materials, the Kerr rotation and ellipticity in the longitudinal configuration are expressed as[224]

$$\phi_k = \theta_k + i\varepsilon_k$$

$$\phi_k = -\frac{\frac{\varepsilon}{\varepsilon_d}(sin^2\theta tan\theta \pm sin\theta\sqrt{\left(\frac{\varepsilon}{\varepsilon_d}\right) - \sin^2\theta})}{(\frac{\varepsilon}{\varepsilon_d} - 1)(\frac{\varepsilon}{\varepsilon_d} - \tan^2\theta)(\sqrt{\left(\frac{\varepsilon}{\varepsilon_d}\right) - \sin^2\theta}} \varepsilon_{zy} \tag{52}$$

As it can be observed, there is not MO effect at normal incidence ($\theta=0$).

- **Transverse configuration (T-MOKE).** In the transverse configuration, the magnetization is parallel to the sample plane but perpendicular to the plane of the incident light. In this configuration, the dielectric tensor becomes:

$$\varepsilon = \begin{pmatrix} \varepsilon_{xx} & 0 & \varepsilon_{xz} \\ 0 & \varepsilon_{yy} & -\varepsilon_{yz} \\ -\varepsilon_{xz} & 0 & \varepsilon_{zz} \end{pmatrix} \tag{53}$$

Whereas in the transverse Kerr effect the p-component of the reflected light manifests a small variation, there is not any variation in

the s-component. In this configuration, there are not changes in polarization but a change in the light intensity of the p component. Typically, the Kerr transverse effect is expressed by means of the relative variation of the p-component of the reflectivity

$$\frac{\Delta R_{pp}}{R_{pp}} = 2\frac{R_{pp}(+M_s) - R_{pp}(-M_s)}{R_{pp}(+M_s) + R_{pp}(-M_s)} \quad (54)$$

Where $R_{pp}(Ms)$ is the reflectivity with a saturating magnetic field. In the case of a single semi-infinite magnetic layer from the vacuum, this variation can be expressed as

$$\frac{\Delta R_{pp}}{R_{pp}} = 2\varepsilon_d \sin(2\theta) Re\left(\frac{\varepsilon_{xz}}{(\varepsilon^2 - \varepsilon_d^2)\cos^2\theta - \varepsilon_d\varepsilon + \varepsilon_d^2}\right) \quad (55)$$

In this configuration, there is not MO Kerr effect at normal incidence of light.

Polar magneto-optical Kerr effect spectroscopy (p-MOKE)

The polar magneto-optical Kerr effect spectroscopy (p-MOKE) is a well-known technique used to study the interaction between the electromagnetic radiation and magnetized matter. It allows to get a spectral analysis of the magneto-optical properties and the hysteretic behavior of the nanostructures when magnetic fields are applied.

A home-made setup is used to measure p-MOKE with a polarization modulation technique (Figure 2.20). It allows to measure simultaneously the Kerr rotation and ellipticity with a high sensitivity. In this configuration the light impact on the surface at normal incidence. The system offers the possibility of measuring the MO hysteresis loops for a specific wavelength, but also of measuring the whole spectra of wavelengths from visible to near infrared range in a magnetically saturated sample.

The light source of the p-MOKE is a Xenon lamp. The light reflects in a series of concave mirrors that focus it to the monochromator. This monochromator

model, a SpectraPro-2150i from Acton Research Corporation, has a 150mm focal length which has the 150mm focal length, dual indexable gratings of 600 grooves/mm (1000nm blaze) and 1200 grooves/mm (500nm blaze), and a spectral resolution of 0.4nm or better for the 10µm wide by 4mm high slits and the standard 1200 grooves/mm grating.

Once the light leaves the monochromator with the desired wavelength, it is polarized by the P_1 polarizer, which has its principal axis oriented 45° with respect to the setup in-plane (p-direction).

The linearly polarized light then crosses the photoelastic modulator M, where it is modulated between the linear and circular polarization states with a modulation frequency ω_m. Thus, the new phase of the light is:

$$\varphi = \varphi_0 \sin(\omega_m t) \tag{56}$$

The modulated light is focused onto the sample surface, which is inside the poles of an electromagnet, with the magnetic field perpendicular to the surface plane. The reflected light is collected by the second polarizer, which acts as analyzer and as calibrator due to the possibility to adjust its principal axis by an angle from the p-direction. Finally, the beam reaches the photodetector that consists of a photomultiplier for the 400-800nm range,

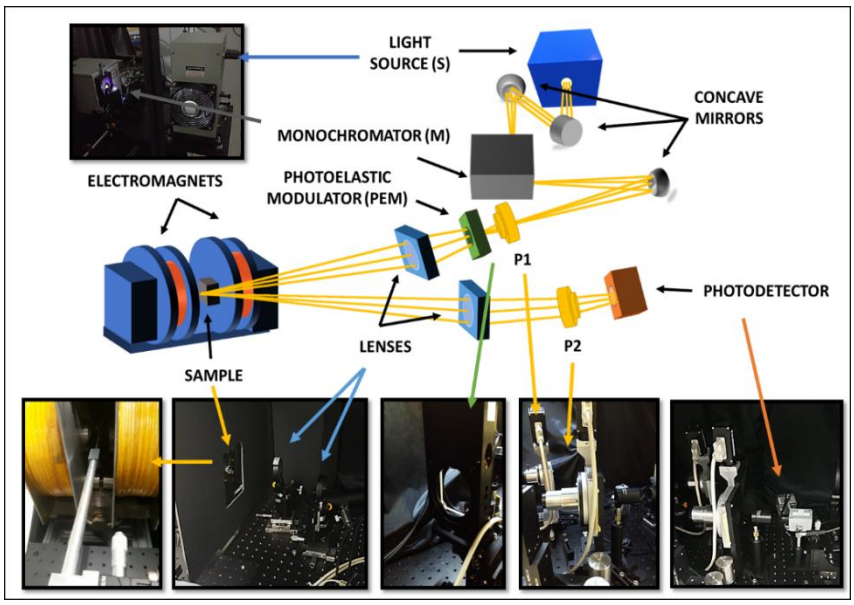

Figure 2.20: Up: Scheme of the different parts of the p-MOKE. Yellow lines mark the direction of the incident light. Lower: images of the different constituent parts of the MOKE.

and a photodiode for 800-1500nm range. The photodetector is connected to a current multiplier, which converts the current into voltage and amplifies the signal. The improved signal and the reference frequency signal from the photoelastic modulator are sent to and filtered in the two lock-in amplifiers, and then compared and analyzed with a computer program in order to obtain the Kerr rotation and ellipticity data.

Normalized Polar Kerr loops in different structures

The presence or absence of hysteresis gives information about the magnetic anisotropy of the samples. The magnetic anisotropy can have different contributions such as the shape, crystallinity, surface or interface[225]. For instance, cubic nanostructures of Au/Co/Au nanosandwiches point out that the magnetocrystalline anisotropy is the main source of the magnetic behaviour[226]. In the nanostructures fabricated in this thesis, P-MOKE curves do not exhibit any hysteresis loops.

By changing the magnetic field normally to the sample plane, the out-of-plane hysteresis are measured with the polar-MOKE. These loops are normalized for each sample at normal incidence and at a fixed wavelength. As the magnetic field is increased, the Kerr ellipticity increases and reaches a saturation value for a magnetic field of around 2000mT. The value obtained corresponds to the magnetic field needed to saturate the magnetization of the Co amount in the nanostructures. This information is relevant to obtain the magnetic contribution to the circular dichroism by spectroscopic ellipsometry. From the shape of the loops, very inclined, the normal axis to the sample plane is a hard magnetization axis. In figure 2.21 the normalized Kerr polar loops of structures fabricated by HMCL and multiaxial evaporation are shown. In comparison with Au/Co/Au nanostructures with similar amount of Cobalt (Figure 2.21(a)), the saturation of the magnetic field is around the range of 1500- 2000 mT[102,227]. Moreover, the shape of the loops is similar in comparison with the structures fabricated (more details in Chapter 4). In these structures there are nanorods composed of (Au/Co) multilayers and dielectric discs at different angles to respect the nanorods: 45º (Figure 2.21(b)), 90º (Figure 2.21(c)) and -45º (Figure 2.21(d)).

The origin of the *Magneto-Optical Activity* (MOA) with and without ferromagnetic material has been analysed. In absence of ferromagnetic materials, the nanostructures fabricated with pure noble metals such as Au,

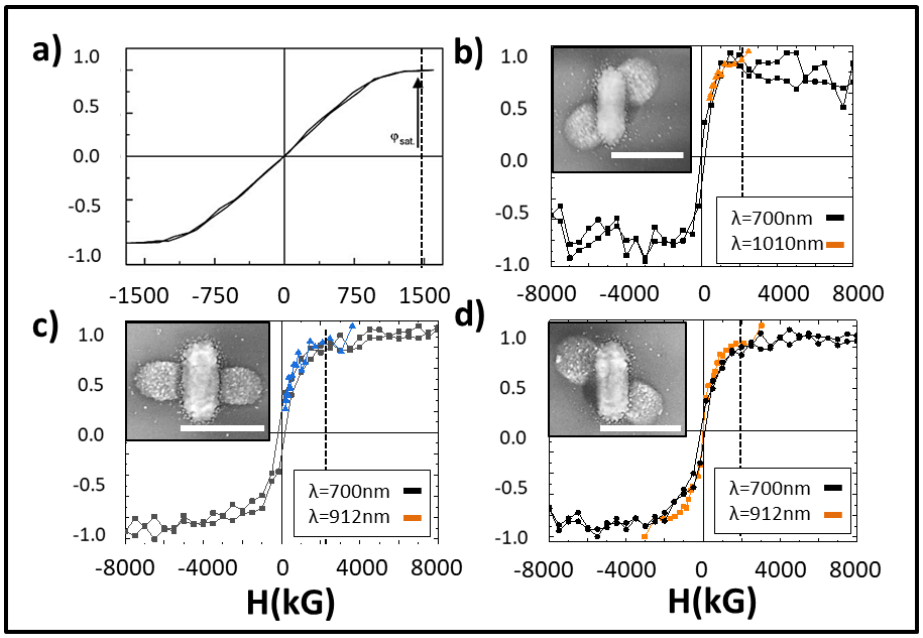

Figure 2.21: Out-of plane magnetic loops of different nanostructures measured from the p-MOKE. (a) The normalized Kerr ellipticity loop of Au/Co/Au nanoparticles with 60nm of diameter Figure adapted from reference112].(b-d) Normalized polar Kerr loops of different Au/Co nanorods with dielectric pillars of CaF2.The insets are the SEM images of the structures with 200nm of scale bar. The dotted lines show the saturation of the magnetic field of around 2000mT.

exhibit MO activity at lower magnetics fields if the *localized surface plasmon resonance* (LSPR) is excited[15]. However, the presence of ferromagnetic materials reduces the magnetic field needed to appreciate the MO activity.

These normalized loops provide information about the magnetic behaviour of the structures. As seen in Figure 2.22(a), the sample consists of arrays of randomly distributed Au/Co/Au nanodisks, with a fixed total thickness of the disks of 32nm. The Co layer is sandwiched between two identical Au layers and its thickness varies from 0 nm (0%) to 10 nm (30%). In figure 2.22(b), the normalized loops varying the Co amount are plotted. Since structures without Co (black squares) with the linear dependence of the magnetization with the magnetic field, representative curve obtained in diamagnetic materials such as Au; to structures with Co (red dots) where the curve is saturated, expected in ferromagnetic materials. In the absorption spectra of the disks, the increment of the amount of Co produces slightly blueshifts as well as the broadening of the peaks[104].

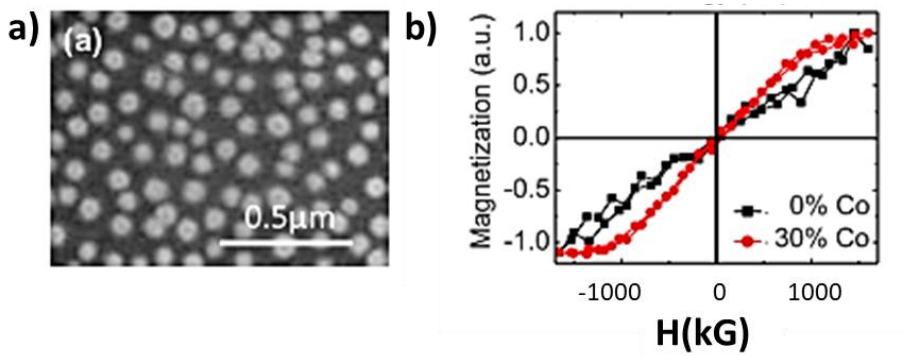

Figure 2.22: SEM image of 60 nm diameter Au/Co/Au nanodisks (b) Normalized polar Kerr loops as function of magnetic field strength for nanodisks with (red dots) and without (black squares) Co within the nanodisks. Adapted from reference 104.

Magnetic Spectroscopic Ellipsometry (MSE)

For the analysis of the magnetic contribution to the circular dichroism (MCD) in the spectroscopic ellipsometer, it is necessary to implement an experimental addition with a home-built setup. The system is formed by a permanent magnet, a fixed column with micrometric screws to control the position of the structures and an electric motor to rotate the magnet during the measurements (Fig 2.23).

To accurately determine the magnetic field applied during measurements as a function of the distance magnet-sample in this experimental system, a calibration study has been carried out. For this purpose, a gauss meter probe with control of the vertical and horizontal position with micrometric screws was used.

From the calibration curve presented in Figure 2.23(a), a range of values is determined from 4kG to -4kG out-of-plane applied magnetic fields, and the vertical separation distance sample-magnet from the case where the sample surface and the magnet are nearly touching up to a separation distance of 22 millimeters.

In the configuration shown in Figure 2.23(c), the sample is fixed, and there is an electric motor to rotate the magnet and to modify the orientation (positive or negative) of the magnetic field applied.

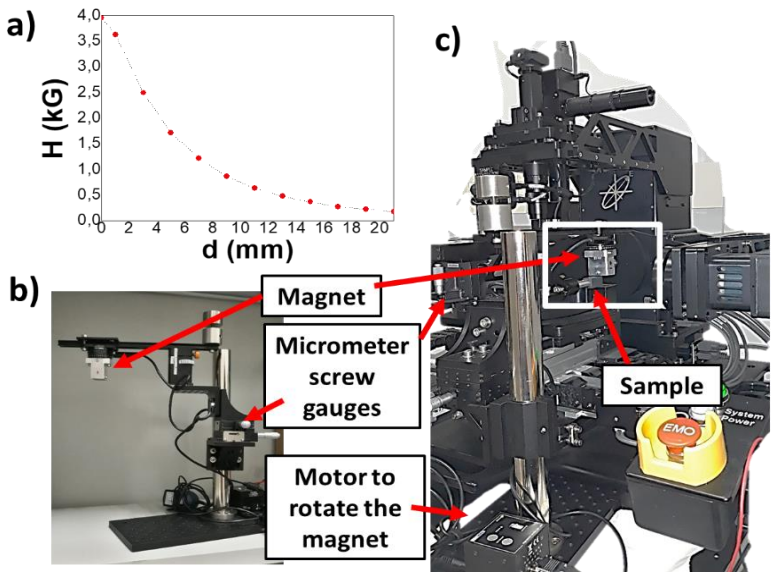

Figure 2.23: (a) The calibration curve for determining the dependence of the applied magnetic field (H) versus the interdistance sample-magnet. (b)Photograph of the experimental setup used in our experiments. (c) Photography of the experimental setup implemented in the spectroscopic ellipsometer. The white square contains the magnet and the sample in an experimental measurement.

In order to corroborate if the magnetic field applied is enough to saturate the samples, the curves in a Polar Kerr spectrometer are analyzed.

Connection between the p-MOKE and the MSE measurements

At normal incidence, the P-MOKE measurements can be understood by means of the change of basis of the dielectric tensor in circular polarizations. The linear polarized light is defined as the superposition of right and left circularly polarized light with the same amplitudes and field vectors rotating towards opposite directions. Each polarization interacts with the magnetized material with different complex refractive indexes (equation 46) and produces elliptically polarized light. The changes in the real parts generate modifications in the polarization plane (Kerr Rotation) whereas the changes in the imaginary parts produce variations in the ellipticity. These differences in the imaginary parts of circularly polarized light are changes between the absorption of the waves ($\Delta A=A^{+}-A^{-}$) and then, differences between the reflected amplitudes of these (+ or-)-circularly polarized light.

$$\phi_k = \theta_k + i\varepsilon_k$$
$$\phi_k = \frac{1}{2}\, arg\left[\frac{r^-}{r^+}\right] + arctan\left[\frac{|r^-| - |r^+|}{|r^-| + |r^+|}\right] \quad (57)$$

While in light transmission measurements, the Faraday rotation and Faraday ellipticity are expressed as:

$$\phi_f = \theta_f + i\varepsilon_f$$
$$\phi_f = \frac{1}{2}\, arg\left[\frac{t^-}{t^+}\right] + arctan\left[\frac{|t^-| - |t^+|}{|t^-| + |t^+|}\right] \quad (58)$$

where *r* and *t* are the reflection and transmission coefficients for right (+) and left (-) circularly polarized light. At small angles $arctan\theta \approx \theta$ and then the ellipticity is rewritten as

$$\varepsilon_f = Im\left[\frac{|t^-| - |t^+|}{|t^-| + |t^+|}\right] \quad (59)$$

Thus, there is a direct connection between the Kerr ellipticity and the Magnetic circular dichroism of the structures[228].

On the other hand, the Mueller matrix elements on non-depolarization and homogeneous media are related to the circular dichroism by the study of the element m_{14} [229]. In the presence of magnetic fields, the total dichroic response may be decomposed in different contributions (explained in subsection 2 in Chapter 2) as a function of the applied magnetic field: non-magnetic and magnetic circular dichroisms.

$$m_{14} = CD = Im\left[\frac{|t^-| - |t^+|}{|t^-| + |t^+|}\right] \quad (60)$$

The magneto-optical characterization of the structures fabricated in this thesis is carried out with both p-MOKE and MSE measurements. Firstly, the p-MOKE loops determine the magnetic behaviour of the nanostructures as well as the magnetic field necessary to saturate the samples. Then, the optical anisotropies of the structures are analysed in the ellipsometer with the home-built setup by studying the Mueller matrix elements.

3. BUILDING BLOCKS

As a previous step to fabricate and study complex chiral plasmonic systems, the first step is optimizing the fabrication and extracting the main optical features of simple structural elements, that will serve as building blocks for the complex structures to be studied in subsequent chapters.

In particular, disk dimers and nanorods with tuneable features such as composition or morphology are fabricated and the dependence of their optical response with morphological parameters explored in order to optimize the complex chiral structure.

Here, planar plasmonic systems that consist of simple nanostructures (nanodisks, nanodisk dimers and nanorods) with tailored properties by means of Hole-mask colloidal lithography are introduced. The schematic representation of the fabrication of different nanostructures is shown in Figure 3.1. By changing parameters such as the polar angle (Θ) by different amplitudes [144] and the azimuthal angle (ϕ), different structures are obtained, such as Figures 3.1 *a)* disks, b) rods and c) disks dimers. In particular, the effort is in nanodisk dimers and nanorods fabrication deposition.

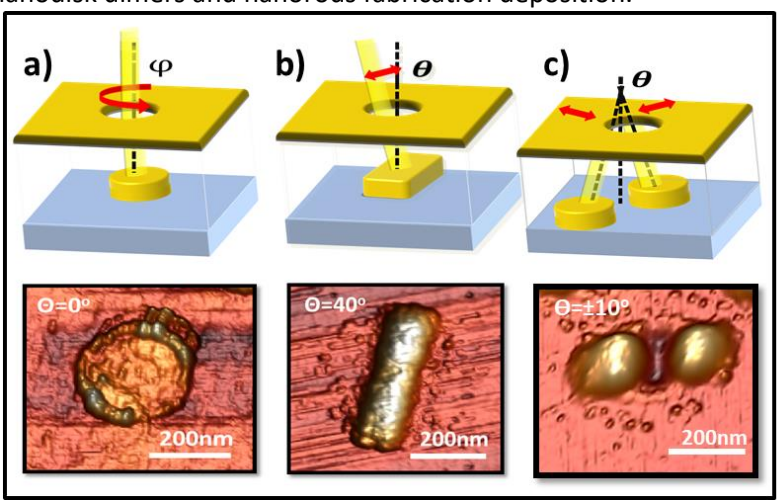

Figure 3.1: Deposition of the nanostructures (from left to right: disk, nanorod and disk dimer) by controlling the oscillation angle from 0° to 40°. Representative AFM images of the corresponding samples are presented.

This way, a well-defined single disk is obtained with a polar fixed angle $\theta=0^o$, a rod is obtained when θ oscillates wide angles (between 20 and 40°), and disk-like dimer structures are obtained when the evaporation is from two opposing and fixed angles ($+\text{-}\theta$, *with* $\theta\neq0^o$) relative to the surface normal. Additionally, the in-plane azimuthal rotation angle (ϕ) may be modified[230], and in this work it is used to rotate in-plane the location of different building blocks with respect to others, both in the fabrication of 2D and 3D composite systems.

In figure 3.2, a representative sketch of the fabrication of disk dimers is shown. In these structures (Figure 3.2(a)), and due to the oblique incidence thorugh a circular hole, the obtained shape is an elipse. To correct this effect and try to achieve a circular disk, the polar angle is fixed and an additional (small) oscillating angle is used. Aditionally, and due to the shrinking hole effect, the second disk necessarily have smaller dimensions than the first one. From the study of the top view, a typical disk dimer is presented where the elliptical shape and differences in size are drawn. The aspect ratio of these dimers is defined as the relation between the short (*m*) and the long (*l*) axes of each disk which forms the dimer. On the other hand, to obtain nanorod structures (Figure 3.2(b)), the polar angle oscillates.

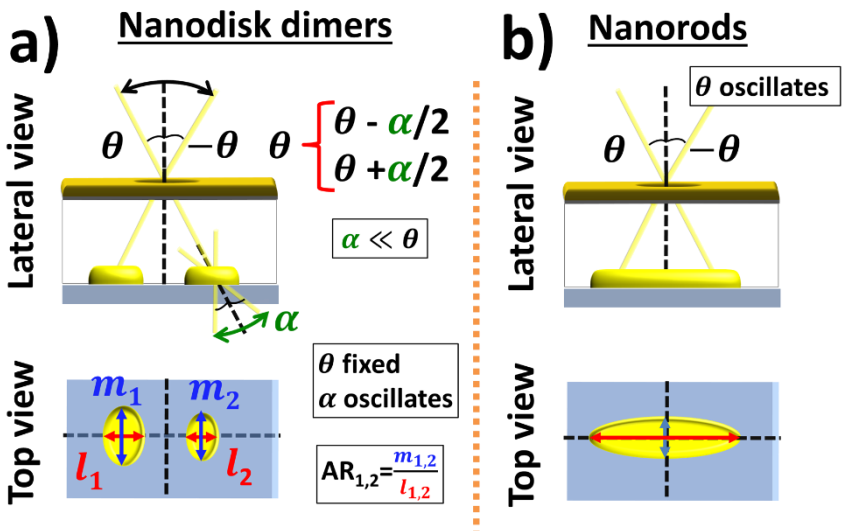

Figure 3.2: Sketch of lateral and top views of the multiaxial deposition through the holes in gold templates for the case of nanodisk dimers(a) and nanorods(b). In the nanodisk dimers, there are a fixed angle θ *and an oscillation angle* α*. However, in the nanorod structures, the polar* angle θ oscillates.

The optical response of these complex systems is influenced by the composition, the morphology, their number as well as by the spatial arrangement of each of the individual structures that constitute them. Hence, there is the possibility of spectrally tuning these optical responses to a desired wavelength, in our case in the visible and near-infrared range, simply by changing these parameters.

The following sections are structured as follows: Firstly, the optical properties of single building blocks with different morphologies such as nanodisks and nanodisk dimers are explored according to their composition and different growth parameters. Secondly, the optical and magneto-optical responses of Au and (Au/Co) multilayers nanorods are presented.

3.1. Disks and Dimers

This subsection is focused on the fabrication of metallic (Au) and dielectric (CaF_2) disk and disk dimer structures. The fabrication process of nanodisk dimers by HMCL is detailed. Moreover, the optical properties such as the transmission and the optical anisotropies obtained from the Mueller matrix elements are investigated (more details in Chapter 2).

3.1.1. Fabrication of disks and disk dimers

The structures are fabricated by means of HMCL with a deposition system which allows modifying the polar deposition angle (θ) during the process. The templates are made on glass substrates (BK7) by the HMCL standard procedure with polystyrene spheres with 124 nm of diameter, the Poly (methyl methacrylate) (PMMA) thickness of 200 nm and 30 nm Au film mask[124]. Afterwards, the nanostructures are grown in a UHV deposition system by evaporation from a Knudsen cell for Au, and electron beam evaporation for Ti and CaF_2. For all the structures, a prior Ti layer is grown to improve the adhesion of the Au and CaF_2 to the glass substrate. The base pressure is lower than $1x10^{-9}$ Torr and the evaporation pressure is lower than $5x10^{-9}$ Torr. The deposition rates are typically 0.03nm/s for Au and 0.02nm/s for both Ti and CaF_2.

Metallic nanodisks and nanodisk dimers

The analysis of metallic nanodisks has been widely carried out in several previous studies[15,103,107,230]. The structures presented here have been fabricated following the same fabrication protocol and deposition system. As mentioned before, the fabrication of gold dimers is carried out by HMCL in a UHV deposition system which allows modifying the deposition angles during the fabrication. The evaporation process is carried out by tilting the sample in a polar fixed angle θ to ±25° and oscillating then the angle α=±10° to try to correct the elliptical shape for disk dimer structures. The obtained samples are a random arrangement of dimers on a glass substrate (~cm^2) all of them aligned along the same in plane direction.

A sketch of the evaporation method through the gold templates is shown in Figs. 3.3 (a). The measured dimensions of gold dimers are obtained by AFM and SEM techniques. The average AFM profiles obtained from a sufficient

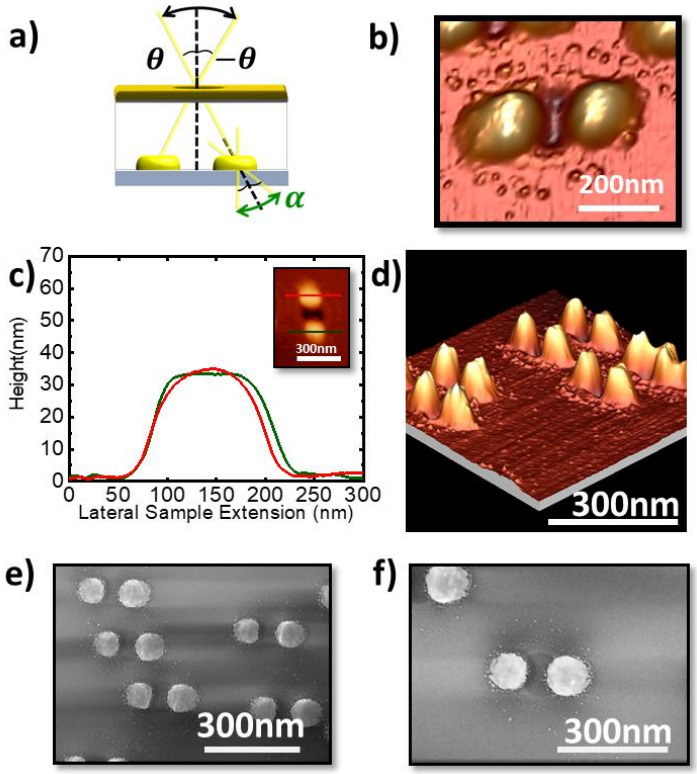

Figure 3.3: (a) Representative sketch of the fabrication process of the gold disk dimers through the HMCL templates. (b)AFM image of a single gold disk dimer. (c) AFM Profiles of the dimers measured along the long axes of the gold nanodisk dimers. (d) 3D AFM image of the nanodisk dimers (e-f) SEM images of the gold dimers at different scales.

number of nanodisks are seen in Figs. 3.3(b-d) with heights of 35±5nm. In Figure 3.3(e-f) representative SEM images are displayed, which show an in-plane random distribution of the dimers, and an average center-to-center distance between the disks of 168±5 nm. The images also reveal a slightly elliptical shape (due to the off-normal deposition through circular hole) with in-plane aspect ratios approximately between 1.09 and 1.15. Both disks have similar dimensions: short axes of around 104±5nm and long axes of 116±3nm.

CaF_2 disk dimers

For the emergence of 3D-structures, it is going to be necessary to use dielectric building blocks that allow to pile up metallic components preventing their electrical contact. The fabrication of dielectric CaF_2 dimers is described next.

The control and optimization of their shape and morphology is a critical aspect in order to obtain later more complex structures. Since CaF_2 is deposited by e-beam evaporation, a much less collimated technique than the Kcell evaporation used for Au, here the control of the shape happens to be much more critical than for Au dimers. For that reason, the dependence of the disks morphology depending on the two main growth parameters such as the oscillation amplitude (θ) and the deposition time are studied firstly. The role of these parameters to obtain nanodisk dimers with similar long vs short in plane axis aspect ratio (AR) and controlled center to center distance (d) is established.

A sketch of the fabrication of the nanodisk dimers, with the relevant angles plotted, is shown in Figure 3.2. In the nanodisk dimer, the polar angle θ is fixed and an additional angle α oscillates. This angle α allows for the correction of the elliptical shape of the disks during oblique evaporation.

In Figure 3.4(a), SEM images show the evolution of the resulting CaF_2 dimers according the deposition time and the off normal incidence angles. Averaged AFM profiles of the structures in Figure 3.4(b) have been vertically shifted for clarity. The thickness of all disks varies between 15 to 30nm. The sketch of the structures in Figure 3.4(c) displays the parameters of the structures: the oscillation angle (α), the polar angle (θ), the center-to-center distance between nanodisks (d) and the dimensions of each disk (with the index 1 or 2) (height (h), long axis (L) and short axis (m)). Finally, the table in Figure 3.4(d)

shows the measured dimensions of the structures obtained by AFM and SEM techniques.

Dielectric dimers are firstly fabricated at a fixed polar angle θ of 20º and an additional oscillation angle of α=±10º (SEM image and AFM profile with black frame are shown in Figures 3.4(a-b)). In these structures, the deposition time is around *t*=6000s and there is a shrinking of the hole in the template and the dimer presents elliptical disk-shape of the disks and high differences in the in-plane aspect ratio (*AR*). From the experimental dimensions extracted in Figure 3.4(d), the AR of 1.78 and 1.37 for the heterodimer, and the heights of 30nm and 16nm, are obtained. Additionally, an overlapping of the structures and the distance center to center of 117nm between them is seen.

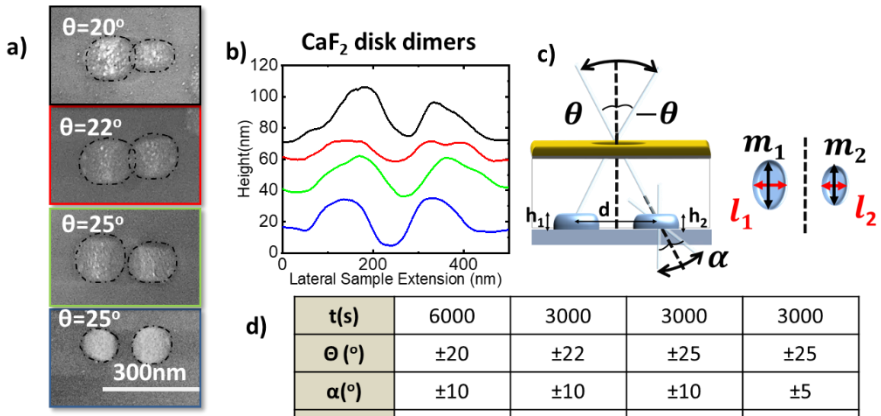

d)

t(s)	6000	3000	3000	3000
Θ (º)	±20	±22	±25	±25
α(º)	±10	±10	±10	±5
d(nm)	117±16	147±07	166±07	163±04
m_1(nm)	142±15	135±09	150±05	109±07
l_1(nm)	104±13	86±04	98±04	95±07
AR (l_1)	1.37	1.57	1.53	1.15
h_1(nm)	30	17	25	16
m_2(nm)	121±18	148±07	137±04	119±06
l_2(nm)	68±12	100±05	89±05	105±05
AR (l_2)	1.78	1.48	1.54	1.13
h_2(nm)	16	18	23	15

Figure 3.4: (a) SEM image of CaF_2 disks dimers from the asymmetric and overlapped case (black square) to the similar and separated case (blue square) according different growth parameters.(b) Averaged AFM profiles of the nanodisk dimers along the long axes for each situation.(c) Sketch of the deposition process through the holes of the gold membrane. Some parameters are represented such as the deposition time of CaF_2 (t), the oscillation angle (Θ) and the oscillation offset angle (Θ_{offset}). The interparticle distance (d) and the dimensions of the structures: length (l) and height (h) are shown. (d) Statistics of the fabrication parameters of the disk dimers obtained by SEM and AFM techniques.

By decreasing the deposition time to *t*=3000s, the distribution of the dielectric material is better and the closing effect of the hole during deposition is partially solved. Then, the aspect ratio between the disks in the dimer improves and both disks present a similar circular shape (differences of up to 2 nm). The heights of the disk dimers vary between 17nm and 25nm.

The role of the oscillation angle α (SEM and AFM profiles are the red, green and blue frames) is shown in Figs 3.4(a-b)with a fixed deposition time *t*=3000s. A fixed polar angle for structures from 22º to 25º is defined and the oscillation angle is modified from 10º to 5º. For the second case at θ=22º (red line frame in Figure 3.4(a)), from the dimensions of the nanodisks, and as shown in the table, the AR are 1.57 and 1.48, which means elliptical shapes. In these structures, the aspect ratio between disks improves, albeit the overlapping exists, and the center to center distance is around 147nm.

By changing the oscillation angle with the same deposition time of *t*=3000s, homodimers with elliptical shapes (green frame in the SEM image and AFM profile presented in Figures 3.4(a-b)) and similar aspect ratios (1.53 and 1.54) are obtained.

Finally, to solve the overlapping problem, the structures grown at θ =25º are fabricated by reduction of the oscillation angle from 10º to 5º (blue frame of the SEM image and blue line in the AFM profile plotted in Figures 3.4(a-b). In this way, homodimers with a better aspect ratio (the *AR* are 1.15 and 1.13) as well as an increased height of the disks (from 18 to 23 nm) were fabricated, with a center-to-center distance between the disks increase up to 168±5 nm. Only in the case when the oscillation angle is small enough, the distance between disks center allows fabricating structures in between them.

3.1.2. Optical characterization of dimers

Whereas the characterization of the optical properties of single Au nanodisks with similar dimensions[114,231] have been previously studied [15,16,144], showing a single resonance (around 700-800nm, depending on the specific disk dimensions) in the transmission spectra; the analysis of the disk dimers has not been previously reported. In the present work, attention is focused on the optical response of these structures.

CaF_2 disk dimers

In the case of the CaF_2 dimers, the dielectric nature of the structures implies the absence of any plasmonic response. The optical spectra in the considered spectral range showing no relevant signals are shown in the appendix section.

Au disk dimers

The transmission spectra and the optical anisotropies extracted from the Mueller matrix elements of gold dimers of around 105nm of diameter, 35nm of height and a center-to-center distance between the disks of 168nm is discussed in detail. This optical response of the Au dimers is characterized with spectroscopic ellipsometry with normal incident light in transmission configuration, as described in Chapter 2.

The transmission spectra (Figure 3.5 (a)) exhibit two in-plane resonances corresponding to dipolar plasmon oscillations along (blue line) and perpendicular (green line) to the interparticle axis. This is in clear contrast with single Au nanodisks with similar dimensions[114,231] which are characterized by a single resonance (around 700-800nm, depending on the specific disk dimensions). The breaking of the symmetry induced by the dimer arrangement induces a splitting into two resonances, which for the dimensions considered here, are centered on 690nm and 773nm. This split into two resonances in the spectral profile can be well explained by a coupled dipole approximation. According to this model, the behavior of our gold dimers may be understood as if each disk is an interacting dipole, whose response is modified by changing the dimensions, composition and interaction distance between the nanodisks in the dimers[108,114,232–234].

To understand in detail the optical response of the fabricated gold dimers, their optical anisotropies are examined by analyzing its Mueller matrix elements under forward and backward configurations (black and red lines respectively). In figures 3.5 (b-d), the ellipsometric measurements of the Mueller matrix elements (m_{12}, m_{13} and m_{14}) for these dimers, whose responses are related to the linear (m_{12}, m_{13}) and circular (m_{14}) dichroisms[229], are presented.

From the Mueller matrix element m_{12} and m_{13}, the linear dichroic response of the dimers is studied. As observed in figure 3.5 (b), the spectra in forward and backward configurations, related to m_{12}, exhibit a characteristic *bisignate*

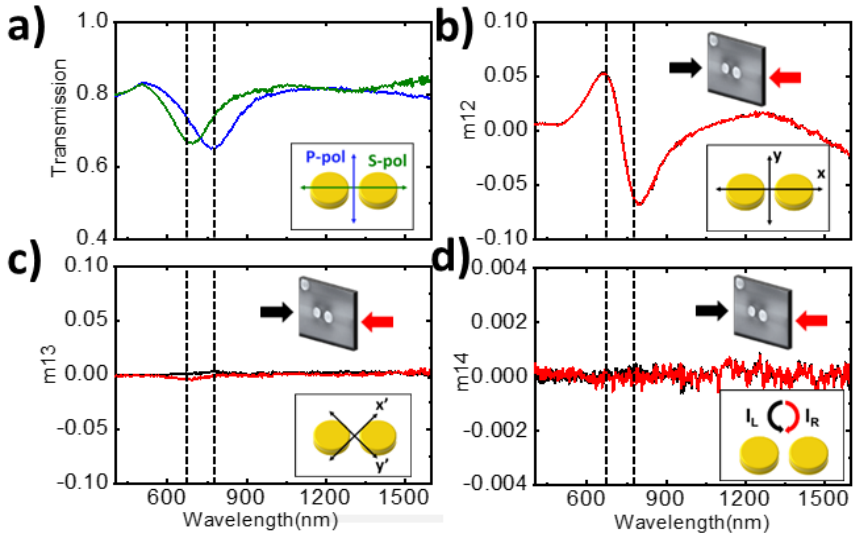

Figure 3.5: (a) Transmission spectra for the parallel (red) and perpendicular (black) polarizations (b-d) Representative Mueller matrix elements (normalized to m_{11}) of the two pure Au disks for forward (black) and backward (red) illuminations.

shape -dip-peak- at the specific plasmon frequencies of the structures (660 and 797nm respectively). In comparison with structures fabricated with similar materials (evaporated gold), the intensities of the linear dichroic signal are in a comparable range (between 10^{-1} and 10^{-2})[40].

Due to the choice of reference axis, aligned with the main axis of the dimmers, the linear dichroism at 45º (m_{13}) is necessarily zero (actually around $5{\cdot}10^{-3}$, probably due to some fabrication asymmetry) (Figure 3.5(c)). As mentioned before, the non-identical morphology of the disks due to inherent limitations of the fabrication process generates the non-zero signal when the structures are illuminated at 45º with respect to the axes of the dimer.

In addition, note that the circular dichroic responses (Figure 3.5(d)) are zero for both configurations, which is consistent with nanostructures with this symmetry.

Thanks to the sensitivity response of the structures to the distance between the particles and the variations of the environment, they have been utilized as "plasmon rulers" with the ability to measure nanoscale distances in biological systems, as well as for the detection and enhancement of the electromagnetic fields in the gap between the disks[52,108,125].

3.2. Nanorods

In this section, the other type of building blocks that constitutes the final complex structures to be fabricated are examined. These are rods, either of Au or of Au/Co multilayers, whose optical and MO responses are characterized, as well as their relation with the morphology or aspect ratio. In addition, CaF_2 rods are deposited onto metallic nanorods, and their effect in the optical response of the rod underneath is also considered.

The spectral position of the rods resonances depends on their dimensions. As mentioned before, two routes are adopted to vary them. One is to keep the substrate oscillation angle fixed and change the deposition time. This way the length of the rods is always the same and the height changes. The second way consists in keeping the deposition time fixed and change the oscillation angle. This way the rods are longer for wider oscillations, but since the material is redistributed over a larger area, longer rods have also lower height. In what follows both approaches are described in detail and an optimized structure is fabricated by tuning these fabrication parameters.

3.2.1. Fabrication of the structures

The nanorods are fabricated by HMCL combined with off-normal deposition through the template as shown in Figure 3.2. The templates are prepared by the standard process with PS spheres of 124nm of diameter and a PMMA thickness of 200nm. The gold membrane has a thickness of 30nm. Through the holes, the structures are grown by oscillating the polar angle (θ) with amplitudes between 20 to 40 degrees, with the azimuthal angle fixed ($\varphi=0^o$). Consequently, the different oscillation amplitudes in the deposition angle (θ) lead to the formation of rods with different lengths[16], as seen in Figure 3.2.
The nanostructures are made of evaporated gold by Kcell with a deposition rate of 0.245Å/s. The Ti adhesion layer is evaporated by e-beam with a rate of 0.2Å/s. By modifying the deposition conditions, namely polar angle and deposition time, the nanostructures have different aspect ratios (*AR*), since heights and lengths change. The length of the rods is controlled by the amplitude of the oscillation angle while their heights are varied by simply varying the deposition time of the material for each specific oscillation angle.

Finally, the fabrication and main optical and MO responses of ferromagnetic rods based on Au/Co MLs are presented. Here the Co layer is evaporated by e-beam with a rate of 0.2Å/s These ferromagnetic rods will be the active component of complex 2D systems to be studied in the next chapter.

3.2.2. Optical characterization of Au nanorods

The optical response of gold nanorods is affected when the dimensions of the structures change. A structure whose dimensions are optimized in order to tune the optical response is fabricated.

Evolution of the optical properties according to deposition time

Gold nanorods are fabricated by changing the deposition time and keeping the oscillation angle total amplitude to ±15° during the deposition. The dimensions of the structures are obtained from AFM and SEM images of the nanorods and are presented in Figure 3.6. Each of the images have a different color of the frame depending on the deposition time. The black frame is the nanorod with 1744s and height of 18nm, the blue frame is for a deposition time of 2828s, with a height of 23nm. Additionally, the AFM profile of the structures with deposition time of 3500 and 4242 s with green and red colors for their frame, is shown. For both nanostructures the thicknesses are 30 and 36nm respectively. The structures show similar widths (around 90-100nm) and lengths which vary between 260 to 300nm.

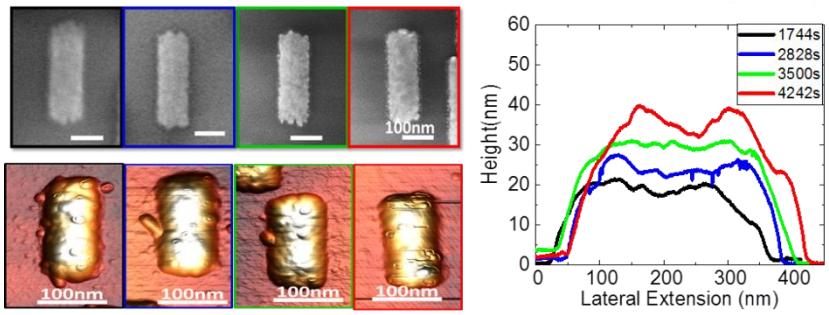

Figure 3.6: SEM images and AFM profiles of the gold nanorods with similar dimensions of 280x95xh (nm) where the height changes from 18nm (black line) with the deposition time of 1744s, 23nm for the nanorods profile of the blue line with the deposition time of 2828s, the green line with the deposition time of 3500s and height of 30nm and finally, the red line with the deposition time of 4242s and a height of 36nm.

Through the average profiles of the structures obtained from AFM, the accumulation of material at the ends of the rods during evaporation is detected. One possible explanation for this effect is that this area is exposed to the beam of material for a longer time overall because it is where the oscillation is reversed.

A compilation of the obtained rods main dimensions is shown in Figure 3.7, where the dimensions and the three aspect ratios (width (*W*) vs height (*H*), length (*L*) vs height, and length vs width) determined for different deposition times are presented. In Figures 3.7(a-c), the length (black dots), width (red dots) and height (green dots) are plotted. The structures have similar lengths and widths, with average values of 280nm and 95nm respectively. As expected, the height of the structures obviously increases with the deposition time. This trend is best observed through the analysis of the aspect ratio of the structures shown in Figure 3.7(b).

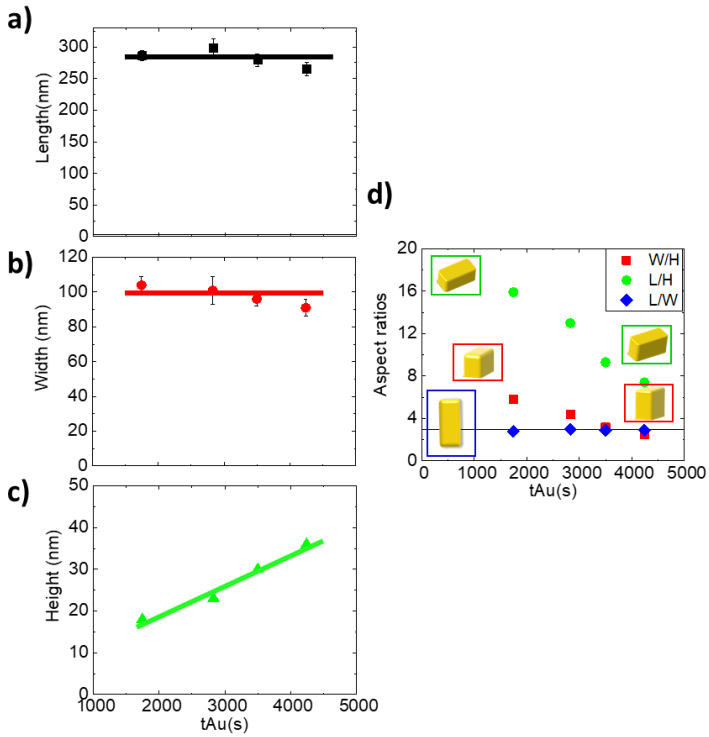

Figure 3.7: Experimental dimensions extracted from the AFM and SEM images where length (a), width (b) and height (c) are presented. (d)Relation of aspects of the structures according the dimensions: width (W), length (L) and height (H).The red points show the aspect ratio width versus height (W/H).The green points are related to the aspect ratio Length versus height (L/H) and finally the blue points are the aspect ratio length versus width (L/W).

As observed, obviously *L/W* does not depend on the deposition time (the eventual shrinking effect of the hole affecting them both in a similar fashion), and the only varying parameter with deposition time is the height of the rods. On the other hand, due to the intrinsic rod shape of the building block, larger values of aspect ratio are obtained for *L/H* (gradually decreasing as more material is deposited), while more modest aspect ratios are obtained for *W/H*.

The plasmon resonance dependence of Au nanorods with typical *LxW* dimensions of 280x95nm according to the height of the structures, is examined for transverse and longitudinal polarizations and shown in Figures 3.8(a) and 3.8(b) respectively.

Whereas in the longitudinal polarization, the shape of the spectra remains roughly the same, and the low energy plasmon resonance position moves towards lower wavelengths when the height of the structure increases, the transverse polarizations show two different shapes with a broadening of the peaks. Much broader, redshifted peaks are observed for 18 and 23 nm high rods, while narrower, blue shifted peaks appear for 30 and 36 nm high rods. This effect can be explained by analyzing the SEM images of these structures shown in Figure 3.9.

In Figures 3.9 (a-b), SEM images show the density and the dimensions of the structures. The higher number of nanorods per area produces aggregates, whose interactions may modify the optical response, producing a broadening of the shape of the plasmon resonances as shown in Figure 3.8 as well as additional peaks related to the interactions between them (for example, the additional peak shown in Figure 3.8(b) at 650nm).

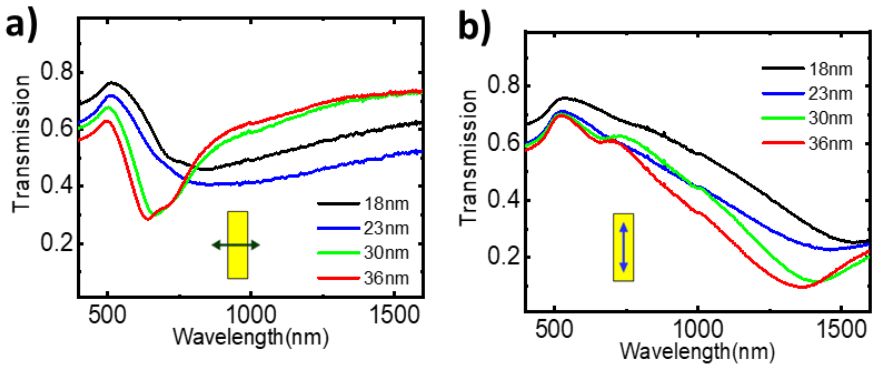

Figure 3.8: Transmission spectra for the transverse and perpendicular to the long axis of the nanorods according the height of the structures for 18nm (black lines), 23nm (blue lines), 30nm (green lines) and 36nm (red lines).

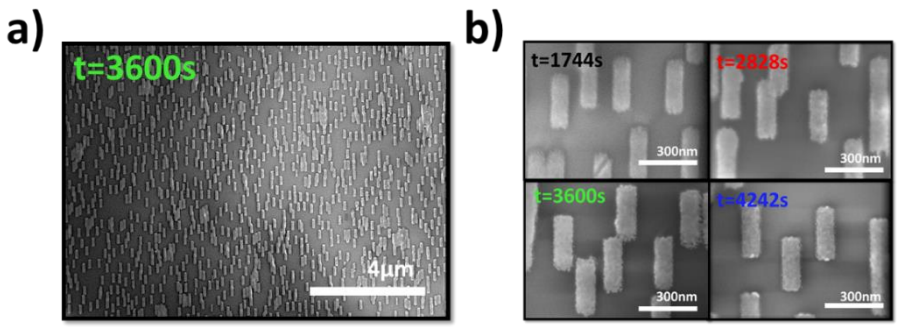

Figure 3.9: SEM images of the nanorods at different scales, where the density and dimensions of these nanorods are presented.

From this image it can be seen that the nanorods concentration is not small enough to neglect possible interactions between the structures, which could lead to a broadening of the plasmonic resonance[104].

From the analysis of the transmission spectra of the nanorods, the evolution of the high and low energy plasmon resonances peaks (Figs. 3.10(a-b) as a function of the height of the structures can be extracted. Figs. 3.10(a-b) show that, as previously mentioned, the transmission peak of the plasmon resonances blue shifts as the height increases for both polarizations. This shift is around 200nm (of the order of 24%) in longitudinal polarization (blue points) and around 170nm in the transverse polarization (green points). In the transmission spectra, the resonance wavelength for longitudinal polarization is larger than the transverse polarization, because of the plasmonic response of the structures depends on the dimension along which the electric field is polarized[235].
These results show the strong dependence of the resonance amplitude and wavelength on the thickness of the nanostructures. For both transverse and longitudinal polarizations, the transmission peaks blue-shift and broaden as the thickness increases (values around 25% and 17% for transverse and longitudinal polarizations). A possible explanation for these effects is the decoupling of charge dipoles at the surfaces of these gold nanorods.

On the other hand, Figs. 3.10(c-d) plot the spectral dependence of the plasmon resonance amplitudes of the nanostructures, extracted from the transmission spectra for the longitudinal (blue solid points) and transverse (green points) polarizations. For both cases the amplitudes are very similar

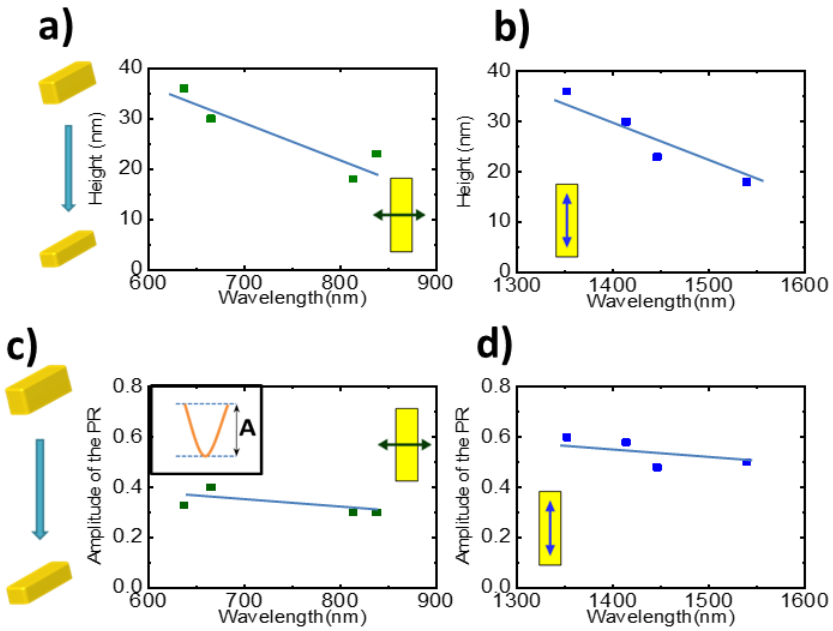

Figure 3.10: Peak resonance positions for each nanorod as a function of the height for both longitudinal (blue points) and transverse (green points) polarizations are shown in (a)and (b) respectively. The amplitude (A) of these peaks of the plasmon resonances (PR) is seen. In both cases light is normally incident along the longitudinal (c) and transverse (d) polarizations. Insets show to top view of the nanorods with polarization direction and the sketch of the amplitude of the plasmon resonances (A).

and show a similar weak wavelength dependence, but the values are larger in the longitudinal polarization (between 0.5 and 0.6) than for transverse polarization, with amplitudes around 0.3-0.4. These results are consistent with previous results on nanorods whose plasmonic response depends on the geometric length along which the electric field is polarized[236].

Evolution of the optical properties according the oscillation amplitude

The results of varying the oscillation amplitude while maintaining the deposition time fixed are shown. Namely, the oscillation amplitude varies between ±10° and ±15° and the deposition time is a constant value of 4000s. This way structures with similar widths (around 97nm) but in which both height and length are varied simultaneously, are obtained. In the case of the heights, the material is redistributed along the rod and longer oscillation angles imply smaller heights ranging from 49nm to 32nm. Likewise, the length

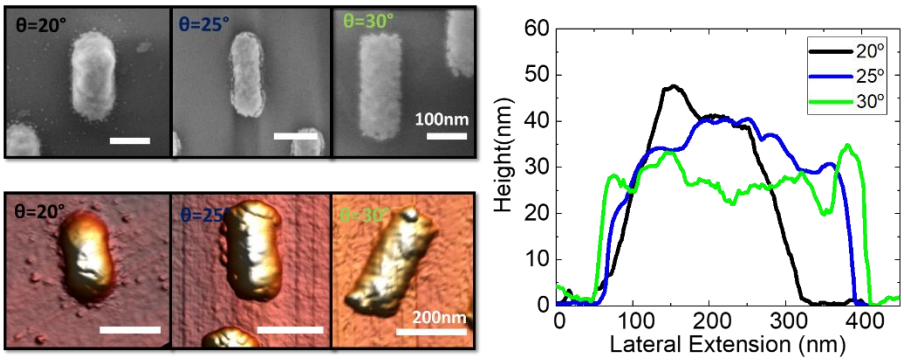

Figure 3.11: SEM images and AFM profiles of the gold nanorods where the height and length changes according the oscillation angle during the fabrication from 20°(black line), 25° for the nanorods profile of the blue line and 30° for the green line.

of the structures obviously varies with oscillation amplitude, ranging from 226nm to 265nm when the oscillation angle changes from 20° to 30°.

The AFM and SEM images of these structures are presented in Figure 3.11. From the AFM profiles of the structures, the redistribution of the Au material during the deposition according the oscillation polar angle is obtained.

The dimensions obtained from the analysis of the AFM and SEM images are shown in Figure 3.12(a). All the structures have similar width, but the length increases as the oscillation angle increases. Taking this into account, Figure 3.12(b) plots the aspect ratio of these structures according to their dimensions: width (*W*), length (*L*) and height (*H*). The length versus height (green solid points) is plotted and an increasing tendency towards higher oscillation amplitude is found. On the other hand, the aspect ratios related to the width (*W/H* and *L/W* for the red and blue solid points, respectively) have not a considerable increase. This is due to similar widths of the nanostructures.

With these geometrical data in mind, the transmission spectra of the structures are analysed. From the typical response showed in Figure 3.13, the plasmon resonances positions for transverse (Figure 3.13(a)) and longitudinal (Figure 3.13(b)) to the long axis of the rods are compared as function of the oscillation amplitude from 20° to 30°.

Figure 3.13 (a) shows plasmon resonance peaks whose position have similar values from 640 to 660nm (Δλ=20nm is the order of 3%), regardless of the

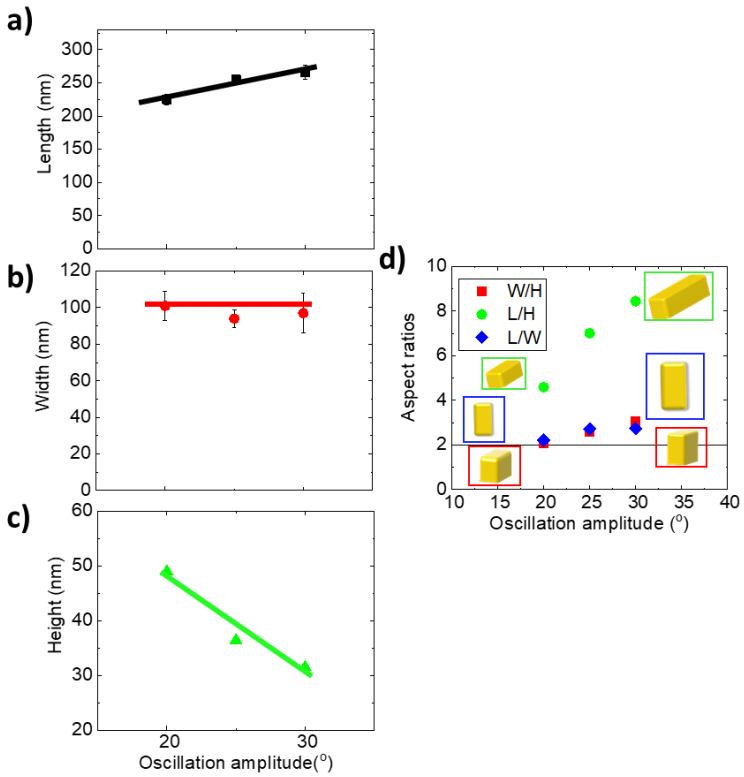

Figure 3.12: (a)Dimensions and (b) aspect ratios of the nanorods with similar deposition time of 4000s but different oscillation amplitude during the deposition. The green solid points show the relation between width (W) and height (H) (W/H). Furthermore, the relations between the length and height (L/H) and length and width (L/W) with green and blue solid points.

oscillation. It should be noted that the response of the sample at 30° presents a broadening of the peak and an intensity whose origin may be due to variations in the density of structures. However, the spectral response is strongly dependent on the angle of oscillation in a polarization parallel to the long axis of the rod with values from 1000 to 1350nm (Δλ=350nm is the order of 26%), with 20° to 30° oscillation amplitudes (Figure 3.13(b)).

This behaviour can be understood by analysing the dimensions of the structures: this set of samples has structures with similar widths but whose length and height vary distributing an identical amount of gold material in all structures, therefore, a longitudinal polarization has greater sensitivity to changes in the long axis obtained by varying the amplitude of oscillation.

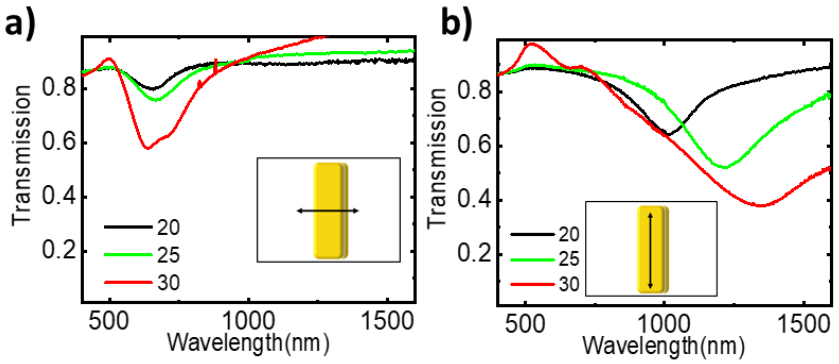

Figure 3.13: Transmission spectra for the transverse (a) and perpendicular to the long axis of the nanorods (b) according the oscillation angle during the fabrication for 20º (black lines),25º (green lines) and 30º (red lines) oscillation angles.

In Fig 3.14(a-b) the position of these peaks is analysed according the oscillation amplitude during the deposition of gold. It can be observed that in the transverse polarization the plasmon resonances are in a very similar spectral region (from 643 to 660nm). The optical response of these structures for the longitudinal polarization is in agreement with nanorods with similar

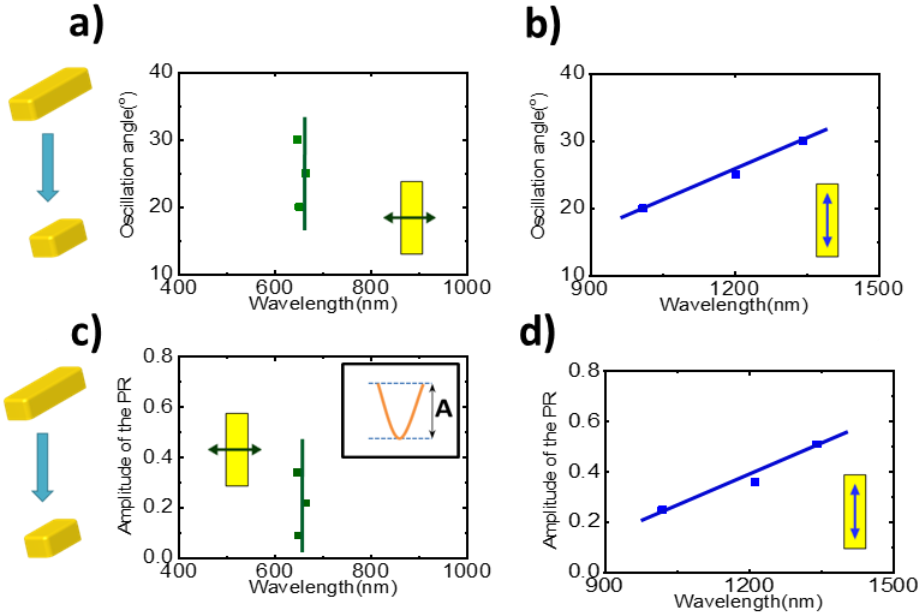

Figure 3.14: Peak resonance positions (p_1 and p_2) for each nanorod as a function of the oscillation angle for both longitudinal (blue points) and transverse (green points) polarizations are shown in (a). In (b), the amplitude (A) of the peaks of the plasmon resonances (PR) is illustrated. In both cases light is normally incident. Insets show to top view of the nanorods with polarization direction and the sketch of the amplitude of the plasmon resonances (A).

dimensions. The increase in the oscillation angle produces an elongation of the structures, which in turns produces a shift towards larger wavelengths of around 375nm. Moreover, the amplitude of the plasmon resonances experiments have a similar behaviour as demonstrated by ellipsometry in Figures 3.14(c-d).

Optimizing the optical response of nanorods

According to the fabrication parameters analyzed previously, an optimized single gold rod with dimensions of 103x226x53nm^3 is fabricated. The low areal density of the structures gives an optical response without any interaction effects.

The transmission spectra and the Mueller matrix elements are analyzed in these structures (Figure 3.15). From the transmission measurement of a single gold rod with dimensions of 103x226x53nm, presented in Figure 3.15(a), two plasmon resonances can be observed in the visible and near infrared range, which are excited when light polarization is parallel to the long axis of the rod (blue line) and the short axis of the rod (green line).

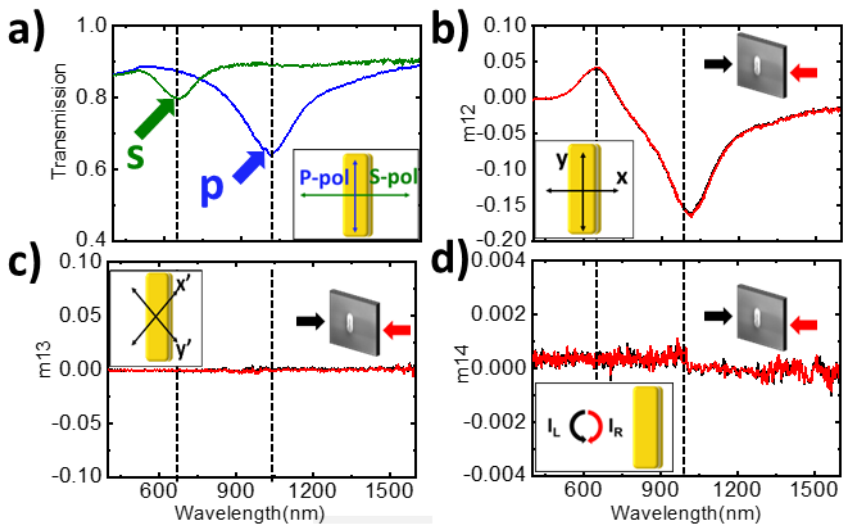

Figure 3.15: Transmission spectra for a typical single rod for both longitudinal and transverse polarizations. In (b) the linear dichroism spectra is shown. Panels (c) and (d) present the null response of these structures to the linear at 45º and circular dichroisms, respectively. The responses of these Mueller matrix elements (m_{12}, m_{13}, m_{14}) are in forward (black line) and backward (red line) configurations.

With regard to optical anisotropies, the m_{12} element shown in Figure 3.14(b) has a characteristic sinusoidal shape in individual rods, whose maximum and minimum peaks position varies according to the dimensions of the structure. In these structures both 45 degrees linear dichroism (Figure 3.15(c)) and circular dichroism (Figure 3.15(d)) are not present.

Change of the optical properties according the presence of dielectric material: CaF_2 rods on Au rods

Fabrication of 3D structures composed of two rods vertically stacked and separated by a dielectric to avoid direct contact is described. To explore the effect of this dielectric rod, two nanostructures with the same amount of gold are fabricated, but with a dielectric CaF_2 layer evaporated over one of the structures. In the following Figure 3.16 the AFM and SEM images of the fabricated nanorods and the AFM profile of the structures are presented. From the AFM images the spatial arrangement and the morphology are extracted. Likewise, the SEM images of the structures allow discerning the similarity of the structures with dimensions of 103x226x53nm and 102x229x75nm where one of the structures has around 22nm of the dielectric material (CaF_2).

In general, the existence of a dielectric layer causes the redshift of the plasmon resonance peak in visible region. This effect is explained theoretically in terms of Rayleigh electrostatic approximation. According to this approximation, the resonance wavelength of nanorod (λ_p) is defined by

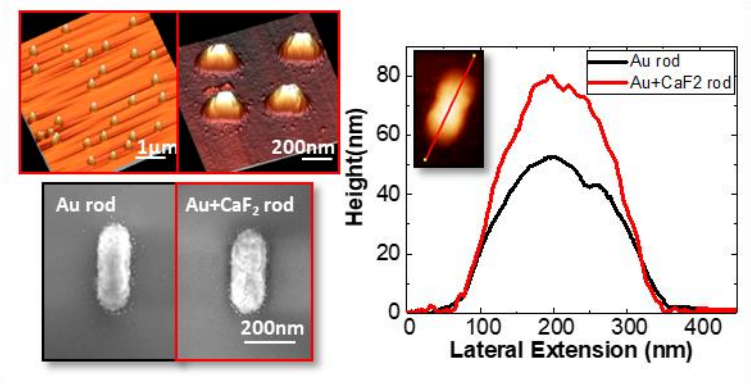

Figure 3.16: AFM and SEM images of nanostructures with dielectric layer of CaF_2 (red line) and without dielectric (black line). From the AFM profile of these two nanostructures, a thickness of 22nm for the dielectric is determined.

$$\lambda_p = \lambda_0 \sqrt{\varepsilon_\infty + (\frac{1}{L_\parallel} - 1)n_m^2} \quad (61)$$

where ε_∞=12.2 is the contribution of interband transitions to the dielectric permittivity according to the Drude model, λ_0=131 nm is the wavelength of plasma oscillations of gold free electrons, n_m is the refractive index of environment, and $L_{//}$ is the geometric depolarization factor for longitudinal resonance, which is smaller than 1/3 for nanorods. Using this Drude-like model for the dielectric function of gold nanoparticles, the dependence of the peak wavelength on refractive index for gold nanorods can be explained: larger refractive index leads to a shift of the plasmon resonance peak towards larger wavelengths. Both nanorods are fabricated on a glass substrate, with the refractive index around 1.5168, but instead of being surrounded by air, there is a dielectric layer of CaF_2 with n =1.4338 in one of them. Therefore, the response of these nanorods should be different, and varies according the Rayleigh approximation. The sensitivity of metal nanostructures to changes in the local refractive index of matter close to the surfaces can register shift values from tens to hundreds of nanometers [237,238].

This shift in the resonance position induced by the presence of a dielectric can and has been used for sensing applications[18].

The study of the optical properties of these nanorods is displayed in Figure 3.17. The transmission spectra for the nanorod capped with dielectric (red lines) and without dielectric layer (black lines) are illustrated in Figure 3.17(a). The tranverse (dotted lines) and longitudinal (solid lines) polarizations have been analyzed and no remarkable differences, in terms of spectral shape, have been observed. In both nanorods, the optical responses are two plasmon resonances related to the short (dotted lines) and long (solid lines) axes. The deposition of the CaF_2 induces a shift, much more evident in the low energy peak, of about 10 nm with respect to that of pure Au rods.

In addition, the *Mueller Matrix Elements* (MME) of these structures are seen in Figures 3.17(b-d). The optical response of the m_{12} is in accordance with the transmission spectra, and it exhibits a shift towards lower wavelengths. Unsurprisingly, the m_{14} and m_{13} do not present optical response in oriented single rods regardless of the presence of a dielectric layer. This absence of

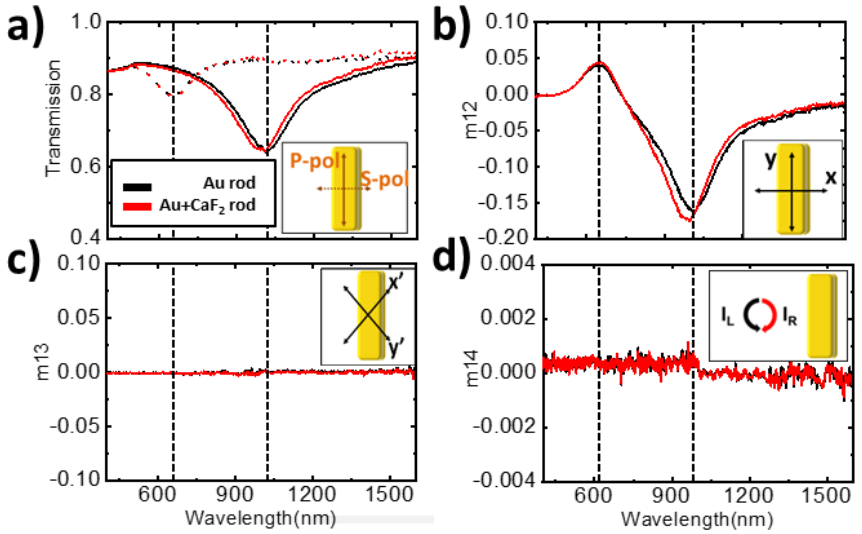

Figure 3.17: Transmission spectra a nanorod with dielectric (red lines) and without dielectric (black lines) for both longitudinal (p-polarization with solid lines) and transverse (s-polarization with dotted lines). In fig (b) the linear dichroism spectra is shown. Figs (c) and (d) present the null response of these structures to the circular and linear at 45º dichroisms, respectively.

effects of the deposited CaF_2 in the studied *Mueller Matrix elements* (MME) is of importance for the later studies of complex 3D systems, since any effect of the CaF_2 other than imposing a spatial separation of the dielectric spacer in the optical response of the structures can be disregarded. This will be mentioned in chapter 6.

3.2.3. Optical and MO characterization of $(Au/Co)_{ML}$

Antennas which simultaneously exhibit plasmonic and MO properties have brought attention in the field of Magnetoplasmonics[16,239]. Combining noble metals, which present low optical losses and well defined plasmonic resonances and ferromagnetic materials, which have larger losses and broad plasmon resonances, the response is optimized and it can be controlled by external agents such as magnetic fields[99].

Following this objective, structures with magneto-optical properties are developed by the use of HMCL templates described in the chapter 2. By the standard procedure of the templates, the deposition process was performed in an ultrahigh vacuum system by the combination of Knudsen cell for Au and electron-beam evaporation for Ti and Co. The deposition rates were 0.02nm/s for both Ti and Co and 0.03nm/s for Au. Additionally, the oscillation amplitude

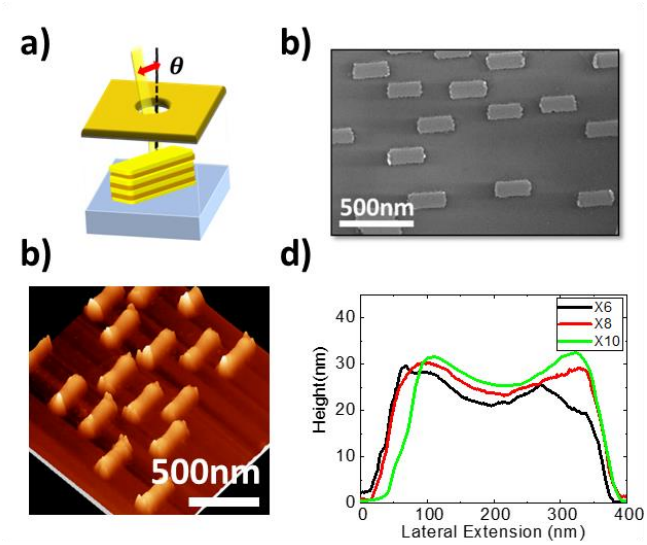

Figure 3.18: a) Schematic sketch of the fabrication method of nanorods with Au/Co multilayers where the material is evaporated through the holes of the templates.(b-c)AFM and SEM images of nanostructures (d)AFM profile of the structures according the different repetitions of Co layers in the structures.

was ±20º to obtain rods of adequate dimensions for their characterization in our available spectral range. Sample morphology was characterized by AFM and SEM, and optical and MO properties by spectral ellipsometric with magnetic fields in setups described in chapter 2.

The studied structures consist of two-dimensional arrays of randomly placed in plane nanorods deposited on glass substrates (Figure 3.18(a)), whose average dimensions are $H \approx 27$nm, $W \approx 107$ nm, and $L \approx 247$ nm. The internal structure is constituted by an Au/Co multilayer (ML) (N x (2.2 nm Au/0.8 nm Co)) covered with 3.4 nm of Au (total thickness between 23 and 30 nm). Three different sets of rods were grown, with a number of repetitions N equal to 6, 8, and 10. In all the structures, a 1 nm thick Ti layer was deposited on top of the glass substrate to improve the adhesion. In Figure 3.18(b) a SEM image of a collection of nanorods and their random spatial arrangement is presented. In Figures 3.18(c-d), the specific morphology of these structures as well as the average AFM profile of them, are shown.

The experimental dimensions and aspect ratio of these structures are shown in Figure 3.19. In these structures, the average dimensions are $W \approx 107$ nm, and $L \approx 247$ nm. The internal structure is constituted by an Au/Co multilayer (ML) (N x (2.2 nm Au/0.8 nm Co)) covered with 3.4 nm of Au (total thickness

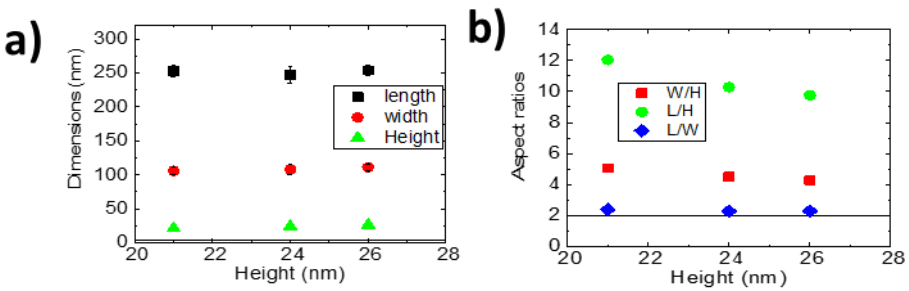

Figure 3.19: (a) Experimental dimensions of (Au/Co) ML as a function of the total height of the structures. (b)Aspect ratios of these structures versus the total height of the nanostructures.

between 21,24 and 26 nm). The thicknesses obtained in these samples do not correlate exactly with the number of repetitions. This may be due to the Co layers, which are extremely thin.

In these structures, there is an accumulation of material in the extremes as in gold nanorods fabricated by the same deposition method, whose values are 6nm higher than at the middle.

From the experimental measurements of the transmission and Mueller matrix elements, it can be extracted a similar behaviour between the structures in spite of the differences in cobalt amount. The ellipsometric and MO features, shown in Figure 3.20, indicate the excitation of the LSPR mode responsible for the observed resonant-like spectra.

Although the nominal dimensions of the nanorods are similar, the variations during the fabrication method give us an error estimation which can be a possible explanation to the differences in the plasmon resonance positions, being a redshift where the ferromagnetic material increases.

The transmission spectra at normal incidence for polarized light along the short axis (dotted lines) and long axis (solid lines) are presented in Figure 3.20(a). In the spectra along the short axis, the minimum values are located at similar wavelengths (650nm) whereas the minimum values along the long axis show a red shift as the length of the rod increases (more details about the fabrication method in chapter 2)).

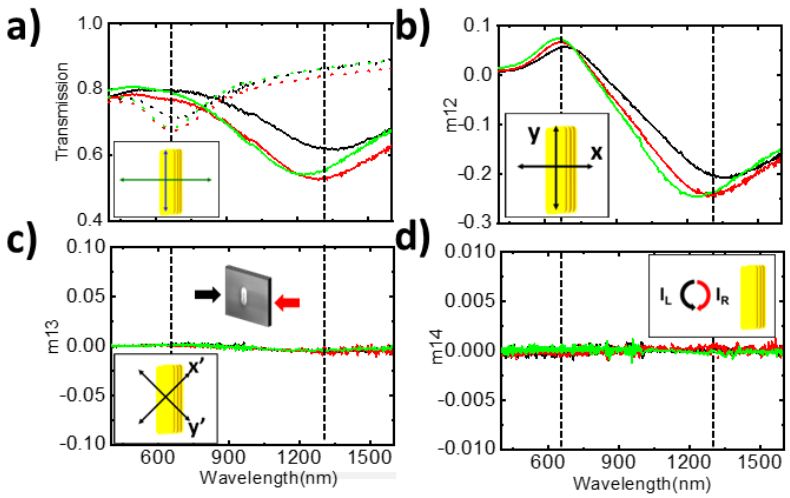

Figure 3.20: Transmission spectra for Au/Co multilayer nanorods where the repetitions of cobalt layers varies from 6 repetitions (black lines), to 8 (red lines) and 10 (green lines), for both longitudinal (p-polarization) and transverse (s-polarization). (b) the linear dichroism spectra are shown. (c) and (d) present the null response of these structures to the circular and linear at 45º dichroisms, respectively.

Similar behaviour to the transmission spectra is obtained in the m_{12} responses of the structures, as shown in Figure 3.20(b).The Mueller matrix element m_{12} shows sensitivityy to the small modifications in the dimensions of the nanostructures. The linear dichroism at 45º related to the element m_{13} is zero in these structures (Figure 3.20(d)). The analysis of the dichroic response is focused on the linear as well as the circular response of the structures.

The analysis of the plasmon resonances obtained from the transmission spectra according the total amount of these layers is shown in Figures 3.21(a-b). In both cases, there is a redshift towards larger wavelengths (of the order of 2% and 10% for transverse and longitudinal polarizations) when a decrease of cobalt amount is presented (Δt=5nm). Similarly, the behaviour of the plasmon resonance positions in these structures, Figures 3.21(c-d) show that the amplitude of these resonances exhibits a displacement towards higher wavelengths (of the order of 24% and 10% for TP and LP respectively). These results are consistent with structures such as nanodisks where an increment in the amount of ferromagnetic material produces slight blueshifts and peak broadening[102,104].

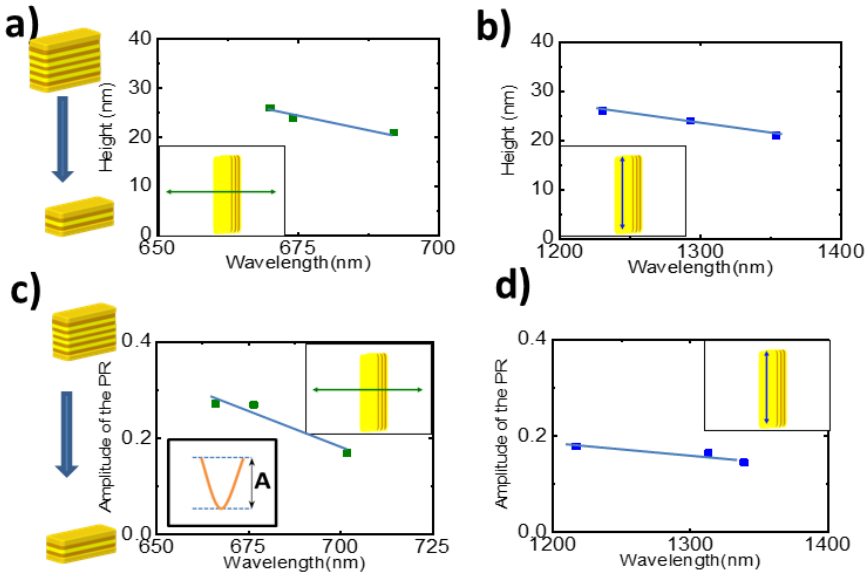

Figure 3.21: Peak resonance position for each nanorod as a function of the total height for both longitudinal (blue points) and transverse (green points) polarizations are shown in (a). In (b), the amplitude (A) of the peaks of the plasmon resonances (PR) is illustrated. In both cases light is normally incident. Insets show to top view of the nanorods with polarization direction and the sketch of the amplitude of the plasmon resonances (A).

Since rods are now of ferromagnetic nature, following the experimental method to determine the optical and magnetic contributions to the dichroic response by the decomposition of the Mueller matrix elements described in Chapter 2, the m_{14} element presented in Figure 3.20(d) is divided into two contributions: non-magnetic and magnetic responses, which can be extracted performing forward and backward illumination measurements in the presence of a magnetic field.

$$\frac{m_{14}(H^+) - m_{14}(H^-)}{2} \qquad Magnetic\ contribution \tag{62}$$

$$\frac{m_{14}(H^+) + m_{14}(H^-)}{2} \qquad Non-magnetic\ contribution \tag{63}$$

The magnetic field needed to saturate magnetically rods is determined by performing polar Kerr loops in the corresponding setup, allowing us to make sure that enough field is applied during the corresponding ellipsometry measurements (more details in Chapter 2). It is shown that in the MME

technique maximum fields up to 3kG are applied, while using MOKE values of up to 10kG can be reached).

Figure 3.22 shows the spectral responses of the magnetic contributions of the arrays of Au/Co nanorods measured by two different techniques: the MME method (upper image) and by MOKE (lower image). The p-MOKE loops were

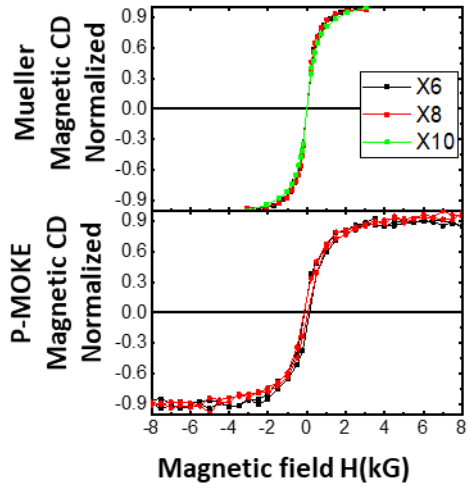

Figure 3.22. Comparative magnetic contribution to the circular dichroism in nanorods of Au/Co with different repetitions of the layers: 6(black loops),8(red loops) and 10(green loops). The loops were obtained by two different experimental methods: Spectroscopic ellipsometry with a home-built system (top graph) and p-MOKE technique (bottom graph).

normalized at 500nm and 600nm for the 6 and 8 repetitions of Co to compare the magnetic behaviour of the structures. Similar spectral dependence is obtained by two different methods with the saturation field is around 2 kG.

The spectral responses of both non-magnetic and magnetic contributions of the arrays of Au/Co nanorods are shown in Figure 3.23. As expected, the non-magnetic contribution of the aligned structures presented in Figure 3.23(a) is zero, which is in accordance with previous results in similar structures (more details in Figure 3.5)[16,148]. The magnetic contribution (MCD) of the Au/Co nanorods to the total CD is studied. The magnitude values of the MCD are varying from 2.5 10^{-4} to 1.5 10^{-4} (in the order of 40%) at 3kG. The effects induced by the presence of Co in comparison to pure Au structures, are the broadening of the plasmon resonances peaks as well as the shifts of these PRs to higher energies (from 1200nm to 1100nm). At saturation, the shifts depend

on mainly the amount of Co, whose distribution inside the structure modifies the electromagnetic field within the nanostructure. These changes in the spectral position of the MO activity can be red-[240,241] or blueshifted[242]

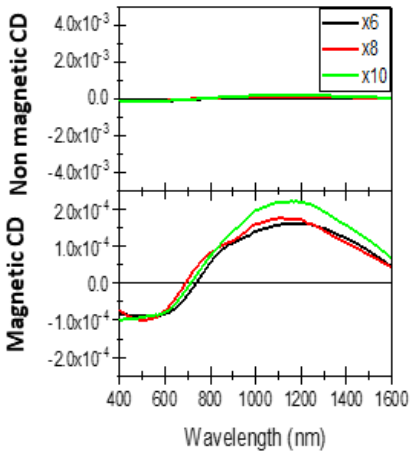

Figure 3.23: Contributions of the dichroic response according the presence of Co material, in nanorods of Au/Co. The top graph shows the nonmagnetic or natural CD according to the number of repetitions of Au/Co:6 (black lines),8(red lines) and 10 (green lines). The bottom graph presents the measured magnetic dichroic response of these structures by Mueller matrix method.

according to the structure, the broadening of the peaks is observed and related to the high absorption of Co[102].

3.3. Chapter Conclusions

Building blocks, such as disk dimers and nanorods, LSPRs can be tuned modifying structural parameters during the fabrication. Changes in the deposition time modify the plasmon resonances (PR) of gold nanorods with a blueshift, and a broadening of the PRs peak. The variations in the spectral positions ($\Delta\lambda$) are around 200nm for both longitudinal and transverse polarizations, and the amplitudes vary up to 17%, being more sensitive to the longitudinal polarization due to the excitation of the PR along the large dimension. On the other hand, changes of the oscillation deposition angle, give variations in the LPR positions of 3% and 28% for the transverse and

longitudinal polarizations, respectively. Both results show the sensitivity of the LPRs in gold nanorods. Insignificant changes in the PR positions *(Δλ*=10nm) happen when a dielectric thin layer is placed on the metal structures.

The addition of ferromagnetic materials in the rods is also examined. The LSPRs are wider that in pure noble metals and the values of *Δλ* are around 2% and 10% for transverse and longitudinal polarizations along the structure. The amplitude values change 25% and 10% respectively.

The sensitivity to growth parameters and to interactions with the environment found in these structures confirms their use as biological sensors.

4. TWO DIMENSIONAL SYSTEMS

This Chapter presents the optical and magneto-optical properties of chiral and achiral plasmonic planar systems that have been built using the building blocks (nanopillars and nanorods) presented in Chapter 3. The optical and magneto-optical properties of these hybrid nanostructures strongly depend on their planar arrangement and their constituent materials. The planar nanostructures are composed of nanorods and nanodisk dimers. Non-magnetic nanorods are fabricated with metallic Au, while ferromagnetic nanorods are deposited in the form of Au/Co multilayers. The disk dimers deposited together with the nanorods have been either metallic Au or dielectric CaF_2 and have been attached to them at different symmetrical position. The results of the nanostructures containing metallic, non-magnetic Au nanorods are presented first, followed by those obtained for nanostructures with metallic, ferromagnetic Au/Co nanorods.

4.1. Non-ferromagnetic nanohybrids

4.1.1. Fabrication geometry

The precise control over the fabrication of the nanostructures, mentioned already in chapter 3, has been achieved by combining colloidal lithography with the rotation of the template and an off-normal deposition at various angles. First, the nanodisk dimers are deposited with an edge-to-edge separation of 60 nm by fixing the angle to $\varphi_{offset}=25^{o}$ and the oscillation angle of $\Theta=\pm5^{o}$. In order to enhance the adhesion of the final nanodisks to the substrate, thin titanium nanodisks of 1-2 nm in thickness have been fabricated prior to the deposition of both the metallic and dielectric nanodisks. The dimers in each sample are evaporated simultaneously, thus resulting in nanodisks of similar height by reducing the effect of closing of the template hole. Nanodisks of Au of 30 nm in thickness and CaF_2 nanodisks of 20 nm in thickness have been obtained for the dimers. Next, the template is rotated in-plane to deposit a nanorod of Au of 30-35 nm in thickness between the nanodisks. The template is rotated at three different angles of $\varphi=45^{o}$, -45^{o} and 90^{o} for different samples, thus resulting in three different configurations of the rod with respect to the nanodisks, as seen in the SEM images in Figure 4.1.

Two dimensional systems

The Au nanorods have been evaporated using an oscillation amplitude of Θ of ±20°. The upper panels of Figure 4.1 (a-c) show SEM images of the planar structures fabricated with metallic nanodisks, while the lower panels (d-f) show corresponding SEM images for the samples with dielectric nanodisks. The specific deposition conditions for metallic and dielectric nanodisks are similar. The planar distribution of the dimers with respect to the Au nanorod in the SEM images is of 45° (left panels in red), -45° (central panels in green) or 90° (right panels in black). For the samples with dielectric dimers (bottom panels), similar nanodisk diameters of 110-120 nm are observed for an off-normal deposition angle of ±5° (more details about the fabrication of these building blocks are in Chapter 3).

The final dimensions of the nanostructures deposited have been obtained by AFM and SEM measurements. The data confirmed the expected height for the Au nanodisks (30 nm) and for the CaF_2 nanodisks (20 nm). The SEM and AFM data also display a slightly elliptical shape due to the off-normal deposition through a circular hole, albeit the average diameters obtained for the Au nanodisks (110 nm) differ only slightly from those of the CaF_2 nanodisks (of 100 nm). For the Au nanorods, SEM and AFM data reveal a total length that ranged between 210-230 nm, and consistent widths and thicknesses of 75 nm

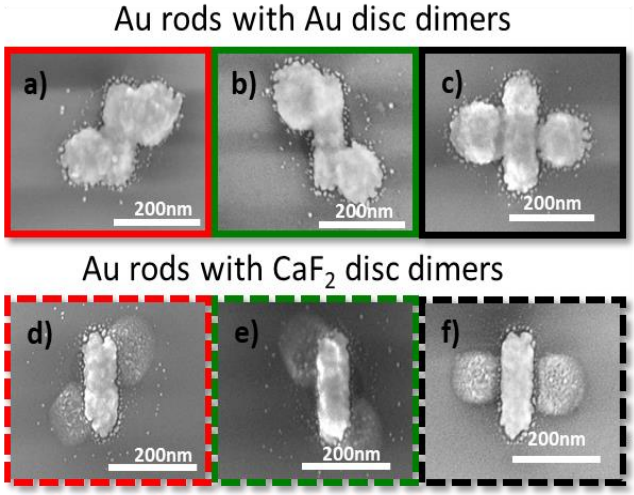

Figure 4.1 SEM images of the non-magnetic nanohybrid structures deposited by combining colloidal lithography and off-normal evaporation) for the nanostructures containing metallic Au nanodisks (upper panels a-c) and dielectric CaF2 nanodisks (lower panels d-f). The nanodisks are bridged by Au nanorods deposited at template angles of 45º (left panels in red). -45º (central panels in green) or 90º (right panels in black).

and 25 nm, respectively. Therefore, given the nominal edge-to-edge separation between the nanodisks of 60 nm, the 75 nm wide nanorods ensure the physical overlapping between all the building blocks of the nanostructure (a further detailed discussion can be found in the appendix section 9.3). The structures exhibit a similar nanostructure density, of the order of 3 nanostructures/μm^2, with nanorods aligned parallel to each other. The nanostructures are randomly distributed over the sample surface with enough distance between them that guarantee that crossed interactions are not an issue.

4.1.2. Optical properties

The optical response measures the transmitted intensity of the hybrid nanostructures and specific Mueller matrix elements. These are obtained by spectroscopic ellipsometry with normally incident light, as described in Chapter 2. Figure 4.2 shows the spectral dependence of those Mueller matrix elements which are connected to optical anisotropies. The top left sketch in Figure 4.2 depicts the different orientations of the Au nanorod with respect to the position of the nanodisks around it, namely 45 º (red lines), -45 º (green lines) and 90 º (black lines). Vertical dashed lines indicate the position of the resonances of the individual rods and dimers.

The responses of the single Au nanorod (blue lines) and the Au nanodisk dimers (yellow lines) are plotted in the left panels of Figure 4.2. Linear dichroic signals (m_{12}) with a z-shape can be observed for the Au nanorod and the Au dimers. The resonant wavelengths highlighted by dashed vertical lines are transferred to the hybrid nanostructure data for comparison purposes. Moreover, the optical anisotropies have been measured under forward (solid lines) and backward illuminations (dashed lines) in order to extract the contributions to the CD signal (this procedure has been detailed in Chapter 2).

The signal obtained for the element m_{12} in the case of structures with dielectric dimers (top right plot in Figure 4.2) shows a linear dichroic response with a similar z-shape to that of the single Au nanorod, and a maximum value at low wavelengths (600 nm) and a minimum value at large wavelengths (1000 nm) regardless of the arrangement of the dielectric dimers with respect to the rod. The intensity of the linear dichroic effects is larger than the circular dichroic ones, having an intensity two orders of magnitude larger and its

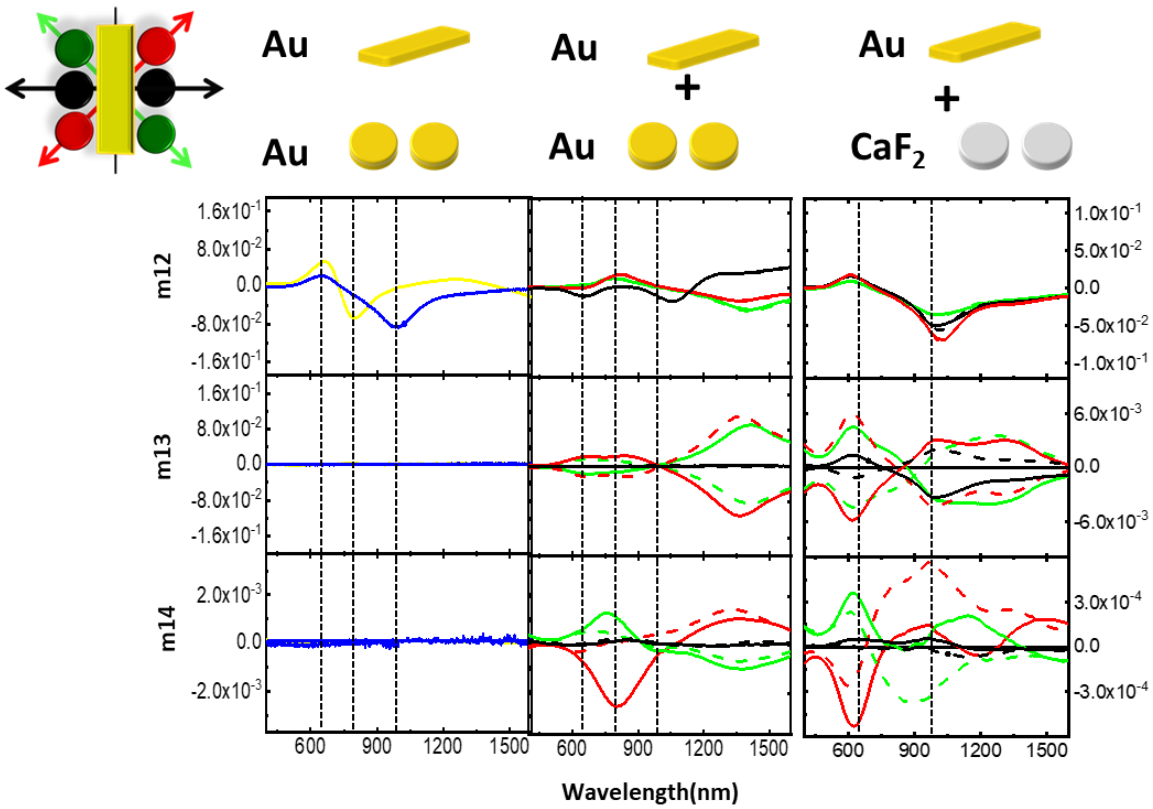

Figure 4.2: Normal incidence ellipsometry data obtained from the non-magnetic nanostructures. Contributions to the non-magnetic Mueller matrix elements m12 (upper panels), m13 (central panels) and m14 (lower panels) are shown. The data is measured on different nanohybrid structures: Au nanorod (blue lines) and Au dimers (yellow lines) independently (left panels), Au nanorod with Au dimers (central panels) and Au nanorod with CaF2 dimers (right panels). The different configurations of the nanorod with the dimers are depicted in the top left sketch, being 45º (red lines), -45º (green lines) or 90º (black lines). Solid lines indicate forward illumination, while dashed lines indicate backward illumination. Vertical dashed lines indicate the position of the resonances of the rods and dimers individually

values being around $2 \cdot 10^{-2}$ and $-8 \cdot 10^{-2}$ and only the line-shape of the m_{12} response is affected. This suggests that single Au nanorods with well-known resonant line-shapes are sensitive to modifications in the dielectric environment[18,243]. Thus, the presence of the dielectric dimers near the corners of the metallic plasmonic nanorod produces changes in both the local near field of the nanorod due to local dielectric perturbations[244]. These shifts and changes of the line-shapes can be understood as alterations of the local field and the charge distribution within the nanorod. Therefore, the detection of these changes due to small variations of the dielectric environment may be

used as a tool for the detection of analytes such as molecules, bacteria or virus[18,116].

Furthermore, the hybrid nanostructures with gold dimers present significant differences in the optical response of the m_{12} element (top central graph in Figure 4.2). These differences can be attributed to the interaction between the metallic elements in the hybrid structure, which give relevance to the planar arrangement[245–247]. In general, the metallic interaction between the nanorod and the nanodisks results in hybridized modes with responses that are shifted, or with modified shapes, with respect to those of the individual building blocks[68]. For the presented nanostructures, the linear dichroism had a z-shape when the dimers were at ± 45°, with the maximum and minimum positions shifted towards higher wavelengths (around 400 nm of difference) compared to structures with dielectric dimers, occurring now at around 800 nm and 1400 nm, respectively. In addition, a change in the shape of the linear dichroic response can be observed when the pillars are at 90°. This response presented an additional minimum and yielded two maxima at 700 nm and 1070 nm and two minima at 800 nm and 1350 nm. The magnitudes for these structures are between $2{\cdot}10^{-2}$ and $-5{\cdot}10^{-2}$, in good agreement with those observed for the dielectric pillars. Linear dichroism is defined as the difference between I_X-I_Y (as discussed in Chapter 2), thus yielding a zero optical anisotropy in symmetric nanostructures such as crossed rods at 90°. However, the non-zero response in the presented dimers at 90° suggest that the contributions from the metallic disks and the nanorod differ along the x and y directions.

Another magnitude sensitive to the planar position of the dimers with respect to the nanorod is the linear dichroism at 45°, which is studied through the Mueller matrix element m_{13}. The data obtained for this element is shown in the horizontal central panels of Figure 4.2. As seen, there is a clear dependence of the spectral response with the spatial arrangement of the dimers and the nanorod, taking a z-shape when the structures are at 45° (red lines), a s-shape when the structures are at -45° (green lines) and a pseudo s-shape at 90° (black lines), although in principle this last value should be zero. The existence of this response shows the planar arrangement of the disk in the nanohybrid nanostructure. Comparing the optical response for different compositions of the dimers, the intensity is 10 times smaller(around to $6{\cdot}10^{-3}$) when the pillars are dielectric with respect to the equivalent structures with metallic Au nanopillars. Although this response is significantly lower than that

of the Au dimers, it still displays modifications in the spectral shape as a function of the position of the pillars, indicating a large sensitivity to minute variations in the position of the pillars. For instance, the effect of the dielectric pillars on the measured m_{13} signal may be due to the overlapping of the nanorod with the dielectric dimers (as seen in the SEM images of Figure 4.1), which modifies its refractive index[248] and, as a consequence, its optical response.

Finally, the dichroic circular response is presented as the m_{14} element in the lower horizontal panels of Figure 4.2. A direct comparison between the data obtained for the dielectric and the metallic dimers shows a signal 4 times smaller in the former. This suggests that the hybrid structures have chiral responses induced by the presence of the dielectric nanodisks, regardless of their electronic nature. However, metallic interactions enhance this chirality signal considerably.

In addition, as discussed in Chapter 2, a more exhaustive analysis of the circular dichroic response can be performed when the m_{14} element is decomposed into two components that account for the linear combination of optical anisotropies (CD_{anis}), such as linear dichroism itself, and another component that originates from the intrinsic chirality of the structure(CD_{Ch}):

$$CD_{total} = CD_{Anis} + CD_{Ch} \quad (64)$$

This intrinsic chirality is usually denominated configurational chirality, provided that it arises from the breaking of the symmetry due to the specific arrangement of the building blocks[203]. Both contributions to the circular dichroism are appealing, albeit difficult to differentiate experimentally since they are usually masked and/or combined with linear optical anisotropies of larger intensities. Figure 4.3 shows the m_{14} signal shown in Figure 4.2 but decomposed in the anisotropic (upper panels) and chiral (lower panels) contributions for the samples with metallic dimers (left panels) and dielectric dimers (right panels) with different configurations between nanorods and nanodisks. A strong dependence can be observed for both contributions on the composition and planar location of the nanodisks within the nanostructures.

According to the composition, structures with Au nanodisk dimers present a spectral response 10 times larger (and of the order of $2{\cdot}10^{-3}$ for both

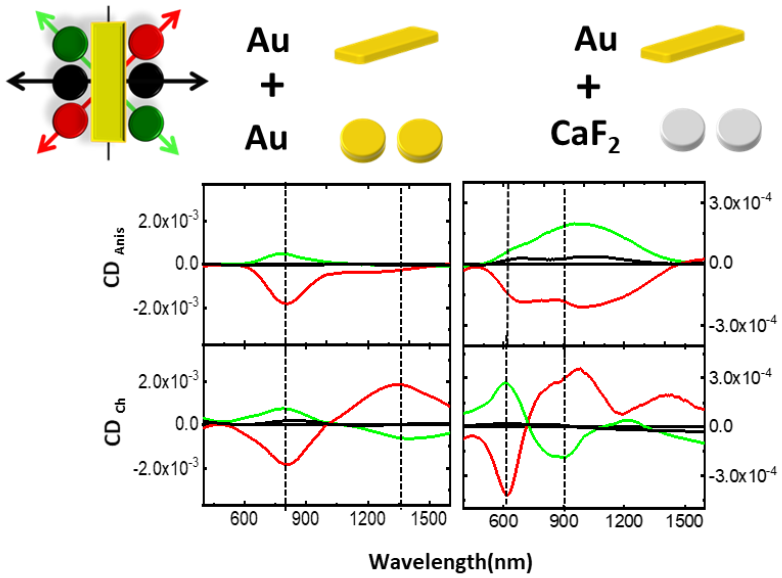

Figure 4.3: Experimental spectra of the element m14 decomposed in the anisotropic (upper panels) and chiral (lower panels) contributions for the samples with non-magnetic nanorods. The data shown corresponds to different configurations between nanorods and nanodisks for the metallic dimers (left panels) and dielectric dimers (right panels).

contributions) than that of the CaF_2 disk dimers. Moreover, clear differences in the shape of the spectra with respect to the arrangement of the disks can be observed. Indeed, the structures with metallic and dielectric dimers at 45º (red lines) present a u-shape dependence in the anisotropic and a s-shape in the chiral contributions, which are inverted for the nanostructures with dimers at -45º. The signal is not perfectly inverted, most likely due to small morphological differences introduced in the fabrication.

Thus, hybrid structures with equivalent planar disposition, the spectral signal corresponding to the chiral contribution yields a similar shape, but differs in intensity, depending strongly on the dielectric or metallic nature of the nanodisks adjacent to the rods. Furthermore, the main spectral features of the structures with dielectric dimers are displaced toward shorter wavelengths (blue-shifted) with respect to those with Au dimers. This can be clearly observed in Figure 4.3, using as a reference the vertical dashed lines. For the case at 45º (red lines), for instance, the minimum and maximum values are found at 800 nm and 1400 nm for the sample with disk Au dimers, while the same peaks are displaced with dielectric nanodisks to 600 nm and about 900

nm, respectively. These differences in the shape of the spectra, as well as the shifts of the peaks, emphasize the impact that the composition of the building blocks has on both the anisotropy and chirality of the Au nanorods. However, these dissimilar contributions to the spectra have a similar weight over the total circular dichroic response regardless of the composition of the dimer nanodisks.

4.2. Ferromagnetic Nanohybrids

Nanostructures with magnetic and plasmonic properties have attracted interest in last decades within the field of Magnetoplasmonics[99,249]. By controlling the fabrication of the constituting building blocks, the Magneto-Optical (MO) activity can be increased due to the electromagnetic field enhancement related to the plasmonic functionalities[20]. Moreover, the magnetic properties of these structures allow to control externally the plasmonic properties The combination of the magnetic and plasmonic properties of these nanostructures appoints them as suitable candidates for various applications, such as integrated photonic devices[250–252] or bio- and chemical sensors[253–255].

The MO active materials also give rise to dichroic responses, which added to the responses of configurational origin shown previously in Chapters 3 and 4 (specific location of the Au or dielectric pillars), allow obtaining an extra degree of freedom for the design of active structures[40,122].

In the following, the tuning of the plasmonic and magnetic responses of ferromagnetic nanohybrid structures is investigated through changes in the spatial arrangement of the ferromagnetic nanorods. In particular, the optical and MO responses of hybrid nanostructures composed by multi-layered nanorods of Au and Co [$(Au/Co)_{ML}$] are studied when combined with nanodisk dimers of CaF_2 and Au.

4.2.1. Fabrication

As discussed in the previous section, nanostructures have been deposited by colloidal lithography in an ultrahigh vacuum system. The deposition of Co has been achieved by means of electron-beam evaporation, while a Knudsen cell has been used for the deposition of Au. Ferromagnetic nanorods have been

realized by alternating layers of metallic (Au) and ferromagnetic (Co) materials with ten repetitions. The addition of active ferromagnetic layers in the nanorods is responsible for the appearance of magnetooptical activity. The thicknesses of the different layers are (from top-to-bottom) 5 nm Au, 10 x (0.6 nm Co/ 2 nm Au)/1 nm Ti. As shown in Chapter 3, nanorods containing a Co thickness of 0.6 nm can be magnetically saturated along the surface normal with the available magnetic fields.

Figure 4.4 shows SEM images of the magnetic hybrid nanostructures deposited with Co and Au multi-layered nanorods and both metallic disk dimers (upper panels a-c) and CaF_2 disk dimers (lower panels d-f).

The average dimensions of the hybrid nanostructures have been obtained from AFM and SEM measurements. As in the previous case for non-ferromagnetic nanohybrid structures, the average thicknesses of the nanodisk dimers of Au and CaF_2 are of 30 nm and 20 nm, respectively, in good agreement with nominal thicknesses.

A similar elliptical shape is also found in both metallic and dielectric dimers, with average diameters of 110-120 nm. Regarding the ferromagnetic $(Au/Co)_{ML}$ nanorods, the AFM and SEM data yielded averaged dimensions of 215 nm in length, 75 nm in width ,and a total thickness of 32 nm.

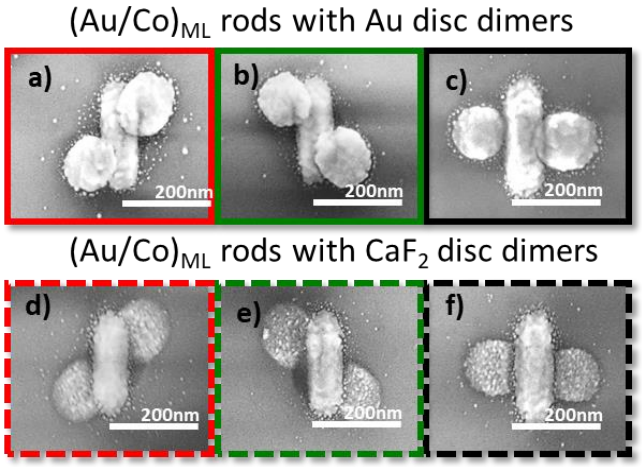

Figure 4.4 SEM images of the magnetic nanohybrid structures deposited by combining colloidal lithography and off-normal evaporation for the nanostructures containing metallic Au nanodisks (upper panels a-c) and dielectric CaF2 nanodisks (lower panels d-f). The nanodisks are bridged by (Au/Co)ML nanorods deposited at template angles of 45º (left panels in red). -45º (central panels in green) or 90º (right panels in black).

4.2.2. Optical properties

Regarding the purely optical response, an analogous behaviour with respect to the case of non-ferromagnetic structures is measured and displayed in Figure 4.5. The top scheme sketches the structure geometry. Similarly, to previous cases the optical responses for each individual building block are plotted in the left column of the figure. The vertical dashed lines are the spectral positions of the single $(Au/Co)_{ML}$ nanorod and Au disk dimer resonances. Analogously to the non-ferromagnetic structures, the linear dichroism has a z-shape spectrum, modifying this line shape in the case of the metallic disks due to the interactions between the constituent elements.

These linear dichroism peaks appear broadened when compared to the non-magnetic nanostructures of Figure 4.2, most likely due to an increase in the optical losses in the rod induced by the presence of Co. Yet, when comparing the single nanorods (blue lines) in the top left panels of Figures 4.2 and 4.5, the linear dichroic responses of the nanorods have similar line shapes. In the presence of dimers, and despite of the modifications introduced by the metallic nanodisks, the spectral position of the peaks and shapes of the linear dichroism data when the disks are placed at ± 45º (red and green lines) are similar to the individual Au/Co nanorod case, with maximum and minimum positions at 600 nm and 1300 nm, respectively.

On the other hand, the presence of dielectric pillars produces a z-shape with maximum and minimum values at about 600nm and 1100nm, whose positions are shifted towards lower wavelengths. In both cases the intensities range between $5 \cdot 10^{-2}$ and $-8 \cdot 10^{-2}$, as in the case for non-ferromagnetic materials. Therefore, linear dichroism between structures with and without ferromagnetic material does not seem to reflect the magnetic nature of the rod, the broadening of the peaks is a characteristic feature presented in these nanostructures (in absence of interactions between the structures).

From the analysis of the linear dichroism at 45º as in the previous section, a similar response to the non-ferromagnetic materials is obtained. The intensities of these m_{13} elements for the metallic and dielectric disk dimers are around $3 \cdot 10^{-2}$and $2 \cdot 10^{-3}$, being 10 times higher than in the last case mentioned. Surprisingly, this dichroic signal is much smaller than that for equivalent structures with Au rods. This may be produced by differences in the dimensions or the overlapping between the building blocks during the fabrication method (appendix section 8.3).

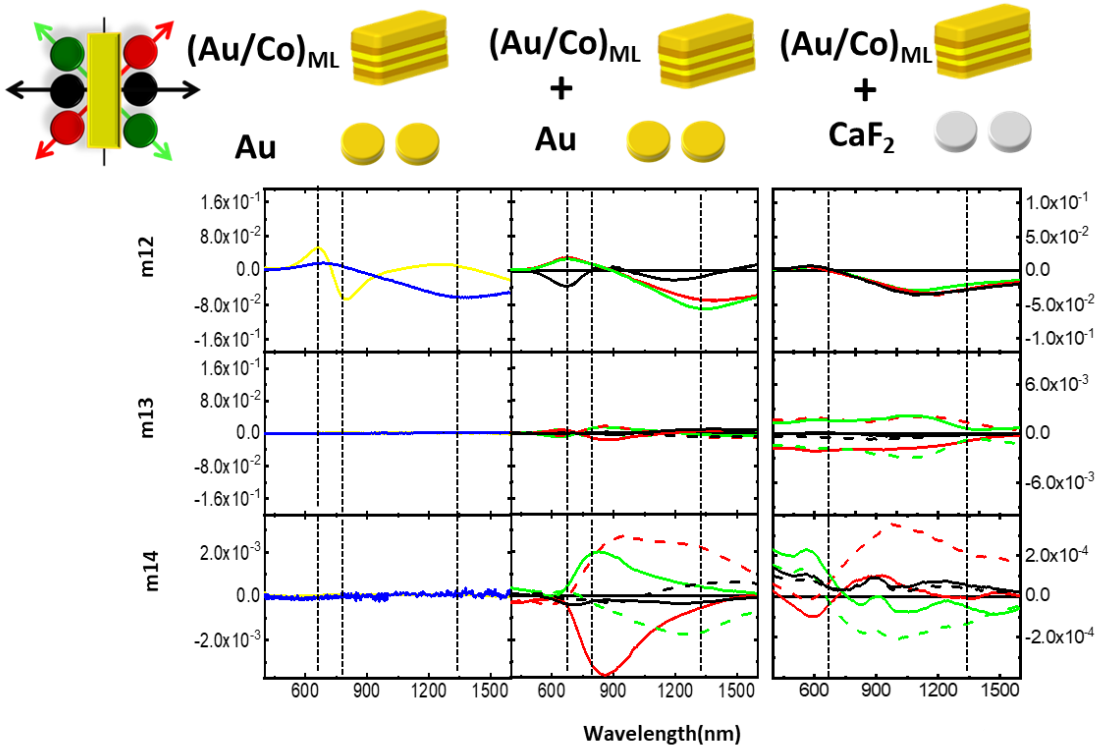

Figure 4.5: Normal incidence ellipsometry data obtained from the magnetic nanohybrid structures. Contributions to the non-magnetic Mueller matrix elements m12 (upper panels), m13 (central panels) and m14 (lower panels) are shown. The data is measured on different nanohybrid structures: (Au/Co) ML nanorod (blue lines) and Au dimers (yellow lines) independently (left panels), (Au/Co) ML nanorod with Au dimers (central panels) and (Au/Co) ML nanorod with CaF2 dimers (right panels). The different configurations of the nanorod with the dimers are depicted in the top left sketch, being 45º (red lines), -45º (green lines) or 90º (black lines). Solid lines indicate forward illumination, while dashed lines indicate backward illumination. Vertical dashed lines indicate the position of the resonances of the rods and dimers individually.

Finally, the analysis of the element m_{14} shows a response in the order of $2 \cdot 10^{-3}$ for the Au nanodisks and a signal 4 times lower for the dielectric disks (in the order of $5 \cdot 10^{-4}$). These circular dichroic responses presented the same intensities than those obtained for the non-ferromagnetic nanohybrid structures. This may indicate that the chiral response depends entirely on the metallic character of the nanorods and its effect on the interaction between the building blocks rather than on the incorporation of the Co.

In order to understand the origin of the chiral response in the magnetic nanostructures, the contributions are extracted following the procedure outlined in Chapter 2. The data obtained is divided in the anisotropic and the

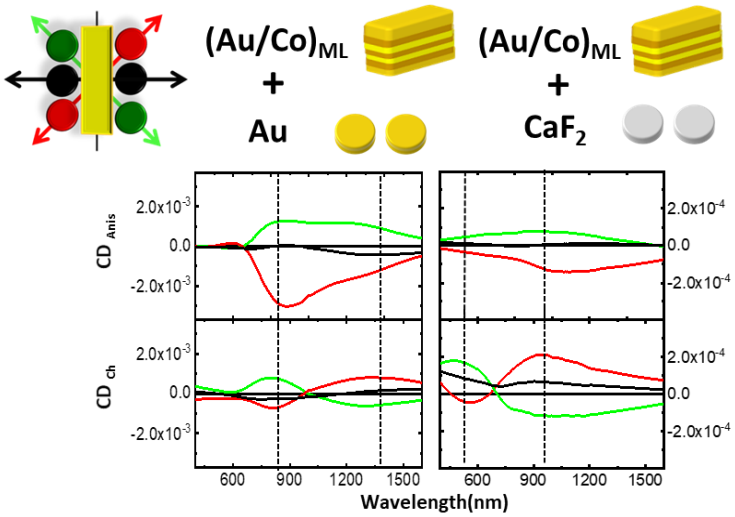

Figure 4.6: Experimental spectra of the non-magnetic contributions to the element m14 decomposed in the anisotropic (upper panels) and chiral (lower panels) for the samples with ferromagnetic nanorods. The data shown corresponds to different configurations between nanorods and nanodisks for the metallic dimers (left panels) and dielectric dimers (right panels).

purely chiral effect in the absence of external magnetic fields and are presented in Figure 4.6.

The presence of the dielectric dimers (top right column in Figure 4.6) yields a signal about 10% weaker to that obtained with the presence of metallic disks. This signal depends on the arrangement of the building blocks, distinguishing an opposite spectral response as the pillars are at ± 45º (red and green lines) for both the metallic and dielectric dimers. In the nanostructures containing CaF_2 nanodisks, the effects of chirality and optical anisotropy in the plane are of the same order (10^{-4}). On the other hand, the presence of metallic disks induces interactions between the building blocks that depend on their location within the sample. Although there is a non-zero chiro-optical response independently of the composition, the intensity obtained from the dichroic spectra with metallic disks is larger.

4.2.3. Magneto-optical properties

The non-magnetic response of the ferromagnetic nanohybrid structures presented has been discussed. Next, *Magneto-Optic Kerr Effect* (MOKE) measurements are performed on the same ferromagnetic nanohybrid

structures in order to determine the effect that the inclusion of ferromagnetic Co has in the magneto-optical response of the Au/Co nanorods. For this purpose, the external magnetic field that is readily available in the ellipsometry setup has to be enough to magnetically saturate the ferromagnetic nanostructures (for more detail, see Chapter 3).

Figure 4.7 combines p-MOKE data with ellipsometry data obtained under the effect of an external magnetic field for a ferromagnetic nanostructure with a relative orientation of the building blocks of 45º. The p-MOKE data, recorded for fields up to 8 kG under an excitation of 750 nm (in black) demonstrates that the ferromagnetic saturation is reached in the $(Au/Co)_{ML}$ nanorods with fields of around 2 kG. Ferromagnetic saturation is also achieved in the spectral ellipsometer with an excitation of 1185nm (in orange) for an external magnetic field of 2.5 kG, thus demonstrating the suitability of this setup for the observation of the magneto-optic effect on these nanostructures.

Next, the optical anisotropies obtained from the Mueller matrix elements are discussed as a function of the applied magnetic field. The data have been measured in a home-built setup which allows to incorporate magnetic fields to a commercial spectral ellipsometer (for further details, see Chapter 2).

The magnetic response for a nanohybrid magnetic structure at 45º is shown in Figure 4.8. The upper panel shows the spectral data of the CD response for external magnetic fields with values that go from 0.17 kG to 2.49 kG. The signal values are 1.7 10^{-4} for an external field of 2.5 kG and decreases to values near

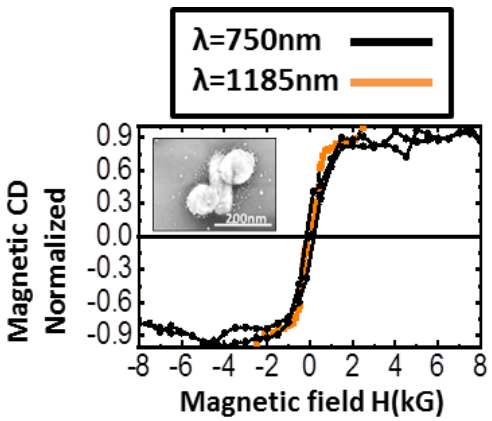

Figure 4.7: Comparative magnetic dependence of the magnetic circular dichroism obtained from a nanohybrid structure with a ferromagnetic nanorod at 45º.Black lines: p-MOKE data obtained with an excitation of 750 nm. Orange lines: spectroscopic ellipsometry data obtained with an excitation of 1185 nm. Inset: SEM image of the analyzed nanostructure.

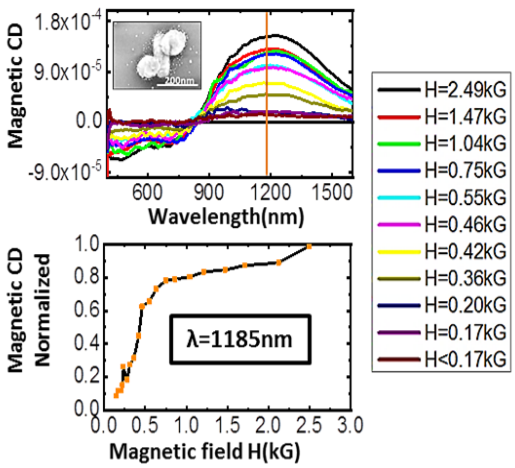

Figure 4.8: Magnetic circular dichroic spectra obtained from a nanohybrid magnetic structure at 45º. Upper panel: circular dichroic response for various external magnetic fields applied. Lower panel: normalized CD response of the above spectra corresponding to a wavelength of 1185 nm as a function of the external field.

zero as the magnetic field is removed. The vertical orange line indicates the wavelength corresponding to the maximum observed in the spectra, which is 1185 nm. The lower panel in Figure 4.8 shows the normalized CD response recorded at 1185 nm for the various magnetic fields applied, reproducing the magnetic field dependence of the p-MOKE signal previously shown.

Finally, the analysis of the Mueller matrix elements according the presence of an external magnetic fields is presented. An additional contribution to the CD signal appears in such ferromagnetic nanostructures when an external magnetic field is applied. As mentioned in Chapter 2, the magnetic and the non-magnetic contributions to the CD can be obtained from the measurement of the element m_{14} in forward and backward illumination, as:

$$\frac{m_{14}(H^+) - m_{14}(H^-)}{2} \qquad Magnetic\ contribution \qquad (65)$$

$$\frac{m_{14}(H^+) + m_{14}(H^-)}{2} \qquad Non-magnetic\ contribution \qquad (66)$$

Both contributions are presented in Figure 4.9 for structures with Au pillars (left panels) and with CaF_2 pillars (right panels). When a saturating magnetic field is applied, an optical response is produced depending on the field whose values are of the order of $2 \cdot 10^{-4}$, being 10 times lower compared to the non-magnetic response. The magnetic signal does not seem to have a great

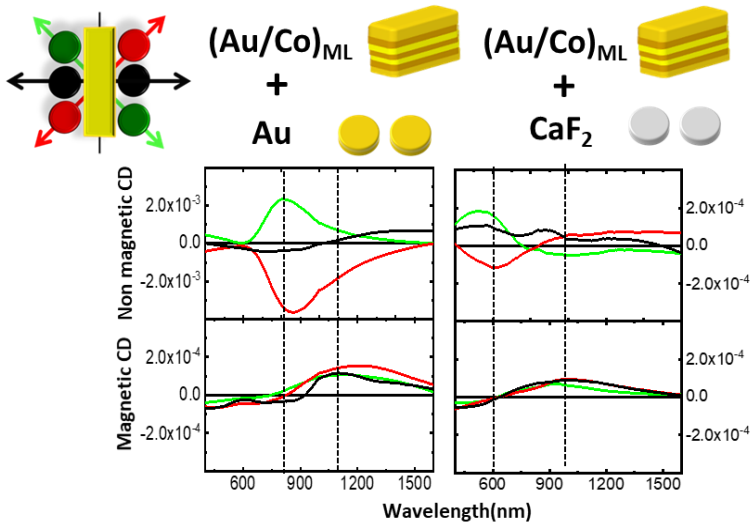

Figure 4.9: Experimental spectral dependence of the non-magnetic (top panels) and magnetic contributions (bottom panels) to the m_{14} element (CD) for structures with gold pillars (left) and with dielectric pillars (right). The sketch illustrates the relative position of the pillars respect to the nanorods, being black at 90º and red and green at 45º and -45º, respectively.

dependence neither on the composition of the dimers nor on its planar disposition, being more sensitive to variations in the near electromagnetic field within the nanorod, such as redistribution of the magnetic material within the structure[103,104],than the changes in the surrounding environment .This may be an explanation for the non-presence of changes in the MCD according to the geometry of the nanostructures.

The non-magnetic signal is similar to that obtained measuring the circular dichroism in the absence of magnetic field (lower panels in Figure 4.5) and it is strongly dependent on the geometry of the structures. While the non-magnetic signal is about 10 times larger than that recorded on the samples containing metallic Au nanodisks, it is of comparable magnitude for the dielectric dimers case.

4.3. Chapter Conclusions

Two-dimensional chiral plasmonic nanostructures have been fabricated and characterized, and additional ferromagnetic elements have been incorporated in the assemblies. The building blocks analysed in Chapter 3 have been combined into three different in-plane arrangements in order to induce configurational chirality in these nanohybrid structures. The presence of

ferromagnetic materials has allowed control of the response by external magnetic fields.

In the case of non-ferromagnetic nanostructures, the metallic or dielectric character of the nanodisk dimers produce distinct responses in the nanostructures, due to a distortion of the electric environment of the nanorod. For dielectric dimers, small modifications (4 times smaller than the metallic case) of the optical anisotropies have been observed, which depend on the nanodisks location in the plane. Furthermore, a hybridized response has been found for the metallic dimers, which has been ascribed to interactions between the nanodisks and nanorods and their in-plane arrangement.

In structures containing $(Au/Co)_{ML}$ ferromagnetic nanorods, corresponding dependencies with the composition and arrangement of the nanodisks have been found, together with a general peak broadening. An additional magnetic contribution to the chiral response has been obtained, with a 5-10% of the response that can be readily manipulated by external magnetic fields for the Au disk case. The response with dielectric disks has been found to be considerably smaller.

Finally, the g-factor of these structures shows values in the range of 10^{-3} to 10^{-2} with g_{max} values around ±0.015. This *g*-factor is similar to others obtained in planar chiral arrangements[40,119], thus enabling these planar active chiral structures for potential applications such as chiral or biological sensing.

Two dimensional systems

5. DESIGN AND MODELLING OF THREE-DIMENSIONAL NANOSTRUCTURES

Various challenges have been faced in the design and the fabrication of chiral structures with tuneable optical properties. In the previous sections, the constituent materials and individual building blocks (Chapter 3) have been introduced, and two dimensional nanosystems have been fabricated using these building blocks (Chapter 4). In the present Chapter, the design and modelling the optical response of three-dimensional systems will be introduced combing several nanostructures and materials. The disposition of the building blocks that form the 3D systems is sketched in Figure 5.1.

The fabrication of the 3D systems started with the deposition of two CaF_2 nanopillars (Figure 5.1(a)), followed by the deposition of an Au bottom rod between them (Figure 5.1(b)). A dielectric CaF_2 rod is then deposited over the bottom rod (Figure 5.1(c)), followed by a final Au rod that is evaporated

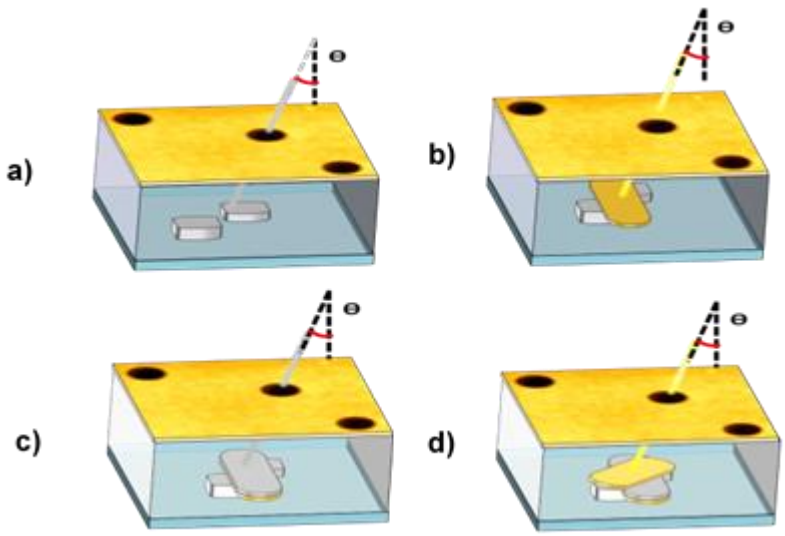

Figure 5.1: Schematic description of the nanorod dimer fabrication process: (a) Initially, two nanopillars of CaF_2 are fabricated through the holes of a gold mask. The dimensions and the distance between the nanopillars can be controlled by the evaporation system. (b) A gold bottom rod is deposited between the nanopillars of CaF_2 (c) Next, a dielectric spacer is deposited over the bottom nanorod. (d) The fabrication process is finished by rotating the structure 45° and evaporating a second Au nanorod on the dielectric spacer and over the dielectric nanopillars.

rotated azimuthally so that it lies on top of the CaF_2 nanopillars (Figure 5.1(d)). The intermediate CaF_2 nanorod suppresses any contact between top and bottom Au nanorods, thus insulating them electrically.

Next, a simplified theoretical model for this 3D system is proposed, based on Lorentzian oscillators assigned to the resonances of each single nanorod. The results predicted by this simplified model will be then compared with data obtained from these 3D nanostructures by means of standard ellipsometry, thus testing its validity. Despite of the simplicity of this model, its satisfactory agreement with the experimental data will put in value the use of simple models for the preliminary and fast design of complex chiral systems.

5.1. Theoretical model and individual building blocks

Our approach is the use of a simple model that considers the chiral three-dimensional system composed of two stacked gold rods separated by a dielectric layer as three layers piled up along the substrate normal, each of which has its effective optical constants. The Au rod layers are described by an anisotropic layer with two Lorentz oscillators, each one representing the longitudinal (ε_{xx}) and transversal (ε_{yy}) plasmon resonances of the rod, respectively. Each oscillator can be defined with the equation: theoretical model is proposed to predict the behavior of the chiral three-dimensional system composed of two stacked gold rods separated by a dielectric layer as three independent layers piled up along the substrate normal, each of them with their own effective optical constants. The Au nanorod layers are described by an anisotropic layer with two Lorentz oscillators, each one representing the longitudinal (ε_{xx}) and transversal (ε_{yy}) plasmon resonances of the nanorod, respectively. Each oscillator can be defined with the equation:

$$\varepsilon_{Lorentz} = \frac{Amp_n Br_n En_n}{En_n^2 - E^2 - iEBr_n} \tag{67}$$

where Amp_n is the oscillation amplitude, Br_n is the full width at half maximum (FWHM) and En_n is the center energy position of the peak[165].

To obtain the dielectric constants of each Lorentz oscillator, ε_{xx} and ε_{yy}, two specific samples have been specifically fabricated. The sample deposited for

the dielectric constants of the bottom nanorod is fabricated as a Au nanorod with two CaF_2 pillars laterally attached to it, as sketched in Figure 5.1 (b). The sample deposited to obtain the dielectric constants of the top nanorod is identical to that sketched in Figure 5.1 (d), but without the bottom Au nanorod. Sketches and representative AFM and SEM images of the final distribution of the nanostructures are shown in Figure 5.2, with approximate dimensions of 100 nm width and 270 nm length for the bottom rod, and 70 in width and 220nm length for the top rod. The estimated thicknesses of these nanorods are 14nm for the bottom and 13nm for the top one.

These two samples were optically characterized in the visible and infrared range (400-1600nm) using a spectroscopic ellipsometer (SE, M200Fi J. A. WoollamCo™) in transmission mode. Transmission measurements up to 2600 nm for the single top rod were carried out using an FTIR Bruker VERTEX 70 spectrometer. In the case of the top rod, measurements were performed up to λ=2400nm to correctly determine the low energy peak. The results are shown in Figure 5.3.

Figure 5.3 collects the experimental polarized transmission measurements (open circles) with the Lorentz model fitting (continuous lines) for the samples containing only bottom and only top Au nanorods. Black and red circles show

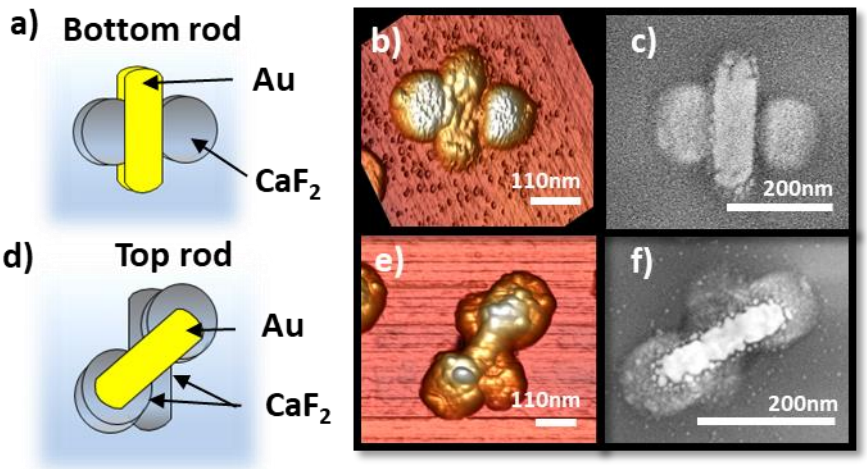

Figure 5.2(a-b) Sketch of the two individual building blocks fabricated. The bottom rod (a-c) is deposited directly on the glass substrate, whereas the top nanorod (d-f) is deposited over a CaF_2 rod, acting as dielectric spacer. In both single nanorods, the dielectric pillars were fabricated in order to imitate the dielectric environment .AFM and SEM images for the bottom nanorod (b-c) and the top nanorod (e-f) are used to determine their final dimensions.

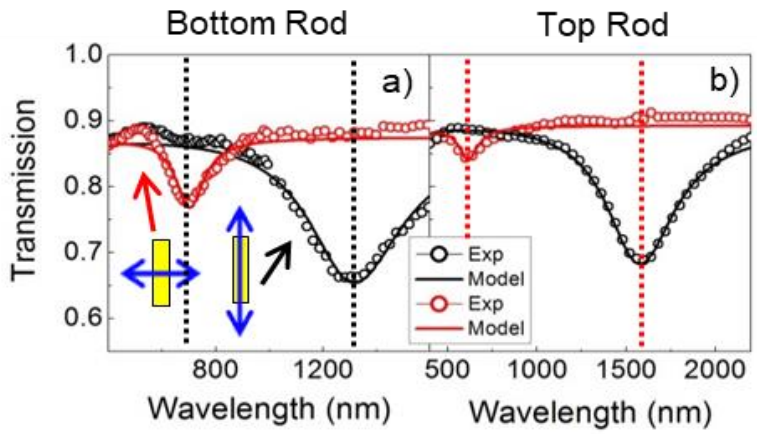

Figure 5.3: Experimental (open circles) and theoretical (continuous lines) polarized transmissions for the two samples corresponding to the individual bottom (a) and top (b) gold rods. Black/red data for light polarization along the long/short rod axis, respectively. Vertical dashed lines are guides to identify the energetic position of the modes.

light polarizations along the long and short axis, respectively, with their resonance positions indicated by vertical dotted lines. The resonances observed for the sample with only bottom nanorods (700nm and 1350nm, Figure 5.3(a) differ from those obtained for the sample with only top nanorods (600nm and 1600nm, Figure 5.3(b)) probably due to the different aspect ratio induced by the template hole closing effect and to the different global dielectric environment. The parameters obtained from the Lorentz fitting model for the nanorod layers are presented in Table 5.1, where the dielectric spacer (CaF_2) has been modelled as an isotropic layer with tabulated optical

Table 5.1: Dielectric constants of the two stacked gold nanorods obtained by fitting the transmission data of the nanorods to the Lorentz equation

		Amp_n (no units)	**Br_n(eV)**	**E_n(eV)**
Top nanorod	ε_{xx}	20.29	0.18	0.78
	ε_{yy}	0.98	0.50	2.01
Bottom nanorod	ε_{xx}	18.32	0.26	0.95
	ε_{yy}	4.27	0.38	1.77

contacts[256] and the glass substrate is defined by the Cauchy model with a refractive index of n=1.503 (more details can be found in the appendix section 8.1).

5.2. Simulations of different types of stacks of rods

With the main optical parameters for both bottom and top Au nanorods extracted from the previous experiment, now is possible to simulate different configurations in which both elements are stacked in several fashions or varying different stacking parameters. The dependence of the optical properties of chiral stacks of nanorods can be now calculated as a function of the rods relative in-plane angle, the dielectric spacer thickness and the relative energy position of the resonances of the nanorods.

5.2.1. Optical properties as a function of the relative in-plane angle

In three dimensional nanostructures with interacting building blocks, some parameters such as the in-plane arrangement or the distance between the building blocks play a fundamental role in the global optical response. In particular, the in-plane angle between these building blocks has acquired interest due to the possibility to control the optical response in the nanostructures by external sources[134]. The effect of the in-plane angle between the different building blocks in the total optical response is analyzed.

Figure 5.4 contains the simulated normalized polarized transmission data for incident light polarized parallel (Figure 5.4(a)) and perpendicular (Figure 5.4(b)) to the bottom nanorod as a function of the in-plane angle between the Au rods are presented. The dielectric spacer between the rods has been selected to be 10 nm thick. Two main modes are observed in Figure 5.4(a) at 1300 nm and 1600 nm, corresponding to the excitation of the longitudinal modes of the two nanorods. The intensity of the signal decreases gradually as the top nanorod is rotated from parallel (0°, black line) to perpendicular (90°, blue line) to the bottom nanorod, thus perpendicular to the direction of light's polarization. Moreover, even though the long axis of the bottom nanorod is always parallel to the light polarization, its intensity also decreases with the rotation of the top nanorod, reaching a minimum at 90°.

On the other hand, the high energy mode at around 600nm behaves in the opposite way, being zero when both nanorods are parallel and reaching a

maximum for an angle of 90°. This peak corresponds to the transverse mode of the top nanorod, which grows in intensity as the nanorod is placed perpendicularly to the incident light polarization. The vertical dashed lines correspond to the energetic position of the modes identified in Figure 5.3 for the individual nanorods.

Figure 5.4(b) shows the normalized transmission spectra calculated for an incident light linearly polarized perpendicular to the long axis of the bottom nanorod. Two resonance peaks can be observed in the high energy range, which correspond the excitation of the transverse mode of each nanorod. The peak corresponding to the bottom nanorod (700 nm) is independent from the relative angle, while the higher energy peak disappears as the top nanorod

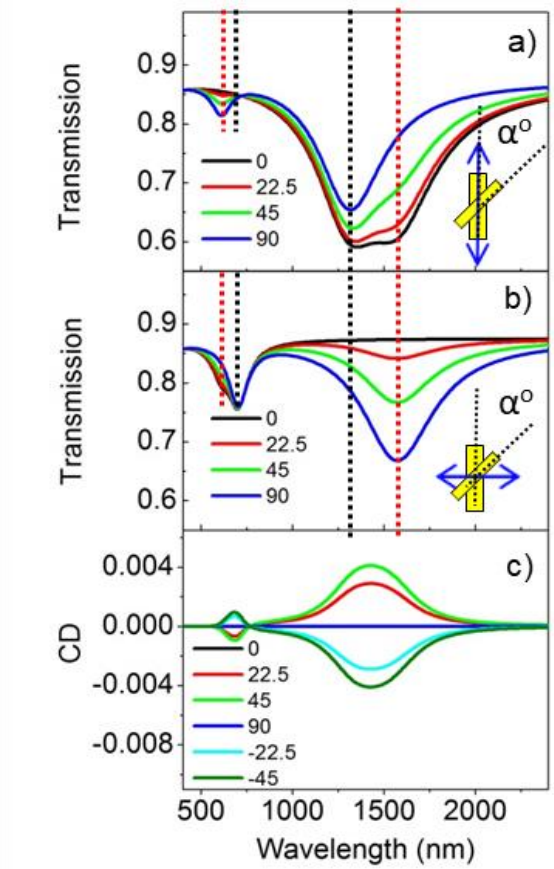

Figure 5.4: Simulations of the transmission of two stacked gold rods with a 10nm spacer as a function of their relative in-plane angle. a) Incident light is linearly polarized parallel to the bottom nanorod long axis. b) Light polarized perpendicular to the bottom nanorod long axis. c) Angular dependence of the Circular Dichroism in the nanostructures. The maximum CD is obtained for a relative angle of 45^0 between the rods. Vertical dashed lines correspond to the energetic positions of modes for the individual rods shown in Figure 5.3.

rotates. On the other hand, a low energy mode develops with rotation of the top nanorod, being zero at 0º and maximum at 90º. Thus, it can be concluded that this peak is generated by the excitation of the longitudinal mode of the top nanorod.

Finally, Figure 5.4(c) shows the simulated angular dependence of the Circular Dichroism (CD) calculated for the same nanorods structure. As it can be seen, CD is zero for 0º and 90º, since the rods are parallel and perpendicular in these two cases, forming an achiral system. For the other relative angles, two dichroic features are observed at high and low energy regions, near to those of the individual rods. The first peak is in a fixed position at 700nm regardless of the angle between the rods, although it undergoes a change of sign being positive and maximum at 45º and opposite in intensity and sign at -45º. At larger wavelengths, a second peak with a larger intensity and opposite sign is observed with respect to the peak at the shorter wavelength. This peak is in a fixed position at 1400nm regardless of the angle between rods. This feature has a similar behavior with a maximum at 45º and a minimum intensity at -45º.The circular dichroism in these stacked nanorods reaches maximum values for 45º and -45º, with responses that have equivalent intensities but opposite signs. Maximum chirality values these angles have been reported in similar nanosystems[80,257,258].

5.2.2. Optical properties as a function of the dielectric spacer thickness

The maximum CD signal can then be achieved with a relative orientation of the bottom and top nanorods of 45º. Next, the dependence of this CD signal on the dielectric spacer thickness is simulated. The results obtained from these calculations are shown in Figure 5.5. Here, the transmission in the Au nanorods is simulated for a fixed angle between the nanorods of 45º, polarizations parallel (Figure 5.5 (a)) and perpendicular (Figure 5.5 (b)) to the bottom Au nanorod and three different thicknesses for the dielectric spacer, of 0 nm (black lines), 10 nm (red lines) and 30 nm (green lines).

From the transmission for a light polarization along the bottom rod, it can be observed in Figure 5.5(a) that the longitudinal mode corresponding to the bottom nanorod (1350nm) is more intense than the same mode for the top

rod (1600nm), due to the partial alignment of the bottom rod with the light polarization. The weak peak observed at higher energies corresponds to the partial excitation of the transverse mode in the top nanorod.

A very small variation of the transmission spectra with light polarization perpendicular to the bottom rod can be observed in Figure 5.5(b) as the spacer gets thicker. Unlike the polarization along the bottom rod case, the spectral dependence has two modes of similar intensity at 700nm and 1600nm. Overall, the variation of the transmission spectra with the spacer thickness is negligible for both polarizations of the incident light.

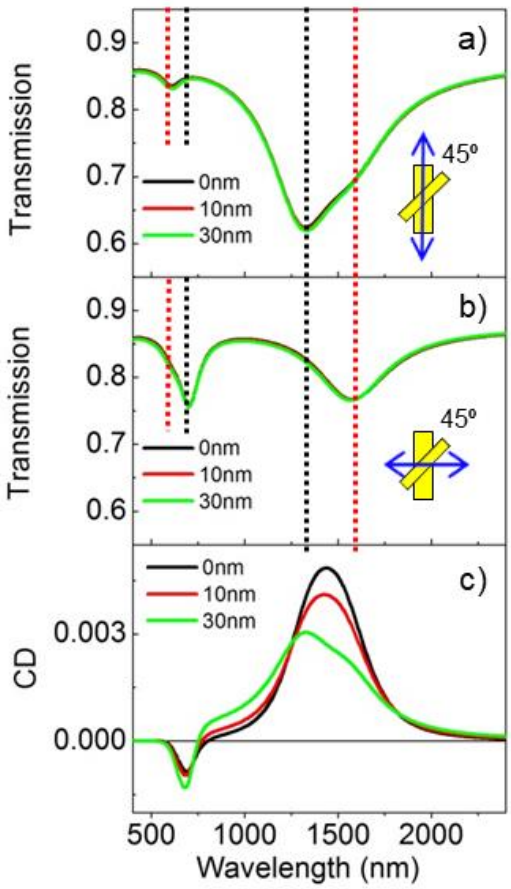

Figure 5.5: Simulated polarized transmission for a stack of two Au rods with a 45º angle as a function of the vertical separation between them for light polarization (a) parallel and (b) perpendicular to the bottom nanorod. c) Vertical separation dependence of the Circular Dichroism (CD) in the nanostructures. Vertical dotted lines correspond to the energetic positions of modes for the individual rods shown in Figure 5.3.

Interestingly the CD clearly varies with the CaF_2 layer thickness Figure 5.5(c). Indeed, an increase of the intensity is observed for the high energy resonance. This intensity variation is also present with opposite sign in the low energy resonance, albeit in this case the intensity change is accompanied by a blueshift from 1400 nm to 1250 nm when the spacer thickness is increased from 10 nm to 30 nm. This behavior indicates that even small variations in the thickness of the dielectric spacer can lead to strong changes in the energy and intensity of the dichroic response of the system, even though the total transmission may remain unaltered.

5.2.3. Optical properties as a function of the relative energy position of the rod resonances

During the previous simulations, the calculations have been carried out using parameters obtained experimentally from the samples containing individual top and bottom nanorods. However, these parameters strongly depend on the dimensions of the nanorods, which can be differ slightly for different fabrication processes. These changes can also affect the spectral position of the resonance modes in the nanorods. To account for this effect, simulations have been performed introducing a gradual energetic tuning/detuning of both high and low energy modes. Figure 5.6 shows the CD spectral data obtained from the simulations of either resonance modes as they are shifted by the indicated amounts. The calculations have been carried out over nanostructures with two Au nanorods separated by a 10 nm dielectric spacer with a relative angle between the nanorods of 45. The 0.0eV dephasing situation curves (orange lines) correspond corresponds to the case for which both the top and bottom nanorods are described by the parameters of the bottom nanorods. Labels indicate the magnitude of the detuning. The progressively increasing detuning energies have been applied only to the position of the resonances of the top nanorod.

Figure 5.6(a) shows the results obtained from the detuning of the low energy mode. Here, the high energy modes are identical and remain unaltered for the two rods, while the low energy modes gradually evolve from a tuned to a detuned situation. For a detuning of -0.12eV, a dramatic effect in the low

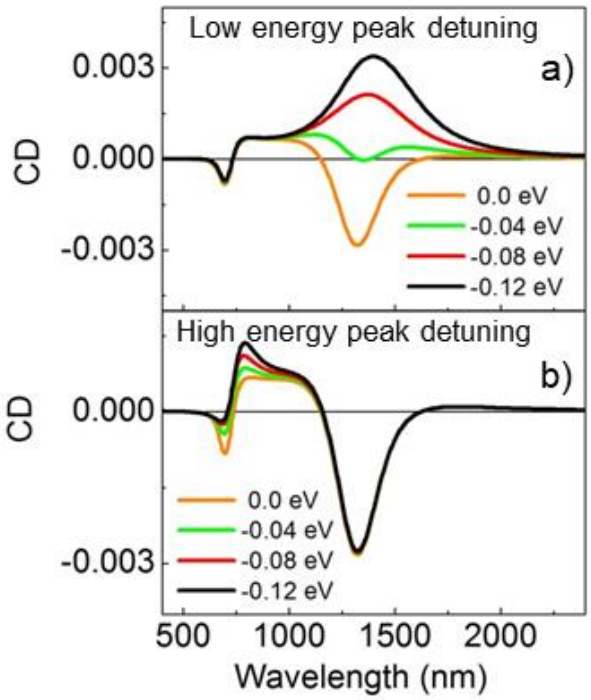

Figure 5.6: Simulated CD for a structure of stacked nanorods with 10 nm vertical spacing and 45º relative angle as a function of the energetic detuning of the a) low energy and b) high energy modes. Bottom rod modes are unaltered and only the energetic position of the top rod modes is modified (zero detuning correspond to bottom and top rods having identical modes).

energy resonance is observed as it evolves from negative to positive intensity and shifts towards lower energies. This is a very interesting result, since it denotes that a change in the CD sign can be obtained in the low energy region by varying the energy detuning of one of the nanorod's modes without changing the configurational disposition of the nanorods. A similar effect, albeit less intense, can be observed if the same detuning is applied on the high energy mode (Figure 5.6(b)). Indeed, for a detuning of -0.12eV, no significant changes are observed in the resulting CD.

5.3. Comparison with fabricated nanostructures

By using a simplified theoretical model for the 3D nanostructures, it has been possible to discover a configuration of Au nanorods and spacer thickness that maximizes the CD signal in the sample. Next, the proposed nanostructures are realized experimentally, taking into account all considerations and results of the preceding sections. Thus, two chiral piled Au nanorod nanostructures, both with a 10nm thick CaF_2 spacer, and similar dimensions to the

nanostructures presented before have been fabricated. One sample has been deposited with a relative angle of -45º. The experimental data obtained from these nanostructures is then compared with the theoretical predictions of the simplified model.

5.3.1. Fabrication of three-dimensional structures

The deposition process used in the fabrication of the chiral stacks of Au nanorods has been described in Figure 5.1. First, two adjacent CaF_2 nanopillars have been deposited by tilting ±5º the substrate surface with respect to the incoming CaF_2 beam, generated by electron beam evaporation (see Figure 5.1(a)). Next, a 45º azimuthal rotation of the substrate and subsequent oscillation about the surface normal enable the deposition of the bottom Au rod between the CaF_2 nanopillars (figure 5.1(b)). The diameter of the hole in the lithography mask determines the width of the nanorod, while the amplitude of the oscillation controls its length with a high level of precision (oscillation angles of Θosc=±5º for nanopillars and Θosc=±20º for nanorods are used)[16].

In order to improve the adhesion of the dielectric pillars and the bottom Au nanorod onto the glass substrate, an intermediate layer of Ti of 3 nm in thickness has been deposited by electron beam evaporation (0.1Å s^{-1} deposition rate). CaF_2 and Ti are deposited by electron beam evaporation (0.5Å s^{-1}), while Au is deposited by thermal evaporation (0.25 Å s^{-1}).

The dielectric nanopillars and the bottom Au nanorod have been deposited with a similar thickness so that the top Au nanorod grows in a horizontal homogeneous fashion on top of the nanostructures underneath. The lateral position of these two pillars with respect to the bottom nanorod has also been selected so that the top Au nanorod will form the desired angle with respect to the bottom nanorod (more details in Chapter 4). As a dielectric spacer, a CaF_2 nanorod has been deposited on top of the bottom Au nanorod following the same method (Figure 5.1(c)). Finally, Figure 5.1(d) shows the deposition of the top Au nanorod with the desired azimuthal rotation (±45º) back to the pillars initial position.

As mentioned in Chapter 3, the gradual diameter reduction of the nanoholes in the mask, due to the accumulation of material in the edges of the hole during deposition at oblique incidences[259], strongly conditions the dimensions

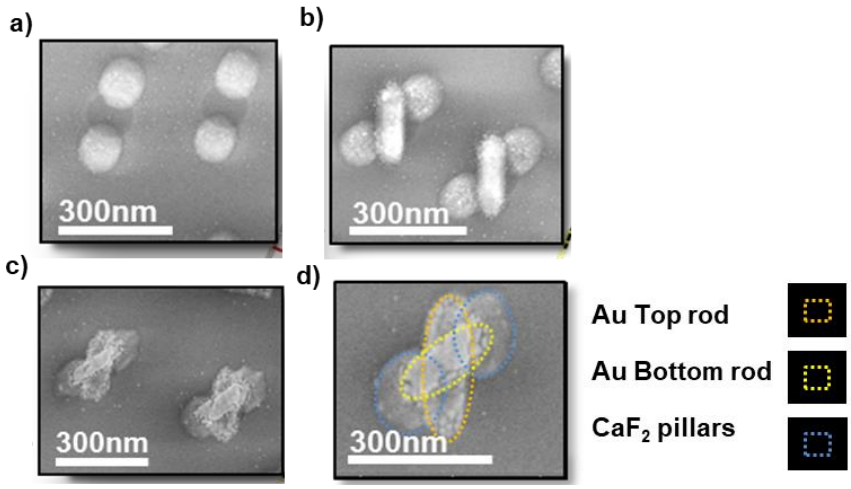

Figure 5.7: SEM images of the intermediate steps during the fabrication process . a) SEM image of the dielectric pillars. b) SEM image of the bottom Au nanorod deposited between the CaF_2 nanopillars. c) SEM image of the CaF_2 spacer nanorod and Au top nanorod at 45^0 with respect to the bottom nanorod. d) SEM image of a complete chiral structure. The main constituents are highlighted by dotted lines (Top nanorod in orange, bottom rod in yellow and dielectric nanopillars in blue).

of the resulting nanostructures. Namely, the final elements in the nanostructures are narrower and, for the same substrate oscillation span, shorter. This gradual hole diameter reduction also limits the total amount of deposited material and, consequently, the final height of the total nanostructure.

Figure 5.7 illustrates with SEM images some of the intermediate steps during the fabrication process of these nanostructures: the dielectric nanopillars (Figure 5.7(a)), the bottom Au nanorod with the dielectric pillars (Figure 5.7(b)), and the final three-dimensional system composed of 2 stacked Au nanorods (Figure 5.7(c)). The main components of these structures are highlighted in Figure 5.7(d). Dotted orange and yellow lines indicate the top and bottom nanorods, respectively; the dotted blue lines enclose the dielectric nanopillars.

5.3.2. Comparison of 3D fabricated and simulated stacks of rods

The final structures to be studied consisted of two Au nanorods vertically stacked and separated by a dielectric spacer. To analyze the optical response of this stacked system, the corresponding individual components (i.e., the bottom rod in direct contact with the substrate and the top nanorod at a given

vertical separation from the substrate) have been fabricated in separated runs and previously studied (section 5.1). The typical individual layer thicknesses used have been, from top to bottom, 15 nm Au, 10 nm CaF_2, 15 nm Au, and 3 nm Ti, with a relative angle between the Au nanorods of 45°.

The optical measurements obtained from these stacked nanorods systems, together with the corresponding theoretical simulations, are presented in Figure 5.8. Figures 5.8 (a-b) show the experimental and theoretical transmission spectra for light linearly polarized parallel (in black) and perpendicular (in red) to the long axis of the bottom nanorod in samples with a 45^o alignment between the nanorods.

It can be observed that there is a reasonable agreement between the data and the simulation for light polarized along the long axis, showing one peak situated in the spectral region of the longitudinal modes of the nanorods. On the other hand, the measured perpendicular spectra slightly differ from the simulation, showing a clear high energy mode, as in the theoretical spectra, and a weaker low energy mode.

The experimental CD spectra for the two samples with 45^o and -45^o angle between the nanorods are presented in Figure 5.8(c). Both spectra have the characteristic low and high energy features with opposite signs upon the reversal of the structure helicity. These experimental results can be compared with the theoretical simulation data for the CD spectra collected in Figure 5.8(d). The low and high energy modes observed in the experimental data are also observed in the CD simulations, which reproduces qualitatively both the sign and the trends. The lack of a more precise matching between theory and the experiments can be attributed to two factors. Firstly, the simplicity of the model used in the simulations does not consider inter-rod interactions, which are an important source of the observed mismatch. Secondly, the model does not take into account any morphological irregularities that may be present in the actual building blocks of the nanostructure. Together, these factors lead to the quantitative differences observed between the optical measurements and the proposed theoretical approach.

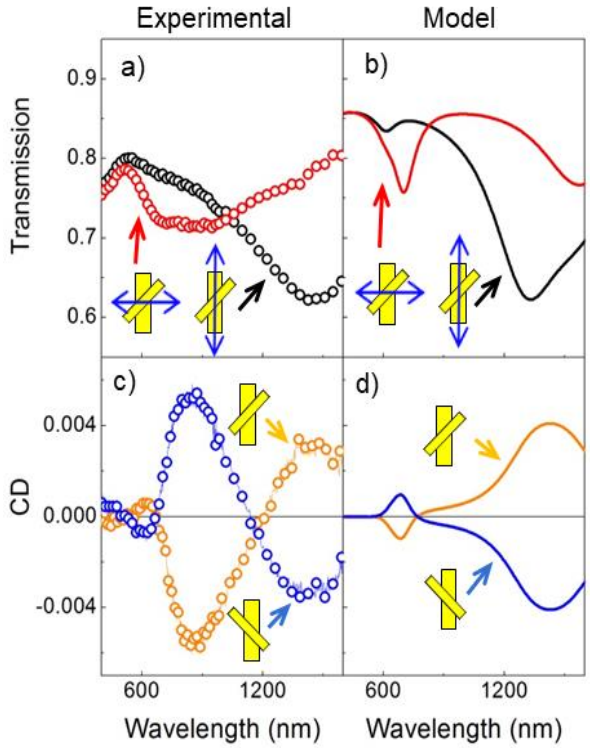

Figure 5.8: a) Experimental polarized transmission for a real nanorod stacks with nominally 45º relative angles and a 10 nm spacer separation. Data for light polarizations along the bottom long/short nanorod axis (black/red circles) are shown. b) Corresponding theoretical transmission data for the same nanorod stacks. c) Experimental CD for two nanorod stacks separated 10 nm and with relative orientations of -45º ((blue circles) and 45º (orange circles) relative orientation. d) Corresponding theoretical CD data for the same samples.

5.4. Chapter Conclusions

Configurations of two stacked Au nanorods have been investigated theoretically as a function of the relative angle between the nanorods, the thickness of the dielectric spacer between them, and possible fluctuations in their resonant energies. Small changes in the thickness can tune the energy and intensity of the CD. The optimized chiro-optical response is found in nanostructures at 45° and a vertical distance at 10nm.

The CD response and transmitted intensity have been also measured in fabricated structures, and compared with the simulations obtained using a simple Lorentz oscillators model, yielding a good qualitative agreement. However, the simplified theoretical model proposed has been demonstrated to lack accuracy on its quantitative predictions for the CD data. Thus, more complete calculations are necessary for a better understanding of the interaction between nanorods and the detailed near field characteristics of the excited modes.

Although simple, it is demonstrated that the basic model allows for a fast and reliable prediction of the overall response of the 3D chiral structures prior to their fabrication.

6. THREE DIMENSIONAL SYSTEMS

In previous chapters, the optical response of different building blocks such as fabricated nanodisks or nanorods have been studied in detail. Then, changes in the optical response because of their in-plane combined arrangement and the interaction between them have been also investigated. Finally, a simple approach has been used to describe the optical response of three-dimensional structures according to parameters such as the vertical spacer or the relative angle between the building blocks, and has been contrasted with experimental data in real structures.

In this final chapter, 3D stacked nanorod dimers are fabricated by multiaxial evaporation through nanohole masks. This permits a complete perspective of the optical response in this kind of systems, considering now also the role of the interactions between the individual building blocks to control both the linear and circular dichroism response. From this approach, the interactions between the building blocks are tuned, and the optical and chirooptical response of stacked nanorods established. The linear dichroic response as well as the optical anisotropy and pure chiral contributions to the circular dichroism are determined, unraveling the role played by interactions between the constituting building blocks. A detailed description of the optical response by the analysis of the Mueller matrix elements of the system, obtained both experimentally and from numerical simulations, is deduced. Finally, the experimental results are compared to a model based on discrete dipoles approximation, providing a more complete understanding of all (sort and long range) electromagnetic interactions between the rods than in the simple approach used in Chapter 5.

6.1. Fabrication

Following the methodology presented in Chapter 5 for the fabrication of three-dimensional nanostructures, a fine control of the relative orientation between the rods and the vertical distance between them in a range of a few tens of nanometers is obtained.

Evaporation of these structures through holes in the HMCL template is performed in multiple steps. Some of them are common to achieve structures with similar dimensions, such as the evaporation with a common oscillation angle (azimuthal angle). However, to acquire structures with a different in-plane angle between the rods, the in the plane rotation of the template during the fabrication process plays an important role, allowing to modify the arrangement in the plane of the dielectric pillars with respect to the axis of the bottom nanorod. It is precisely the control of the multiple axes during fabrication which has allowed obtaining three-dimensional structures with a wide variety of morphologies. In this chapter, stacked nanorod dimers with a range of angles of 45º, -45º and 90º and dielectric thicknesses from 0nm to 10nm are experimentally obtained.

The deposited heights of the different elements of the nanostructure are Au(12nm)//CaF_2(6nm)//Au(12nm)//Ti(3nm)//BK7(0.5mm). The typical width and length for these structures are 95 nm x 235 nm for the bottom rod, and 75 nm x 220 nm for the top rod. The diameter of the CaF_2 pillars are 135nm and 100nm respectively with a similar 20nm thickness.

6.2. Optical properties

As in previous chapters, the optical response of the fabricated structures is characterized with a *spectroscopic ellipsometer* in transmission mode at normal incidence in the 400-1600 nm spectral range.

From the measurements of the *Mueller Matrix Elements* (MME) of the system[178,260], which contain full information about the optical properties of these structures[179,261], the main relevant optical properties of the systems, such as linear dichroism or circular dichroism are acquired .

As schematically indicated in the left of Figure 6.1, in transmission mode, the element m_{12} is directly related to the absorption difference for light that is polarized parallel or perpendicular to the *x-axis* ($m_{12} = (I_X - I_Y)/2$, linear dichroism (LD)). On the other hand, m_{13} is related to the difference in the absorption of light polarized parallel and perpendicular to an axis rotated 45º with respect to the *x-axis, x'-axis*, ($m_{13} = (I_{X'} - I_{Y'})/2$, linear dichroism at 45º (LD')). Finally, m_{14} is related to the difference in absorption for left and right-handed circularly polarized light ($m_{14} = (I_R - I_L)/2$ or circular dichroism (CD)). The MME measured is normalized to the m_{11} element, which gives an overall

transmission; because they do not provide any information about the total optical phase shift of the sample.

It is known that in complex systems, where optical anisotropy and chirality coexist, like those presented in this work, the CD signal has two contributions. It is possible to elucidate their relative weights by carrying out forward and backward experimental measurements, since these two magnitudes behave differently for forward and backward illumination[40]. Therefore, the experimentally measured circular dichroism can be decomposed in the chiral and optical anisotropy components ($CD_{Tot} = CD_{Ch} + CD_{Anis}$) where

$$CD_{Ch} = \frac{(m_{14}^{F} + m_{14}^{B})}{2}$$
$$CD_{Anis} = \frac{(m_{14}^{F} - m_{14}^{B})}{2} \quad (68)$$

6.2.1. Optical properties varying the angle

Changes in the relative position between the two Au nanorods forming the 3-D dimer nanostructure modify the optical response and produce chirooptical response due to break of the in-plane symmetry

For the experimental determination of the MME, the structures are mounted on a rotational stage with the in-plane rotation angle carefully controlled. They are aligned along the *y-axis*, so the long axes of the bottom rod are oriented parallel.

The evolution of the optical response as a function of the relative angle between the rods are presented in Figure 6.1 where the measured MME for three fabricated structures is shown. SEM images for individual structures are presented above the columns with the corresponding results. At the first column, the spectral dependence is determined in the case of a single Au nanorod with CaF_2 pillars symmetrically positioned at both sides of the rod. Subsequently, nanorods dimers oriented at 45° and -45° from each other are shown respectively.

Notice for each nanostructure that the spectral dependence of the linear dichroic response related to the m_{12} (Figures 6.1(a-c)) are very similar with values around 0.2, confirming that the main contribution to the linear dichroism comes from the bottom nanorod. In the case of single nanorods

(Figures 6.1 left column), the y-polarized light excites only the resonance along the principal axis of the rod, which is located at a lower energy than the corresponding for the short axis (which is only excited using x-polarized light). For all the structures, the m_{12} element has a sigmoidal spectral shape with a dip centered at the position of the long axis resonance of the rod and a positive peak at the position of the short axis resonance. Notice as well that the m_{12} intensity is the similar for both 45° and -45° orientations, of the order of 0.15, and it presents a similar shape to the single rod but about 25% less intense.

On the other hand, the m_{13} element related to the LD at 45° manifests a characteristic response according the relative angle between the nanorods in the dimer case with intensities about 0.15.

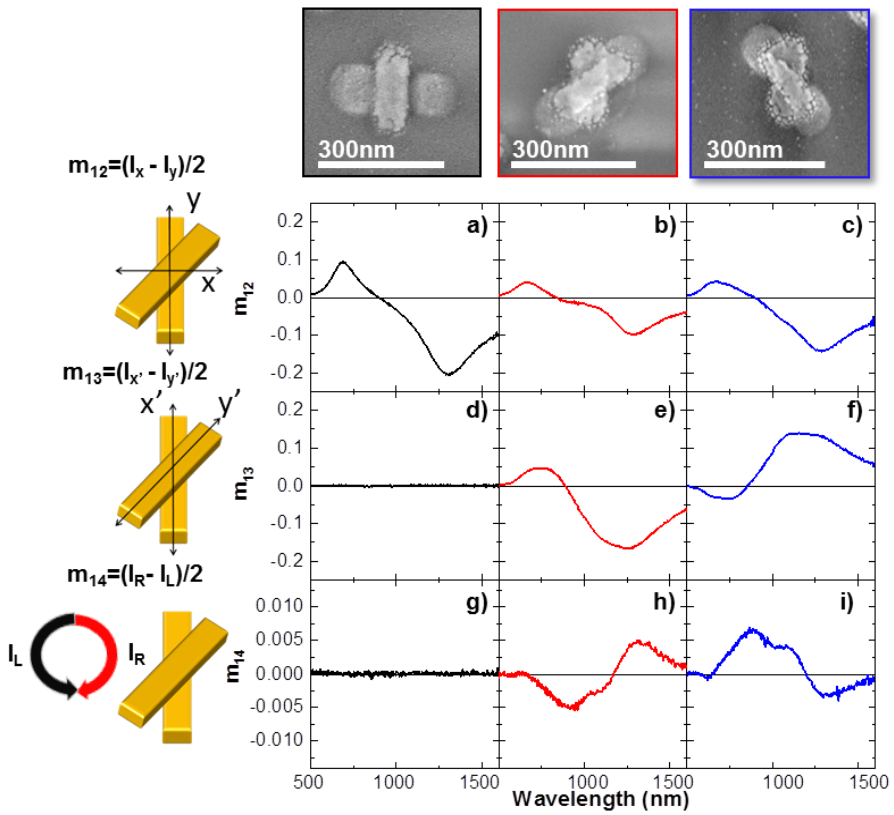

Figure 6.1: Spectral evolution of the optical properties in different metasurfaces with common building blocks. Upper part: SEM images of the different metastructures. Left hand side: schema of the configuration of the axes that define the MME shown. (a-c) Linear dichroism, m_{12} as a function of the rotation of the structure is presented for: single rod with pillars (SR), rod dimers placed at 45° (RD) and rod dimers placed at -45° respectively. (d-f). Linear dichroism at 45º, m_{13}, for SR, RD at 45° and RD at -45°. (g-i) Circular Dichroism, m_{14}.

Three dimensional systems

In the case of single nanorods (Figure 6.1(d)), the light polarized along x' or y' axes excites both long and short axes resonances and therefore, the m_{13} values for all the wavelengths are zero. A similar behavior is observed for the circular dichroism value, m_{14} for these structures (Figure 6.1(g)).

The presence of the top rod in the 3-D structure leads to a non-zero circular dichroism, as a result of the optical excitation of the top rod by the x'-and y'-polarized light. The change of sign of this Mueller matrix element is associated to the relative orientation between the nanorods and allows discerning the handedness of the system (Figure 6.1(e) and Figure 6.1 (f)).

Finally, the circular dichroism, m_{14}, results from the twisted nature of the 3-D structure with magnitudes around 0.005. The change in sign is due to the different twist and is zero in the single nanorod case (Figures 6.1(g-i)).

These results indicate that the presence of the top rod introduces a decrease in the optical symmetry of the system, inducing an additional linear and circular dichroism signal, where the signs depend on the relative alignment between top and bottom nanorods.

To understand better the observed behavior, a complex analysis of the contributions present in the dichroic response is needed. It is worth noticing that it is possible to apply this methodology thanks to the correlated orientation between each other rod provided by the specific fabrication technique[33,176].

The spectral dependence of the m_{14} element for forward and backward illumination is displayed in Figure 6.2 for structures at 45° and -45°. As observed in Figure 6.2(a) vs Figure 6.2(d), there are differences in the spectral dependence for each illumination, which denotes the presence of two distinct contributions. By comparing the spectra of the samples for forward and backward configurations (black and red lines respectively), their mirror images are obtained.

To clarify the nature of the different contributions to the CD in the structures, the intrinsic chirality (CD_{Ch}) (Figure 6.2(b) and Figure 6.2(e)), and the optical anisotropy (CD_{Anis}) (Figure 6.2(c) vs Figure 6.2(f)), are presented. The anisotropic contribution is the linear part of the CD response originating from the combination of the linear optical properties ($CD_{Anis}=1/2(LBLD'-LB'LD$) (more details in Chapter 2). Moreover, this contribution comes from the

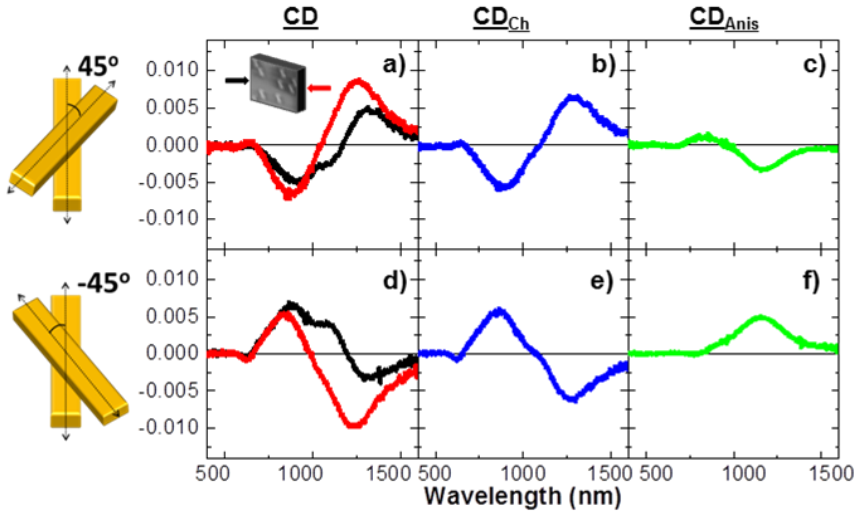

Figure 6.2: The spectral dependence of the m14 element and its contributions for nanorod dimers at 45° and at -45°. Black (red) curves in (a) and (d) represent the spectral responses of m_{14} for the structures in backward (forward) configurations. CD has been separated in its two contributions: chirality depicted as blue curves in (b) and (e) and the optical anisotropy depicted as green curves in (c) and (f). The insets on the left-hand side shows the sketch of the measurement in forward (F) and backward (B) configurations.

anisotropy of the sample by means of the preferential in plane ordering of the structures in the array configuration, as well as effects due to overlapping.

On the other hand, the intrinsic contribution of the linear dichroism or chirality (CD_{Ch}) within the dipolar theory of the plasmon-plasmon interaction have typically a peak-dip shape (*bisignate* shape)[74,262]. This contribution is due to the handedness of the structures and also the interactions or coupling between the rods.

The spectral shape in the chiral contribution has intensities around 0.007 and a sigmoidal like shape, whose sign depend on the relative arrangement of the dimers. However, the optical anisotropy contribution consists of a broad peak whose sign also depends on the twist and the values are around 0.004.

6.2.2. Optical properties varying the dielectric spacer

As the changes in the relative positions between the nanorods generate alterations in the global optical response, the vertical distance between them also modifies their response. In order to explore this fact, structures where the dielectric spacer is varied are fabricated. The dimensions of the metastructures without spacer are 12x95x235nm for the bottom rod and

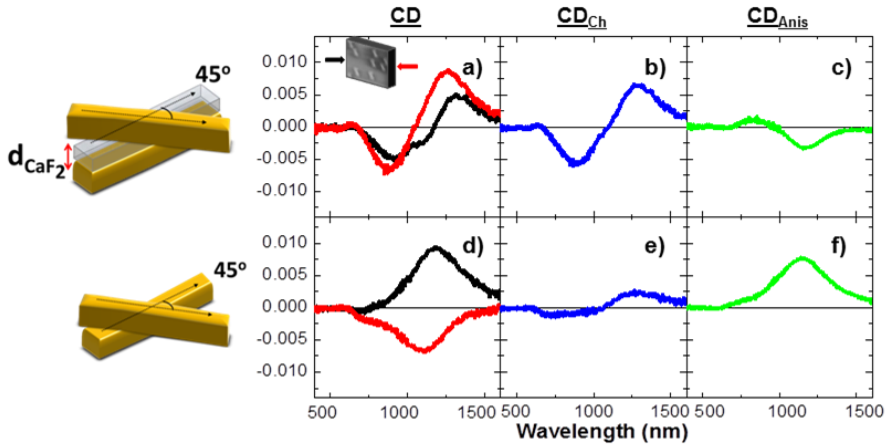

Figure 6.3. Dependence of the dichroic signal as a function of the dielectric spacer for gold rods at 45º. The m14 in forward (F) (black lines) and backward (B) configurations (red lines) is shown in the cases of 6nm and 0nm of dielectric thickness. From the dichroic signal, chirality (blue lines) and optical anisotropy (green lines) are extracted.

12x75x220nm for top rod, while in the presence of the spacer they are 14x99x280nm and 12x80x244nm for the bottom and top rod respectively.

Similar to the previous case, the total and individual contributions of the CD for two similar rod dimer structures with and without a 6nm thick dielectric CaF_2 spacer are shown in Figure 6.3. Regarding the total CD response, the structures present a different behavior: for the structure without dielectric separator, the change in the illumination direction produces a net sign reversal of the m_{14} element (Figure 6.3(d)) with intensities about 0.007, whereas in presence of the dielectric separator this change is less dramatic and the intensity changes rather than the sign (Figure 6.3(a))with similar values of intensity around 0.007. These results can be understood by a coupled dipole model (more details in appendix section 8.2) where the sign and shape of the circular dichroism comes from the interactions between the rods.

For the sake of more complete characterizations, the optical interaction of circularly polarized light with structurally chiral optical antennas results in two independent contributions to the circular dichroism (Figures 6.3(b-f)). The lack of the dielectric layer gives a chiral contribution smaller than in presence of the CaF_2 although in both structures the spectral dependence has a sigmoidal shape with a similar relative sign (Figure 6.3(b) vs Figure 6.3(e)). The difference between the magnitude intensities is around 60% by modifying only 6nm material. On the other hand, the anisotropic contribution CD_{anis}, has the opposite behavior: in structures without the CaF_2 the anisotropic signal

dominates the CD response and it has a peak shape, whereas this contribution is less intense and there is a sign reversal when the dielectric is incorporated (Figure 6.3(c) vs Figure 6.3(f)). The difference between the intensities is approximately 57%. Then, the results obtained corroborate the relevance of the interactions between the nanorods in the final optical response and they show how the pure chiral contribution may be increased. Due to its configurational origin, the relative intensity of the chiral and optical anisotropy contributions depends on the interaction between the rods.

6.3. Numerical Experiments

In order to understand the observed behavior of the stacked nanorod dimers, a complete theoretical calculation using *Finite-Difference Time Domain* (FDTD) method has been performed with Lumerical software[263] by Alba Lucía Jiménez and Dr Antonio García Martín at IMN.

By this simulation method, which takes into account all (short and long range) electromagnetic interactions between the rods[263], it is possible to reproduce the ellipsometric response of the nanorods at a fixed angle at 45° in a chiral arrangement. The dimensions for the simulated structures are based on the experimental fabricated structures and they are 12x95x235nm for the bottom rod and 12x75x220nm for the top rod. The dielectric permittivity of glass (SiO_2) has been obtained from references[256,264] and the dielectric permittivity of gold has been modeled using a Drude-type formula: $\varepsilon = \varepsilon_\infty - \omega_P^2/[2\pi\omega(i\gamma_c + 2\pi\omega)]$, where ε_∞=5.9752, γ_c=3.4629610^{14}rad s^{-1} and ω_p=1.1449510^{16}rad s^{-1}. With just these parameters a very good agreement in the position and broadening of the long axis resonance for the single rods is obtained.

To analyze the role of the interactions in these structures, the circular dichroism spectra has been simulated, studying a set of 3D-systems where the distance between bottom and top rods varies from 6nm edge-to-edge to the planar case where they are fully overlapped. The total CD response is presented in Figure 6.4. Left panels show the evolution of Circular dichroism as a function of the vertical separation between the two rods. Red and black lines represent forward and backward configurations of the measurements,

respectively. This dichroic signal is divided into chiral (central panels) and anisotropic (right panels) components.

When the rods are separated by a 6 nm of dielectric spacer (Figures 6.4(a-c)), the CD presents a sigmoidal shape, similar to the shape of the chiral contribution (Figure 6.4(b)) and has a total intensity around 0.04. Whereas the intensity magnitude is around 0.03 for the chiral contribution, the anisotropic contribution is smaller (of the order of 0.01) (Figure 6.4(c)). This behavior is constant while the distance between the rods is reduced until they are in contact (d=0 nm) (Figures 6.4(d-f)). In this case, the dichroic response signal has a sigmoidal shape for both forward and backward illuminations. Moreover, the chiral response shows a sigmoidal shape with intensities of the

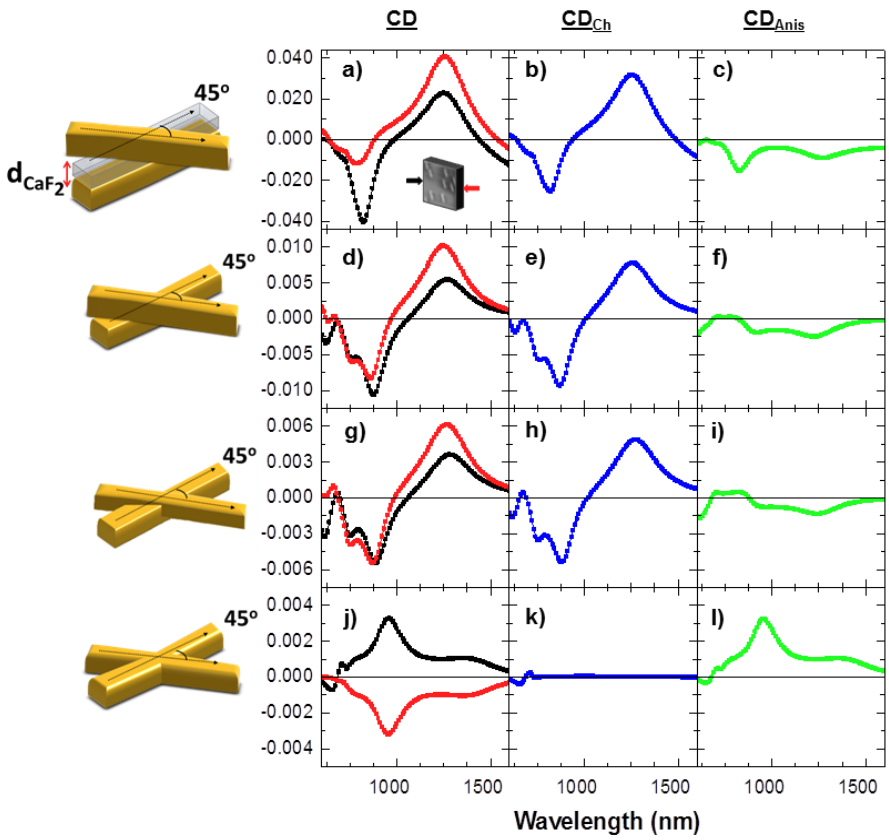

Figure 6.4: Spectral dependence of the simulated MME for a rod dimer at 45º, where the evolution from a CD dominated by the chiral contribution to a CD where anisotropy governs the signal is clearly shown. (a-c) CD, CD_{Ch}, CD_{Anis} respectively, for a 6nm spacer between the bars. (d-f) The same for touching dimers (no spacer). (g-i) Top bar halfway embedded into the bottom bar. (j-l) Fully overlapping rods, leading to a planar structure.

order of 0.007 (Figure 6.4(e)). Figure 6.4(f) presents the anisotropic response with intensities around 0.003. In this case, it is remarkable to point out the reduction in the dichroic response intensity, that varies from $4{\cdot}10^{-2}$ when the rods are separated by the spacer to $4{\cdot}10^{-3}$ when they are in a planar case, changing the response one order of magnitude. As the rods start to overlap, both the CD and its separated components present the same behavior as when they are in contact (Figures 6.4(g-i)), but their intensity is reduced about 60%.

This tendency continues as the nanorods are overlapping until the extreme case where the rods are overlapped and there is a planar situation (Figures 6.4(j-l)). Here the CD response is totally opposite for backward and forward illuminations (Figure 6.4(j)). Moreover, the chiral contribution changes when the structure is planar, and it is almost zero. In contrast, the anisotropic contribution has an inverse behavior in comparison to the chiral contribution, being more relevant in the planar case with magnitude intensities of the order of 0.003 (Figure 6.4(l)). These results are in line with similar structures where the system is planar and geometry considerations advise to expect a mostly vanishing chiral contribution. Thus, the signal should go from a CD dominated by the chiral contribution to be fully governed by anisotropy, since the spectral overlap of the hybrid resonances decreases as the distance is reduced [105,106]. Figure 6.4 shows the overall quantitative reduction of the CD as the distance between the dimers decreases, being almost zero chiral signal in the planar nanostructure. It is worth noticing that, since in the modeling all interfaces are crisp and defect free, the chiral contribution keeps governing the CD down close to the planar case.

In the experimental case, the spacer free system already shows an almost vanishing chiral contribution, which may be attributed to the natural fabrication constrains, such as porosity, misalignments (especially in the height of the auxiliary pillars) that largely affects chirality and tends to increase anisotropy.

Finally, the chiral response of these structures has been compared with other chiral nanostructures fabricated with similar materials and measurement configurations[130,199] through the anisotropy factor or *g-factor* (more details in chapter 2). From the transmission values $T{\approx}0.78$ and the chiral experimental maximum (CD_{Ch}) around 0.008 in the gold dimers at 45, the maximum anisotropy factor is in the order of $g_{max}{=}{\pm}0.058$. Chiral structures composed of

pillars and nanorings with similar composition and the same fabrication and characterization methods give similar range of values g_{max}=±0.03 at the same wavelengths[40]. Moreover, nanorods dimers fabricated by chemical methods exhibit lower values of the anisotropy factor than in structures fabricated with HMCL with multiaxial evaporation, with values from the range of 10^{-3} in nanorod dimers[135,213] to a maximum value g_{max} around 0.02 in helical arrangements of 9 nanorods[80]. Then, the range of *g*-factor values in the nanostructures described here validate the interest in applications as chiral devices.

6.4. Chapter Conclusions

The influence of structural parameters, like vertical distance or in-plane angle between elements, in the chirooptical properties has been studied through the fabrication and a numerical model of three-dimensional Au nanorod dimers. The CD response can be modified by changing the in-plane angle between the rods, obtaining maxima values around $8 \cdot 10^{-3}$ at ±45º. Significant changes in the CD intensity (of the order of 72%) are experimentally obtained by modifying the thickness of the dielectric spacer by just 6nm. Moreover, the role of the contributions to the total CD response is evaluated, being more relevant the chirality than the anisotropy as the thickness increases (of the order of 66%). By FDTD numerical simulations a better understanding of CD responses of the nanostructures is obtained. The CD response decreases intensity about 90% as the separated nanostructures are brought to the planar configuration. According to the vertical distance, the main contribution to the total CD response changes from the planar case where is mainly anisotropy (chirality nearly zero) to the separated structures where both anisotropy and chirality have importance.

Three dimensional systems

7. CONCLUSIONS

Different strategies to manipulate light-matter interaction have been explored fabricating, characterizing and modelling active chiral and achiral nanostructures. The goal has been advancing towards their functionalization in novel device concepts for future plasmonic electronics, merging photonics and electronics at nanoscale dimensions. Two different routes have been presented: coupling of plasmonic building blocks to obtain chirality driven by the spatial arrangement, and the introduction of ferromagnetic materials to produce a magnetooptical response controlled by magnetic fields. The main results are:

The possibility of engineering *Localized Surface Plasmon Resonances* (LSPR) in the visible and infrared spectral range, as a strategy to manipulate the optical response at nanoscale, has been demonstrated. These plasmonic structures consist on nanodisk dimers and nanorods made of Au, CaF_2 and Au/Co multilayers, whose LSPR positions can be controlled up to hundreds of nanometers through structural parameters. Changes in the deposition angle and/or time during the fabrication produce spectral shifts in the LSPR positions. In addition, there is a strong dependence of the resonance amplitude and wavelength on the thickness of the nanostructures. For both transverse and longitudinal polarizations, the transmission peaks blue-shift and broaden as the thickness increases. Non-significant perturbations are found in the optical response of the structures when a dielectric layer of CaF_2 is incorporated in the structure. The sensitivity of these structures to small variations in shape or surrounding environment validates the application as plasmonic rulers or sensors of biological molecules.

Two dimensional structures, where disk dimers are placed at different angles, and of different electronic structure with respect to a central rod, are fabricated. The CD when the dimers are dielectric is 30% with respect to the metallic dimer case. This demonstrates the environmental sensitivity to the electrical local landscape due in one case to modifications of the rod resonance and in the other to plasmon-plasmon interactions. This CD appears only when the dimers are at $\pm 45^{o}$. The incorporation of a magnetic material to the central rod introduces a magnetic contribution to this CD. This MCD varies

proportionally with the applied field, peaks at 1185nm, and it is about 10% of the non-magnetic CD at magnetic saturation.

Three dimensional nanostructures where the rod dimers are placed at ±45 ^{o} and separated by a 10 nm dielectric layer are designed and fabricated. These structures validate a very simple Lorentz oscillators model, obtaining a reasonable agreement with the measured circular dichroism. According to this model, small changes in the thickness of the dielectric separator (up to 30nm) can tune the spectral CD peak position up to 200nm. However, this theoretical model is not capable to predict with accuracy the quantitative values of the CD signal. This basic model, however, allows for a fast and reliable prediction of the overall expected response of fabricated 3D chiral structures, although it is not precise quantitatively due to the absence of near field interactions between the rods in the model. When a more detailed model, which considers the interactions between nanorods, is used, a much better agreement is found. This is proved by fabricating and characterizing Au nanorod dimers helically stacked. The dependence of the linear and circular dichroism to modifications in the structural properties demonstrates an increase of the circular dichroism (up to 1 order of magnitude) with the thickness of the dielectric separator. By a careful analysis of the Mueller Matrix Elements and dedicated FDTD numerical simulations, it is shown that there is a nearly proportional increase of the chiral contribution (magnitudes from 0 to 0.003), and a dramatic change of the anisotropic part (from values around 0.003 to 0.02), when departing from the planar situation. These findings highlight that the contributions to circular dichroism can be controlled by carefully acting on the morphology.

Conclusions

8. APPENDIX

8.1. Theoretical oscillator models

To characterize the optical properties of three-dimensional structures by using a simple theoretical approach, there are different approximations depending on the material and the wavelength range considered[165]. The Drude model is typically used for free-carrier absorption of metallic materials in the visible and infrared range. The Lorentz model is used for electric polarization in the visible/UV range and the Cauchy model uses an empirical relationship between the wavelength of the light and the refractive index of a transparent material. In the three-dimensional systems analyzed during this thesis, the simplest model used to characterize the optical properties is formed by multilayers. Anisotropic layers composed of Lorentzian oscillators represent each individual nanorod and the isotropic layer defined by a Cauchy model contains the optical constants of the glass substrate (Chapter 5).

8.1.1. Lorentz model

Lorentz model assumes the nucleus of the atom is much more massive than the electron, so the movement of the electron can be described as if it was a spring connected to an infinite mass, which does not move. The approximation that the binding force behaves like a spring is justified for small displacements. In this scheme, electrons vibrate like a damped harmonic oscillator in presence of an electromagnetic field like:

$$E = E_0 e^{i\omega t} \tag{69}$$

Assuming that the electron behaves like oscillating into a viscous fluid with a damping coefficient T and a restoring force between it and the nucleus, the electron movement can be described using Newton's second law:

$$m_e \frac{d^2x}{dt^2} = -m_e T \frac{dx}{dt} - m_e \omega_0^2 x - eE_0 e^{i\omega t} \tag{70}$$

where e and m_e are the electron's charge and mass, respectively, and ω_0 is the resonant frequency. The first term of the equation describes the viscous force, which is proportional to the electron speed, the second term is the restoring force, and the third term is the driving force due to the electric field. The solution of the equation has the form:

$$x(t) = ae^{i\omega t} \tag{71}$$

with

$$a = -\frac{eE_0}{m_e}\frac{1}{(\omega_0^2 - \omega^2) + iT\omega} \tag{72}$$

the dielectric polarization in the material can be expressed as:

$$P = -eN_e x(t) \tag{73}$$

Therefore, dielectric constant of the material can be defined as:

$$\varepsilon = 1 + \frac{P}{\varepsilon_0 E} = 1 + \frac{e^2 N_e}{\varepsilon_0 m_e}\frac{1}{(\omega_0^2 - \omega^2) + iT\omega} \tag{74}$$

being ε_0 the vacuum dielectric constant. This equation can be expressed as a function of the photon energy instead of frequency:

$$\varepsilon = 1 + \sum_j \frac{A_j}{E_{n_{0j}}^2 - E_n^2 + iT_j En} \tag{75}$$

with *En* the photon energy. Here, the dielectric function is described as a sum of a number j of oscillators where E_n is the resonant energy, T_j the damping coefficient and A_j the strength of the *j* oscillator.

8.1.2. Cauchy model

The Cauchy model corresponds to a wavelength range where the imaginary part of ε is close to zero in the Lorentz model. It can be derived by assuming $T \to 0$ at low ω ($<<\omega_0$). With these considerations, the equation can be written as:

$$\varepsilon' = n^2 = A + \sum_j \frac{B_j \lambda^2}{\lambda^2 - \lambda_{0j}^2} \tag{76}$$

where $\frac{\lambda}{2\pi} = \frac{c}{\omega}$, and $\lambda_0 = \frac{2\pi c}{\omega_0}$

This is known as the Sellmeier model. The Cauchy model is obtained from the series expansion of the previous equation:

$$n = A + \frac{B}{\lambda^2} + \frac{C}{\lambda^4} + \cdots \tag{77}$$

This model is commonly used in transparent materials and it is useful for our glass substrate for modelling the BK7 material.

8.2. Optical response of dielectric disk dimers

The characterization of the optical response of CaF_2 disk dimers is carried out by spectroscopic ellipsometry. No optical response is observed in these dielectric structures.

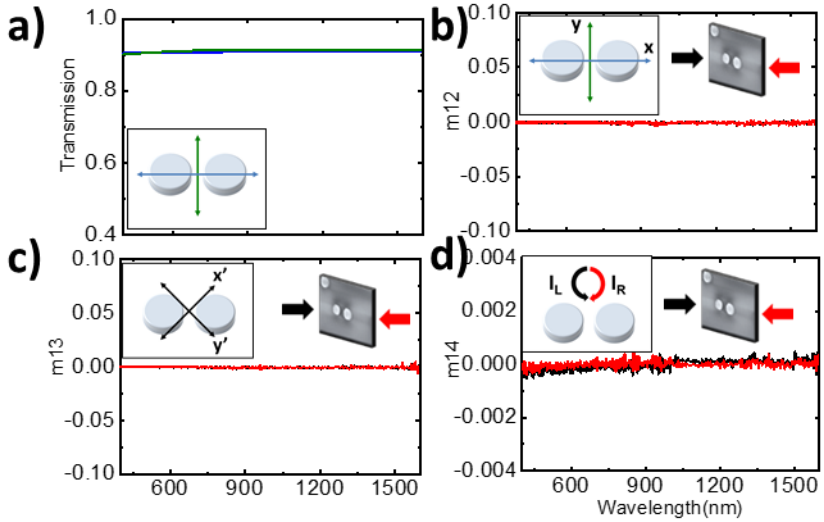

Figure 8.2.1: Optical response of dielectric disk dimers. (a) Transmission spectra along and transverse the long axis of the dimer.(b-d) Mueller matrix elements in forward(black lines) and backward(red lines) configurations.

8.3. Analysis of the heights of hybrid structures

In hybrid structures, the optical properties are influenced by the dimensions and the in-plane ordering of each element which composed the structure. By analyzing the AFM profiles, the overlap between the discs and the nanorod is measured. This effect can clearly influence the response of the structures, becoming a source of anisotropy. In this appendix the profiles of the samples presented in Chapter 4 are reviewed.

8.3.1. Non-ferromagnetic nanohybrids

The AFM images of structures composed by Au nanorods and Au or CaF_2 disk dimers are shown in Figure 8.3.1.

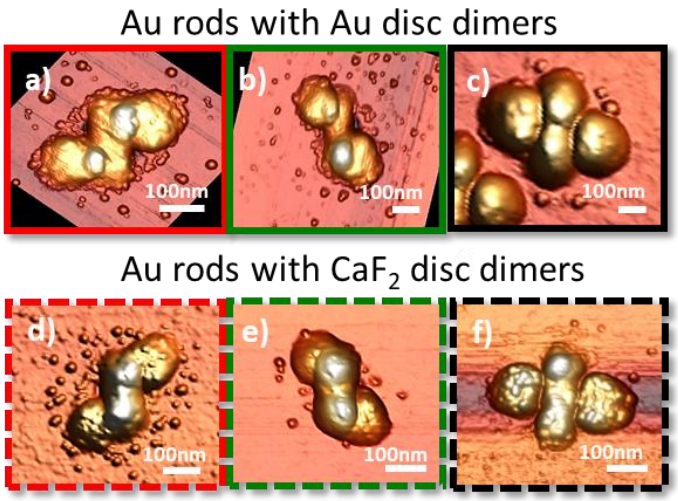

Figure 8.3.1 AFM images of nanohybrid structures with gold dimers (a-c) and dielectric dimers of CaF_2 (d-f). For both structures the nanorods are made of multilayers with gold and the dimers are at 45º (a-d), -45º (b-e) and 90º (c-f).

These structures show areas where the material overlaps, producing a difference in height measured in AFM of up to 30nm.

The AFM height profile of one nanohybrid structure with an Au rod and Au disk dimers at 45 degrees is presented in Figure 8.3.2. The profiles of each building block of this nanostructure show average heights of 25nm for each Au nanodisk and 20nm for the Au nanorod. However, there are overlapped areas where the material is piled up and the height increases up to 30nm.The height of these overlapping areas is ΔH, and this factor depends on fabrication parameters such as the oscillation angle or the deposition time.

Appendix

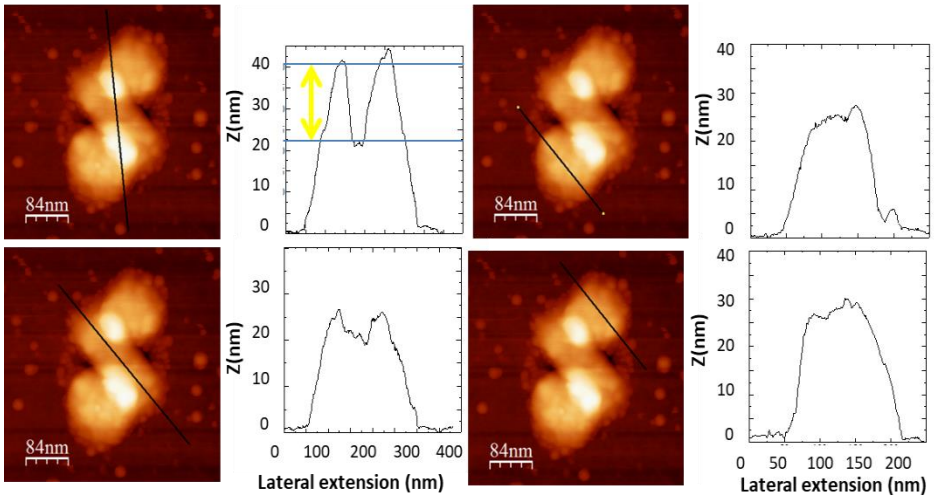

Figure 8.3.2 AFM images and AFM profiles of each building block of a nanohybrid structure with gold disk dimers and Au nanorod (a) The overlapped areas and the difference of height between the nanorod and these points (b-d)AFM profile of each nanodisk(c) AFM profile of the nanorod.

In order to study this overlapping, the present table introduces the difference of heights in the hybrid structures composed by the Au rod and the nanodisk dimers at different positions (45, -45 and 90 degrees):

	ΔH(nm) +45°	**ΔH(nm) -45°**	**ΔH(nm) 90°**
Au	20	30	0
CaF_2	5	10	0

Table 8.3.1 Table with the difference of height or an average overlapping area (ΔH) for non-ferromagnetic nanohybrid structures.

The table is divided into three columns and two rows according the arrangement of the disk dimers with respect the rod and the material of the disk dimers, respectively. As seen in table, the dielectric nature of the material is important in the overlapping areas, obtaining less overlapping in the case of CaF_2 disk dimers. Moreover, the overlapping is produced when the disk dimers are at +45 and -45 degrees.

8.3.2. Ferromagnetic nanohybrids

As in the case of structures where the nanorod is fabricated of a noble metal (gold), the relation between the heights obtained by AFM images are studied. The profiles show structures where the discs overlap with the rods, generating areas with higher heights.

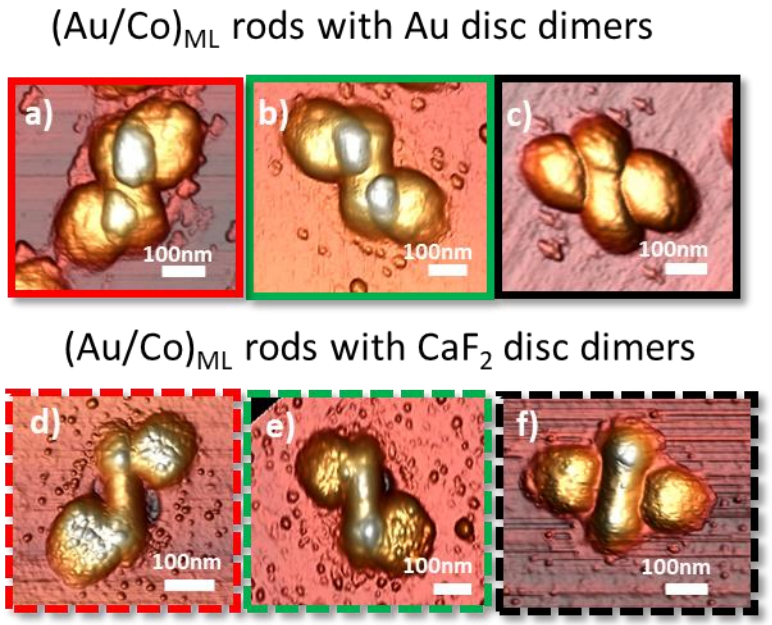

Figure 8.3.3 AFM images of nanohybrid structures with gold disk dimers (a-c) and dielectric disk dimers of CaF_2 (d-f). For both structures the nanorods are made of multilayers with cobalt and gold and the dimers are at 45º (a-d), -45º (b-e) and 90º (c-f).

The overlapping parameter in these ferromagnetic nanohybrid structures is shown in table 8.3.2.

	ΔH(nm) +45°	ΔH(nm) -45°	ΔH(nm) 90°
Au	25	20	0
CaF_2	5	5	0

Table 8.3.2 Table with the difference of height or an average overlapping area (ΔH) for ferromagnetic nanohybrid structures.

As in the case of structures without ferromagnetic material, the overlap of material is higher in the gold dimers than for the dielectric dimers, also the

position of the disks at the 45 and -45 angles produces the stacking of the material. However, the structures with disks at 90 degrees do not exhibit the overlapping areas of the material.

8.4. Dipole approximation model for three-dimensional stacked nanorods

To describe the three-dimensional structures, a coupled dipole model, based in the dipole-dipole interaction mechanism is used[76,139,262]. In this model the system is idealized as two dipoles ($\mathbf{p_1}$ and $\mathbf{p_2}$) oriented along the long axis of each nanorod. When light passes through the structures, each dipole radiates an electromagnetic field which interacts with the other dipoles. This interaction between dipoles is related to the energy separating (V_{12}) the energy levels into new two hybridization modes (symmetric (ω_+) and antisymmetric (ω_-) modes).

$$V_{12} = \frac{p_1 p_2}{n r_{12}^3}(\hat{\boldsymbol{e}}_1 \cdot \hat{\boldsymbol{e}}_2 - 3(\hat{\boldsymbol{e}}_1 \cdot \hat{\boldsymbol{e}}_{12})(\hat{\boldsymbol{e}}_2 \cdot \hat{\boldsymbol{e}}_{12})) \qquad (78)$$

Where $\boldsymbol{r_{12}}$ is the vector joining the dipoles, is $\hat{\mathbf{e}}_{1,2}=\mathbf{p}_{1,2}/\|\mathbf{p}_{1,2}\|$ and $\hat{\mathbf{e}}_{1,2}=\mathbf{r}_{12}/\|\mathbf{r}_{12}\|$. The circular dichroism of these structures is the sum of the extinction bands associated to each hybrid mode.

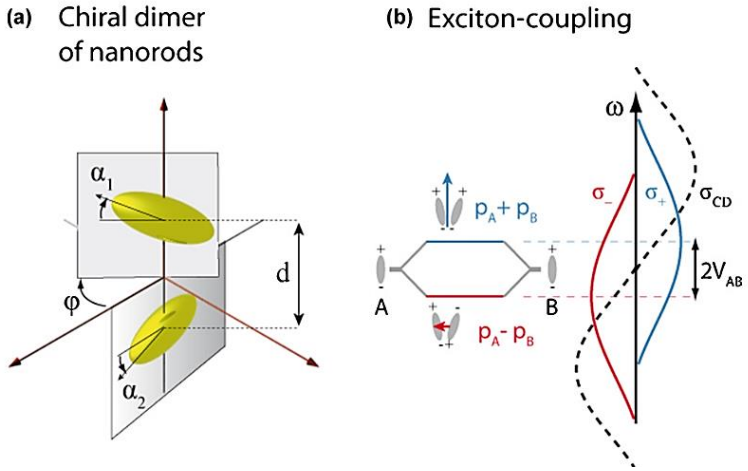

Figure 8.4.1: Schematic representation of a three-dimensional structure of gold nanorods. (b) Illustration of the hybridization of the plasmonic modes of two identical dipoles pA and pB, and the circular dichroism spectrum formed according to exciton-coupling theory. Adapted from Ref. [262].

The sign and the strength of this response is described by the rotational strength *R*, where the electric and magnetic dipole moments.

$$R = \frac{\pi}{2\lambda_0} \boldsymbol{r}_{12} \cdot (\boldsymbol{p}_1 \mathrm{x}\, \boldsymbol{p}_2) \tag{79}$$

Where λ_o is the wavelength of the uncoupled LSPR. The *bisignate* line shape of the CD spectrum has its origin from these hybrid bands and the sign is given by the dihedral angle φ. This rotational strength is optimized when $\boldsymbol{r}_{12}$ and $\boldsymbol{p}_1 x \boldsymbol{p}_2$ are parallel. however, the structure is achiral when $\boldsymbol{p}_1$ is perpendicular to $\boldsymbol{p}_2$ and the modes are degenerated ($V_{12}=0$)[262].

8.5. Evolution of the MME with the in-plane rotation angle

Figure 8.5.1 shows the evolution of the elements m_{12}, m_{13} and m_{14} according to the rotation within the sample plane for different structures. In the first column, the response of a single gold rod with two dielectric discs is studied. The m_{12} element signal has a maximum value at 0 degrees and a minimum value at 45 degrees. Element m_{13} has an inverse behaviour to element m_{12}, being a minimum at 0 degrees and a maximum at 45 degrees. In this structure the m_{14} remains unchanged with respect to the angle with a value of zero.

In the case of the structure formed by a cross of nanorods placed at 90 degrees, the elements m_{12} and m_{13} should be zero at 0 degrees. However, experimentally non-zero values are obtained (with intensities around 0.01). This can be understood because of small fabrication differences, producing non- identical nanorods and therefore m_{12} and m_{13} give us information about dimension differences. The element m_{14} should be zero, experimentally finding a value almost zero.

Finally, the analysis of the m_{14} in a chiral structure of gold dimers at -45 degrees gives information about the evolution of the constant value regardless the in-plane rotation angle. Moreover, the m_{12} and m_{13} elements have similar values to the obtained in the single rod.

To conclude, the figure displays the dependence of the MME for different structures, and how the in-plane optical anisotropies such as the linear dichroism present an angular dependence which force to orient the

nanostructure in the plane with respect to the illumination source. The element m_{14} related to the chirality of the structure is independent of the in plane rotation angle.

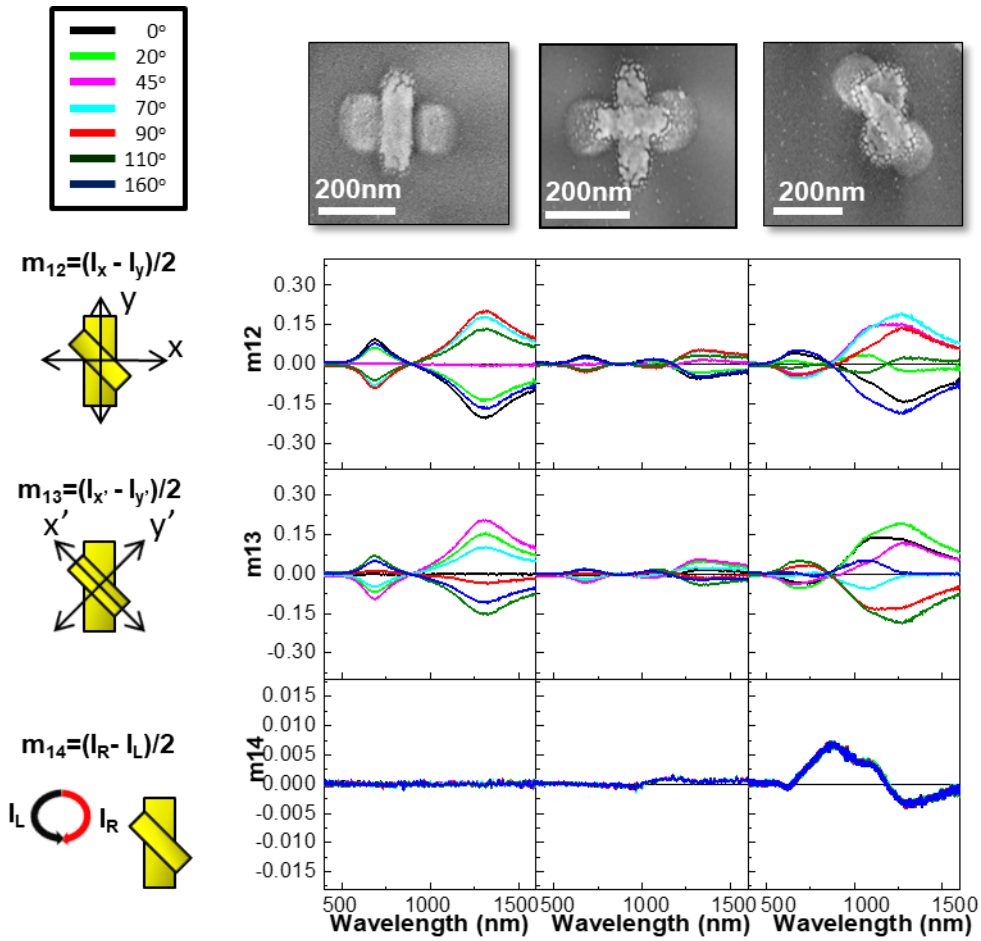

Figure 8.5.1. Experimental evolution of the MME(m_{12},m_{13} and m_{14}) according the in-plane rotation angle in three of gold nanorods (left panel) and dimer structures at 90 (central panel) and at 45(right panel).The rotation angle varies from 0 to 160 degrees (0,20,45,70,90,110 and 160 degrees).

Appendix

9. BIBLIOGRAPHY

1. Maier, S. A. *Plasmonics: Fundamentals and Applications*. *springer* (Springer Berlin Heidelberg, 2007). doi:10.1088/1751-8113/44/8/085201

2. Mejía-Salazar, J. R. & Oliveira, O. N. Plasmonic Biosensing. *Chem. Rev.* **118**, 10617–10625 (2018).

3. Kelly, K. L., Coronado, E., Zhao, L. L. & Schatz, G. C. The Optical Properties of Metal Nanoparticles: The Influence of Size, Shape, and Dielectric Environment. *J. Phys. Chem. B* **107**, 668–677 (2003).

4. Hecht, E. *Optics*. (1997). doi:10.1063/1.3068822

5. Kumar, J. & Liz-Marzán, L. M. Recent Advances in Chiral Plasmonics — Towards Biomedical Applications. *Bull. Chem. Soc. Jpn.* **92**, 30–37 (2019).

6. Lee, Y. Y., Kim, R. M., Im, S. W., Balamurugan, M. & Nam, K. T. Plasmonic metamaterials for chiral sensing applications. *Nanoscale* **12**, 58–66 (2020).

7. Jung, J., Park, H., Park, J., Chang, T. & Shin, J. Broadband metamaterials and metasurfaces: a review from the perspectives of materials and devices. *Nanophotonics* **9**, 3165–3196 (2020).

8. Shalaev, V. M. Optical negative-index metamaterials. *Nat. Photonics* **1**, 41–48 (2007).

9. Smith, D. R., Pendry, J. B. & Wiltshire, M. C. K. Metamaterials and negative refractive index. *Science (80-.).* **305**, 788–792 (2004).

10. Shalaev, V. M. *et al.* Negative index of refraction in optical metamaterials. *Opt. Lett.* **30**, 3356 (2005).

11. Pendry, J. B., Holden, A. J., Robbins, D. J. & Stewart, W. J. Magnetism from conductors and enhanced nonlinear phenomena. *IEEE Trans. Microw. Theory Tech.* **47**, 2075–2084 (1999).

12. Chen, P.-Y. & Alù, A. Subwavelength Imaging Using Phase-Conjugating Nonlinear Nanoantenna Arrays. *Nano Lett.* **11**, 5514–5518 (2011).

13. Alù, A. Mantle cloak: Invisibility induced by a surface. *Phys. Rev. B* **80**, 245115 (2009).

14. Aigouy, L. *et al.* Strong near-field optical localization on an array of gold nanodisks. *J. Appl. Phys.* **110**, 1–5 (2011).

15. Sepúlveda, B., González-Díaz, J. B., García-Martín, A., Lechuga, L. M. & Armelles, G. Plasmon-induced magneto-optical activity in nanosized gold disks. *Phys. Rev. Lett.* **104**, 147401 (2010).

Bibliography

16. Armelles, G., Cebollada, A., García, F., García-Martín, A. & de Sousa, N. Far- and Near-Field Broad-Band Magneto-Optical Functionalities Using Magnetoplasmonic Nanorods. *ACS Photonics* **3**, 2427–2433 (2016).

17. Querejeta-Fernández, A., Chauve, G., Methot, M., Bouchard, J. & Kumacheva, E. Chiral Plasmonic Films Formed by Gold Nanorods and Cellulose Nanocrystals. *J. Am. Chem. Soc.* **136**, 4788–4793 (2014).

18. Vigderman, L., Khanal, B. P. & Zubarev, E. R. Functional Gold Nanorods: Synthesis, Self-Assembly, and Sensing Applications. *Adv. Mater.* **24**, 4811–4841 (2012).

19. Feng, H. Y. *et al.* Magnetoplasmonic nanorings as novel architectures with tunable magneto-optical activity in wide wavelength ranges. *Adv. Opt. Mater.* **2**, 612–617 (2014).

20. Feng, H. Y. *et al.* Active magnetoplasmonic split-ring/ring nanoantennas. *Nanoscale* **9**, 37–44 (2017).

21. Duan, X., Yue, S. & Liu, N. Understanding complex chiral plasmonics. *Nanoscale* **7**, 17237–17243 (2015).

22. Maier, S. A. *Plasmonics: Fundamentals and Applications*. *book* (Springer US, 2007). doi:10.1007/0-387-37825-1

23. Xu, H., Bjerneld, E. J., Käll, M. & Börjesson, L. Spectroscopy of Single Hemoglobin Molecules by Surface Enhanced Raman Scattering. *Phys. Rev. Lett.* **83**, 4357–4360 (1999).

24. Kucsko, G. *et al.* Nanometre-scale thermometry in a living cell. *Nature* **500**, 54–58 (2013).

25. Atwater, H. A. & Polman, A. Plasmonics for improved photovoltaic devices. *Nat. Mater.* **9**, 205–213 (2010).

26. Hentschel, M., Schäferling, M., Duan, X., Giessen, H. & Liu, N. Chiral plasmonics. *Sci. Adv.* **3**, e1602735 (2017).

27. W.T. Kelvin, B. *Lectures on Molecular Dynamics and the Wave Theory ofLight (CJ Clay and Sons, London, 1904)*. (Johns Hopkins university, 1904).

28. Schäferling, M. Chirality in Nature and Science. in *Springer Series in Optical Sciences* **205**, 5–42 (2017).

29. Tang, Z. T. *Chiral Nanomaterials: Preparation, Properties and Applications*. *book* (Wiley-VCH Verlag GmbH & Co. KGaA, 2018). doi:10.1002/9783527682782

30. Papakostas, A. *et al.* Optical Manifestations of Planar Chirality. *Phys. Rev. Lett.* **90**, 4 (2003).

31. Plum, E. *et al.* Metamaterials: Optical activity without chirality. *Phys. Rev. Lett.* **102**, 1–4 (2009).

32. Kuwata-Gonokami, M. *et al.* Giant optical activity in quasi-two-dimensional planar nanostructures. *Phys. Rev. Lett.* **95**, 1–4 (2005).

Bibliography

33. Menzel, C. *et al.* Asymmetric Transmission of Linearly Polarized Light at Optical Metamaterials. *Phys. Rev. Lett.* **104**, 253902 (2010).

34. Hendry, E. *et al.* Ultrasensitive detection and characterization of biomolecules using superchiral fields. *Nat. Nanotechnol.* **5**, 783–787 (2010).

35. Tang, Y. & Cohen, A. E. Enhanced Enantioselectivity in Excitation of Chiral Molecules by Superchiral Light. *Science (80-.).* **332**, 333–336 (2011).

36. Tang, Y. & Cohen, A. E. Optical Chirality and Its Interaction with Matter. *Phys. Rev. Lett.* **104**, 163901 (2010).

37. Agranat, I., Caner, H. & Caldwell, J. Putting chirality to work: The strategy of chiral switches. *Nat. Rev. Drug Discov.* **1**, 753–768 (2002).

38. Urban, M. J. *et al.* Chiral Plasmonic Nanostructures Enabled by Bottom-Up Approaches. *Annu. Rev. Phys. Chem.* **70**, 275–299 (2019).

39. Zubritskaya, I., Maccaferri, N., Inchausti Ezeiza, X., Vavassori, P. & Dmitriev, A. Magnetic Control of the Chiroptical Plasmonic Surfaces. *Nano Lett.* **18**, 302–307 (2018).

40. Feng, H. Y., de Dios, C., García, F., Cebollada, A. & Armelles, G. Analysis and magnetic modulation of chiro-optical properties in anisotropic chiral and magneto-chiral plasmonic systems. *Opt. Express* **25**, 31045–31055 (2017).

41. Maccaferri, N. *et al.* Nanoscale magnetophotonics. *J. Appl. Phys.* **127**, 080903 (2020).

42. Shahbazyan, T. V. & Stockman, M. I. *Plasmonics: Theory and Applications*. *Plasmonics: Theory and Applications* **15**, (Springer Netherlands, 2013).

43. Wood, R. W. On a Remarkable Case of Uneven Distribution of Light in a Diffraction Grating Spectrum. *Proc. Phys. Soc. London* **18**, 269–275 (1902).

44. J. C. Maxwell Garnett. XII. Colours in metal glasses and in metallic films. *Philos. Trans. R. Soc. London. Ser. A, Contain. Pap. a Math. or Phys. Character* **203**, 385–420 (1904).

45. Mie, G. Beiträge zur Optik trüber Medien, speziell kolloidaler Metallösungen. *Ann. Phys.* **330**, 377–445 (1908).

46. R. H. Ritchie. Plasma Losses by Fast Electrons in Thin Films. *Phys. Rev.* **106 N.5**, 8 (1956).

47. Pines, D. Collective Energy Losses in Solids. *Rev. Mod. Phys.* **28**, 184–198 (1956).

48. Kretschmann, E. & Raether, H. Notizen: Radiative Decay of Non Radiative Surface Plasmons Excited by Light. *Zeitschrift für Naturforsch. A* **23**, 2135–2136 (1968).

49. Otto, A. Excitation of nonradiative surface plasma waves in silver by the method of frustrated total reflection. *Zeitschrift für Phys. A Hadron. Nucl.* **216**, 398–410 (1968).

50. Craig F. Bohren, D. R. H. *Absorption and scattering of light by small particles*. *John Wiley & Sons* (1983).

51. Lee, K. S. & El-Sayed, M. A. Gold and silver nanoparticles in sensing and imaging:

Sensitivity of plasmon response to size, shape, and metal composition. *J. Phys. Chem. B* **110**, 19220–19225 (2006).

52. Jain, P. K. & El-Sayed, M. A. Plasmonic coupling in noble metal nanostructures. *Chem. Phys. Lett.* **487**, 153–164 (2010).

53. de Sousa, N., Froufe-Pérez, L. S., Sáenz, J. J. & García-Martín, A. Magneto-Optical Activity in High Index Dielectric Nanoantennas. *Sci. Rep.* **6**, 30803 (2016).

54. Albaladejo, S. *et al.* Radiative corrections to the polarizability tensor of an electrically small anisotropic dielectric particle. *Opt. Express* **18**, 3556–67 (2010).

55. Hanarp, P., Käll, M. & Sutherland, D. S. Optical Properties of Short Range Ordered Arrays of Nanometer Gold Disks Prepared by Colloidal Lithography. *J. Phys. Chem. B* **107**, 5768–5772 (2003).

56. Abdulrahman, N. A. *et al.* Induced chirality through electromagnetic coupling between chiral molecular layers and plasmonic nanostructures. *Nano Lett.* **12**, 977–983 (2012).

57. Hentschel, M., Schäferling, M., Metzger, B. & Giessen, H. Plasmonic Diastereomers: Adding up Chiral Centers. *Nano Lett.* **13**, 600–606 (2013).

58. Shao, L. & Zheng, J. Fabrication of plasmonic nanostructures by hole-mask colloidal lithography: Recent development. *Appl. Mater. Today* **15**, 6–17 (2019).

59. Wang, Z., Cheng, F., Winsor, T. & Liu, Y. Optical chiral metamaterials: a review of the fundamentals, fabrication methods and applications. *Nanotechnology* **27**, 412001 (2016).

60. Saranathan, V. *et al.* Structure, function, and self-assembly of single network gyroid (I4132) photonic crystals in butterfly wing scales. *Proc. Natl. Acad. Sci.* **107**, 11676–11681 (2010).

61. Mendoza-Galván, A. *et al.* Mueller matrix spectroscopic ellipsometry study of chiral nanocrystalline cellulose films. *J. Opt. (United Kingdom)* **20**, (2018).

62. Arteaga, O. Natural optical activity vs circular Bragg reflection studied by Mueller matrix ellipsometry. *Thin Solid Films* **617**, 14–19 (2016).

63. Davies, N. M. & Wei Teng, X. Importance of Chirality in Drug Therapy and Pharmacy Practice: Implications for Psychiatry. *Adv. Pharm.* **1**, 242–252 (2003).

64. Eyring, H., Liu, H.-C. & Caldwell, D. Optical rotatory dispersion and circular dichroism. *Chem. Rev.* **68**, 525–540 (1968).

65. C. A. Emeis, L. J. O. and G. D. V. Numerical evaluation of Kramers—Kronig relations. *Proc. R. Soc. London. Ser. A. Math. Phys. Sci.* **297**, 54–65 (1967).

66. Boriskina, S. V. & Zheludev, N. I. *Singular and Chiral Nanoplasmonics*. *book* (Jenny Stanford Publishing, 2014). doi:10.1201/b17632

67. Govorov, A. O., Fan, Z., Hernandez, P., Slocik, J. M. & Naik, R. R. Theory of Circular Dichroism of Nanomaterials Comprising Chiral Molecules and Nanocrystals: Plasmon

Enhancement, Dipole Interactions, and Dielectric Effects. *Nano Lett.* **10**, 1374–1382 (2010).

68. Prodan, E. A Hybridization Model for the Plasmon Response of Complex Nanostructures. *Science (80-.).* **302**, 419–422 (2003).

69. Fan, Z. & Govorov, A. O. Plasmonic Circular Dichroism of Chiral Metal Nanoparticle Assemblies. *Nano Lett.* **10**, 2580–2587 (2010).

70. Shen, X. *et al.* 3D plasmonic chiral colloids. *Nanoscale* **6**, 2077 (2014).

71. Kuzyk, A., Jungmann, R., Acuna, G. P. & Liu, N. DNA Origami Route for Nanophotonics. *ACS Photonics* **5**, 1151–1163 (2018).

72. Kuzyk, A. *et al.* Reconfigurable 3D plasmonic metamolecules. *Nat. Mater.* **13**, 862–866 (2014).

73. Hentschel, M., Schäferling, M., Weiss, T., Liu, N. & Giessen, H. Three-dimensional chiral plasmonic oligomers. *Nano Lett.* **12**, 2542–2547 (2012).

74. Govorov, A. O. *et al.* Chiral nanoparticle assemblies: circular dichroism, plasmonic interactions, and exciton effects. *J. Mater. Chem.* **21**, 16806 (2011).

75. Haken, H. & Wolf, H. C. *Molecular Physics and Elements of Quantum Chemistry*. (Springer Berlin Heidelberg, 2004). doi:10.1007/978-3-662-08820-3

76. Fan, Z. & Govorov, A. O. Plasmonic Circular Dichroism of Chiral Metal Nanoparticle Assemblies. *Nano Lett.* **10**, 2580–2587 (2010).

77. Gansel, J. K. *et al.* Gold helix photonic metamaterial as broadband circular polarizer. *Science (80-.).* **325**, 1513–1515 (2009).

78. Cui, Y., Kang, L., Lan, S., Rodrigues, S. & Cai, W. Giant Chiral Optical Response from a Twisted-Arc Metamaterial. *Nano Lett.* **14**, 1021–1025 (2014).

79. Govorov, A. O. Plasmon-Induced Circular Dichroism of a Chiral Molecule in the Vicinity of Metal Nanocrystals. Application to Various Geometries. *J. Phys. Chem. C* **115**, 7914–7923 (2011).

80. Lan, X. *et al.* Au nanorod helical superstructures with designed chirality. *J. Am. Chem. Soc.* **137**, 457–462 (2015).

81. Yue, S., Liu, S., Hou, Y. & Zhang, Z. Tailorable chiral optical response through coupling among plasmonic meta-atoms with distinct shapes. *Opt. Lett.* **43**, 1111 (2018).

82. Gennaro, S. D. *et al.* The Interplay of Symmetry and Scattering Phase in Second Harmonic Generation from Gold Nanoantennas. *Nano Lett.* **16**, 5278–5285 (2016).

83. Hu, J. *et al.* All-dielectric metasurface circular dichroism waveplate. *Sci. Rep.* **7**, 1–9 (2017).

84. Jing, Z. *et al.* Tunable circular dichroism of composite metamaterial on the basis of the phase transition of VO 2. *EPL (Europhysics Lett.* **125**, 35001 (2019).

85. Neubrech, F., Hentschel, M. & Liu, N. Reconfigurable Plasmonic Chirality:

Fundamentals and Applications. *Adv. Mater.* **1905640**, (2020).

86. Leitereg, T. J., Guadagni, D. G., Harris, J., Mon, T. R. & Teranishi, R. Chemical and sensory data supporting the difference between the odors of the enantiomeric carvones. *J. Agric. Food Chem.* **19**, 785–787 (1971).

87. Valev, V. K., Baumberg, J. J., Sibilia, C. & Verbiest, T. Chirality and Chiroptical Effects in Plasmonic Nanostructures: Fundamentals, Recent Progress, and Outlook. *Adv. Mater.* **25**, 2517–2534 (2013).

88. Solomons, T. W. Graham; Fryhle, C. *Organic Chemistry*. (2004).

89. Kuwata-Gonokami, M. *et al.* Giant Optical Activity in Quasi-Two-Dimensional Planar Nanostructures. *Phys. Rev. Lett.* **95**, 227401 (2005).

90. Valev, V. K. *et al.* Plasmonic Ratchet Wheels: Switching Circular Dichroism by Arranging Chiral Nanostructures. *Nano Lett.* **9**, 3945–3948 (2009).

91. Gansel, J. K. *et al.* Gold Helix Photonic Metamaterial as Broadband Circular Polarizer. *Science (80-.).* **325**, 1513–1515 (2009).

92. Decker, M. *et al.* Strong optical activity from twisted-cross photonic metamaterials. *Opt. Lett.* **34**, 2501 (2009).

93. Liu, N., Liu, H., Zhu, S. & Giessen, H. Stereometamaterials. *Nat. Photonics* **3**, 157–162 (2009).

94. Decker, M., Zhao, R., Soukoulis, C. M., Linden, S. & Wegener, M. Twisted split-ring-resonator photonic metamaterial with huge optical activity. *Opt. Lett.* **35**, 1593 (2010).

95. Verbiest, T., Kauranen, M., Van Rompaey, Y. & Persoons, A. Optical Activity of Anisotropic Achiral Surfaces. *Phys. Rev. Lett.* **77**, 1456–1459 (1996).

96. Belardini, A. *et al.* Circular Dichroism in the Optical Second-Harmonic Emission of Curved Gold Metal Nanowires. *Phys. Rev. Lett.* **107**, 257401 (2011).

97. Noguez, C. & Garzón, I. L. Optically active metal nanoparticles. *Chem. Soc. Rev.* **38**, 757 (2009).

98. Kuzyk, A. *et al.* DNA-based self-assembly of chiral plasmonic nanostructures with tailored optical response. *Nature* **483**, 311–314 (2012).

99. Armelles, G., Cebollada, A., García-Martín, A. & González, M. U. Magnetoplasmonics: Combining Magnetic and Plasmonic Functionalities. *Adv. Opt. Mater.* **1**, 10–35 (2013).

100. Zubritskaya, I., Maccaferri, N., Inchausti Ezeiza, X., Vavassori, P. & Dmitriev, A. Magnetic Control of the Chiroptical Plasmonic Surfaces. *Nano Lett.* **18**, 302–307 (2018).

101. Maccaferri, N. *et al.* Polarizability and magnetoplasmonic properties of magnetic general nanoellipsoids. *Opt. Express* **21**, 9875 (2013).

102. González-Díaz, J. B. *et al.* Plasmonic Au/Co/Au nanosandwiches with enhanced

magneto-optical activity. *Small* **4**, 202–205 (2008).

103. Meneses-Rodríguez, D. *et al.* Probing the Electromagnetic Field Distribution within a Metallic Nanodisk. *Small* **7**, 3317–3323 (2011).

104. González-Díaz, J. B., Sepúlveda, B., García-Martín, A. & Armelles, G. Cobalt dependence of the magneto-optical response in magnetoplasmonic nanodisks. *Appl. Phys. Lett.* **97**, (2010).

105. Armelles, G. *et al.* Mimicking electromagnetically induced transparency in the magneto-optical activity of magnetoplasmonic nanoresonators. *Opt. Express* **21**, 27356 (2013).

106. De Sousa, N. *et al.* Interaction effects on the magneto-optical response of magnetoplasmonic dimers. *Phys. Rev. B - Condens. Matter Mater. Phys.* **89**, 205419 (2014).

107. Banthí, J. C. *et al.* High magneto-optical activity and low optical losses in metal-dielectric Au/Co/Au-SiO 2 magnetoplasmonic nanodisks. *Adv. Mater.* **24**, OP36-41 (2012).

108. Zubritskaya, I. *et al.* Active magnetoplasmonic ruler. *Nano Lett.* **15**, 3204–3211 (2015).

109. Kataja, M. *et al.* Surface lattice resonances and magneto-optical response in magnetic nanoparticle arrays. *Nat. Commun.* **6**, 7072 (2015).

110. Kataja, M. *et al.* Hybrid plasmonic lattices with tunable magneto-optical activity. *Opt. Express* **24**, 3652 (2016).

111. Klös, G., Andersen, A., Miola, M., Birkedal, H. & Sutherland, D. S. Oxidation controlled lift-off of 3D chiral plasmonic Au nano-hooks. *Nano Res.* **12**, 1635–1642 (2019).

112. Matuschek, M. *et al.* Chiral Plasmonic Hydrogen Sensors. *Small* **14**, 1702990 (2018).

113. Li, J. & Kotov, N. A. Circular extinction of plasmonic silver nanocaps and gas sensing. *Faraday Discuss.* **186**, 345–352 (2016).

114. Zheng, Y. B., Juluri, B. K., Mao, X., Walker, T. R. & Huang, T. J. Systematic investigation of localized surface plasmon resonance of long-range ordered Au nanodisk arrays. *J. Appl. Phys.* **103**, 1–9 (2008).

115. Ou, J.-Y., Plum, E., Zhang, J. & Zheludev, N. I. An electromechanically reconfigurable plasmonic metamaterial operating in the near-infrared. *Nat. Nanotechnol.* **8**, 252–255 (2013).

116. Cao, J., Sun, T. & Grattan, K. T. V. Gold nanorod-based localized surface plasmon resonance biosensors: A review. *Sensors Actuators, B Chem.* **195**, 332–351 (2014).

117. Yin, X. *et al.* Active Chiral Plasmonics. *Nano Lett.* **15**, 4255–4260 (2015).

118. Duan, X., Kamin, S., Sterl, F., Giessen, H. & Liu, N. Hydrogen-Regulated Chiral Nanoplasmonics. *Nano Lett.* **16**, 1462–1466 (2016).

Bibliography

119. Yan, W. *et al.* Self-assembly of chiral nanoparticle pyramids with strong R/S optical activity. *J. Am. Chem. Soc.* **134**, 15114–15121 (2012).

120. Armelles, G. *et al.* Magnetic field modulation of chirooptical effects in magnetoplasmonic structures. *Nanoscale* **6**, 3737 (2014).

121. Yannopapas, V. & Vanakaras, A. G. Strong Magnetochiral Dichroism in Suspensions of Magnetoplasmonic Nanohelices. *ACS Photonics* **2**, 1030–1038 (2015).

122. Armelles, G. *et al.* Interaction Effects between Magnetic and Chiral Building Blocks: A New Route for Tunable Magneto-chiral Plasmonic Structures. *ACS Photonics* **2**, 1272–1277 (2015).

123. Rechberger, W. *et al.* Optical properties of two interacting gold nanoparticles. *Opt. Commun.* **220**, 137–141 (2003).

124. Fredriksson, H. *et al.* Hole–Mask Colloidal Lithography. *Adv. Mater.* **19**, 4297–4302 (2007).

125. Jain, P. K., Huang, W. & El-Sayed, M. A. On the Universal Scaling Behavior of the Distance Decay of Plasmon Coupling in Metal Nanoparticle Pairs: A Plasmon Ruler Equation. *Nano Lett.* **7**, 2080–2088 (2007).

126. Xu, L., Sun, M., Ma, W., Kuang, H. & Xu, C. Self-assembled nanoparticle dimers with contemporarily relevant properties and emerging applications. *Mater. Today* **19**, 595–606 (2016).

127. Tabor, C., Haute, D. Van & El-Sayed, M. A. Effect of orientation on plasmonic coupling between gold nanorods. *ACS Nano* **3**, 3670–3678 (2009).

128. Taubert, R., Ameling, R., Weiss, T., Christ, A. & Giessen, H. From Near-Field to Far-Field Coupling in the Third Dimension: Retarded Interaction of Particle Plasmons. *Nano Lett.* **11**, 4421–4424 (2011).

129. Esposito, M. *et al.* Nanoscale 3D chiral plasmonic helices with circular dichroism at visible frequencies. *ACS Photonics* **2**, 105–114 (2015).

130. Yeom, B. *et al.* Chiral plasmonic nanostructures on achiral nanopillars. *Nano Lett.* **13**, 5277–5283 (2013).

131. He, Y., Larsen, G. K., Ingram, W. & Zhao, Y. Tunable three-dimensional helically stacked plasmonic layers on nanosphere monolayers. *Nano Lett.* **14**, 1976–1981 (2014).

132. Mark, A. G., Gibbs, J. G., Lee, T.-C. & Fischer, P. Hybrid nanocolloids with programmed three-dimensional shape and material composition. *Nat. Mater.* **12**, 802–807 (2013).

133. Tan, S. J., Campolongo, M. J., Luo, D. & Cheng, W. Building plasmonic nanostructures with DNA. *Nat. Nanotechnol.* **6**, 268–276 (2011).

134. Kuzyk, A. *et al.* A light-driven three-dimensional plasmonic nanosystem that translates molecular motion into reversible chiroptical function. *Nat. Commun.* **7**, 10591 (2016).

Bibliography

135. Ma, W. *et al.* Chiral plasmonics of self-assembled nanorod dimers. *Sci. Rep.* **3**, 1934 (2013).

136. Cecconello, A. *et al.* DNA Scaffolds for the Dictated Assembly of Left-/Right-Handed Plasmonic Au NP Helices with Programmed Chiro-Optical Properties. *J. Am. Chem. Soc.* **138**, 9895–9901 (2016).

137. Fasold, S. *et al.* Disorder-Enabled Pure Chirality in Bilayer Plasmonic Metasurfaces. *ACS Photonics* **5**, 1773–1778 (2018).

138. Yin, X., Schäferling, M., Metzger, B. & Giessen, H. Interpreting Chiral Nanophotonic Spectra: The Plasmonic Born–Kuhn Model. *Nano Lett.* **13**, 6238–6243 (2013).

139. Guerrero-Martínez, A., Alonso-Gómez, J. L., Auguié, B., Cid, M. M. & Liz-Marzán, L. M. From individual to collective chirality in metal nanoparticles. *Nano Today* **6**, 381–400 (2011).

140. Wang, L.-Y. Y. *et al.* Circular Differential Scattering of Single Chiral Self-Assembled Gold Nanorod Dimers. *ACS Photonics* **2**, 1602–1610 (2015).

141. Azizi, A., Ranjbar, B., Moghadam, T. T. & Bagheri, Z. Plasmonic Circular Dichroism Study of DNA–Gold Nanoparticles Bioconjugates. *Plasmonics* **9**, 273–281 (2014).

142. Sveinsson, H. Modelling of multimode and layer structure by transfermatrices. *tesis* (2010).

143. Frederiksen, M., Bochenkov, V. E., Ogaki, R. & Sutherland, D. S. Onset of bonding plasmon hybridization preceded by gap modes in dielectric splitting of metal disks. *Nano Lett.* **13**, 6033–6039 (2013).

144. Meneses-Rodríguez, D., Armelles, G. & Cebollada, A. From disk to ring: Aspect ratio control of the magnetoplasmonic response in Au/Co/Au nanostructures fabricated by hole-mask colloidal lithography. *Appl. Phys. Lett.* **106**, 083105 (2015).

145. Verre, R. *et al.* Directional Light Extinction and Emission in a Metasurface of Tilted Plasmonic Nanopillars. *Nano Lett.* **16**, 98–104 (2016).

146. Jana, D. *et al.* Tunable Au-Ag nanobowl arrays for size-selective plasmonic biosensing. *Analyst* **141**, 4870–4878 (2016).

147. Bochenkov, V. E. & Sutherland, D. S. From rings to crescents: A novel fabrication technique uncovers the transition details. *Nano Lett.* **13**, 1216–1220 (2013).

148. de Dios, C. *et al.* Mueller matrix study of the dichroism in nanorods dimers: rod separation effects. *Opt. Express* **27**, 21142 (2019).

149. Sani, S. R., Persson, J., Dmitriev, A., Käll, M. & Åkerman, J. Hole mask colloidal lithography on magnetic multilayers for spin torque applications. *J. Phys. Conf. Ser.* **200**, (2010).

150. Chen, S., Svedendahl, M., Duyne, R. P. V. & Käll, M. Plasmon-enhanced colorimetric ELISA with single molecule sensitivity. *Nano Lett.* **11**, 1826–1830 (2011).

151. Niesen, B. *et al.* Plasmonic efficiency enhancement of high performance organic solar

cells with a nanostructured rear electrode. *Adv. Energy Mater.* **3**, 145–150 (2013).

152. Mendes, M. J. *et al.* Self-organized colloidal quantum dots and metal nanoparticles for plasmon-enhanced intermediate-band solar cells. *Nanotechnology* **24**, (2013).

153. Pennanen, A. M. & Toppari, J. J. Direct optical measurement of light coupling into planar waveguide by plasmonic nanoparticles. *Opt. Express* **21**, A23 (2013).

154. Jönsson, G. *et al.* Solar Transparent Radiators by Optical Nanoantennas. *Nano Lett.* **17**, 6766–6772 (2017).

155. Dubas, S. T. & Schlenoff, J. B. Factors controlling the growth of polyelectrolyte multilayers. *Macromolecules* **32**, 8153–8160 (1999).

156. Cataldo, S. *et al.* Hole-mask colloidal nanolithography for large-area low-cost metamaterials and antenna-assisted surface-enhanced infrared absorption substrates. *ACS Nano* **6**, 979–985 (2012).

157. Syrenova, S., Wadell, C. & Langhammer, C. Shrinking-hole colloidal lithography: Self-aligned nanofabrication of complex plasmonic nanoantennas. *Nano Lett.* **14**, 2655–2663 (2014).

158. Frey, H. & Khan, H. R. *Handbook of Thin-Film Technology*. *Handbook of Thin-Film Technology* (Springer Berlin Heidelberg, 2015). doi:10.1007/978-3-642-05430-3

159. Saito, K. & Tatsuma, T. Chiral Plasmonic Nanostructures Fabricated by Circularly Polarized Light. *Nano Lett.* **18**, 3209–3212 (2018).

160. Savale, P. A. Physical Vapor Deposition (PVD) Methods for Synthesis of Thin Films: A Comparative Study. *Arch. Appl. Sci. Res.* **8**, 1–8 (2016).

161. Seshan, K. *Handbook of Thin Film Deposition*. *Book* (Elsevier, 2012). doi:10.1016/C2009-0-64359-2

162. Binnig, G., Quate, C. F. & Gerber, C. Atomic Force Microscope. *Phys. Rev. Lett.* **56**, 930–933 (1986).

163. von Ardenne, M. Das Elektronen-Rastermikroskop. *Zeitschrift für Phys.* **109**, 553–572 (1938).

164. Instituto de Micro y Nanotecnología. http://www.imn.cnm.csic.es/en/noticias/detalle/21. (2019).

165. Fujiwara, H. *Spectroscopic Ellipsometry*. *Wiley* (John Wiley & Sons, Ltd, 2007). doi:10.1002/9780470060193

166. Oates, T. W. H., Wormeester, H. & Arwin, H. Characterization of plasmonic effects in thin films and metamaterials using spectroscopic ellipsometry. *Prog. Surf. Sci.* **86**, 328–376 (2011).

167. Garcia-Caurel, E., De Martino, A., Gaston, J.-P. & Yan, L. Application of Spectroscopic Ellipsometry and Mueller Ellipsometry to Optical Characterization.

168. Postava, K., Sýkora, R., Legut, D. & Pištora, J. Determination of Anisotropic Crystal

Optical Properties Using Mueller Matrix Spectroscopic Ellipsometry. *Procedia Mater. Sci.* **12**, 118–123 (2016).

169. Dreher, A. W., Reiter, K. & Weinreb, R. N. Spatially resolved birefringence of the retinal nerve fiber layer assessed with a retinal laser ellipsometer. *Appl. Opt.* **31**, 3730 (1992).

170. Wang, M., Gompf, B., Dressel, M., Destouches, N. & Berrier, A. Pure circular dichroism by curved rows of plasmonic nanoparticles. *Opt. Mater. Express* **8**, 1515 (2018).

171. J. A. Wollam Co. Inc. https://www.jawoollam.com/. doi:https://www.jawoollam.com/

172. J. A. Wollam Co. Inc. *CompleteEASE ™ Data Analysis Manual*. (2011).

173. Schubert, M. Polarization-dependent optical parameters of arbitrarily anisotropic homogeneous layered systems. *Phys. Rev. B* **53**, 4265–4274 (1996).

174. Bruggeman, D. A. G. Berechnung verschiedener physikalischer Konstanten von heterogenen Substanzen. I. Dielektrizitätskonstanten und Leitfähigkeiten der Mischkörper aus isotropen Substanzen. *Ann. Phys.* **416**, 636–664 (1935).

175. Clark Jones, R. A New Calculus for the Treatment of Optical Systems IV. *J. Opt. Soc. Am.* **32**, 486 (1942).

176. Menzel, C., Rockstuhl, C. & Lederer, F. Advanced Jones calculus for the classification of periodic metamaterials. *Phys. Rev. A* **82**, 053811 (2010).

177. Singh, R. *et al.* Terahertz metamaterial with asymmetric transmission. *Phys. Rev. B - Condens. Matter Mater. Phys.* **80**, 4–7 (2009).

178. Tompkins, H. G. & Irene, E. A. *Handbook of Ellipsometry*. (Springer Berlin Heidelberg, 2005). doi:10.1007/3-540-27488-X

179. Arteaga, O. & Canillas, A. Pseudopolar decomposition of the Jones and Mueller-Jones exponential polarization matrices. *J. Opt. Soc. Am. A* **26**, 783 (2009).

180. Le Roy-Brehonnet, F. & Le Jeune, B. Utilization of Mueller matrix formalism to obtain optical targets depolarization and polarization properties. *Prog. Quantum Electron.* **21**, 109–151 (1997).

181. Laskarakis, A., Logothetidis, S., Pavlopoulou, E. & Gioti, M. Mueller matrix spectroscopic ellipsometry: Formulation and application. *Thin Solid Films* **455–456**, 43–49 (2004).

182. Agarwal, N. *et al.* Spatial evolution of depolarization in homogeneous turbid media within the differential Mueller matrix formalism. *Opt. Lett.* **40**, 5634 (2015).

183. Arteaga, O. & Kahr, B. Characterization of homogenous depolarizing media based on Mueller matrix differential decomposition. *Opt. Lett.* **38**, 1134–6 (2013).

184. Devlaminck, V. Physical model of differential Mueller matrix for depolarizing uniform media. *J. Opt. Soc. Am. A* **30**, 2196 (2013).

Bibliography

185. Schmidt, D., Briley, C., Schubert, E. & Schubert, M. Vector magneto-optical generalized ellipsometry for sculptured thin films. *Appl. Phys. Lett.* **102**, 123109 (2013).

186. Chandel, S. *et al.* Mueller matrix spectroscopy of fano resonance in plasmonic oligomers. *Opt. Commun.* **432**, 84–90 (2019).

187. Wang, M., Löhle, A., Gompf, B., Dressel, M. & Berrier, A. Physical interpretation of Mueller matrix spectra: a versatile method applied to gold gratings. *Opt. Express* **25**, 6983 (2017).

188. Arwin, H. *et al.* Structural circular birefringence and dichroism quantified by differential decomposition of spectroscopic transmission Mueller matrices from Cetonia aurata. *Opt. Lett.* **41**, 3293 (2016).

189. Mendoza-Galván, A., del Río, L. F., Järrendahl, K. & Arwin, H. Graded pitch profile for the helicoidal broadband reflector and left-handed circularly polarizing cuticle of the scarab beetle Chrysina chrysargyrea. *Sci. Rep.* **8**, 6456 (2018).

190. Azzam, R. M. A. Propagation of partially polarized light through anisotropic media with or without depolarization: A differential 4 × 4 matrix calculus. *J. Opt. Soc. Am.* **68**, 1756 (1978).

191. Arteaga, O. & Canillas, A. Analytic inversion of the Mueller-Jones polarization matrices for homogeneous media. *Opt. Lett.* **35**, 559 (2010).

192. Nordén, B. Applications of linear Dichroism Spectroscopy. *Appl. Spectrosc. Rev.* **14**, 157–248 (1978).

193. Rodger, A., Dorrington, G. & Ang, D. L. Linear dichroism as a probe of molecular structure and interactions. *Analyst* **141**, 6490–6498 (2016).

194. R. M. A. Azzam, N. M. B. *Ellipsometry and Polarized Light*. *North-Holland Pub. Co.* (1987).

195. Schellman, J. & Jensen, H. P. Optical spectroscopy of oriented molecules. *Chem. Rev.* **87**, 1359–1399 (1987).

196. Thomas, A. *et al.* Mueller Polarimetry of Chiral Supramolecular Assembly. *J. Phys. Chem. C* **122**, 14205–14212 (2018).

197. Kim, M., Ulibarri, L. & Bustamante, C. Differential polarization imaging. II. Symmetry properties and calculations. *Biophys. J.* **52**, 929–946 (1987).

198. Schulz, M. *et al.* Giant intrinsic circular dichroism of prolinol-derived squaraine thin films. *Nat. Commun.* **9**, 2413 (2018).

199. Guerrero-Martínez, A. *et al.* Intense Optical Activity from Three-Dimensional Chiral Ordering of Plasmonic Nanoantennas. *Angew. Chemie Int. Ed.* **50**, 5499–5503 (2011).

200. Singh, J. H., Nair, G., Ghosh, A. A. A. & Ghosh, A. A. A. Wafer scale fabrication of porous three-dimensional plasmonic metamaterials for the visible region: Chiral and beyond. *Nanoscale* **5**, 7224–7228 (2013).

Bibliography

201. Kong, X.-T., Besteiro, L. V., Wang, Z. & Govorov, A. O. Plasmonic Chirality and Circular Dichroism in Bioassembled and Nonbiological Systems: Theoretical Background and Recent Progress. *Adv. Mater.* **1801790**, 1801790 (2018).

202. Arteaga, O. Useful Mueller matrix symmetries for ellipsometry. *Thin Solid Films* **571**, 584–588 (2014).

203. Berova, N., Bari, L. Di & Pescitelli, G. Application of electronic circular dichroism in configurational and conformational analysis of organic compounds. *Chem. Soc. Rev.* **36**, 914–931 (2007).

204. Zhao, Y. *et al.* Chirality detection of enantiomers using twisted optical metamaterials. *Nat. Commun.* **8**, 14180 (2017).

205. Berova, N., Polavarapu, P. L., Nakanishi, K. & Woody, R. W. *Comprehensive Chiroptical Spectroscopy*. *Analysis* **1**, (John Wiley & Sons, Inc., 2011).

206. Qin, J. *et al.* Switching the Optical Chirality in Magnetoplasmonic Metasurfaces Using Applied Magnetic Fields. *ACS Nano* **14**, 2808–2816 (2020).

207. Barron, L. D. *Molecular Light Scattering and Optical Activity*. *book* (Cambridge University Press, 2004). doi:10.1017/CBO9780511535468

208. Smith, K. W. *et al.* Chiral and Achiral Nanodumbbell Dimers: The Effect of Geometry on Plasmonic Properties. *ACS Nano* **10**, 6180–6188 (2016).

209. Lu, X. *et al.* Circular dichroism from single plasmonic nanostructures with extrinsic chirality. *Nanoscale* **6**, 14244–14253 (2014).

210. Ogier, R., Fang, Y., Svedendahl, M., Johansson, P. & Käll, M. Macroscopic Layers of Chiral Plasmonic Nanoparticle Oligomers from Colloidal Lithography. *ACS Photonics* **1**, 1074–1081 (2014).

211. Liu, J., Yang, L. & Huang, Z. Chiroptically Active Plasmonic Nanoparticles Having Hidden Helicity and Reversible Aqueous Solvent Effect on Chiroptical Activity. *Small* **12**, 5902–5909 (2016).

212. Lu, J. *et al.* Chiral Plasmonic Nanochains via the Self-Assembly of Gold Nanorods and Helical Glutathione Oligomers Facilitated by Cetyltrimethylammonium Bromide Micelles. *ACS Nano* **11**, 3463–3475 (2017).

213. Ma, W. *et al.* Attomolar DNA detection with chiral nanorod assemblies. *Nat. Commun.* **4**, 1–8 (2013).

214. Hauge, P. S. & Dill, F. H. A rotating-compensator fourier ellipsometer. *Opt. Commun.* **14**, 431–437 (1975).

215. J.A. Woollam Co. https://www.jawoollam.com/products/m-2000-ellipsometer.

216. Faraday, M. I. Experimental researches in electricity.—Nineteenth series. *Philos. Trans. R. Soc. London* **136**, 1–20 (1846).

217. Kerr, J. XLIII. On rotation of the plane of polarization by reflection from the pole of a magnet. *London, Edinburgh, Dublin Philos. Mag. J. Sci.* **3**, 321–343 (1877).

Bibliography

218. Sepúlveda, B., Huttel, Y., Martínez Boubeta, C., Cebollada, A. & Armelles, G. Linear and quadratic magneto-optical Kerr effects in continuous and granular ultrathin monocrystalline Fe films. *Phys. Rev. B* **68**, 064401 (2003).

219. Voigt, W. *Magneto- und elektrooptik*. (Leipzig, B. G. Teubner, 1908).

220. Pershan, P. S. Magneto-optical effects. *J. Appl. Phys.* **38**, 1482–1490 (1967).

221. Stupakiewicz, A. *et al.* Direct imaging of the magnetization reversal in microwires using all-MOKE microscopy. *Rev. Sci. Instrum.* **85**, 103702 (2014).

222. Smith, A. J., Jaramillo, D. E. & Osorio, J. Revisión del efecto Kerr magneto óptico. *Rev. Mex. Fis. E* **55**, 61–69 (2009).

223. Sugano, S. & Kojima, N. *Magneto-Optics*. **128**, (Springer, 2000).

224. Zvezdin, A. K. & Kotov, V. A. *Modern Magnetooptics and Magnetooptical Materials*. *Modern Magnetooptics and Magnetooptical Materials* (IOP Publishing Ltd, 1997). doi:10.1887/075030362x

225. Martín, J. I., Nogués, J., Liu, K., Vicent, J. L. & Schuller, I. K. Ordered magnetic nanostructures: Fabrication and properties. *J. Magn. Magn. Mater.* **256**, 449–501 (2003).

226. Kikuchi, Y. & Tanaka, T. Strengthen of magnetic anisotropy of Au/Co/Au nanostructure by surface plasmon resonance. *Sci. Rep.* **9**, 1–7 (2019).

227. Armelles, G. *et al.* Magnetoplasmonic nanostructures: systems supporting both plasmonic and magnetic properties. *J. Opt. A Pure Appl. Opt.* **11**, 114023 (2009).

228. Višňovský, Š. *et al.* Polar magneto-optics in simple ultrathin-magnetic-film structures. *Phys. Rev. B* **52**, 1090–1106 (1995).

229. Arteaga, O. Number of independent parameters in the Mueller matrix representation of homogeneous depolarizing media. *Opt. Lett.* **38**, 1131–3 (2013).

230. Feng, H. Y., Armelles, G., Cebollada, A. & Luo, F. From disk to ring: Aspect ratio control of the magnetoplasmonic response in Au/Co/Au nanostructures fabricated by hole-mask colloidal lithography. *Appl. Phys. Lett.* **106**, 083105 (2015).

231. Knechtel, J. *et al.* Toward Physically Unclonable Functions From Plasmonics-Enhanced Silicon Disc Resonators. *J. Light. Technol.* **37**, 3805–3814 (2019).

232. Rahmani, M. *et al.* Beyond the Hybridization Effects in Plasmonic Nanoclusters: Diffraction-Induced Enhanced Absorption and Scattering. *Small* **10**, 576–583 (2014).

233. Aćimović, S. S., Kreuzer, M. P., González, M. U. & Quidant, R. Plasmon near-field coupling in metal dimers as a step toward single-molecule sensing. *ACS Nano* **3**, 1231–1237 (2009).

234. Verre, R. *et al.* Polarization conversion-based molecular sensing using anisotropic plasmonic metasurfaces. *Nanoscale* **8**, 10576–10581 (2016).

235. Ghosh, P. K., Debu, D. T., French, D. A. & Herzog, J. B. Calculated thickness dependent

plasmonic properties of gold nanobars in the visible to near-infrared light regime. *PLoS One* **12**, e0177463 (2017).

236. Song, M. *et al.* Polarization properties of surface plasmon enhanced photoluminescence from a single Ag nanowire. *Opt. Express* **20**, 22290 (2012).

237. Miller, M. M. & Lazarides, A. A. Sensitivity of Metal Nanoparticle Surface Plasmon Resonance to the Dielectric Environment. *J. Phys. Chem. B* **109**, 21556–21565 (2005).

238. Khlebtsov, N. G., Trachuk, L. A. & Mel'nikov, A. G. The effect of the size, shape, and structure of metal nanoparticles on the dependence of their optical properties on the refractive index of a disperse medium. *Opt. Spectrosc.* **98**, 77–83 (2005).

239. Vavassori. Magneto-Plasmonic Nanostructures and Crystals. *Proceedings* **26**, 2 (2019).

240. Ban, Z., Barnakov, Y. A., Li, F., Golub, V. O. & O'Connor, C. J. The synthesis of core-shell iron@gold nanoparticles and their characterization. *J. Mater. Chem.* **15**, 4660–4662 (2005).

241. Zhang, J. *et al.* Laser-assisted synthesis of superparamagnetic Fe@Au core-shell nanoparticles. *J. Phys. Chem. B* **110**, 7122–7128 (2006).

242. Sobal, N. S. *et al.* Synthesis and Structure of Colloidal Bimetallic Nanocrystals: The Non-Alloying System Ag/Co. *Nano Lett.* **2**, 621–624 (2002).

243. Khlebtsov, B. N. & Khlebtsov, N. G. Multipole plasmons in metal nanorods: Scaling properties and dependence on particle size, shape, orientation, and dielectric environment. *J. Phys. Chem. C* **111**, 11516–11527 (2007).

244. Wen, F. *et al.* Plasmon transmutation: Inducing new modes in nanoclusters by adding dielectric nanoparticles. *Nano Lett.* **12**, 5020–5026 (2012).

245. Hentschel, M. *et al.* Transition from Isolated to Collective Modes in Plasmonic Oligomers. *Nano Lett.* **10**, 2721–2726 (2010).

246. Rahmani, M. *et al.* Nonlinear Symmetry Breaking in Symmetric Oligomers. *ACS Photonics* **4**, 454–461 (2017).

247. Rahmani, M. *et al.* Influence of symmetry breaking in pentamers on Fano resonance and near-field energy localization. *Opt. Mater. Express* **1**, 1409 (2011).

248. Ferry, P. P. and V. E. Tunable optical chirality in a metamaterial platform with off-resonantly coupled metal – dielectric components. *Opt. Express* **26**, 17289–17296 (2018).

249. Maccaferri, N. *et al.* Nanoscale magnetophotonics. *J. Appl. Phys.* **127**, (2020).

250. Gosciniak, J. *et al.* Thermo-optic control of dielectric-loaded plasmonic waveguide components. **18**, 1207–1216 (2010).

251. Parys, W. Van, Member, S., Thourhout, D. Van & Baets, R. Amplifying Waveguide Optical Isolator With an. **19**, 1949–1951 (2007).

252. Kimel, A. V *et al.* Ultrafast non-thermal control of magnetization by instantaneous

photomagnetic pulses. **435**, 655–657 (2005).

253. Kong, X. T., Besteiro, L. V., Wang, Z. & Govorov, A. O. Plasmonic Chirality and Circular Dichroism in Bioassembled and Nonbiological Systems: Theoretical Background and Recent Progress. *Adv. Mater.* **1801790**, 1–14 (2018).

254. Fan, Z. & Govorov, A. O. Plasmonic Circular Dichroism of Chiral Metal Nanoparticle Assemblies. *Nano Lett.* **10**, 2580–2587 (2010).

255. Eslami, S. *et al.* Chiral Nanomagnets. *ACS Photonics* **1**, 1231–1236 (2014).

256. Palik, E. *Handbook of Optical Constants of Solids*. (Elsevier, 1985). doi:10.1016/C2009-0-20920-2

257. Wang, Z. *et al.* Circular Dichroism Metamirrors with Near-Perfect Extinction. *ACS Photonics* **3**, 2096–2101 (2016).

258. Tian, M. *et al.* Plasmon hybridization in stacked nanorods dimer. *Opt. Commun.* **311**, 20–25 (2013).

259. Syrenova, S., Wadell, C. & Langhammer, C. Shrinking-hole colloidal lithography: Self-aligned nanofabrication of complex plasmonic nanoantennas. *Nano Lett.* **14**, 2655–2663 (2014).

260. Fujiwara, H. Appendix 4: Jones–Mueller Matrix Conversion. in *Spectroscopic Ellipsometry* 353–355 (John Wiley & Sons, Ltd, 2007). doi:10.1002/9780470060193.app4

261. Arteaga, O. *et al.* Relation between 2D/3D chirality and the appearance of chiroptical effects in real nanostructures. *Opt. Express* **24**, 2242 (2016).

262. Auguié, B., Alonso-Gómez, J. L., Guerrero-Martínez, A. & Liz-Marzán, L. M. Fingers Crossed: Optical Activity of a Chiral Dimer of Plasmonic Nanorods. *J. Phys. Chem. Lett.* **2**, 846–851 (2011).

263. Lumerical Inc. https://www.lumerical.com/products.

264. Johnson, P. B. & Christy, R. W. Optical constants of the noble metals. *Phys. Rev. B* **6**, 4370–4379 (1972).

Bibliography

10. LIST OF PUBLICATIONS

This work has produced the following papers

1. *Mueller matrix study of the dichroism in nanorods dimers: rod separation effects*
   Carolina de Dios, Alba Jiménez, Fernando García, Antonio García-Martín, Alfonso Cebollada and Gaspar Armelles
   Optics Express Volume: 27 Issue: 15 Pages: 21142 (2019)

2. *Analysis of the Optical Properties of Chiral Au Nanorod Stacks*
   Carolina de Dios, Hua Yu Feng, Fernando García, Alfonso Cebollada and Gaspar Armelles.
   Plasmonics, Volume: 13 Issue: 6 Pages: 2061 (2018)

3. *Analysis and magnetic modulation of chiro-optical properties in anisotropic chiral and magneto-chiral plasmonic systems*
   Hua Yu Feng, **Carolina de Dios**, Fernando García, Alfonso Cebollada and Gaspar Armelles.
   Optics Express, Volume: 25 Issue: 25 Page 31045 (2017)